NPL REPORT CIRM 42

Proceedings of NPL Workshop on Recent Advances in Calorimetric Absorbed Dose Standards.

Edited by A J Williams and K E Rosser

Workshop held December 8 - 10 1999

Proceedings of NPL Workshop on Recent Advances in Calorimetric Absorbed Dose Standards

Edited by
A J Williams and K E Rosser

December 2000

ISSN 1369-6793

National Physical Laboratory
Teddington, Middlesex, UK, TW11 0LW

Approved on behalf of Managing Director, NPL,
by Martyn Sené, Head of Centre, Centre for Ionising Radiation Metrology.

CONTENTS

From left to right: Ian Stoker, Andrew Williams, Malcolm McEwen, Tony Aalbers, Marc Pieksma, Achim Krauss, Gerhard Stucki, Jileen Shobe, Josianne Daures, Bob Huntley, Alan DuSautoy, Joakim Medin, David Burns, Hugo Palmans, Carl Ross, Antonia Guerra and Aimé Ostrowsky. Not present in photograph: Noriah Mod Ali, Beate Planskoy, Jan Seuntjens.

LIST OF PARTICIPANTS

Aalbers, Tony,	aaalbers@nmi.nl, NMi Van Swinden Laboratorium, PO Box 654, Delft, 2600AR Delft, Netherlands.
Mod Ali, Noriah,	noriaha@mint.gov.my, Malaysian Institute for Nuclear Technology Research (MINT), Bangi 43000, Kajang, Malaysia
Burns, David,	dtb@si.bipm.fr, Bureau International des Poids et Mesures (BIPM), Pavillion de Breteull, F-92310 Sèvres Cedex, France
Daures, Josiane,	josiane.daures@cea.fr, BNM-LNHB, CEN Sac Pay BP No. 52, Gif sur Yvette, 91993 Gif sur Yvette, France
Duane, Simon,	simon.duane@npl.co.uk, NPL, Queens Road, Teddington, Middlesex, TW11 0LW, UK
DuSautoy, Alan,	Alan.Dusautoy@npl.co.uk, NPL, Queens Road, Teddington, Middlesex, TW11 0LW, UK
Gall, Ken,	gall@simmons.swmed.edu, UTSW Medical Center, 5323 Harry Hines Blvd, Dallas, Texas, TX 75235-9122, USA
Guerra, Antonio,	guerra@casaccia.enea.it, ENEA - INMRI, via Angvillarese 301 00060 S. Maria di Galeria, Roma, Italy
Huntley, Robert,	robert.huntley@health.gov.au, ARPANSA, Lower Plenty Road Yallambie, Victoria, Victoria 3085, Australia
Krauss, Achim,	achim.krauss@ptb.de, PTB, Bundesallee 100, Postfach 3345, Braunschweig, 38028 Braunschweig, Germany
McEwen, Malcolm,	Malcolm.Mcewen@npl.co.uk, NPL, Queens Road, Teddington, Middlesex, TW11 0LW, UK
Medin , Joakim,	Joakim.Medin@rfa.mas.lu.se, Dept. of Radiation Physics, Malmö University Hospital, SE-205 02 MALMÖ, SWEDEN
Ostrowsky, Aimé ,	aime.ostrowsky@cea.fr, BNM-LNHB, Cen Sac Pay BP No. 52, Gif sur Yvette, 91193 Gif sur Yvette, France
Palmans, Hugo,	hugo.palmans@rug.ac.be, University of Gent, Proeftuinstraat 86, Gent, B900 Gent, Belgium
Pieksma, Marc,	mpieksma@nmi.nl, NMi Van Swinden Laboratorium, Princetonplein 1, Utrecht, 3584 CC Utrecht, Netherlands
Planskoy, Beate,	beate@medphys.ucl.ac.uk, University College London, 1st Floor Shropshire House, 11-20 Capper Streer, London, WC1E 6JA, United Kingdom
Ross, Carl,	carl.ross@nrc.ca, National Research Council Canada, Montral Road M-35, Ottawa, ON, K1A 0R6, Canada
Seuntjens, Jan,	jseuntjens@medphys.mcgill.ca, McGill University, Medical Physics Unit, Montreal General Hospital, 1650 Cedar Av., Montreal, Quebec, CANADA, H3G 1A4
Sharpe, Peter,	Peter.Sharpe@npl.co.uk, NPL, Queens Road, Teddington, Middlesex, TW11 0LW, UK
Shobe, Jileen,	shobe@nist.gov, N.I.S.T, 100 Bureau Drive Stop 8460, Gaithersburg, MD, MD 20899, USA
Stoker, Ian,	ian.stoker@npl.co.uk, NPL, Queens Road, Teddington, Middlesex, TW11 0LW, UK
Stucki, Gerhard,	gerhard.stucki@eam.admin.ch, Swiss Federal Office for Metrology (OFMET), Lindenweg 50, Bern-Wabern, CH-3003, Switzerland
Thomas, Russell,	russell.thomas@npl.co.uk, NPL, Queens Road, Teddington, Middlesex, TW11 0LW, UK
Williams, Andrew,	aw@rpunn.org.uk, Norfolk and Norwich Health Care NHS Trust, Brunswick Road, Norwich, NR1 3SR, UK

A Real-time Graphite Calorimeter

N. Mod Ali[1], F.A. Smith[2] and M.R. McEwen[3]
[1] MINT, Malaysia, [2] Queen Mary and Westfield College, UK, [3] NPL, UK

Abstract

A real-time calorimeter for use with a self-shielded radiation processing facility is described. The prototype graphite calorimeter, having the capability to include thin film dosimeters in front of the graphite core, was designed to fulfil the requirement for a reliable method of dose assessment for electron energies down to 200 keV.

The system was designed to incorporate a datalogger for use on a self-shielded facility such as the EBC-200 irradiator at MINT. With this technique, the calorimeter could start logging temperature a short time before it passed under the beam and the data could be retrieved at any time after the calorimeter had emerged from the irradiator.

I. INTRODUCTION

The increasing use of the low energy electron beams (~ 200 to 500 keV) for industrial processing presents unique problems in the monitoring and diagnosis of the radiation field of interest. Electron accelerators at these energies are generally able to produce much higher dose-rates at shallow depths (~ 20 - 80 mg.cm^{-2}) than the higher energy electron or radionuclide-based facilities. Higher dose-rates at shallow depths in a material restrict the choice of a dosimeter system, both for dose measurement and for the calibration of routine dosimeters at low-energy electron facilities. The small thicknesses of dye films make these the most suitable candidates.

Although thin dye films (down to a few 10's of micrometres) provide an advantage as routine dosimeters because they do not perturb the electron spectrum to any great extent, most rely on a calibration carried out at low dose-rate, high energy electron or ^{60}Co photon beams. This is clearly inadequate for high dose-rate, low energy electron irradiations, since some of the film dosimeters are known to be dose-rate dependent. Very little standardization has been carried out in this area, so a suitable dosimeter is increasingly necessary if the output of industrial low-energy electron sources are to be properly standardized.

A prototype of a real-time low energy graphite calorimeter was designed and fabricated for determining the electron energy fluence (electron energy per unit area) together with the simultaneous irradiation of a thin film dosimeter. The work was initiated by the Malaysian Institute for Nuclear Technology Research (MINT) and the Radiation Physics Group of Queen Mary and Westfield College, in collaboration with the National Physical Laboratory. The standard package, containing a graphite core, thermistor and data-logger, was tested at the MINT electron beam facilities. These used a scanned beam at 500 keV and a self-shielded electron irradiator at 200 keV. The system proved to be a useful reference dosimeter, especially for the self-shielded facility, in the calibration of both the machine output and the standardization of routine film dosimeters.

II. EXPERIMENTAL

A. Calorimeter Design

A cross-section of the calorimeter (Figure 1) shows the graphite core, 50 mm in diameter and 2 mm in thickness, enclosed by a graphite scatter ring. The entire graphite system rests on a 14 mm thick polystyrene foam block. Thermal

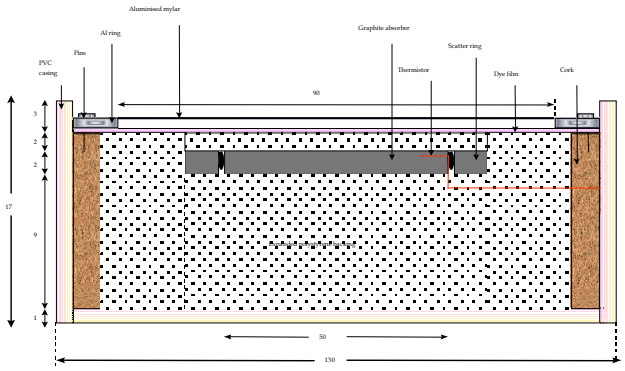

Figure 1: Schematic cross-section of calorimeter

insulation above the graphite core is achieved with a 1 mm thickness of polystyrene foam and a 8 μm thick aluminized mylar film stretched across an aluminium ring. These minimize the upward heat losses from the core, mostly caused by the compressed air cooling of the accelerator window.

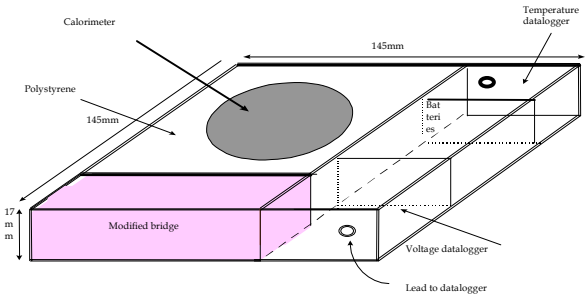

Figure 2: The real-time low-energy electron calorimter

A 0.5 mm diameter thermistor was used as a temperature sensor. This was connected to one arm of a Wheatstone bridge whose out-of-balance voltage was detected using a commercially available "TINYTALK" voltage data-logger. The latter was incorporated within the complete calorimeter assembly (Figure 2). By using suitable circuitry it was possible to increase the equivalent temperature resolution of the voltage data-logger to 0.09 ˚C.

The system could be set to start logging temperature a short time before the calorimeter passed under the beam and to continue taking data until well after the end of the irradiation. Data could be retrieved at anytime after the calorimeter had emerged from the irradiator. With the window-based host software, the off-loaded data could be viewed, saved, printed or exported to another program if desired. The data-logger, bridge and batteries were all contained within the same PVC box as the calorimeter and were shielded from the radiation by a thin sheet of lead.

B. Irradiation Facilities

Irradiation at 200 keV was performed using the Electron Beam Curetron (EBC-200-AAC) with a 17.5 μm titanium window. This is a self-shielded accelerator, producing energies between 150 and 200 keV and beam currents from 2 to 20 mA. Irradiation at 500 keV could be carried out at the Electron Processing System (EPS-3000) with energies in the range 0.5 to 3 MeV. This system has a 50 μm titanium window and a distance between the surface of calorimeter to the beam window that was adjusted to be 20 cm.

C. Calibration of Film Dosimeters

The design of the calorimeter provided an opportunity to insert thin film dosimeters, e.g. cellulose triacetate (CTA) and blue cellophane (BC), in between the graphite core and the aluminized thermal mylar reflector. Calibration of the thin film dosimeters - CTA of thickness 125 μm and BC of thickness 25 μm - was accomplished by the sequential measurement of temperature rise with and without the insertion of film above the graphite core.

The total film thickness was chosen to be equivalent to approximately one third of the projected range of 200 and 500 keV electrons in the film material. This gave a good indication of both the optical densities measured by film and the temperature rise in the core due to the deposition of the remaining beam energy. A calibration factor or a set of characteristic curves could then be generated using the measured film absorbance as a function of dose absorbed in the film. The latter was determined from the difference in temperature rise measured with and without the film in the calorimeter system.

III. Results and Discussion

A. Calorimeter Response

Typical temperature-time plots for the real-time calorimeter at 200 keV and 500 keV are shown in Figure 3 and 4. A slow temperature drift before irradiation begins is followed by a rapid rise during irradiation and then a slow cooling after the end of the irradiation. A difference in the shape of the post-irradiation curve was observed with smaller cooling rates at 200 keV compared with those in the 500 keV beam.

The temperature rise, which is proportional to the amount of energy imparted to the graphite core, was determined from the extrapolation of the pre- and post- irradiation part of the curves to the mid-point time of the irradiation. The accuracy in this determination of temperature rise is determined primarily by the accuracy of this extrapolation.

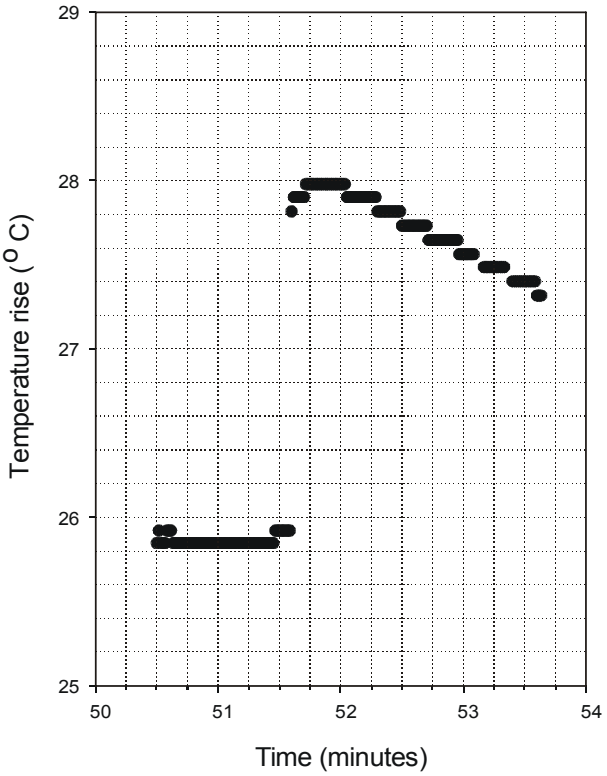

Figure 3: Temperature - time pattern at 200 keV (12 mA, 22.5 m.min^{-1}).

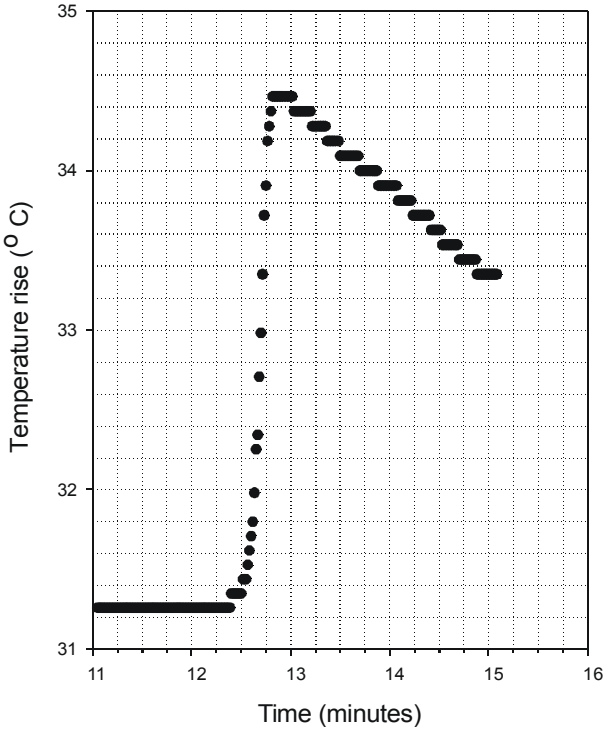

Figure 4: Temperature - time pattern at 500 keV (1 mA, 1.47 m.min^{-1}).

For the 500 keV beam, the temperature rise is determined with an error better than ± 0.5 °C, given that the post-irradiation

curve is slightly concave upwards. The post-irradiation fall at 200 keV is sufficiently linear to give the determination of the temperature rise with an error better than ± 0.1 ˚C. However, when film dosimeters are inserted above the core, the curve is initially concave downwards before becoming linear at longer times (Figures 5 and 6).

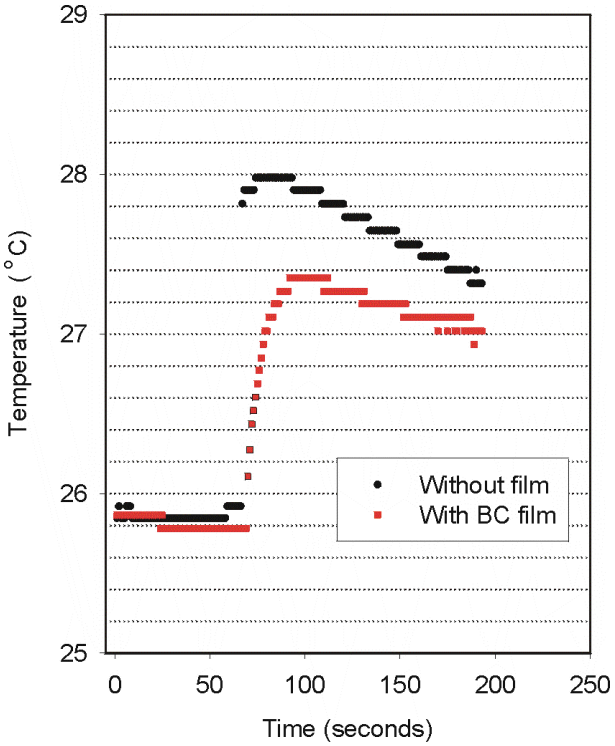

Figure 5: Temperature - time pattern with a film dosimeter above the calorimeter core at 200 keV (12 mA, 22.5 m.min^{-1}).

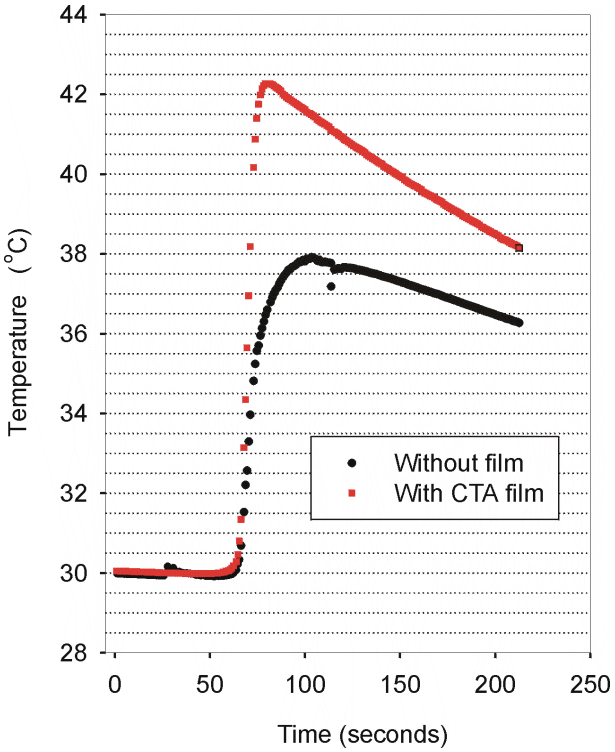

Figure 6: Temperature - time pattern with a film dosimeter above the calorimeter core at 500 keV (4 mA, 1.45 m.min^{-1}).

B. *Beam Calibration*

At both initial energies (200 and 500 keV) the temperature rise was found to be linearly dependent on the energy and beam current at constant conveyor speed (Figures 7 and 8) and to the reciprocal of the conveyor speed at a constant beam current. The intrinsic resolution of the data-logger (~0.09 ˚C) limited the minimum temperature rise to 1 ˚C, i.e. to beam currents greater than 4 mA in the 200 keV beam.

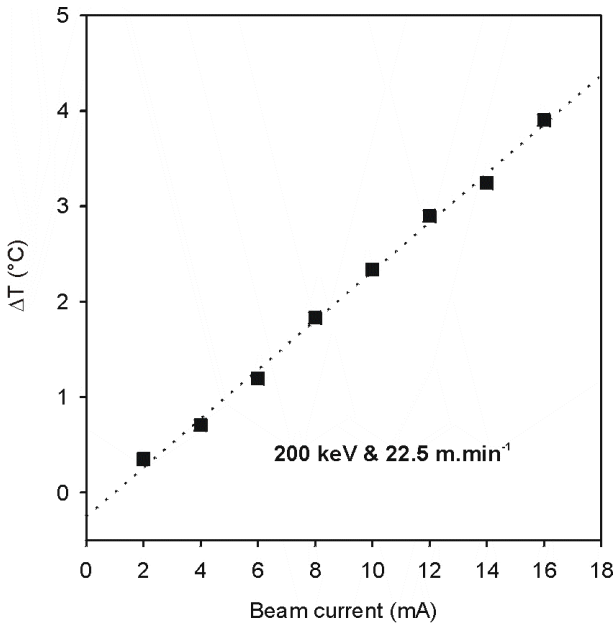

Figure 7: Relation between temperature rise and beam current for 200 keV electrons.

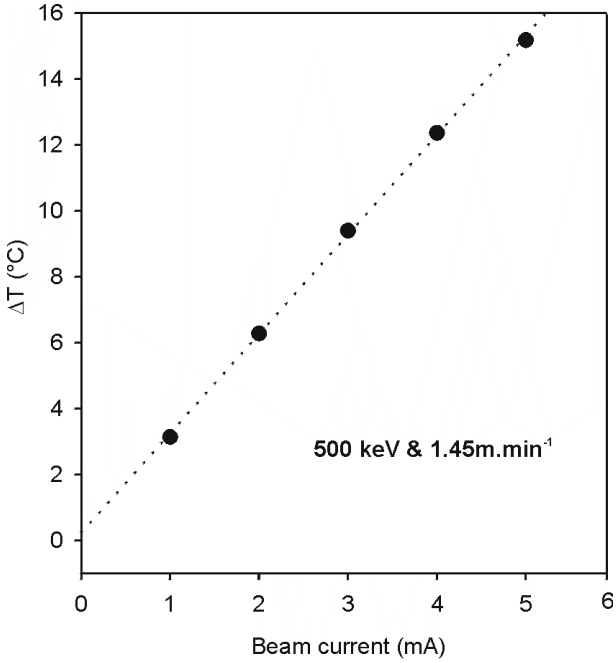

Figure 8: Relation between temperature rise and beam current for 500 keV electrons.

The best fit to the measured temperature rise has a small negative intercept at 200 keV and a small positive intercept at 500 keV. These non-zero intercepts indicate the uncertainties in the temperature rise determination and are related to the

non-linear shape of the cooling curve, thereby affecting the accuracy of extrapolation.

The measured temperature rise can also be related to the average dose in the graphite core through the following equation:

$$D_{ave}(Gy) = \frac{E}{m} = C_{graphite} \times \Delta T \qquad \textbf{(1)}$$

where E is the deposited energy, T is the temperature rise induced by the radiation, and m and $C_{graphite}$ are the mass and the specific heat of the graphite core respectively.

A more convenient quantity may be calculated by expressing the energy absorbed per unit irradiated area, F:

$$F(J.cm^{-2}) = \frac{\Delta T.C_{graphite}.m}{s} \qquad \textbf{(2)}$$

where s is the effective area of the graphite core. The quantity F is independent of the material, the mass and the irradiated area of the absorbing body, provided that back-scatter and other losses can be neglected. Figures 9 and 10 show the total energy absorbed per unit area of graphite core irradiated at different beam currents at 200 and 500 keV.

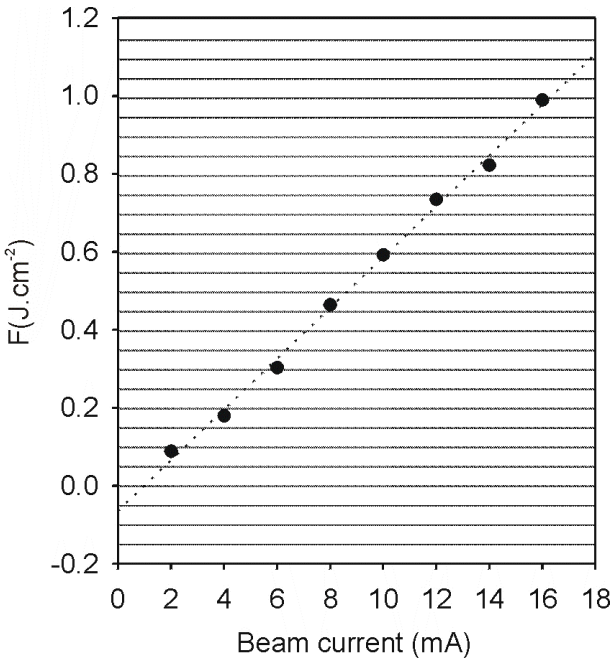

Figure 9: Total energy dissipated in the graphite core at 200 keV (22.5 m.min^{-1}).

The validity of the F-values can be checked by comparing them with the values obtained from a depth dose distribution in a film dosimeter. The distribution is obtained by irradiating a stack of calibrated films that cover the whole range of the depth penetration into the dosimeter (Figure 11).

By evaluating the dose readings of the individual samples in the stack, the depth dose distribution can be obtained (Figure 12). Integration of the depth dose distribution irradiated at the same parameters as the calorimeter, yields values of 0.135 J.cm^{-2} and

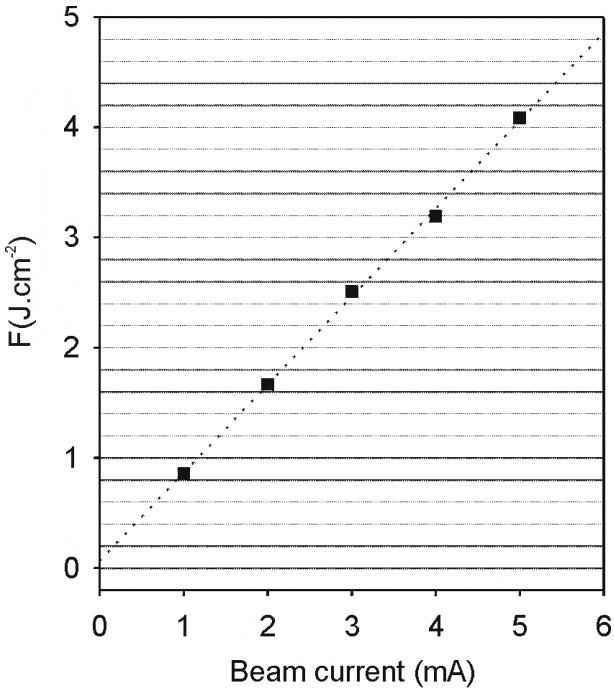

Figure 10: Total energy dissipated in the graphite core at 500 keV (1.45 m.min^{-1}).

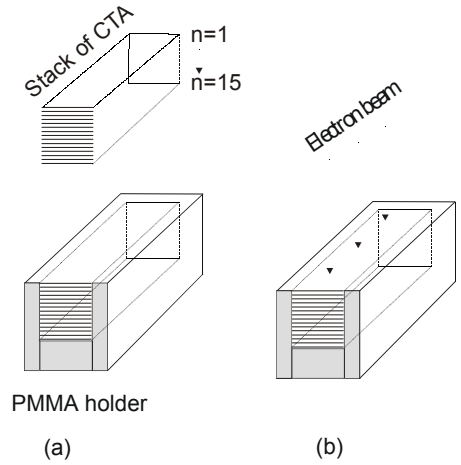

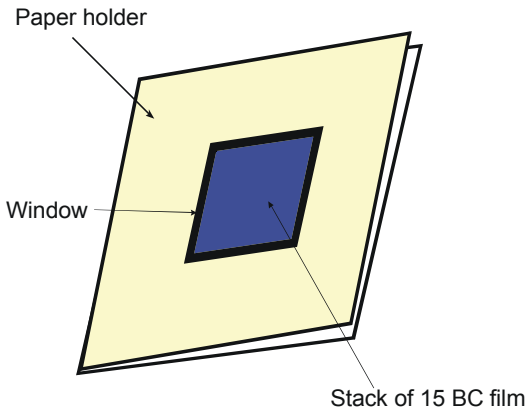

Figure 11: The arrangement of the films for the measurement of depth dose in BC and CTA at 200 and 500 keV respectively.

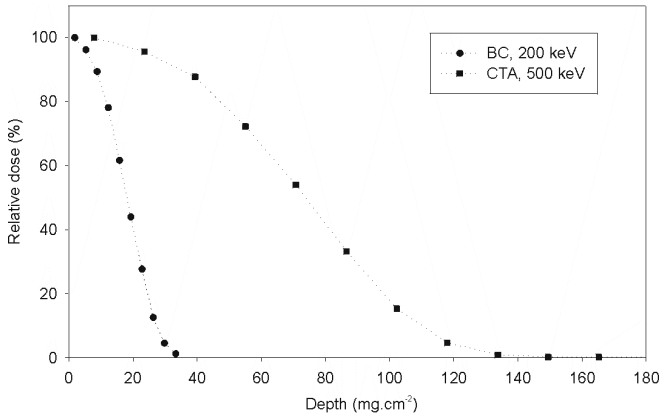

Figure 12: Depth dose distribution in BC and CTA at 200 and 500 keV respectively.

0.751 J.cm^{-2} at 200 keV and 500 keV respectively. The fact that there is good agreement ($\leq$5%) with the calorimeter system, and good linearity of F with different beam parameters demonstrates that the real-time graphite calorimeter can be used for a routine initial calibration of the accelerator.

Another significant parameter, the surface dose, is also used as a guide in setting up an effective electron irradiation process. These doses are determined using CTA film and are normally related to beam parameters such as energy, beam current and conveyor speed. A simple approximation can be used to derive a surface dose from the knowledge of average dose to the full thickness of the graphite core. The relation between the surface dose and the average dose in the graphite calorimeter can be given as follows:

$$K_{s,ave} = \frac{D_s}{D_{ave}} \qquad \textbf{(3)}$$

where $K_{s,ave}$ is the energy-dependent factor that relates the surface dose, D_s, to the average dose, $D_{s,ave}$. Values for $K_{s,ave}$ were found to be 32.53 and 4.76 at 200 and 500 keV respectively. With the appropriate factor, a surface dose versus beam parameters can then be derived from the measurement of average dose in the graphite calorimeter.

C. *Calibration of the Thin Film Dosimeter*

Having established the procedure for measuring absorbed energy with the calorimeter, the technique could be used to calibrate different batches of the CTA and BC film dosimeters. The addition of these dosimeters above the graphite core reduced the measured temperature rise (Figures 5 and 6), the difference of temperature rise recorded with and without the film stacks giving the absorbed dose in the films. Radiation induced absorbance, ΔA, was measured spectrophotometrically at 280nm and 630 nm for the CTA and BC films respectively. The response, when plotted against average dose, gave the calibration curves for BC and CTA films (Figures 13 and 14).

The relation between absorbance of the CTA film and the dose measured by the calorimeter gives a linear calibration factor for CTA, k, which is specified as [3]:

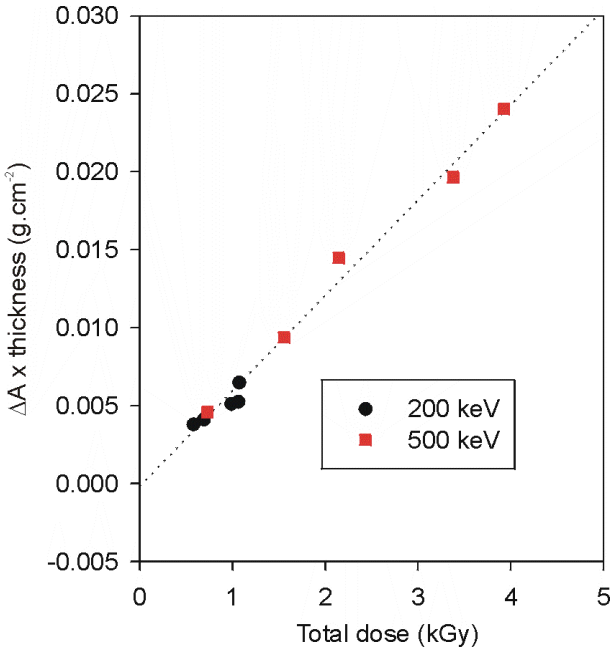

Figure 13: Calibration curve for CTA film dosimeter.

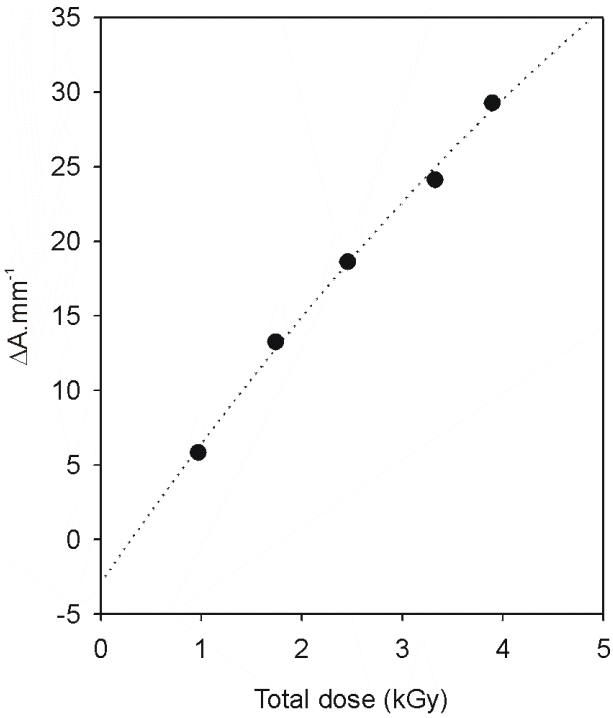

Figure 14: Calibration curve for BC film dosimeter.

$$k = \frac{z.\sum_{i=1}^{5} A_i}{D_{ave}} \qquad \textbf{(4)}$$

In equation (4), k is the calibration factor in kGy^{-1}, D_{ave} is the total dose measured by the calorimeter in kGy (i.e the difference for measurements with and without the film), A_i is the absorbance of an individual film dosimeter i in the stack and z is the corresponding film thickness in g. cm^{-2}.

Table 1.
Comparison of calibration factors obtained by other institutions for CTA-125.

Institution	Calibration factor , kGy^{-1}	Method of calibration
JAERI, Japan [Sunaga *et al.,* 1993]	0.0063	Comparison of absorption and CTA stack at 2 -3 MeV
Riso, Denmark [Janovsky *et al.*, 1987]	0.0065	Comparison of absorption calorimeter with CTA stack at 0.4MeV
Austrian Research Centre [Gehringer *et al.*, 1985]	0.0067	Applying an energy balance for estimating dose for 0.5 MeV

The calibration factor calculated for the CTA film dosimeter determined in this fashion was $0.0062 \pm 0.0002\ kGy^{-1}$, - a value very close to that obtained from other institutions using several other, and different, approaches to estimate the dose delivered to the CTA film [2] (Table 1).

A slight non-linearity was observed in the calibration curve for the BC film. Although a second-order polynomial could be fitted without difficulty, the film response was found to be greater for the low-energy electrons used in this work than for the higher energy electrons and photons used previously [2], [4].

IV. Conclusion

This work has demonstrated a simple and accurate method for determining absorbed dose in low-energy electron beam facilities using a real-time graphite calorimeter. The system provides a reliable method for the initial calibration of an accelerator in terms of energy deposited per unit area against the beam parameters. When combined with the measured values from a calibrated film dosimeter, these can be used to give the surface dose that can then be related to the beam parameters.

The particular advantages of the calorimeter are:

1. it permits use on both the scanned and the self-shielded facilities.
2. it is suitable for daily use, since data can be retrieved at any time after the calorimeter has been removed from the irradiation area.
3. it provides a precise method for calibrating both the accelerator output and also some widely-used film dosimeters.

References

[1] A.Miller, (1983) Dosimetry for Electron Beam Applications, 159-186, IAEA-TECDOC-321.

[2] Igor Janovsky and Arne Miller, (1987) A Calorimeter For Measuring Energy Deposition in Materials and Calibrating the Response of Dosimeters Irradiated by Low-Energy Industrial Electron Accelerators Appl. Radiat.Isot. 38 931-937.

[3] N.Mod Ali, (1998) Low-Energy Electron Calorimetry for Industrial Processing, Ph.D Thesis, University of London.

[4] N.Mod Ali & F.A.Smith (1998). A Real-Time Low-Energy Electron Calorimeter, IAEA-SM-356/40, IAEA-TECDOC-1070.

[5] N.Mod Ali & F.A.Smith (1999). Development of A Real-Time Low-Energy Electron Calorimeter, Proceedings of RadTech Asia '99.

Questions and Answers

Ken Gall: What kind of precision is required for the kind of processing that you are doing?

Noriah Mod Ali: 5% is considered good for radiation processing because it is quite difficult to get lower than that.

Ken Gall: For the process, how far off can they be before the process is no good?

Noriah Mod Ali: The process itself does not require an accurate dose unlike for radiotherapy and medical sterilisation. When we go to medical sterilisation we really need to have a very accurate dose measurement and dose accuracy.

Ken Gall: For sterilisation?

Noriah Mod Ali: Yes, it depends on the application.

Ken Gall: What is the requirement for sterilisation?

Noriah Mod Ali: Well, we should be as precise as possible. My experience is with gamma rays and not with electron beams: with gamma rays it is easy because we can have series which are very precise, ± 3%. For electrons, we are not as precise as that, especially at low and medium energys. At 10 MeV we haven't a problem because we have the standard calorimeter which has just been developed by NPL, RISO and NIST, but at 3 MeV we do have some problems getting a very precise measurement.

Ken Gall: Yes, I appreciate that it is difficult and the question is how hard one should try and how hard you should try depends on how hard you have to try. So if the person making the product doesn't care if you are 10% off, then you should try to 5% and stop.

Noriah Mod Ali: But still, for us, since we are from the dosimetry section we need to give as great a degree of accuracy as possible in order to reduce the redundancy of the energy.

Tony Aalbers: Is it not true that if you are in the business of radiation processing or sterilisation of medical goods that you should fulfil certain requirements about the minimum dose level

that you should exceed? For example, I know that for a company in the Netherlands, they have to fulfil a requirement which is at a certain dose level and they should be about that level always.

Ken Gall: But my impression is that for sterilisation 10% is fine.

Peter Sharpe: Anything above 10% would be a problem. It's unrealistic to say in an industrial setting you could get better then 5% but if you got an inaccuracy of much more than 10% then you are heading for trouble so that is the sort of band in which you are trying to work.

Ken Gall: I guess it somewhat depends on what you are trying to sterilise too. If you are sterilising surgical steel you could probably go over by a factor of two and not affect the product too much.

Peter Sharpe: As long as you are going over by a factor of two and not under by a factor of two. You've always got the bottom line.

Ken Gall: Yes, but 10% around a factor of two is plenty safe enough. There are some things that I am sure you can't go over by too much: if there is plastic in it, for example, then you could degrade the plastic. I am just asking because it is not obvious to me what precision is required.

Alan DuSautoy: There is also a cost implication. If you are overdosing everything by 10% basically your conveyor is running 10% slower so you are producing 10% less product.

--

Carl Ross: You pointed out that it is a total absorption device because of the thickness but the electron stopping power is changing very rapidly at low energy so when you put the layer of film on to calibrate it I don't see clearly the relationship between the total energy absorbed and the calibration of the film. The film is sampling electrons of energy, say, 500 keV passing through but the slab of graphite is absorbing all of the electrons up to zero energy.

Andrew Williams: But as it is a difference measurement, does it matter?

Peter Sharpe: It's the difference measurement you are interested in. If you've got a calorimeter element going through with no films on top of it that is giving the total energy for the beam.

Carl Ross: I see, so you're using the difference!

--

Dave Burns: You drew a graph of the temperature rise as a function of the beam current which did not pass through the origin. Do you use that offset as a correction?

Noriah Mod Ali: Yes.

Dave Burns: And it is the same correction for any beam current?

Noriah Mod Ali: Yes.

David Burns: What is the source of the beam current data and how did you measure the beam current?

Noriah Mod Ali: I don't actually measure it - I base it on the current set up by the operator. Maybe the error is from this beam current setting.

David Burns: It's just something you could investigate - I don't know how reliable these devices are.

Noriah Mod Ali: I never checked that out but I intend to proceed with this sort of investigation in order to refine the results and the system.

BIPM Comparisons of Standards for Air Kerma and Absorbed Dose in ^{60}Co γ-Radiation

D.T. Burns and P.J. Allisy-Roberts

Bureau International des Poids et Mesures, Pavillon de Breteuil, F-92312 Sèvres Cedex

Abstract

A system of international comparisons and calibrations provides the basis for the traceability of radiotherapy dosimetry throughout the world. Under an arrangement signed by the Directors of NMIs whose countries are signatories to the Metre Convention, the results of comparisons of national primary standards are being used to derive international key comparison reference values and to determine the degrees of equivalence between NMI standards.

National primary standards for air kerma and for absorbed dose to water are compared every ten years with those of the BIPM. The results of these key comparisons are presented. At its meeting in 1999 the CCRI decided to take the BIPM determination of these quantities as the key comparison reference value, a stable and practical approach which avoids problems associated with the evaluation of mean values and their subsequent reappraisal. The degrees of equivalence arising from this choice are shown.

Comparisons of primary standards for absorbed dose to graphite are also carried out at the BIPM. Following a decision of the CCRI, these are considered to be supplementary rather than key comparisons. The results of these comparisons are also presented.

I. Introduction

The traceability of measurements throughout the world is underpinned by a system of international comparisons and calibrations. Under the auspices of a mutual recognition arrangement [1] signed in 1999 by the Directors of thirty-eight national metrology institutes (NMIs) whose countries are signatories to the Metre Convention, the results of comparisons of national primary standards organized by the consultative committees of the Comité International des Poids et Mesures (CIPM) are being used to derive international key comparison reference values and to determine the degrees of equivalence between NMI standards. Comparisons carried out by regional metrology organizations extend these links to other NMIs in their region.

For countries who do not have a primary standard, traceability of radiotherapy dosimetry internationally is assured by the regular calibration of secondary standard ionization chambers held by the NMI, either directly by the Bureau International des Poids et Mesures (BIPM) or another primary laboratory, or through the network of secondary standard dosimetry laboratories of the International Atomic Energy Agency.

This paper presents the results of BIPM comparisons of standards for air kerma and absorbed dose in ^{60}Co γ-radiation and evaluates the degrees of equivalence between NMI standards.

II. Primary Standards and Uncertainties

The primary standards for air kerma used by the NMIs in ^{60}Co γ-radiation are graphite-walled cavity ionization chambers of different shapes and volumes. The combined relative standard uncertainty in the determination of air kerma in ^{60}Co γ-radiation is about 0.4 per cent for the BIPM standard and from 0.3 per cent to 0.6 per cent for NMI standards.

The standards for absorbed dose are of various types, including graphite calorimeters, water calorimeters, chemical dosimeters and the BIPM ionometric standards. For the determination of absorbed dose to water in ^{60}Co γ-radiation, the combined relative standard uncertainty is about 0.4 per cent for the BIPM standard and from 0.2 per cent to 1.0 per cent for NMI standards. Despite that fact that uncertainty estimates are generally higher than those of standards for air kerma, the diverse nature of the standards for absorbed dose reduces the possibility of common errors, a situation which might be considered to be more robust.

III. Comparison Methods

National primary standards for air kerma and for absorbed dose to water are compared with those of the BIPM under the reference conditions recommended by the Consultative Committee for Ionizing Radiation (CCRI). Following a recommendation of the CCRI, the period of recalibration should not exceed ten years. To date, twenty-one NMIs have participated in comparisons at all or some of the reference radiation qualities.

Comparisons in ^{60}Co γ-radiation are made either directly using the national primary standards or indirectly using transfer ionization chambers. When a direct comparison is undertaken at the BIPM, the NMI and the BIPM each measure the rate of air kerma or absorbed dose to water using their own standard, and the comparison result is expressed as the ratio R_{NMI} of the two values (BIPM in the denominator) and the uncertainty of this ratio. For an indirect comparison, each laboratory calibrates each transfer instrument at their own institute. A comparison result is obtained for each transfer instrument (a minimum of two transfer instruments being desirable), expressed as the ratio of the two calibration factors for that instrument. The final comparison result R_{NMI} is normally taken as the mean of these results.

Comparisons may be made at the BIPM at any time and it is important that the long-term stability of the BIPM standards and measuring equipment be verified regularly. Several Shonka-type ionization chambers have been calibrated in the BIPM ^{60}Co beam

in terms of air kerma over a period of twenty years. The standard uncertainty of the distribution of the calibration factors for each chamber over this period is better than 0.05 per cent. These results confirm that national standards can be reliably compared with each other through the BIPM standards.

IV. Comparison Results

The results of BIPM comparisons are published, usually as BIPM reports, and compilations of such data are published periodically [2], [3]. The uncertainty of each comparison result R_{NMI} takes into account the uncertainty of the determinations of air kerma or absorbed dose to water using the NMI and BIPM standards and also the method of comparison, direct or indirect. Correlations between the standards must be taken into account, for example the determinations of air kerma are correlated through the common use of physical quantities such as W_{air} / e. The resulting relative standard uncertainty of R_{NMI} for air-kerma comparisons in ^{60}Co γ-radiation is typically 0.2 per cent to 0.3 per cent. The results are shown in Figure 1; the relative standard uncertainty of the distribution is 0.19 per cent.

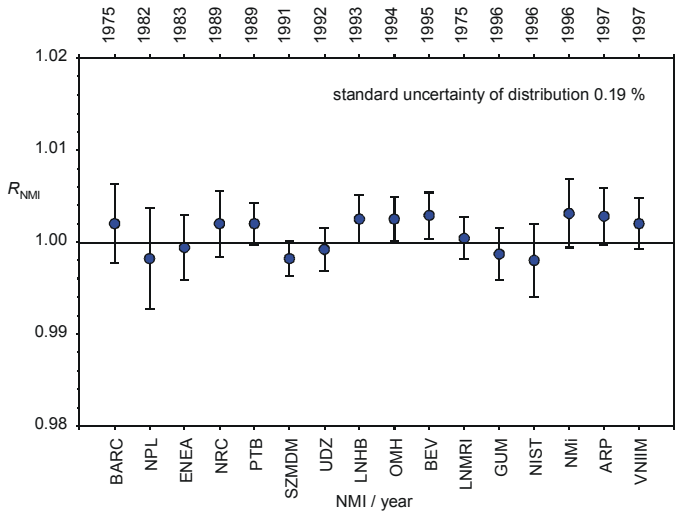

Figure 1: The results of BIPM comparisons of standards for air kerma in ^{60}Co γ-radiation. The uncertainty bars represent the standard uncertainty of each comparison result R_{NMI}.

For absorbed dose to water, the BIPM ionometric standard has little in common with the standards used by the NMIs. Consequently, the standard uncertainty of R_{NMI} is higher, in the range from 0.5 per cent to 0.9 per cent. The results are shown in Figure 2, where the relative standard uncertainty of the distribution is 0.22 per cent. This is not significantly different from that arising from comparisons of standards for air kerma.

Following a decision of the CCRI, comparisons in terms of absorbed dose to graphite are considered to be supplementary rather than key. This is because the quantity of key interest is absorbed dose to water and graphite standards generally exist as a means to determine this quantity. Nevertheless, supplementary comparisons of standards for absorbed dose to graphite are of interest as they may shed some light on the underlying reasons for observed differences in standards for absorbed dose to water.

The results of comparisons of standards for absorbed dose to graphite are shown in Figure 3. The relative standard uncertainty of the distribution is 0.34 per cent, dominated by a single value which, if removed, results in a standard uncertainty of 0.15 per cent.

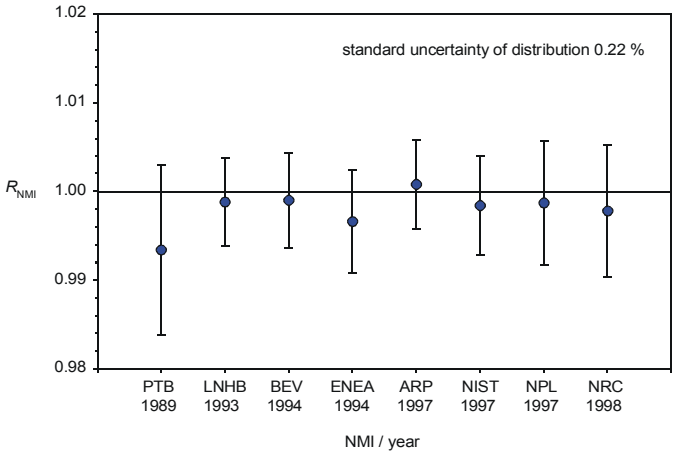

Figure 2: The results of BIPM comparisons of standards for absorbed dose to water in ^{60}Co γ-radiation. The uncertainty bars represent the standard uncertainty of each comparison result R_{NMI}.

It should be noted that the uncertainty bars of Figures 1 to 3 represent the standard uncertainty of each comparison result R_{NMI} and include correlations which arise from the use of the BIPM standard in each comparison, as well as any correlations between the NMI standards themselves.

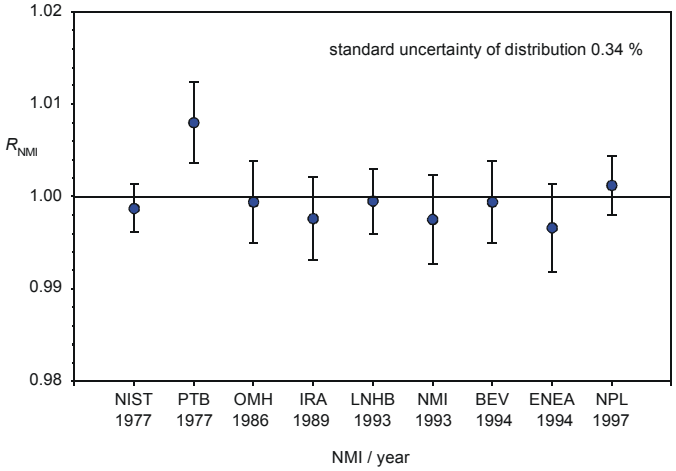

Figure 3: The results of BIPM comparisons of standards for absorbed dose to graphite in ^{60}Co γ-radiation. The uncertainty bars represent the standard uncertainty of each comparison result R_{NMI}.

V. Key Comparison Reference Value

At its meeting in 1999 the CCRI decided to take the BIPM determinations of the quantities air kerma and absorbed dose to water as the reference values. In consequence, the key comparison reference value R_{ref} pertaining to a comparison result R_{NMI} is the value unity (with no uncertainty). This is a stable and practical approach which avoids problems associated with the evaluation of mean values and their subsequent reappraisal. The

robust calculation of mean values is non-trivial for data sets which may contain subjective uncertainty estimates and suspected outliers. Furthermore, such a mean value would need a reappraisal by the CCRI on the basis of new comparison data, in principle every time a BIPM comparison is made with any NMI. An invariant reference value means that, for a given NMI, the difference between R_{NMI} and R_{ref} remains constant throughout the ten-year period between two comparisons with that NMI.

VI. DEGREES OF EQUIVALENCE

The degree of equivalence of a given measurement standard is the degree to which this standard is consistent with the key comparison reference value [1]. The degree of equivalence is expressed quantitatively as the difference between the NMI value of a given quantity and the reference value, and the uncertainty of this difference at the 95 per cent confidence level. For comparisons in radiation dosimetry, R_{ref} is unity and so the degree of equivalence of a given NMI standard is $R_{NMI} - 1$. The uncertainty of this value is the uncertainty of R_{NMI}. As an example, the degrees of equivalence for standards for absorbed dose to water in ^{60}Co γ-radiation are presented in Figure 4.

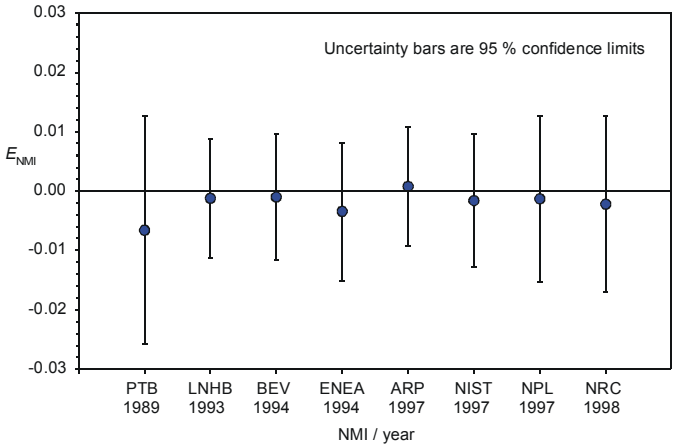

Figure 4: The degrees of equivalence for determinations of absorbed dose to water in ^{60}Co γ-radiation. E_{NMI} is the difference R_{NMI} - R_{ref} and the uncertainty of this difference at the 95 % confidence level. For comparisons in radiation dosimetry, the key comparison reference value $R_{ref} = 1$.

The degree of equivalence between any pair of NMI standards is the difference between their respective values for R_{NMI} and the uncertainty of this difference at the 95 per cent confidence level, taking into account correlations. The most obvious correlation is the use of the BIPM standard in both comparisons, but significant correlations may exist between the NMI standards themselves. The task of removing such correlations for each pairing of NMIs is non-trivial. It is clear from this definition of the degree of equivalence between any pair of NMI standards that it is independent of the choice of key comparison reference value R_{ref}.

For each key comparison a matrix of these degrees of equivalence will be published in the BIPM key comparison database. Table 1 is given as an example of such data for standards for absorbed dose to water in ^{60}Co γ-radiation,

Table 1.

Example calculation of the degrees of equivalence $E_{i,j} = R_{NMI,i} - R_{NMI,j}$ between pairs of NMIs i and j, for standards for absorbed dose to water in ^{60}Co γ-radiation. Also given (in brackets) is the uncertainty of each value at the 95 % confidence level. Correlations between each pair of comparison results have not been removed.

NMI,j \ NMI,i	PTB	LNHB	BEV	ENEA	ARP	NIST	NPL	NRC
PTB		0.0054 (0.018)	0.0056 (0.018)	0.0032 (0.019)	0.0074 (0.018)	0.0050 (0.019)	0.0053 (0.020)	0.0044 (0.021)
LNHB	-0.0054 (0.018)		0.0002 (0.008)	-0.0022 (0.009)	0.0020 (0.007)	-0.0004 (0.009)	-0.0001 (0.012)	-0.0010 (0.013)
BEV	-0.0056 (0.018)	-0.0002 (0.008)		-0.0024 (0.010)	0.0018 (0.008)	-0.0006 (0.009)	-0.0003 (0.013)	-0.0012 (0.014)
ENEA	-0.0032 (0.019)	0.0022 (0.009)	0.0024 (0.010)		0.0042 (0.009)	0.0018 (0.011)	0.0021 (0.014)	0.0012 (0.014)
ARP	-0.0074 (0.018)	-0.0020 (0.007)	-0.0018 (0.008)	-0.0042 (0.009)		-0.0024 (0.009)	-0.0021 (0.012)	-0.0030 (0.013)
NIST	-0.0050 (0.019)	0.0004 (0.009)	0.0006 (0.009)	-0.0018 (0.011)	0.0024 (0.009)		0.0003 (0.013)	-0.0006 (0.014)
NPL	-0.0053 (0.020)	0.0001 (0.012)	0.0003 (0.013)	-0.0021 (0.014)	0.0021 (0.012)	-0.0003 (0.013)		-0.0009 (0.016)
NRC	-0.0044 (0.021)	0.0010 (0.013)	0.0012 (0.014)	-0.0012 (0.014)	0.0030 (0.013)	0.0006 (0.014)	0.0009 (0.016)	

although correlations between NMI standards have not been removed from these data. It is interesting to note from this table that the degree of equivalence between the NMI with the highest value for R_{NMI} and that with the lowest is 0.74 per cent, with an uncertainty of this difference of 1.8 per cent at the 95 per cent confidence level. Statistically, this result is improbable and is due in part to the fact that correlations have not yet been removed, but may also indicate that certain components of uncertainty have been overestimated.

VII. Conclusions

Twenty-one member states of the Metre Convention have compared their primary dosimetry standards with those of the BIPM. For each measurement standard, the degree of equivalence with respect to the key comparison reference value has been determined. The degrees of equivalence between pairs of measurement standards are currently being evaluated for inclusion in the BIPM key comparison database.

References

[1] Comité International des Poids et Mesures, Mutual recognition of national measurement standards and of calibration and measurement certificates issued by national metrology institutes, *BIPM*, 12 p, 1999. Available from BIPM, Pavillon de Breteuil, F-92312 Sèvres Cedex.

[2] T.J. Quinn, Results of recent international comparisons of national measurement standards carried out by the BIPM, *Metrologia*, vol. 33, pp.271-287, 1996.

[3] A. Leitner, J. Witzani, M. Boutillon, P. Allisy-Roberts, F. Delaunay, E. Leroy, P. Lamperti, C. Strachotinsky and I. Csete, International comparisons of air kerma standards in ^{137}Cs radiation, *Metrologia*, vol. 34, pp.169-175, 1997.

Questions and Answers

Alan DuSautoy: Is there any interest in having comparisons in high energy photon beams or even in high energy electron beams? Of course they would have to be bilateral...

David Burns: Yes. There is a scheme being developed using transfer ionisation chambers which are held at the BIPM and circulated to labs for use at higher energies. That's going ahead.

Tony Aalbers: I thought a few years ago, there was a Working Group of the CCRI in which NPL, PTB and NRC at least took part looking at the measurement of high energy photons. I thought that they were doing this. Isn't that correct?

Simon Duane: It's still planned - we haven't done the measurements at NPL yet, but the chambers are here - it's not forgotten.

David Burns: For the moment, we've been establishing the stability of the transfer chambers at the BIPM, and we are planning to make measurements at the national laboratories. They should have been done already at the NPL, but there were some problems with the LINAC.

--

Simon Duane: Can I ask a question about the emphasis here on equivalence between national primary standards. For this to be useful to secondary standards holders who log on to the database, they need to be assured that their secondary standard calibration comes from the same point as contributed to the database. Is that guaranteed in the mutual recognition arrangement?

David Burns: I think the kind of comparison that I mentioned at the end, the supplementary comparison, looks more closely at what the user's getting as a calibration factor.

Simon Duane: Like an audit?

David Burns: Yes, I think that's the kind of process that needs to be carried out to gain confidence in how the standard had been disseminated. That will form part of the information that is in Appendix C of the mutual recognition agreement.

NPL Calorimetry: The Evolution so Far

A R. DuSautoy
Centre for Ionising Radiation Metrology, National Physical Laboratory
Teddington, Middlesex TW11 0LW, United Kingdom

Abstract

In this paper I will endeavour to cover the history of radiation calorimetry at NPL, from the earliest efforts up to the present day calorimeters. I hope to put all the NPL calorimeters that you are going to hear about in the workshop into context and present some interesting ideas from early calorimeters.

I. Introduction

Many people have contributed to the evolution of calorimetry at NPL - too many to mention them all. I will just mention some of the main contributors:

Lloyd Kemp - early theoretical designs.

Mike Baker - early construction and operation.

Brian Owen - project leader for photon beam therapy level graphite calorimeter.

Alan Calverd - electronics design.

Christine Cross - construction.

Alan DuSautoy - computer software.

Ian Stoker - electronics and operation.

Bob Burns - conversion from graphite to water.

Dave Burns - simple high dose electron beam calorimeter and therapy level calorimeter.

Trevor Morris - high dose calorimeter.

Malcolm McEwen - work on all electron calorimeters.

Simon Duane - theory and design of portable calorimeter.

Noriah Mod Ali - low energy calorimeter.

Karen Rosser - ice calorimeter and water calorimeter.

Andy Williams - water calorimeter.

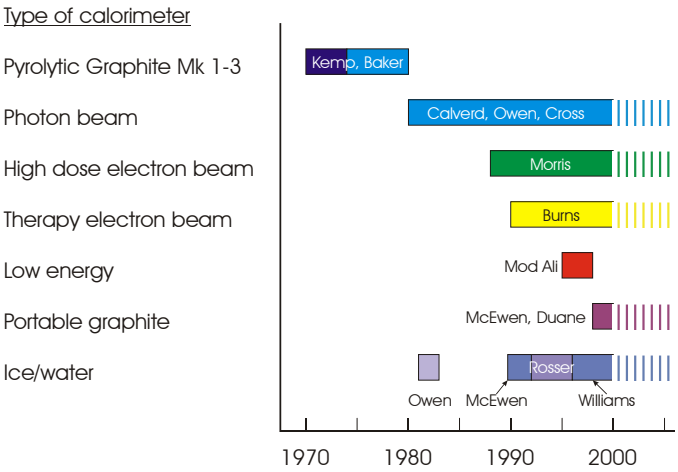

Figure 1: History of calorimetry at NPL

II. Early Graphite Calorimeters up to 1980.

A. Principles of calorimetry

Absorbed Dose D is the energy absorbed E in an element of some specified medium divided by the mass m of that element

$$D = dE/dm \quad (1)$$

according to ICRU report 33 [1]. The temperature rise on irradiation is measured and the energy deposited E is equal to heat capacity multiplied by temperature rise. There are two ways to measure the heat capacity either 1. measure the heat capacity *in situ* by electrical heating; or 2. use a known (or previously measured) heat capacity.

B. The Pyrolytic Graphite Calorimeter

Interest in calorimeters at NPL was prompted in 1969 by ICRU report 14 [2]. Initial work lead Kemp *et al* to designs for a pyrolytic graphite calorimeter [3-10]. The heat capacity was measured *in situ* and the pyrolytic graphite itself was used as the heating element. Pyrolytic graphite has a higher resistance perpendicular to the plan of the crystals (as shown in Table 1) and the calibration heating utilised this intrinsical resistance to obtain uniform heating.

Table 1.

Properties of Pyrolytic graphite

	electrical conductivity / ohm cm	**thermal conductivity / W m^{-1} K^{-1}**
a-direction:	0.4 E-3	20
c-direction:	1	0.14

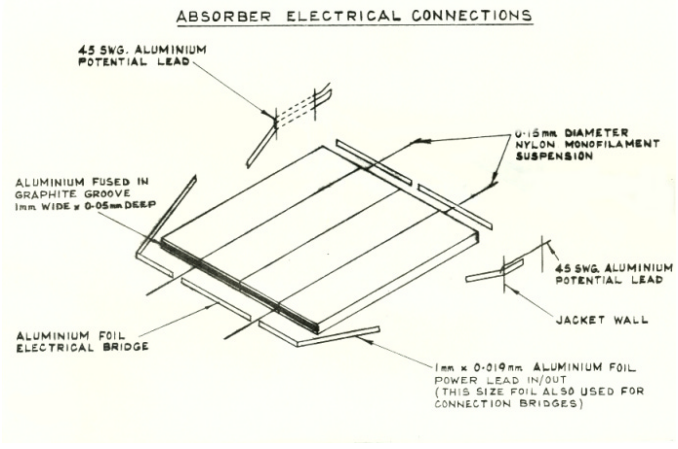

Figure 2: Pyrolytic graphite absorber (i.e. central component)

Figure 2 shows the pyrolytic graphite calorimeter absorber. Aluminium electrodes connect the heating circuits to the graphite slabs. Great effort was made to make good contact resistance and the zig zag design increased the resistance and distributed the heat more evenly.

Figure 3 shows an external view of the pyrolytic graphite calorimeter. The top is the vacuum entrance off of which is the electronics port and the front shows the temperature controlled snout.

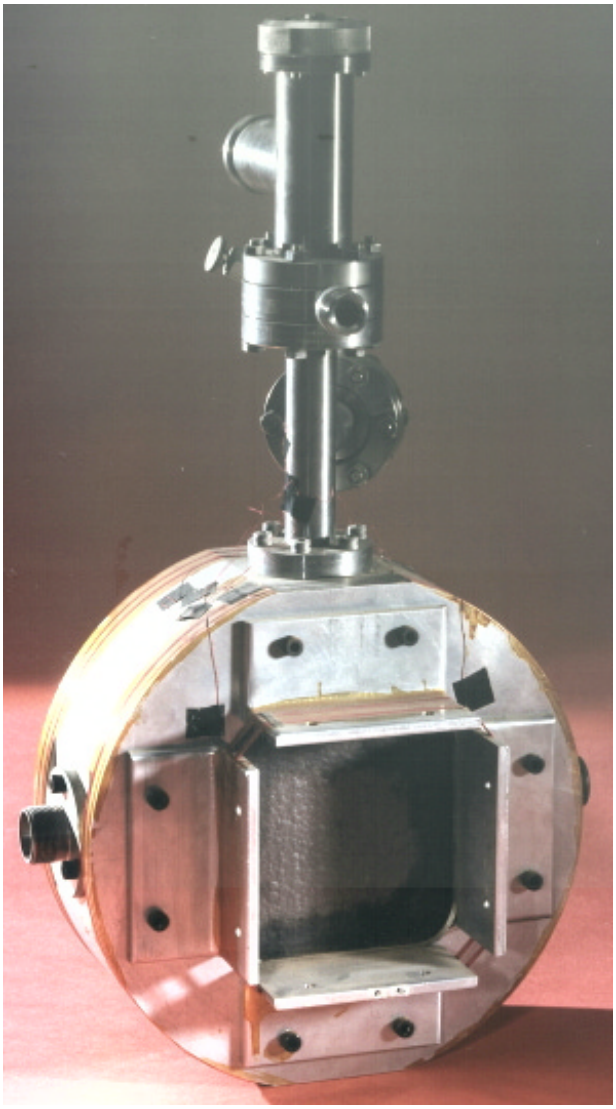

Figure 3: External view of Pyrolytic graphite calorimeter

A novel dynamic-equilibrium mode of operation was introduced (see Figure 4). A program is sent into a servo amplifier to generate the heating required in the absorber to maintain a temperature equal to the program temperature. For example if the program is a constant temperature the servo will generate heating power to raise the temperature of the absorber until the absorber temperature equals the program temperature and then the servo would switch off. In dynamic equilibrium mode the program is a ramp in temperature. The required heating is uniform but the heating can be supplied by either irradiation or electrically. The reduction in electrical power is a measure of the beam power from

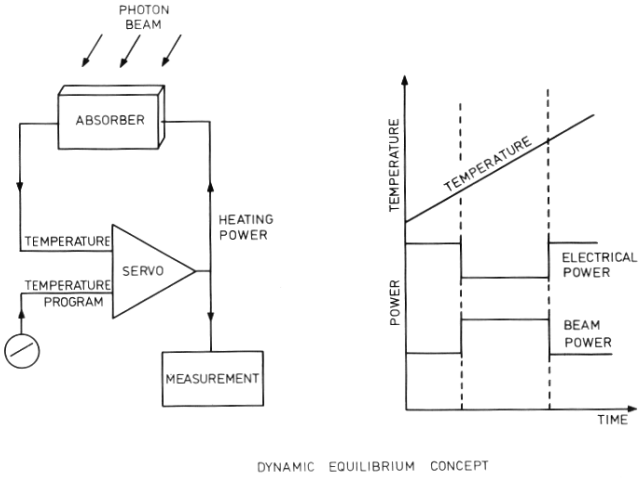

Figure 4: Dynamic equilibrium mode calibration

which the dose absorbed can be derived. Work on this calorimeter proceeded until about 1980. A later development of the dynamic equilibrium mode was made by Joseph Witzani called the isothermal mode [11]. The dynamic equilibrium mode system requires a very high gain amplifier and was quite ambitious for the electronics of the 1970's.

A drawback of the pyrolytic graphite calorimeter was the precision with which dynamic equilibrium mode measurements could be made. Also the low resistance (relative to insulators) of the graphite heating elements made making aluminium contacts extremely difficult. However a major advance was the introduction (in the late 1970's) of A C measurement bridges.

C. The Photon Beam Graphite Calorimeter

In 1983 a homogeneous graphite therapy level calorimeter was built to a design by Steve Domen (see Figure 5)[12]. The philosophy was to measure therapy level doses in photon beams

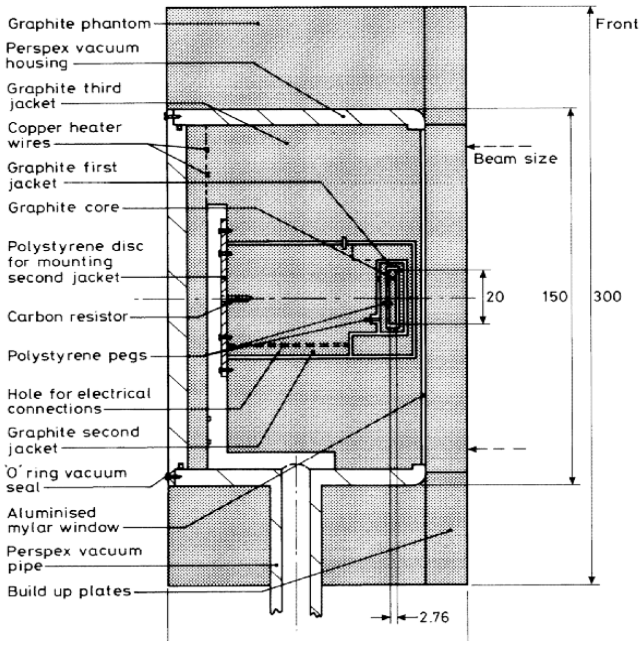

Figure 5: Homogeneous therapy-level graphite calorimeter

or electron beams at one gray, and one gray per minute. The system was computer controlled.

The therapy level calorimeter is the current primary standard for photon beam absorbed dose measurement and chemical dosimetry services. There is a later paper on the therapy level calorimeter by Simon Duane. The calorimeter was described in detail at the last calorimeter workshop in 1996 and other papers [13-19]. Absorbed dose to graphite is converted to absorbed dose to water by the scaling theorem method. This is described in detail by Bob Burns [20,21]. The UK adopted a code of practice for high energy photon therapy based on this calorimeter in 1990 [22].

III. Electron Beam Graphite Calorimeters.

Electron beam calorimeters were designed at NPL in the 1980s. The philosophy was to produce a simple design. The calorimeters were initially used for high dose and therefore designed for a large temperature rise. The calorimeters worked very well and are still used for high dose work [23]. Figure 6 shows the high dose electron beam calorimeter.

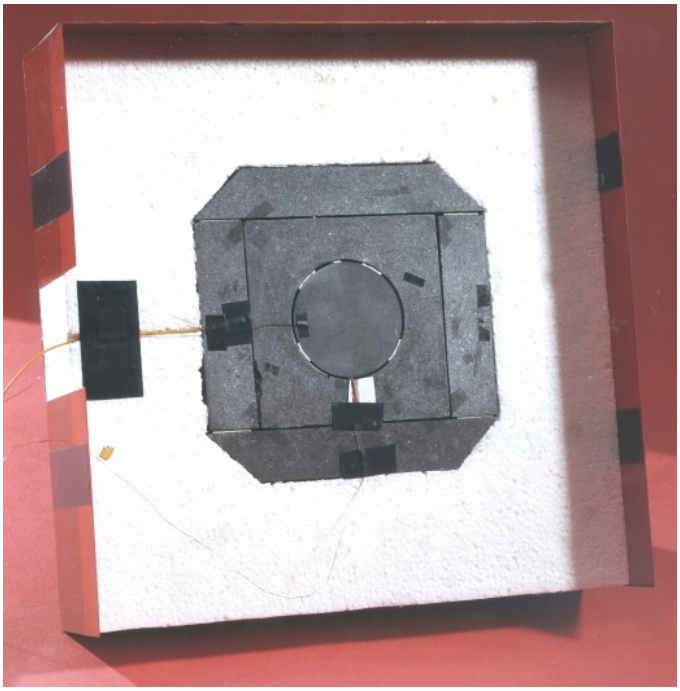

Figure 6: High dose calorimeter

The electron beam calorimeter with minor design changes lead onto a therapy level electron beam graphite calorimeter [24-27], which looks very similar. The use of this calorimeter and the conversion from graphite to water is described in [28-30]. This led to the worlds first electron beam absorbed dose calibration service and had two more spin-offs.

First the low energy calorimeter Figure 7. Here the philosophy was to design a calorimeter for use in low energy electron beams of energy less than 500 keV. The low energy calorimeter [31] will be described later by Noriah Mod Ali.

The other spin-off is a portable graphite calorimeter. Here the philosophy is to keep the calorimeter design simple but pro vide good temperature control. This will be described in a later paper by Malcolm McEwen.

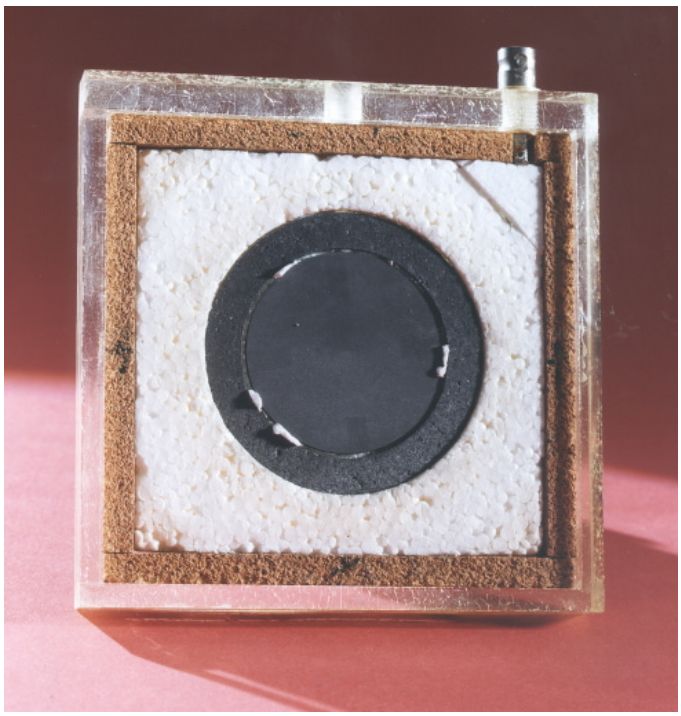

Figure 7: Low energy calorimeter

IV. Water Calorimetry

Water calorimetry at NPL had three false starts. First Brian Owen produced a water calorimeter similar to NRC's stirred water calorimeter and it was used to calibrate Fricke dosemeters. His calorimeter is shown in Figure 8. Although the high purity water was contained in a quartz or glass vessel the dissolved gasses in

Figure 8: Early water calorimeter

the water were not kept under control. Therefore this calorimeter had a variable heat defect and was unsuitable as a standard.

The second water calorimeter was produced by Malcolm McEwen [32] for use in electron beams but electron beams tend to give steeper depth dose gradients and therefore temperature gradients. He therefore decided to pursue the therapy graphite calorimeter in preference. Karen Rosser produced an ice calorimeter [33] for low energy X-rays. This did produce some results but they were not of sufficient precision to replace graphite calorimeters or ion chambers. The most recent water calorimeter [34-36] has been produced by Karen Rosser and Andrew Williams (see Figure 9) and will be described by Andrew Williams later in this conference.

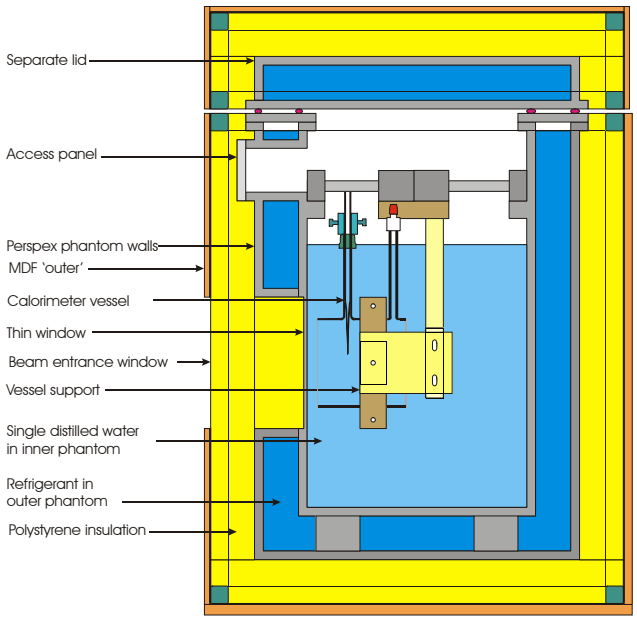

Figure 9: Recent water calorimeter

V. Conclusion

In summary, I have described various types of calorimeters; early calorimeters graphite high dose, graphite therapy and water calorimeters and I hope I have put the various calorimeters into context.

References

[1] International Commission on Radiation Units and Measurements (ICRU) 1980 Radiation quantities and units. ICRU Report 33 (Washington, DC: ICRU)

[2] ICRU 1969 Radiation dosimetry: x-rays and gamma rays with maximum photon energies between 0.6 and 50 MeV. ICRU Report 14 (Washington, DC: ICRU)

[3] L A W E Kemp. Preliminary theoretical design studies for a local absorbed dose microcalorimeter. NPL Report RS(INT)4A, February 1970

[4] L A W E Kemp, A R S Marsh and M J Baker. Pyrolitic graphite microcalorimeter for the measurement of X-ray absorbed dose. Nature, Vol. 230, No. 5288, pp41-42, March 5, 1971.

[5] L A W E Kemp. The transient behaviour of a block of self-heated pyrolitic graphite having non-uniform C-direction resistivity. NPL Report RS(INT)5A,

[6] L A W E Kemp. The initial heating transient in a self heated pyrolytic graphite block having non-uniform C-direction resistivity. NPL Report RS(INT)6, February 1971.

[7] L A W E Kemp. A proposed graphite configuration for a Mark 2 local absorbed dose microcalorimeter. NPL Report RS(INT)7, February 1971.

[8] M J Baker. A proposed graphite configuration for a Mark III local absorbed dose microcalorimeter. NPL Report Rad. Sci. 22, January 1974.

[9] L A W E Kemp. An analysis of the effectiveness of the 'heat sinking' of leads, with special reference to thermistor leads, in the NPL local absorbed dose microcalorimeter. NPL Report Rad. Sci. 34, October 1975.

[10] L A W E Kemp. The commissioning of the NPL pyrolytic graphite local absorbed dose microcalorimeter - An analysis of experimental methods of deriving the basic time constants and establishing the adiabatic heating condition as between absorber and jacket. NPL Report Rad. Sci. 35, November 1975.

[11] Witzani J, Duftschmid K E, Strachotinsky Ch and Leitner A 1984 A graphite absorbed-dose calorimeter in the quasi-isothermal mode of operation. Metrologia **20** 73–9

[12] Domen S R and Lamperti P J 1974 A heat-loss-compensated calorimeter: theory, design and performance. J. Res. NBS 78A 595–610

[13] Cross C 1988 The construction of a graphite microcalorimeter for the measurement of absorbed dose National Physical Laboratory Report RS(EXT) 96

[14] DuSautoy A R 1985 The measuring assembly for a primary standard absorbed dose calorimeter National Physical Laboratory Report RS(EXT) 74

[15] Burns J E, Dale J W G, DuSautoy A R, Owen B and Pritchard D H 1988 New calibration service for high energy X-radiation at NPL Proc. Int. Symp. on Dosimetry in Radiotherapy (Vienna, 1987) vol 2 (Vienna: IAEA) pp 125–32

[16] DuSautoy A R 1991 The UK primary standard calorimeter for absorbed dose measurement National Physical Laboratory Report RSA(EXT) 25

[17] Stoker I and DuSautoy A R 1991 The measuring assembly for the primary standard absorbed dose graphitecalorimeter at therapy levels National Physical Laboratory Report RSA(EXT) 23

[18] Rosser K E, Owen B, DuSautoy A R, Pritchard D H, Stoker I and Brend C 1993 The NPL absorbed dose to water calibration service for high-energy photons Proc. Int.

Symp. on Measurement Assurance in Dosimetry (Vienna, 1993) (IAEA-SM-330/35) (Vienna: IAEA) pp 73–81

[19] Owen B and DuSautoy A R 1990 NPL absorbed dose graphite calorimeter correction for the effect of the gaps around the core National Physical Laboratory Report RSA(EXT) 12

[20] J E Burns and J W G Dale. Conversion of absorbed-dose calibration from graphite into water. NPL Report RSA(EXT)7, April 1990.

[21] Burns J E 1994 Absorbed-dose calibrations in high-energy photon beams at the National Physical Laboratory: conversion procedure Phys. Med. Biol. 39 1555–75

[22] Code of Practice for high-energy photon therapy dosimetry based on the NPL absorbed dose calibration service. Phys. Med. Biol. 1990, Vol 35, No 10, 1355-1360

[23] Burns D T and Morris W T 1991 A graphite calorimeter for electron-beam dosimetry Proc. Int. Symp. on High Dose Dosimetry for Radiation Processing (Vienna, 1990) (Vienna: IAEA) pp 123–36

[24] Burns D T, McEwen M R and Williams A J 1994 An NPL absorbed dose calibration service for electron-beam radiotherapy Proc. Int. Symp. on Measurement Assurance in Dosimetry (Vienna, 1993) (Vienna: IAEA) pp 61–71

[25] A J Williams, M R McEwen and A R DuSautoy. A calculation of the water to graphite perturbation factor ratios for the NACP type 02 ionisation chamber using Monte Carlo techniques. CIRM 13, NPL Report, June 1998

[26] M R McEwen, A J Williams and A R DuSautoy. Trial calibrations of therapy level electron beam ionisation chambers in terms of absorbed dose to water. NPL Report CIRM 20, November 1998.

[27] A DuSautoy, M McEwen and A Williams. A new absorbed dose calibration service for electron beam radiotherapy. Medical Physics, Vol 25, No 7, p A151, July 1998, Part 1

[28] M R McEwen, A R DuSautoy and A J Williams. The calibration of therapy level electron beam ionization chambers in terms of absorbed dose to water. Phys. Med. Biol. 43 (1998) 2503–2519

[29] D T Burns, S Duane, and M R McEwen. A new method to determine ratios of electron stopping powers to an improved accuracy. Phys. Med. Biol. 40 (1995) 733-739

[30] D T Burns, S Duane, and M R McEwen. Comments on 'A new method to determine ratios of electron stopping powers to an improved accuracy'. Phys. Med. Biol. 41 (1996) 785-788

[31] Noriah Mod Ali, Low energy electron calorimetry for industrial processing (1998). PhD Thesis. Queen Mary and Westfield College, University of London.

[32] M R McEwen. The electron-beam water calorimeter project at the National Physical Laboratory. NPL Report RSA(EXT)30, February 1992.

[33] K E Rosser, PhD Thesis. Measurement of absorbed dose to water for medium energy X-rays. NPL Report CIRA(EXT)006, May 1996

[34] A R DuSautoy, A J Williams, K E Rosser, S J P Gnaniah 1997. A water calorimeter for high energy photon beams, *Med. Biol. Eng. Comput.* Vol 35 Suppl. Part 2, 1091.

[35] A J Williams and K E Rosser. A status report on the NPL water calorimeter. NPL Report CIRM 22, December 1998.

[36] K E Rosser and A J Williams. Comparison of the NPL water calorimeter with other dosimetric techniques for high energy photon beams. NPL Report CIRM 23, March 1999.

QUESTIONS ANS ANSWERS

Malcolm McEwen: Are there any of the early ideas that you think should be re-visited that were just prevented due to technology, or what was available?

Alan DuSautoy: We made some investigations early-on with the photon-beam therapy calorimeter looking at the iso-thermal mode of operation, and I believe that some of Simon Duane's talk is about the problems in temperature control in that system.

I am sure we could now improve the temperature control in this calorimeter because of the work that has been done on temperature control for the portable electron calorimeter. You could apply this work to the old photon-beam calorimeter and then be able to use it in iso-thermal mode which would probably reduce some of the uncertainties. So that's possibly the only idea that should be revisited. However, it's a matter of whether you want to pursue this really rather complicated system - I believe that we should develop our efforts in the portable calorimeter and turn that into a primary standard - at least for electron beams and maybe even for photon beams in the future.

--

Jan Seuntjens: What will you do when the water calorimeter will be in place? What is the plan with the photon beam graphite calorimeter? Will you keep it as two systems in parallel?

Alan DuSautoy: Yes. What I would expect to happen is for the uncertainties to come down on the water calorimeter. When the uncertainty on the water calorimeter is perhaps of the order of the graphite calorimeter we will probably have a standard which is a combination of the two. So what will probably happen is that the calibration of a 2561 chamber will gradually change from being based on the graphite calorimeter to the water calorimeter.

Jan Seuntjens: So you will blend both calorimeters?

Alan DuSautoy: Yes, we'll probably blend the results of them.

Jan Seuntjens: What is the level of difference that you will be happy with? If the calorimeters are different by no more than 0.X% for example?

Alan DuSautoy: Ultimately it's not a matter of the level of difference - it's a matter of the uncertainties. If we think the uncertainties of the water calorimeter are really lower than the uncertainties in the graphite calorimeter, no matter what the

difference, we'll be forced to move to a situation where the absorbed dose is based more on the water calorimeter.

Ken Gall: That would be a very interesting predicament - to have two systems where your uncertainties didn't overlap.

Alan DuSautoy: It maybe interesting but it's not unusual. Actually, with most new primary standards the advances in the techniques mean that this is often the case, where you introduce a new primary standard and the uncertainties don't really overlap with the old one. It's surprisingly common.

--

Dave Burns: One of the factors that allowed us to have such a simple design for the electron beam calorimeters was that we chose to do chamber calibrations at 10 grays per minute rather than 1 gray per minute. We did a lot of work on recombination to do the conversion from 10 to 1 via ion chambers.

Are the recent developments aimed at operating at 1 gray per minute - would you argue that it's necessary?

Alan DuSautoy: Certainly the lower dose-rate you can operate the calorimeter at the better because the less extrapolation you make. What you are really asking is 'What's the uncertainty in changing from say 5 grays per minute to 1 gray per minute with an ion chamber?' and that's a very tricky question. At the moment, I believe it introduces uncertainties that are comparable with the initial absorbed dose in graphite, but that's just a feeling - and it's to do with if you think recombination is the main factor, do we understand recombination well enough? Certainly in NACP chambers for instance, if you plot reciprocal voltage against reciprocal volume the line curves and it's not absolutely sure why. In some early chambers based on films, we know that as you increase the voltage the size of the volume changed, but for other good chambers, we don't really know why. There's possibly three competing things - [1] it's something to do with the insulation itself - as you increase the voltage the insulation is behaving slightly non-linearly, [2] it's a geometry change or a field configuration change, for instance, with the Markus chamber as you change the voltage you get larger recombination corrections because the field's non-uniform, [3] It might be due to localised high fields in the chamber cavity where a point of a wire is sticking into the cavity for example and that will produce a recombination. So these are the uncertainties that add to going from 5 grays per minute to 1 gray per minute.

--

Mark Pieksma: Are there any other groups that have pursued ice calorimetry?

Alan DuSautoy: Not in that form, as far as I know. There were some experiments about 1920 on ice calorimeters. They worked by measuring the amount of water that dripped of the ice when you irradiated it, so it wasn't the same sort of thing.

Mark Pieksma: What are thought to be the main advantages of ice compared to water?

Alan DuSautoy: It doesn't convect - that's quite a big advantage. The heat capacity is lower so the temperature rise is higher by a factor of about 5. But the difficulties of containing ice are just too difficult, so I wouldn't suggest that it's really a way to go at the moment.

Jan Seuntjens: The problem with ice is that the thermal diffusivity is not low so you don't preserve your dose profile. Therefore it's much more difficult to get a proper measurement with an ice calorimeter unless you make it like a graphite calorimeter in which you have an isolated body. There are also problems with the heat effect

Mark Pieksma: The thermal properties of ice are closer to graphite than to water?

Alan DuSautoy: But you want absorbed dose to water, so you then have to convert from absorbed dose to ice to absorbed dose to water because they are not the same. Also the binding of the electrons make a difference so you may have different dosimetry factors in there. I definitely wouldn't suggest it is a good way to go.

Calorimetry for Absorbed-dose Measurements at BNM-LNHB

J. Daures, A. Ostrowsky, P. Gross J.P. Jeannot and J.Gouriou
BNM-LNHB, CEA/Saclay, Bat 534, F-91191 Gif-sur-Yvette Cedex

Abstract

At BNM-LNHB, the references in terms of absorbed dose to water are based on graphite calorimeter measurements. In the cobalt-60 beam, measurements were performed directly with the graphite calorimeter in a graphite phantom. Absorbed dose to water in a water phantom was then determined using a transfer method by means of relative measurements made with ionisation chambers and Fricke dosimeters. Our medical linac (Saturne 43 from GE-Medical Systems) is being characterised in the same way for three photon beam qualities 6 MV, 12 MV and 20 MV.

Special attention was given to the vacuum-gaps correction, one of the most important source of uncertainty. We carried out measurements in a graphite device similar to the calorimeter, using a very small diode embedded in a body corresponding to the calorimeter core. Measurements were made alternatively with and without vacuum gaps in the graphite phantom. The ratio of the results leads directly to the vacuum-gap correction factor. Monte-Carlo calculations were also carried out using both EGS4 and PENELOPE codes. The results are in good agreement, regarding the uncertainties.

At present, a water calorimeter is being realised. The aim is to get an absorbed dose standard independent of and complementing those based on graphite calorimetry. Particular attention will be devoted to the possibilities in terms of uncertainty compared with those attainable using graphite calorimetry.

I. Introduction

The BNM-LNHB is the French national laboratory for absorbed dose metrology.

The first of July 1999, the former LPRI changed its name to LNHB, which means National Laboratory Henri Becquerel.

The graphite calorimeter is the standard of absorbed dose to graphite. At present the references of absorbed dose to water are derived from this standard. Considering the importance of the graphite calorimetric technique, the laboratory has to maintain and improve it carefully. As the vacuum-gaps correction is the main source of uncertainty, it was decided to measure it by means of very small diode and to calculate it again for our cobalt-60 beam and for high-energy photon beams (6 MV, 12 MV, and 20 MV) from our GE-Saturne 43 medical type linear accelerator. Experimental and theoretical results are in good agreement and confirm the previous estimation in the cobalt-60 beam.

The tissue-equivalent calorimeter developed by the laboratory in the early 80's for the calibration of neutron-therapy and proton-therapy beams is maintained operational.

Water calorimetry is now in progress with high-level priority.

II. Evolution of the Calorimetric Technique at BNM-LNHB

Since the early seventies, the laboratory did constant efforts in the calorimetry field and built several instrument versions.

The graphite calorimeter n° 4 was compared to Domen's one in our cobalt-60 beam in 1975. The French reference was 0.3 % lower than the US one [1]

In 1977 and 1993, measurements were performed in the BIPM cobalt-60 beam for comparison using different calorimeters with good results. In 1977, the graphite calorimeter n° 5 was used. The result was 0.01 % lower than the BIPM reference at 5 $g.cm^{-2}$ depth [2]. In 1993, the graphite calorimeter n° 8 showed with a difference of -0.05 % compared to BIPM [3]. For this last calorimeter, the improvement consisted in the electrical calibration by Joule effect through specific thermistors instead of conducting resin. In the meantime, measurements were carried out in a linear accelerator in Saclay for the determination of W_{air} and G for Fricke solutions with 35 MeV photon and electron beams using the graphite calorimeter n° 6. The feed-back control of the jacket was introduced at that time. Aimé Ostrowsky thus built a total of eight graphite calorimeters and two T. E. calorimeters

The present references of absorbed dose to water in cobalt-60 and high-energy photon beams at BNM-LNHB are based on measurements with the graphite calorimeter n° 8.

The tissue-equivalent calorimeter was developed around 1980. It is made of A150 Shonka plastic whose hydrogen and nitrogen compositions are similar to those of tissue. At this time, neutron therapy seemed very promising (high LET secondary particles). Later on, proton treatment was developed for its ballistic qualities. In hospitals, the dosimetry is mainly performed by means of tissue-equivalent ionisation chambers calibrated in terms of air kerma. The protocols give guidance on methodology and recommend values for the needed parameters. The overall uncertainty, for one standard deviation, is more than 4 %, mainly due to the poor knowledge of the mean energy expended to create an ion pair in the gas of the cavity and gas-to-wall stopping power ratios for neutrons or protons.

For radiotherapy purpose, it has been proven by clinical studies that the total uncertainty must be lower than 5 % in the tumour volume [4]. Then it is important to reduce the uncertainty on the reference dose to give some safety margin for treatment planning.

In neutron or proton beams, the uncertainty obtained with the tissue-equivalent calorimeter is about 0.7 % for one standard deviation. It is higher than for the graphite calorimeter because of the heat defect correction, but the determination of absorbed dose to tissue is easier, especially for neutrons. Direct calibration

of ionisation chambers in the user's beam by means of the calorimeter, although long and delicate, reduces considerably the uncertainties [5]. Moreover the ratio of the corresponding calibration factor in terms of absorbed dose to that in terms of air kerma in a cobalt-60 beam gives a measured value of *Cn* or *Cp* coefficients.

Measurements were performed with our first tissue equivalent-calorimeter in the cyclotron neutron-therapy beam of Orléans (1982) and Louvain la Neuve (1983) [6,7]. The results were in agreement with the *Cn* values calculated with the protocol.

The second tissue-equivalent calorimeter was used in the Orsay proton-therapy beam in 1991. Measurements were performed at three energies (32, 52, 169 MeV). Several European centres came to perform ionisation measurements. At that time there was a significant difference between calorimetric and ionometric measurement results. Applying the new values of stopping powers published later, the ionometric results felt in agreement with the calorimetric determination [8].

A comparison with the PTB standards took place in 1984 in its cyclotron neutron beam (d(13.35 MeV) + Be) [9]. The calorimetric absorbed dose was in good agreement with the Monte Carlo calculation and the ionometric measurement of PTB.

No comparison with any other tissue equivalent calorimeter could be done yet.

III. Graphite Calorimeter

A. Design

The diagram of the graphite calorimeter n° 8 is given in figure 1. The core is a flat cylinder (3 mm thick and 16 mm in diameter). The jacket surrounding the core is 2 mm thick. The shield surrounding these two first bodies is 2 mm thick. These three bodies are kept in position and glued in the block by three silk threads. The gaps between each bodies and the block are evacuated to reduce thermal transfers. The dimensions of these gaps are close to 1 mm along the axis and about 2 mm perpendicular to the axis.

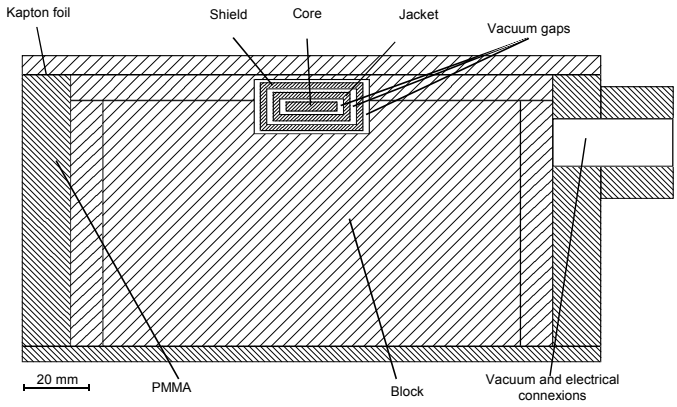

Figure 1: Diagram of the graphite calorimeter n° 8.

B. Temperature Control

Since the sensitivity of the graphite calorimeter is only a millikelvin per gray, the stability of the core temperature before and after irradiation must be better than 10 microkelvins.

The shield is the first thermal control step. Its temperature is kept constant at about 2 degrees above the room temperature, which is the cold source of the system. A thermistor embedded in the shield and associated to a DC Wheatstone bridge measures the temperature. If the temperature decreases, a PID thermal regulator sends an adjusted electrical power to the shield heating supply (8 thermistors). The shield control system is shown on the right of figure 2.

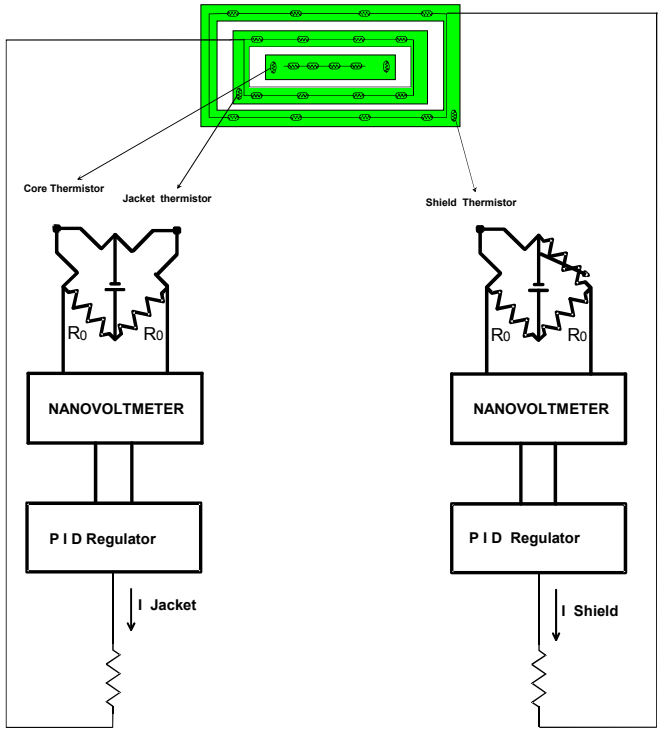

Figure 2: Thermal control of graphite and tissue-equivalent calorimeters.

The jacket temperature is controlled to follow, as closely as possible, the core temperature, minimising thus the thermal transfers between the core and the jacket. One thermistor embedded in the core and another in the jacket make two opposite arms of a DC Wheatstone bridge. The two thermistors are carefully selected to have the same characteristics. An electrical power is sent to the jacket heating supply (8 thermistors) by means of a PID regulator on the base of the Wheatstone bridge voltage. This jacket thermal feed-back is shown on the left of figure 2. This is the essential difference with Domen-type graphite calorimeters [10]. This jacket thermal feed-back has improved the stability and the flexibility of this calorimeter.

C. Measuring System and Electrical Calibration

During irradiation or electrical calibration heating, the temperature rise is measured with a thermistor embedded in the core. The thermistor used for the measurement is identical to the

one used for thermal control. These thermistors are of the "pearl type covered" from Fenwall; type GB38j14. Their mass is about 0.5 mg. Their diameter is close to 0.35 mm. Their relative sensitivity is about 3.8 10^{-2} K^{-1}. Their resistance values are close to 8 kΩ at 20 °C.

The relative variation of the thermistor resistance, L, is measured by means of a very precise DC Wheatstone bridge shown on figure 3. High-accuracy and high-precision Vishay resistors; type VHP 103; are used. They were chosen for their very low temperature coefficient (<10^{-6} K^{-1}) as they are usually outside the regulated irradiation room. A mercury battery provides a 1.35 V potential. A Keithley 181 nanovoltmeter is used to measure the bridge voltage. As it is impossible to balance the bridge during the measurement, it works out off equilibrium. Just before irradiation or electrical calibration, the sensitivity of the bridge is measured, in similar conditions, by introducing in the other arm a resistor of known value.

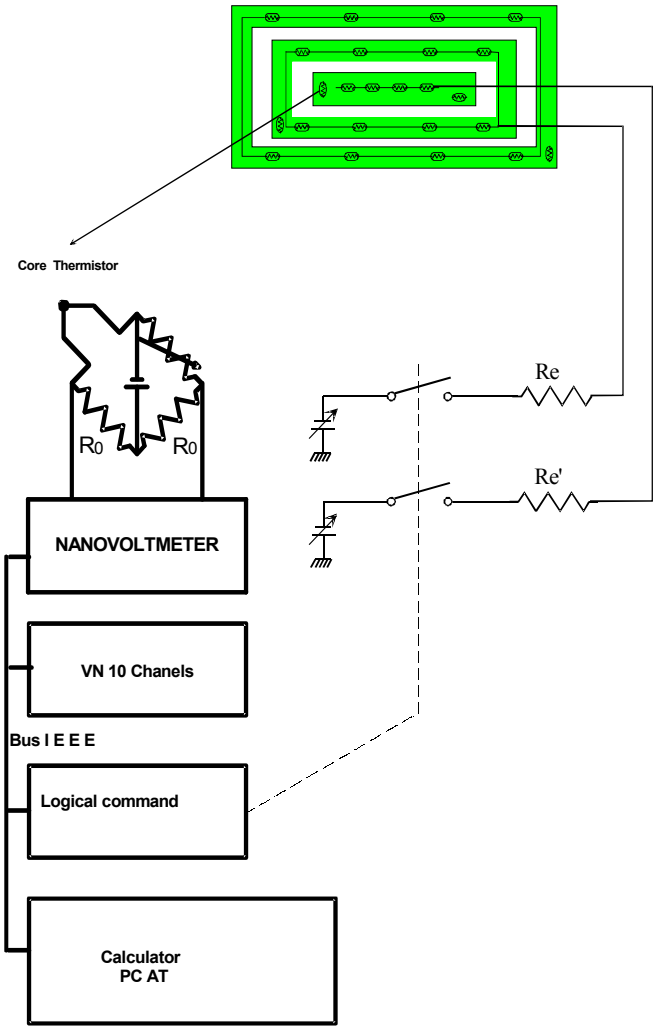

Figure 3: Calorimetric measurement.

The electrical calibration of the calorimeter consists in measuring L_{el}, when dissipating in the core, Q_{el}, a well measured electrical power through four specific embedded thermistors. The electrical calibration factor, F, is the ratio of those two quantities. Then, the heat capacity of the core, the temperature calibration of the thermistor and the residual heat transfers between the core and the surrounding have not to be precisely known.

D. Performances and Analysis of Uncertainties

As an example, the uncertainty components relative to the reference absorbed dose to graphite in the BNM-LNHB cobalt-60 beam are given in table 1

Table 1

Values and uncertainties for graphite calorimetric determination of the reference absorbed dose rate at 5 $g.cm^{-2}$ depth in graphite phantom in BNM-LNHB cobalt-60 beam.

Term	Value	Uncertainties (1s, %)	
		s	u
F	}1.42488 36655 $J.s^{-1}$	0.015	0.016
L		0.026	
M	1.1177 g		0.02
r_{cal}	1.0000		0.1
k_f	1.0000		0.05
k_v	0.9909		0.15
k_i	0.9989		0.1
k_{gr}	1.0002		0.01
k_{tf}	0.9988		0.01
k_k	0.9999		<0.01
k_{et}	1.0000		0.05
k_{fant}	1.0045		0.1
k_z	1.0017		0.01
k_d	1.0003		0.01
k_{air}	1.0000		<0.01
		0.03	0.24
$\dot{D}_g$ (Gy h^{-1})	45.66	0.24	

$$\dot{D}_g = \frac{L \cdot F}{m} \cdot r_{cal}^{-1} \cdot k_f \cdot k_v \cdot k_i \cdot k_{gr} \cdot k_{tf} \cdot k_k \cdot k_{et} \cdot k_{fant} \cdot k_z \cdot k_d \cdot k_{air} \quad (1)$$

With :

F : electrical calibration factor

L : relative variation of the thermistor resistance

m : mass of the core

r_{cal} : calorific yield, equivalent to heat defect correction

k_f : correction for difference of thermal transfers between electrical calibration and irradiation

k_v : correction for vacuum gaps

k_i : correction for impurities

k_{gr} : correction for absorbed dose gradient in the core

k_{tf} : correction for the calorimeter front slab

k_k : correction for the front kapton foil

k_{et} : correction for the PMMA back and radial thickness

k_{fant} : correction for density difference between the phantom and the calorimeter

k_z : correction for depth measurement

k_d : correction for source-reference point distance

k_{air} : correction for air attenuation

A typical set of fifteen runs was involved in this experiment. The uncertainties are given for one standard deviation.

A statistical uncertainty better than 0.03 % has been achieved in a cobalt-60 beam of 0.7 Gy.min^{-1} dose rate. In the high-energy photon beams of the Saturne 43, this uncertainty is higher as beam monitoring introduces an irreducible fluctuation. The overall uncertainty of the reference absorbed dose to graphite is 0.24 % in the cobalt-60 beam.

The main component of the uncertainty stems from the vacuum-gaps correction. Its value is estimated at 0.15 % .

The improvement of the absorbed dose to graphite measured by calorimetry depends on the knowledge of the vacuum gaps correction.

IV. Vacuum-gap Correction Factor Determination

The definition for the vacuum gaps correction at BNM-LNHB is quite different from the definition published by BIPM [11]. The distance between the reference point and the entrance surface phantom is kept constant. The vacuum gaps correction factor is defined as the ratio *R* of the mean absorbed dose in the core with "vacuum gaps" filled with graphite, to the value with "vacuum gaps" empty.

Measurements or simulations are performed in the same conditions.

A. Experimental Determination Based on Diode Measurements

A new experimental determination of that correction has been performed by means of a very small detector inserted in a reproduction of our graphite calorimeter at the centre of the body simulating the core.

The detector is a p-type silicon diode EDE from Scanditronix. Epoxy and build-up cap for medical application were removed. The resulting outside dimensions are 0.4 mm for thickness and 4 mm for diameter.

Two different measurements are done, according to figures 4 and 5, at the reference depth in the graphite phantom. The value of the vacuum gaps correction factor is determined from the ratio of these two measurements. During the experiment gaps were filled with air.

Compared to the ionisation chamber [12, 13], the diode presents a density closer to graphite than air. In addition the perturbation introduced by insulating material is minimised. The symmetry allows the determination of the whole gaps effect (front, back and annular) at the same time. Moreover the small size of the diodes leaves a large amount of graphite in the body simulating the core.

The ionisation current of the diode is measured by a classical ionometric system based on a Keithley 642. No bias voltage is applied to the diode.

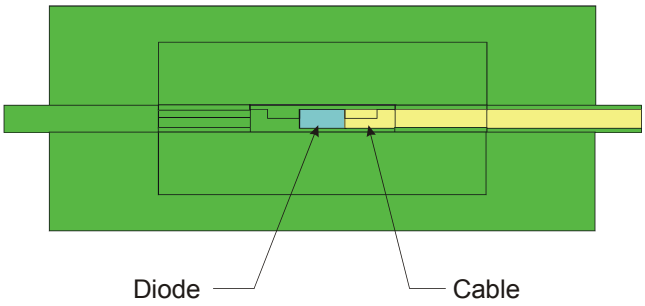

Figure 4: ≪Vacuum gaps≫ filled with graphite.

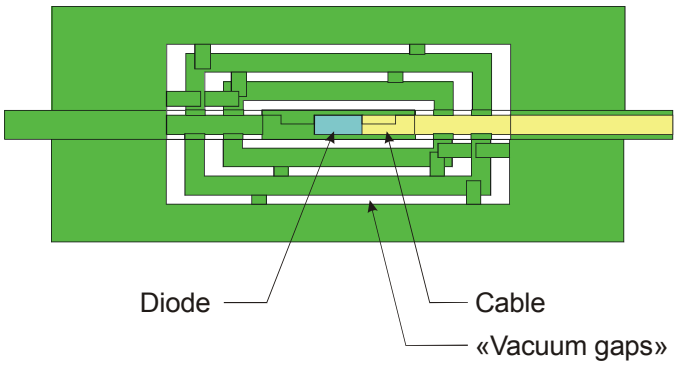

Figure 5: ≪Vacuum gaps≫ filled with air.

The copy of the calorimeter is quasi symmetric, and it was irradiated on each side for each configuration.

Measurements were performed in a cobalt-60 beam and high-energy photon beams (6 MV, 12 MV and 25 MV) from the G. E. Saturne 43. The values of the effective attenuation coefficient measured with the diode is different from the one measured with ionisation chambers, especially in the cobalt beam. This is an effect of the diodes hyper-sensitivity to low-energy photons (compared to ionisation chambers) due to the presence of silicium of higher atomic number. The ratio of ionisation currents, *R*, is corrected for this difference of effective attenuation coefficient applied to a graphite thickness equal to that of vacuum gaps.

The results are summarised in table 2.

B. Monte-Carlo Determination using EGS4-Dosimeter and PENELOPE Codes

For cobalt-60, the photon spectrum in air at the front face of the phantom was measured by gamma spectrometry, replacing the source with an identical one of much lower activity. Both sources had the same geometry and were positioned the same way [14].

For the high-energy photon beams, the spectra were calculated by Monte-Carlo simulation with EGS4 [15]and PENELOPE [16] codes.

The vacuum gaps correction factors were then calculated using EGS4-DOSIMETER [15] and PENELOPE [17].

The results are reported in table 2.

Hundred millions histories were necessary to obtain 0.1 % standard deviation.

Table 2

Vacuum-gaps corrections for graphite calorimeter.

	Co60	**6 MV**	**12 MV**	**20 MV**
k_v (f1)	0.99	0.9917	0.9929	0.9948
k_v (f2)	0.9907	0.9916	0.9924	0.9942
mean experimental k_v	0.9903	0.9917	0.9926	0.9945
EGS4 et ITS3 JD 1994	0.9909			
EGS4-dosimeter JG 1999	0.9909	0.9920	0.9929	0.9951
PENELOPE JM 1999		0.9910	0.9923	0.9931
Mean MC k_v	0.9909	0.9915	0.9926	0.9941

(f1) face 1 toward the source

(f2) face 2 toward the source

In the cobalt-60 beam, the agreement between the former values and the new simulations is excellent. For high-energy photons, the values obtained with both codes agree within the uncertainties.

C. Results in a Cobalt-60 Beam and High Energy Photon Beams (6 MV , 12 MV and 25 MV)

The experimental results and Monte-Carlo determinations of the vacuum gaps correction factor are given in table 2. They are consistent for all beam qualities.

V. Reference Absorbed Dose to Water

A. Based on Absorbed Dose to Graphite Standard

The primary standard of absorbed dose to water at BNM-LNHB in cobalt-60 beam and high energies photons from Saturne 43 is based on graphite calorimetry measurements in a graphite phantom. The absorbed dose to water in a water phantom is derived by a transfer procedure using ionisation chambers and Fricke chemical dosimeter [18].

The overall uncertainty is 0.35 % for cobalt-60 and is under evaluation for the other qualities.

B. Water Calorimeter

In complement to these references, it was decided to develop a water calorimeter.

The principle of the water calorimeter is attractive because the measurement is directly performed in water, the reference material, avoiding the transfer from graphite to water. Moreover the low diffusivity of water allows temperature variation measurement without thermal insulation of the sensitive volume. The delicate determination of the perturbation of the thermal insulating material does not exist (like vacuum gaps for graphite calorimeter).

In practice, there are unfortunately many problems which basically do not exist for graphite calorimeters. The heat defect of water is difficult to control and to determine. At present a realistic evaluation of its uncertainty leads to a value of the same order than the overall uncertainty estimated for the absorbed dose to water derived from the graphite absorbed dose (cf section V.A.). To reduce the convections present in water measurements can be done at 4 °C (and with a vessel). Thermal transfers and heat excesses coming from the vessel containing the purity controlled water have to be thoroughly investigated.

A first probe was built in the laboratory. It is a thermistor bead (0.18 mm in diameter) embedded in a quartz capillary 0.5 mm tube thickness filled by epoxy. The thermistor resistance change is measured with a DC Wheatstone bridge and a nano-voltmeter. We plan to use a lock-in amplifier for measurements.

After some tests at ambient temperature, a thermostatic enclosure was built in order to regulate the water phantom at 4°C. The drift rate obtained with this system is lower 0.5 µK/s compared to an irradiation drift of 700 µK/s in cobalt-60 beam.

VI. Conclusion

At the present time, graphite calorimetry is for us a well-established technique. The very good reproducibility of the measurements is most likely due to our specific thermal control. Moreover regular experiments with graphite calorimeters as well as TE calorimeters in our laboratory, or even in other laboratories or radiotherapy units, helped us to maintain and improve the technique. In the cobalt-60 beam whose dose rate is about 0.7 Gy/min the typical overall uncertainty on the reference absorbed dose to graphite is 0.24 % for one standard deviation. The precision of the absorbed dose to graphite is confirmed by the new experimental and Monte-Carlo determinations of the correction factor for vacuum gaps which is the main source of uncertainty.

After a period of interest in neutron-therapy (seventies, eighties) and then in proton-therapy (early nineties) where experiments with TE calorimeters have allowed to corroborate protocols (neutron) or to confirm new stopping powers values (proton), these kind of measurements are now rare. But this TE calorimeter is kept operational.

A water calorimeter is being built. It will be operated at 4 °C. This calorimeter will be considered as a metrological complement to measurements based on graphite calorimetry

References

[1] Guiho, J.P., Simoen, J.P., Domen, S.R., Comparison of BNM-LMRI and NBS absorbed dose standards for 60Co gamma rays, Metrologia 14 (1978) 63-68

[2] Boutillon, M., Revision of the results of international comparison of absorbed dose in graphite in a 60Co beam, Rapport BIPM-90/4

[3] Perroche, A.M. et al., Comparison of the standards of air kerma and of absorbed dose of the LPRI and the BIPM for 60Co g rays, Rapport BIPM-94/6

[4] ICRU Report 24 (1976), Determination of absorbed dose in a patient irradiated by beams of X or gamma rays in radiotherapy procedures

[5] Caumes, J., Simoen, J.P., A TE-calorimeter as a primary standard for neutron absorbed dose calibrations, Journal Européen de Radiothérapie 5 (1984) 235-239

[6] Caumes, J. et al. Direct calibration of ionisation chambers with a TE calorimeter at the Orléans cyclotron neutron facility, Strahlentherapie 160 (1984) 114-130

[7] Caumes, J., Ostrowsky, A., Steinschaden, K., Mesures dosimétriques dans les faisceaux de neutrons de haute énergie. Utilisation du calorimètre étalon, Congrès SFPH Tours juin 1985

[8] Delacroix, S. et al., Proton dosimetry comparison involving ionometry and calorimetry, Int. J. Radiation Oncology Biol. Phys. 37 (1997) 711-718

[9] Brede, H.J., Schlegel-Bickman, D., Dietze, G., Daures-Caumes, J., Ostrowsky, A., Determination of absorbed dose within an A-150 plastic phantom for a d(13.35 MeV)+Be neutron source, Phys.Med.Biol. 33 (1988) 413-426

[10] Domen, S.R., Lamperti, P.J., A heat-loss-compensated calorimeter : theory, design, and, performence, J. of Res. of the N.B.S. A. Phys. and Chem. 78A (1974) 595-610

[11] Boutillon, M., Gap correction for calorimetric measurement of absorbed dose in graphite with a 60Co beam, Phys. Med. Biol. ,34, n°12 (1989) 1809-1821

[12] Owen,-B., DuSautoy,-A.R., Correction for the effect of the gaps around the core of an absorbed dose graphite calorimeter in high energy photon radiation, Phys. Med. Biol. (1991) 36 1699-1704

[13] Gerrra, A.S., Laitano, R.F. and Pimpinella, Gaps effects at various depths in graphite calorimeter : experimental determination with variable field size at Co-60 gamma-ray beam, NPL Calorimetry Workshop, 12-14 october 1994

[14] Morel, J., Etcheverry, M., Vallée, M.,Characterisation of the spectral distribution of scattered photons for the french national primary 60Co beam, (1995) Note technique LPRI/95/010 presented at ICRM congress 15-19 july 1995 in Paris

[15] Gouriou, J., Modélisation à l'aide de la méthode de Monté-Carlo du facteur de correction de perturbation lié à la présence des interstices de vide dans le calorimètre en graphite du BNM-LPRI placé dans un faisceau de cobalt 60 (1998), Note Technique LPRI/98/019

[16] Mazurier, J., Salvat, F., Chauvenet, B., Barthe, J., Simulation of photon beams from a Saturne 43 accelerator using the code PENELOPE, Physica Medica 15 (1999) 101-110

[17] Mazurier, J.,Gouriou, J., Chauvenet,B. ,Adaptation of the Monte Carlo code PENELOPE for absorbed-dose metrology : calculation of the perturbation correction factors for some reference dosimeter. (will be submitted to PMB.

[18] Chauvenet, B., Baltès, D. and Delaunay, F., Comparison of graphite to water absorbed-dose transfers for 60Co photon beams using ionometry and Fricke dosimetry, Phys. Med., Biol. 42 (1997) 2053-2063

QUESTIONS AND ANSWERS

Carl Ross: The BIPM devoted considerable effort to measuring the vacuum gaps. As I remember, they gave a way of getting the correction for different sizes of gaps. How do your numbers compare to theirs?

Josiane Daures: Our correction factor is less than 1. Is that your question? The k_v factor calculated by the BIPM for our calorimeter and for the ^{60}Co beam of BIPM is 0.5%. When they performed the measurement they put an additional thickness of graphite in front of the calorimeter whose thickness is equal to the vacuum gaps, but in our case we do not add this. The thickness of the three vacuum gaps is about 3.31 mm and we do not add 3mm in front of the phantom so our correction factor is 0.99 and not 1.005. It is not a mistake.

Alan DuSautoy: There is a difference of material at the front. Can you say whether or not you get agreement because it is easy to remove this attenuation. Whether or not you have material at the front, you can correct for it. So are you in agreement with the BIPM calculations?

Josiane Daures: We are in agreement with the BIPM because if we compare strictly the attenuation and the k_v, k_v is higher than expected if we only take into account the attenuation because when the vacuum gaps are present they induce a leak of scattered photons. We can't simply do with a transmission correction. We agree with the calculation of BIPM. Our calculation, the calculation of BIPM and measurements with the diode are very consistent.

Alan DuSautoy: How do you compare with the NPL measurement?

Josiane Daures: With the ionisation chamber?

Alan DuSautoy: Yes.

Josiane Daures: At the time when you published the paper I noticed quite slight differences and I know you tried to calculate it with EGS4. Have you got some results?

Alan DuSautoy: The results for then, which was a while ago, were for a compensated mode where you have added the graphite from the gaps at the front. We got 0.5% from ionisation chamber measurements and about 0.7% from the EGS4 calculations - I don't know if that agrees with your results.

Josiane Daures: I am not a specialist on Monte Carlo code but J Jeannot in our lab is very able. In 1994 I made some calculations, as a common user of EGS4, and I was very

surprised - the values of J Jeannot are exactly the same as what we have found now. It is quite miraculous!

--

Jan Seuntjens: The uncertainty on the temperature rise measurement, is this the sample standard deviation on the mean?

Josiane Daures: This is the uncertainty for the electrical calibration factor. It is one standard deviation on the mean.

Jan Seuntjens: How many measurements are involved?

Josiane Daures: About 15. The graphite calorimeter is very precise. This result was for the measurements made in a ^{60}Co beam. In the linear accelerator the uncertainty is a bit higher but we paid a lot of attention to monitoring because our LINAC is very stable so we can have very a low uncertainty.

Alan DuSautoy: This is in dose to graphite?

Josiane Daures: Yes.

Jan Seuntjens: What is the reason that the standard deviation is low. Is it because of the specific heat capacity of graphite? The temperature rise is much more easily measured?

Josiane Daures: We do not have to know the heat capacity of graphite because of the electrical calibration factor.

Jan Seuntjens: Yes, but why can you get this uncertainty on 15 measurements when in a water calorimeter we have to make 500 measurements to get this uncertainty. Is it because of the specific heat capacity of graphite?

Josiane Daures: The heat capacity? No, because it is only 5 times higher. I think that thermal control for the graphite calorimeter is easier than with water calorimetry. It is because of the thermal control.

Jan Seuntjens: It must be the signal because the thermal control of the drift rates in the water calorimeter are very low. It is just the signal which is small in the water calorimeter.

Tony Aalbers: Yes, you have stronger signals in the graphite calorimeter.

Alan DuSautoy: For the graphite calorimeter at the NPL the absorbed dose to graphite has exactly the same total uncertainty but random uncertainty I believe is slightly higher. So your temperature measurements are very good.

Josiane Daures: The feedback on the adjacent body to the core is a very good system.

Alan DuSautoy: If you repeat the same measurement exactly the same way you might get a very low random uncertainty but you have got to decide whether that is the right temperature.

Josiane Daures: I don't understand.

Alan DuSautoy: I'll have to think about that.

A Status Report on the NIST Water Calorimeter

K.P. Gall

The University of Texas Southwestern Medical Center, Dallas, Texas 75235, USA

Abstract

A sealed water calorimeter has been constructed following Domen's original design. After reviewing the methods being used in the construction and use of water calorimeters at NIST, PTB Germany, INEA Italy, NPL UK and NRC Canada several modifications were made to Domen's original design. Each of these modifications was made with the intent of simplifying the construction and use of the calorimeter. The thermistor probes were constructed from commercially available glass capillary tubes and the glass bead thermistors were sealed within the capillary with a UV curing plastic. The seal between the capillary and the glass core is made with Teflon. The bridge excitation is done with alternating current and readout is done with an AC lock-in amplifier. The amplifier readout is controlled with a PC computer interface. Additionally the water tank surrounding the sealed glass core was made to be sealed so that it could be oriented for both vertical and horizontal radiation beams. The ability to make depth adjustment of the core was included. Allowance for both mechanical stirring of the surrounding water and inclusion of plastic baffles was made. Like Domen's original design the calorimeter is designed to operate at room temperature. The sealed glass core has been modified with separate inlet and outlet valves to more easily facilitate its filling with appropriately prepared high purity water. The rational for these choices, their effect on the operation of the calorimeter and suggestions for further modifications will be discussed.

QUESTIONS AND ANSWERS

Jileen Shobe: You said that it was set up to run in a horizontal and vertical beam but I only saw that it was set up to run in a vertical beam.

Ken Gall: Yes, but we just turn the calorimeter sideways - it doesn't leak.

Jileen Shobe: That's all you do? Just turn it sidewards?

Ken Gall: Yes

Jileen Shobe: And then you fill it from the side?

Ken Gall: No, you fill it up first and then, as it's a sealed box, just turn it sideways.

Andrew Williams: Have you checked for deflections in your front window when you turn it on its side because a 1mm window is quite thin. So you might find your front window deflecting under the water pressure.

Ken Gall: I haven't checked.

Carl Ross: It will!

Jan Seuntjens: But you can always adjust the position of your vessel.

Carl Ross: But he can't get into it any more it's sealed. Is that right?

Ken Gall: Yes. The point is the way we've got it set up you set up the vessel with the thing turned upside down and then you can quite easily site along the inside surface and set the level of the probes and that is quite easy, then you put it inside the box. One thing we were a little worried about was whether there were any sort of mechanical deflections having turned it upside down and immersing it in water. So we did sight along it while it was immersed in water and we couldn't see any appreciable deviations. I have not looked for window deflections turning it sideways but this is pretty easy to do just by using a depth micrometer.

--

Jan Seuntjens: If you intend to operate at 4 ˚C it is going to shrink. We have seen appreciable changes in dimensions when we run down to 4 ˚C.

Ken Gall: This calorimeter was designed for operating at room temperature. Obviously given recent information it would be prudent to run it at 4 ˚C and we have at least the conceptual design of a cooling system to be included in the housing which could allow for that. However, there are these issues of what happens to the mechanical integrity of the system and making sure that no pressures are going to be built up or decreased causing these glass walls to crack and so forth. But most people operate at 4 ˚C without causing their vessels to crack and so I'm not particularly worried about that. I worry a little bit about the big sealed tank but it turns out that the hoses that we have going in there for the electrical connections are more than enough to take the differences in pressure.

--

Andrew Williams: Did you find that the capacitance of the twisted pair cable that runs from the AC bridge to the thermistors changed much?

Ken Gall: Yes, we did and it is appreciable and measurable but it does not change the net resistance that you read. I talked to Jan about this a little while ago and we were worried about it but it turns out the Stanford Research lock-in separates that reactive part from the resistive part of the overall impedance really well so what we don't see is resistive changes.

Andrew Williams: If you are not spot on the resistive phase you will change your output.

Ken Gall: That's just it, the Stanford research amplifier really just looks at the resistive phase and then the reactive phase differently and so it will tell you what the total phase angle is. We found that you don't have to worry about it. I was quite worried about it for sometime and then we played with the cables and we found some differences such that if you were going out and yanking around on them you could cause net deflections.

However, in the end we calibrated the thermistors at the end of cable and we got the same thermistor calibrations and the same small deflections when you have set them up on the bridge versus changes in the decade box and so I don't think it is a problem. But these are things that we do have to keep our eye on.

Jan Seuntjens: What is the noise level if you ultimately put your thermistor probes in the bridge - you didn't show any figures?

Ken Gall: That is because our noise level is still pretty bad and it is something that we are working on right now to understand where the noise is coming from. Operating in the LINAC beam we got a lot of noise given that we had taken a lot of care in grounding the system.

Jan Seuntjens: It might be something to do with your thermistor probe. Is it related to operating in a LINAC beam or if you just set up the system and you look at the drifts?

Ken Gall: No, just sitting in the room, the noise looks quite reasonable.

Jan Seuntjens: How large is it?

Ken Gall: It was in the couple of microvolts range that we were looking at so it was not horrible. It was well below our signals. I don't remember the figures right now - I'll have to go back and look at that but the noise was not bad compared to the temperature drifts that we were seeing and trying to stabilise.

Andrew Williams: You would probably improve your system by not building your bridge on a breadboard because all those solder joints are bad news. Your two precision thermistors were just dangling around. I would recommend getting a circuit board made so that there are less connections.

Ken Gall: Yes, we put that together to be able to patch components together. In the end when we had settled on the final bridge design we were going to put together a set of solid connections but we were patching in and out different resistors. This was just what we were using for investigative purposes and it is possible that it is causing some of our noise problems.

Malcolm McEwen: Were you saying that you were using twisted pair cable?

Ken Gall: That's right, the cable that runs from the bridge out to the thermistor probes are twisted pairs which are individually foil insulated and then that whole lot is in a cable grade.

Malcolm McEwen: Wouldn't coaxial cable be better for a.c.?

Andrew Williams: The only benefit of coax is that the capacitance is less variable.

Alan DuSautoy: You may have ground loops as well. You say that you earth everything but you don't want to earth everything - you want to make sure that there are breakages in the earth loops.

Ken Gall: I understand what you are saying but we did bring our expert electrician from across the hall and he looked it over with an eye towards ground loops and thought that we had done a good job of bringing everything through one ground and not leaving an opportunity for ground loops. But these things are sort of insidious and can crop up anywhere and so we had an eye towards looking at that again.

Andrew Williams: Is the final cable running within the box twisted pair or are there single leads from your thermistors to a connector on the box.

Ken Gall: It is single leads. But the box should carry the shields outside - it's part of the ground so it shouldn't be an issue.

Preliminary Measurement Results by Water Calorimetry At ENEA

A.S. Guerra[1,3], P. Fattibene[2,3], E. Gargioni[1], R.F. Laitano[1,3], S. Onori[2,3], A. Petrocchi[1]

[1]Istituto Nazionale di Metrologia delle Radiazioni Ionizzanti, ENEA, C.R. Casaccia c.p. 2400, 00100 Rome, Italy

[2]Physics Laboratory, Istituto Superiore di Sanità, Viale Regina Elena, 299, 00161 Rome, Italy

[3]Istituto Nazionale di Fisica Nucleare, Sezione Roma I, Piazzale Aldo Moro 2, 00161, Rome, Italy

Abstract

A water calorimeter of the "sealed water" type was designed and built at the ENEA-INMRI. The present work was carried out in collaboration with the Italian National Institute of Health (ISS) since this calorimeter was intended also for use in the framework of a project on proton therapy supported by ISS. The water calorimeter was designed to perform measurements in horizontal beams at variable depth in water both at ambient temperature and at 4 ˚C. The measuring system can be operated in both AC and DC mode. Results on heat flow calculations, performed to optimize the dimensions of the sealed glass ampoule, are also reported, together with preliminary results on calorimeter performance at the ENEA-INMRI 18 MeV electron beam.

I. Introduction

The absorbed dose to water standard currently working at the Italian national standards institute for radiation measurement (ENEA-INMRI) is based on graphite calorimeter. In order to have a direct and independent standard of absorbed dose to water, a water calorimeter of the "sealed water" type was designed and built at ENEA-INMRI. The present work was carried out in collaboration with the Italian National Institute of Health (ISS) since this calorimeter was intended also for use in the framework of a project on proton therapy supported by ISS.

The water calorimeter was designed to perform measurements in horizontal beams at variable depth in water. To this end the glass ampoule inside which the thermistor probes are located is movable along the beam axis in the calorimetric water tank. Detailed studies on the temperature distribution in a calorimeter water tank were made in operational conditions with vertical radiation beams [1]. In irradiations with horizontal beams the temperature distribution is different from that occurring with vertical beams [2]. The optimal dimensions of the glass ampoule (size and wall thickness) can on principle vary when using different irradiation geometries. To investigate this aspect heat transport calculations are necessary to assess the effects of temperature gradients occurring at the variable depths where the calorimetric ampoule can be positioned. Another aspect worth to be more thoroughly analyzed regards the choice of the operation mode of the measuring system. The calorimetric bridge can be operated both in DC and AC mode. The choice of the procedure should be on principle based on the characteristics of the method rather than on the possibility that a measuring system is more easily available than another one. Measurements with both the systems should be then performed to choice eventually the method that gives the best signal-to-noise ratio and hence the best precision. Clearly, if working in AC mode, the measurement result may depend on the circuitry reactance. This reactance depends also on type and length of the signal cables. A study of the bridge output vs. the bridge operating frequency is then needed to find the optimum operational frequency of the bridge voltage source. The purpose of the present work was to study all of the above aspects related to calorimeter design and operation mode. The calorimeter was originally designed for measurement at ambient temperature. This choice was suggested by the possibility of operating an experimental apparatus more simple and less bulky than that operating at 4 ˚C. Such characteristics are convenient if the calorimeter is intended to be moved for use in different accelerator plants. To compare the calorimeter performance at low and ambient temperature, a 4 ˚C measuring system was also built and operated.

II. Materials and Methods

A. Calorimeter Characteristics

1) Calorimeter Components

The most relevant features of the SW calorimeter are shown in Fig. 1 (not to scale).

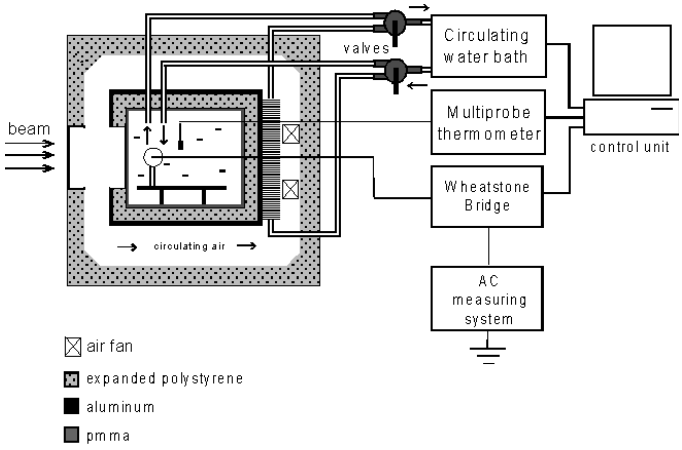

Figure 1: Schematic diagram of the sealed-water calorimeter. Working temperature 277 K or 297 K.

The calorimeter tank consists of a 30 cm side polymethylmetacrylate (PMMA) cube with 1 cm thick walls. At the centre of the tank front wall a 11 x 11 cm^2 entrance window is machined. The window thickness is 3 mm. The cubic tank, filled with once-distilled water, is covered by a PMMA lid. Plates of insulating material (expanded polystyrene) 5 cm thick, are mounted all around the wall of the calorimeter tank. A 5 mm thick electrically grounded aluminum case surrounds the expanded polystyrene plates. The tank entrance window is

covered by a removable 5 cm thick polystyrene plate. The aluminum case is enclosed in a insulating cubic housing, made of 5 cm thick expanded polystyrene. The gap between the case and the housing is 10 cm wide. Air at a temperature near to the calorimeter working temperature is forced to circulate in this gap. The internal surface of the housing is covered by a 1.5 mm thick copper sheet acting as a shield against EMF stray radiation and as antistatic shield. The copper shield acts also as temperature equalizer for the air circulating in the gap. At the position in front of the calorimeter window, the EMF shield is thinner to reduce the beam attenuation and consists of a 0.2 mm aluminum foil instead of the 1.5 mm copper.

The calorimeter working temperature is 277 K or, alternatively, 297 K. The stability of the working temperature is obtained by a thermostatic system. This system consists of a refrigerated circulating water bath. The circulating water bath acts both as heater and refrigerator. The water flow of the circulating bath can be switched by a valve system to the water tank or the radiator circuit according to the needs for thermal stabilization. The radiator circuit consists of four groups of radiators and fans placed at the edges of the aluminum case. Additional fans are placed at the top and at bottom of the aluminum case. The resulting thermal stability of the air in the gap is of the order of some mK/h for a maximum daily room temperature fluctuation within ±1 K. The fine control of the temperature in the water tank of the calorimeter is obtained by two immersion heaters and a pump for water stirring. The temperature in the water tank and in the air of the gap is monitored by a digital thermometer with five calibrated platinum resistance temperature probes (RTD) with resolution of 1 mK. The circulating bath and the thermometer are remotely controlled by RS232 and GPIB interfaces.

2) Glass Ampoule

The glass ampoule filled with high purity water is basically similar to that described by Domen [1]. The ampoule dimensions were optimized by the heat flow calculations described below. The ampoule has an external diameter of 36 mm and a length of 120 mm. The wall thickness of the glass ampoule is of 0.3 mm ± 10%, as determined by mechanical measurements over around the ampoule. The thermistor probes pass through fitting holes in bushings of low density polyethylene [1].

The two thermistor probes can be adjusted such to lay on the same plane normal to the beam axis. The distance between the two thermistors is about 1 cm.

3) Thermistor Probe

The temperature probe consists of a glass capillary tube inside which the thermistor is mounted together with two 0.025 mm enamelled copper extension wires. The procedure of embedding the thermistor in the capillary tube is substantially similar to that described by Domen [1]. The thermistors have a diameter of about 0.25 mm and a nominal resistance of 10 kΩ at 25 ˚C. The capillary tube was obtained from 1.5 mm external diameter pyrex pipettes stretched by using an electric heating coil. After heating and pulling down, the external diameter of the glass capillary resulted to be 0.4 mm. The thermistor probe total length is 110 mm. The length of the probe capillary part is 40 mm. A PMMA waterproof adapter was made to connect to the external circuitry the signal wires emerging from the pyrex pipettes.

4) Ampoule Holder

The ampoule holder is made of PMMA and allows the ampoule to rotate around its main axis. The ampoule rotation is necessary to check the thermistor positioning at the same depth in water whenever the ampoule is installed in the calorimetric tank. The ampoule holder can be moved along the beam axis to be able to position the measuring point at variable depths in water (2-25 cm). The measurement depth is set by mechanical measurements between the entrance window and a reference point on the ampoule holder.

5) Gas Flow System

The system to allow gases to be bubbled through the water in the glass ampoule is similar to that described by Domen [1]. It consists of a hydrogen cylinder with a pressure regulator, a gas flowmeter and a glass column (300 cm^3) for bubbling hydrogen in water. The glass ampoule, with the inside thermistor probes, is connected to the glass column by means of a gas-thigh device designed to avoid contamination of the ampoule water by air. All the tubes of the circuit are made of teflon or glass.

The system used for high purity water production is constituted by a demineralizing unit, a reverse osmosis unit, a 60 l polypropylene tank reservoir provided with a sanitization module (UV lamp at 254 nm), and an ultra-filtration unit. The high-purity water produced by this system has a resistivity of about 18.2 MΩ cm at 25 ˚C, as measured on line (type I reagent grade characteristic).

B. Calorimeter Circuitry

1) The Wheatstone Bridge

The Wheatstone bridge used for the present calorimeter can be operated both in AC and DC mode. Two opposite arms of the bridge are formed by high precision metal foil resistors (0.6 ppm/K of temperature stability, 0.01% accuracy). To allow a greater measurement sensitivity a thermistor was mounted in each of the other two arms of the bridge. The thermistors were selected among a number of samples so to have the most similar sensitivity and resistance at a given temperature.

The bridge can be powered by an AC or DC voltage source. The change of the thermistor resistance is measured as a voltage variation at the bridge output. This output is processed by means of a two-phase lock-in amplifier [3] (AC mode) or alternatively by a DC amplifier [4] (DC mode). The output is then measured by balancing the bridge by high precision decade resistors (5 ppm/K of temperature stability, 0.01% accuracy). The lock-in amplifier (or alternatively the DC amplifier) is remotely controlled by GPIB interface.

2) Thermistor Calibration

Before calibration, some pairs of thermistors with nearly the same sensitivity were selected. To this end a number of dummy probes were made similar to the calorimetric probes. Pyrex

pipettes were used with the capillary parts larger in diameter (about 1 mm) than the capillary part of the thermistor probe used for the calorimeter (see sub-subsection A.3). These dummy probes were made so to allow the thermistor and the extension wires to be easily removed from the pipette to be finally mounted in the calorimeter thermistor probe. An array of 10 dummy probes was immersed in water in a dewar of 15 cm internal diameter connected to the refrigerated circulating water bath, with a calibrated RTD probe at the centre of the pipettes array. The thermistor resistance was measured by a high input impedance electrometer. The water temperature in the dewar was varied by ± 3 K around 277 K and around 297 K. Following this procedure, pairs of similar thermistors were chosen and then mounted in thermistor probes.

For the scope of determining the material constant, β, [1] couples of thermistor probes, selected as described above, were calibrated against reference platinum resistance probes traceable to the national temperature standards. The thermistor calibration was made after mounting the thermistor probes in the calorimeter glass ampoule. Then the ampoule was immersed in a thermally isolated PMMA tank connected to the refrigerated circulating water bath. The water temperature was varied by ± 3 K around 277 K and by ± 5 K around 297 K. The resistance of the thermistors in the glass ampoule was measured using the Wheatstone bridge.

C. Heat Flow Calculation

For heat transport calculations a very accurate method was utilized to obtain the numerical solutions of the equations describing heat convection and conduction effects in a fluid. To this end the FORTRAN code ANSYS was used [5]. Heat conduction and convection effects were accounted for in these calculations with particular reference to the temperature gradients due to the heat excess in the irradiated non-water materials.

To describe conduction and convection effects in water, the Boussinesq approximation for the fluid dynamics equations [6] was used. This approximation, which is realistic in our experimental conditions, is based substantially on assuming for water only laminar motion and constant viscosity, specific heat capacity and thermal conductivity with respect to temperature. Moreover variations of water density are assumed to cause only buoyant forces. With the above approximations the fluid dynamics equations can be written as:

$$\nabla \cdot \vec{u} = 0 \qquad \textbf{(1)}$$

$$\frac{\partial}{\partial \mathrm{t}}(\vec{u}) + \vec{u}(\nabla \cdot (\vec{u})) = -\frac{1}{\rho}\nabla p + \nu \nabla^2 \vec{u} - \vec{g}\beta\Delta T \qquad \textbf{(2)}$$

$$\frac{\partial T}{\partial t} + \vec{u} \cdot \nabla T = \alpha \nabla^2 T + \frac{Q}{\rho c} \qquad \textbf{(3)}$$

where g is the gravity acceleration, Q represents the heat rate per unit volume from any source (due to irradiation and others), and the following parameters refer to the water fluid: u is the velocity, p the pressure, T the temperature, ρ the density, ν the kinematic viscosity, α the thermal diffusivity, β the volumetric expansion coefficient and c the specific heat. The three equations describe: (1) the water flux conservation in the volume considered, (2) the water motion and (3) the heat transport, respectively. The solution of the non linear fluid dynamics equations can be found by numerical methods. To this end the "finite element" method [7] was used in the present study. This method applies even to complex 3D geometry with not necessarily symmetric conditions. In the "finite element" method the volume of interest is divided into a number of regions referred to as finite elements. The equations for any individual element are then formulated to obtain numerical solutions that are interpolated within each element. The smaller the volume element, the more accurate the numerical solutions. The interpolated solutions referring to any individual element are suitably assembled to represent the whole region, by imposing continuity at the element boundaries.

The heat source term, Q, in equation (3) was assumed to be constant during the irradiation time and spatially uniform over the water regions considered in the calculations. The change of Q in the region corresponding to the glass wall of the ampoule was accounted for. The heat source term, Q, was zeroed to calculate the temperature changes after the end of irradiation.

D. Performance of the AC Bridge

A study of the bridge output as a function of the bridge operating frequency was performed by replacing the calorimeter thermistors with two precision resistors (0.6 ppm/K of temperature stability, 0.01% accuracy). The precision resistors had the same resistance as that of the thermistors at the operating temperature. The bridge output was measured at different AC source frequencies using signal cables of different type and different length. Cables of different capacitance per unit length were tested, i.e. 250 pF/m, 120 pF/m and 75 pF/m. For the 250 pF/m cable type three lengths were used, i.e. 1 m (referring to bridge test condition), 15 m and 25 m. These two cable lengths were used in different calorimeter irradiation conditions.

The bridge output was measured using the lock-in amplifier in the differential operation mode. The lock-in output in this operation mode, hereinafter referred to as (A-B), is the difference of the signals addressed to the channels A and B of the lock-in amplifier. In the following, the in-phase and the quadrature components of this output is denoted as $(A\text{-}B)_x$ and $(A\text{-}B)_y$, respectively. The lock-in performance in terms of the amplifier capability of nulling the quadrature component was studied as a function of frequency. To this end the signal supplied from the bridge AC source was split and addressed, by 20 cm cables, to the two channels A and B of the lock-in amplifier. The quadrature component $(A\text{-}B)_y$ of the lock-in output (A-B) will be hereinafter referred to as the lock-in intrinsic signal.

E. Comparison Between AC and DC Operation Mode

The comparison between the AC and DC operation modes concerned the reproducibility of measurements performed in the two modes. To exclude possible instability effects due to temperature changes of water, the calorimeter thermistors were replaced by two precision variable resistors (5 ppm/K of temperature stability, 0.01% accuracy) whose resistance values

were varied to simulate the thermistor resistance change. In the DC operation mode a very accurate cable shielding and reduction of spurious emf sources were necessary. To this end a 1.5 mm thick copper shield was placed all over the inner surface of the calorimeter housing.

F. Measurement Conditions

The irradiation tests with the calorimeter operating at 4 ˚C were performed in a 18 MeV electron beam at the ENEA-INMRI. A 10 x 10 cm^2 beam size at SSD = 100 cm was used. The dose rate was about 1.6 Gy/min at the measurement depth in water of 3.5 cm.

III. RESULTS

A. Thermistor Calibration

The β parameter was obtained by the fitting equation:

$$\ln R = \ln R_0 - \frac{\beta}{T_0} + \frac{\beta}{T} \qquad \textbf{(4)}$$

where R is the thermistor resistance and T the water temperature. The results on the dependence of β on the working temperature are shown in Figure 2 and Figure 3 referring to 297 K and 277 K midrange temperatures, respectively. The β values for four thermistor probes (referred to as T3, T6, T7, T9 in the figures) are reported in the figure legend. For both the midrange temperatures the β values (i.e. the thermistor sensitivity) of the four thermistor probes differ by about 0.3 % from each other. For each of the selected pairs of thermistors the resistance value at a given temperature differs by about 0.4%. For a given thermistor, β varies by about 2% when changing the working temperature from 277 K to 297.

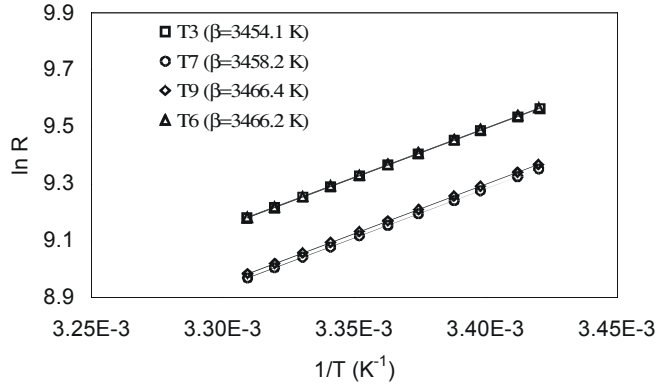

Figure 2: Logarithm of the thermistor resistance as a function of the inverse of temperature at 297 K midrange temperature.

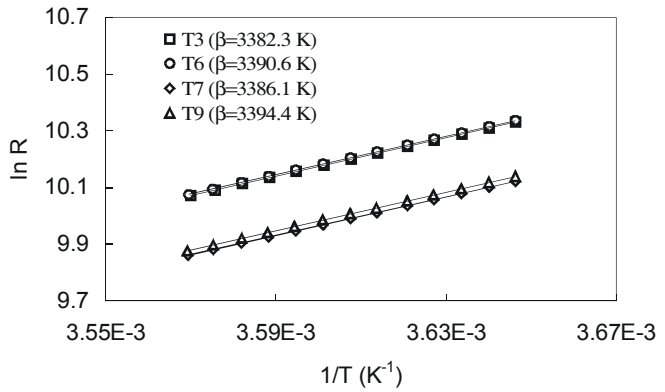

Figure 3: Logarithm of the thermistor resistance as a function of the inverse of temperature at 277 K midrange temperature.

B. Heat Flow Calculation

The curves in Figure 4 show the temperature increase at the centre of the ampoule (i.e. the measurement point, P) due to the heat excess in the ampoule glass wall originating from an absorbed dose of 2 Gy delivered in about 1 min. The difference of temperature between the ampoule glass and the water within the ampoule causes conduction and convection effects. Convection effects were found however negligible even at the temperature of 297 K. The temperature increase in P after irradiation is less than 0.3 % within 60 s elapsed after the end of the irradiation. Therefore for the purpose of absorbed dose determination, a linear extrapolation of the post irradiation drift curve to the mid-run time can be made if this extrapolation is based on the output data referring to a time interval within the first 60 s after the end of irradiation. For the usual values of doses and irradiation time the temperature increase in P due to the heat excess in the ampoule glass was found to be negligible in the period of time during the irradiation. The results in Figure 5 apply to an ampoule of 18 mm radius. The figure shows that, within one minute after the end of the irradiation, the heat flow rate and hence the conduction effects due to the heat excess in the ampoule wall are less than 0.7 % for an ampoule wall thickness up to 1 mm. The curves (a) in Figure 4 and (c) in Figure 5 refer to the same ampoule radius and thickness, like the one used in the present calorimeter. Therefore for the modalities of the linear extrapolation of the post irradiation drift curve, the same considerations as above apply.

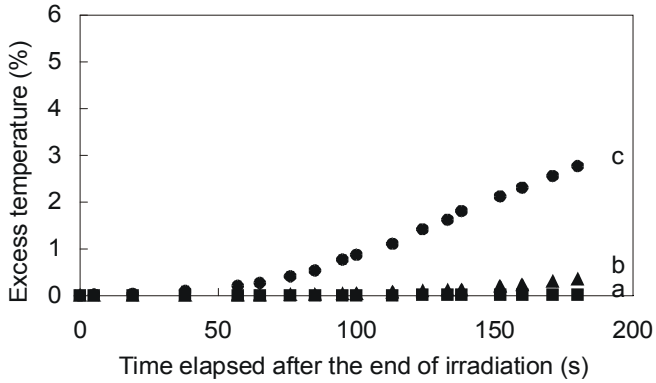

Figure 4: Temperature increase at the measurement point in water, in ampoules of different radius and of 0.3 mm wall thickness as a function of the time elapsed after the end of irradiation. The curves refer to ampoule radius of 36 mm (a), 25 mm (b) and 18 mm (c).

C. Performance of the AC Bridge

In the AC mode the output voltage measurement depends on the circuit reactance due to the possible inductance and capacitance of cables and resistors. In the two-phase lock-in

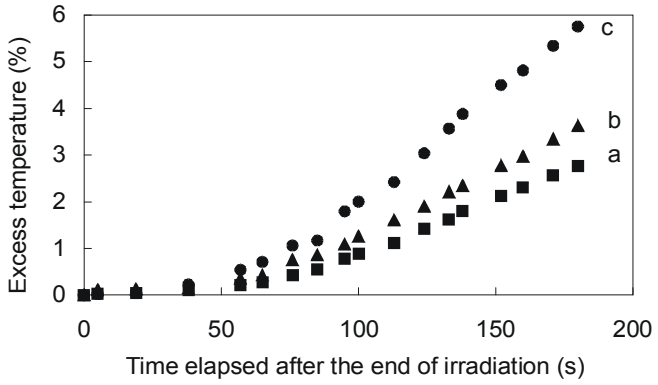

Figure 5: Temperature increase at the measurement point in water, in ampoules of different wall thickness and of 18 mm radius as a function of the time elapsed after the end of irradiation. The curves refer to ampoule wall thickness of 0.3 mm (a), 0.5 mm (b) and 1 mm (c).

amplifier the in-phase component V_x and the quadrature component V_y of the output signal are related to the resistive and to the inductive and/or capacitive loads of the circuit, respectively. When operating in differential mode the optimal value of the working frequency was found as the one at which the $(A\text{-}B)_y$ component of the lock-in output is minimum. Signal cables of different length, as mentioned in Section II D, were used for this analysis. The variation of the $(A\text{-}B)_y$ output as a function of frequency is shown in Figure 6 for three length values of the same cable type. The $(A\text{-}B)_y$ curves show a minimum at frequency values depending on the cable length. The frequency corresponding to the minimum decreases with cable length and changes from 45 Hz to 20 Hz about when the length of the bridge signal cable is changed from 1m to 25 m. As shown in Figure 7 a net signal is obtained if the lock-in intrinsic output signal is subtracted to the overall $(A\text{-}B)_y$ output. The net signal is linearly increasing with frequency. If using longer cables the net signal increases whereas the minimum value of the overall $(A\text{-}B)_y$ output moves to lower frequencies. When changing the cable type the curves show a similar trend. Clearly the cable capacitance per metre is the major parameter that changes the dependence of the overall $(A\text{-}B)_y$ output on the AC source frequency.

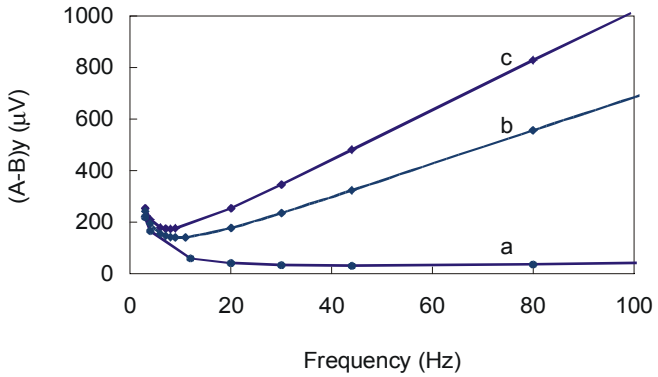

Figure 6: Lock-in output, $(A\text{-}B)_y$, as a function of the frequency of the AC power source for three cables of the same type (about 250 pF/m) and different length: 1 m (a), 15 m (b) and 25 m (c).

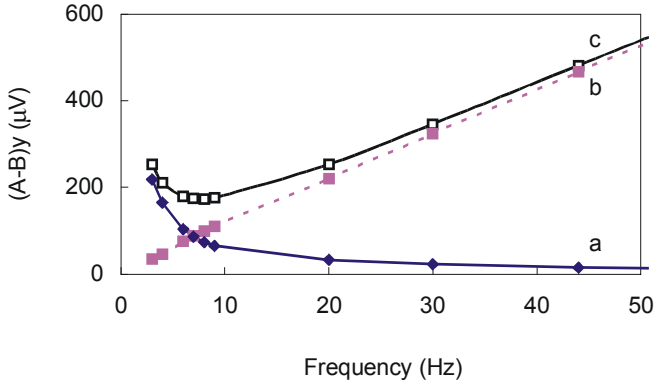

Figure 7: Dependence of the lock-in output $(A\text{-}B)_y$ on the frequency of the AC power source. Curve (a) shows the intrinsic lock-in output, curve (b) shows the net output signal and curve (c) is the overall lock-in output when using a 25 m cable of 250 pF/m capacitance per unit length.

D. Comparison Between AC and DC Operation Mode

The choice between AC and DC operation modes was made after comparison of the measurement reproducibility in the two operation modes. For the evaluation of the short term reproducibility, ten series of ten output signal readouts were performed. The measurement was repeated for four bridge input voltage values V_{in}, corresponding to different electric power, P, dissipated in the thermistors. The experimental standard deviations, σ_{DC} and σ_{AC}, were evaluated and the typical values obtained are reported in Table 1. The table also shows the electric power values, the bridge output as expected from calculation, V_{out}(calc), and the output voltages measured in DC and AC modes, $V_{out(DC)}$(exp) and $V_{out(AC)}$(exp), respectively. In the AC mode, $V_{out(AC)}$ corresponds to $(A\text{-}B)_x$.

Table 1.

Measurement reproducibility of the output signal with the AC and DC systems in terms of the relative experimental standard deviations σ_{DC} and σ_{AC} (1s) of ten repeated measurements. For the symbols, see the text.

P (µW)	V_{out} (calc) (µV)	$V_{out(DC)}$ (exp) (µV)	σ_{DC} (%)	$V_{out(AC)}$(exp) (µV)	σ_{AC} (%)
2.9	3.33	3.35	0.6	3.33	0.1
5.9	4.76	4.76	0.5	4.76	0.1
11.6	6.67	6.67	0.2	6.66	0.1
23.8	9.52	9.54	0.1	9.50	0.1

As shown in the table, for values of the dissipated power lower than 10 µW the reproducibility of ten repeated series of measurements with the AC system is better than that made with the DC system. For dissipated power values higher than 10 µW the AC and DC operation modes are substantially equivalent.

The stability of the measuring system during a continuous measurement of about 1 hour was also determined for the two operation modes (Figure 8). The advantage of the AC system is evident. The noise levels (about 0.03 µV) were similar for the two operation modes. When operating in DC mode a random

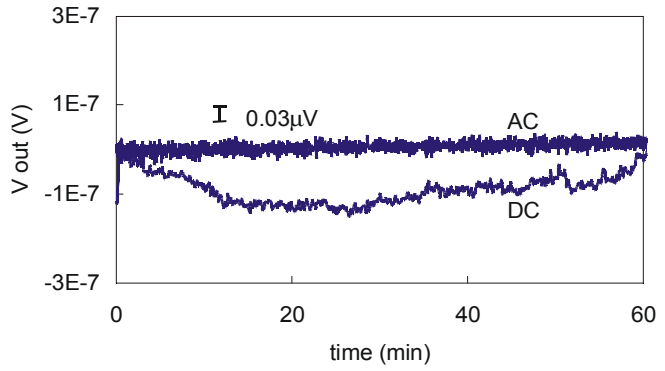

Figure 8: The (AC) and (DC) curves show the stability of the bridge measuring system operated (for a duration of about 1 h) in AC mode and DC mode, respectively.

drift of about 0.1 μV per hour was observed whereas in AC mode the output drift is negligible in the same time interval.

E. Calorimeter Performance

Figure 9 shows an example of drift of the calorimeter output before irradiation. The thermal drift, at the calorimeter operating temperature of 4 ˚C, is of the order of 0.03 μV/min, corresponding to about 3 μK/min. The noise level is of the order of 0.1 μV. This level of thermal stability is obtained typically after 5 hours from switching on the refrigerating system.

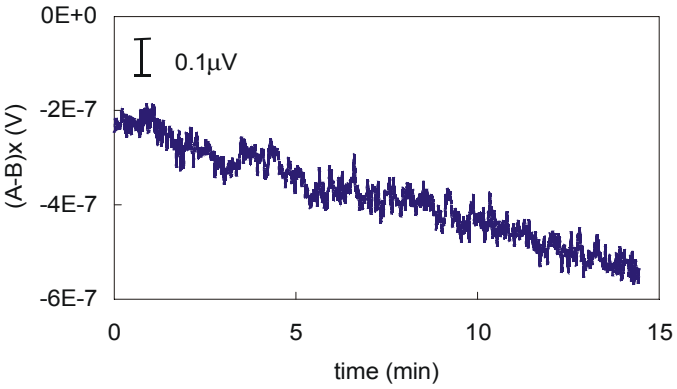

Figure 9: Example of the calorimeter output drift in a period of 15 minutes.

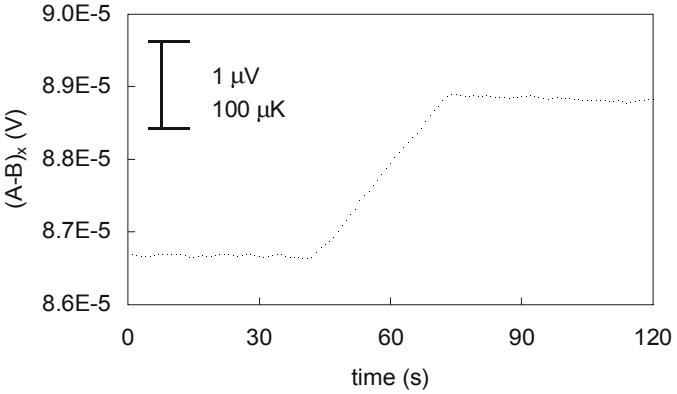

Figure 10: example of 30 s irradiation run using a 18 MeV electron beam with a dose rate of about 1.6 Gy/min.

Figure 10 shows an irradiation run using a 18 MeV electron beam with a dose rate of about 1.6 Gy/min. The pre-irradiation drift is of the order of 10 μK/min. The electric power dissipated in the thermistors is of about 3 μW.

IV. Conclusions

Considerable efforts are being spent at present for improving the electron beam monitoring performance to be able to complete the reproducibility measurements programme. Present instability problems regarding the microtron do not allow to assess the calorimeter reproducibility at levels below 2%.

Acknowledgments

The authors are indebted to Dr. Steve Domen (formerly at NIST) for his suggestions and assistance in calorimeter design. The valuable technical contribution by E. Petetti (ISS) and M. Quini (ENEA-INMRI) is also acknowledged.

References

[1] S.R. Domen, "A sealed water calorimeter for measuring absorbed dose", *J. Res. Natl. Inst. Stand. Technol.* Vol. 99, pp. 121-141, 1994.

[2] J. Seuntjens and H. Palmans, "Correction factors and performance of a 4 ˚C sealed water calorimeter", *Phys. Med. Biol.* Vol. 44, pp.627-646, 1999.

[3] Lock-in amplifier mod. 7260 manufactured by EG&G Instruments, PO Box 2565, Princeton, NJ 08543-2565.

[4] Nanovoltmeter mod. 181 manufactured by Keithley Instruments Inc., 28775 Aurora Road, Cleveland, Ohio 44139.

[5] ANSYS Code version 5.2 manufactured by ANSYS Inc. 275 Technology Drive, Canonsburg, PA 15317.

[6] D.J. Tritton, Physical Fluid Dynamics, Oxford: Clarendon Press, 1988.

[7] J.O. Reddy, An Introduction to the Finite Element Method, New York: J. Wiley & Sons, 1995.

Questions and Answers

Andrew Williams: Your water phantom is cooled by pumping water out of the phantom, cooling it and pumping it back in, is that right?

Antonio Guerra: Yes. The temperature stability of water is monitored (within some tenths of degree) both by the thermostatic system of the circulating water bath and by two temperature probes inserted in the water phantom. Unfortunately we are not able to do many runs because after 5 runs drifts are present.

Jan Seuntjens: This is in electrons?

Antonio Guerra: Yes.

Jan Seuntjens: To five runs?

Antonio Guerra: All the data refer to electrons.

Jan Seuntjens: That is consistent with what we have seen also. In electrons you have much more heat loss than in photon beams and so the number of runs you can do is just three or four. The reason for this is the temperature gradients: are they modelled in the heat flow calculations or is it only the vessel which is modelled and with a uniform dose? Also, do you model conduction only or conduction and convection?

Antonio Guerra: For heat transfer calculations the calorimeter components (vessel, ampoule, probes) were modelled with uniform dose distributions. Actually real electron beams may have less uniform distribution than those assumed in our calculations. Our heat transport calculations include both conduction and convection.

Jan Seuntjens: You model convection also at 4 ˚C?

Antonio Guerra: Yes but only because our calculation was made not only at 4 ˚C but also at ambient temperature conditions.

Jan Seuntjens: The probe effect will pull up the extrapolation. Do you think you can not include it?

Antonio Guerra: Yes, because I have not seen so far any similar effect.

Jan Seuntjens: What is the integration time of the lock in amplifier?

Antonio Guerra: 0.5 seconds.

The Australian Standard of Absorbed Dose

R.B. Huntley, K.N. Wise and J.F. Boas
Australian Radiation Protection And Nuclear Safety Agency
Lower Plenty Road, Yallambie, Victoria 3085, Australia

Abstract

The Australian absorbed dose standard is a graphite calorimeter of the Domen design.

It is operated in the "heat-flow" mode, whereby radiation and electrical heating are used alternately to maintain a steady state. This requires only minor corrections to yield the absorbed dose to graphite, and is used at ^{60}Co and MV X-ray qualities.

The core mass is corrected for buoyancy, and for impurities including the measuring and heating thermistors. The vacuum gap correction has been evaluated as a function of radiation beam size by Monte-Carlo modelling.

The absorbed dose to water and other materials is evaluated using the Photon Fluence Scaling Theorem at ^{60}Co. The effective centre of the ^{60}Co source has been defined with an uncertainty of 0.2 mm. For linac X-ray beams, cavity ionization theory is used to find the absorbed dose to water. These two methods are described, and are compared with the IAEA TRS 277 dosimetry protocol at ^{60}Co.

The Australian standard of absorbed dose to water was compared in 1997 with the reference standard of the BIPM for ^{60}Co. The agreement was within the uncertainty of the Australian calibrations. Bilateral comparisons with UK in 1995 and Canada in 1998 have yielded similar results.

I. Introduction

The Australian Radiation Protection And Nuclear Safety Agency (ARPANSA) was formed [1] on the 5th of February 1999 from the Australian Radiation Laboratory (ARL) and the Nuclear Safety Bureau (NSB), which previously oversaw the operation of the Australian research reactors at the Australian Nuclear Science and Technology Organisation (ANSTO).

ARPANSA is a Primary Standard Dosimetry Laboratory (PSDL) in the IAEA network of dosimetry laboratories. It maintains Australian primary standards of absorbed dose[1], by delegation [2] from the Commonwealth Scientific and Industrial Research Organization (CSIRO).

ANSTO maintains Australian secondary standards of absorbed dose[1], also by delegation from the CSIRO. The ANSTO secondary standards are calibrated by ARPANSA, and may be used to calibrate therapy dosemeters for hospitals (User 2 in Figure 1).

ARPANSA calibrates secondary standard dosemeters for hospitals using the primary standard (User 1).

[1] and of exposure

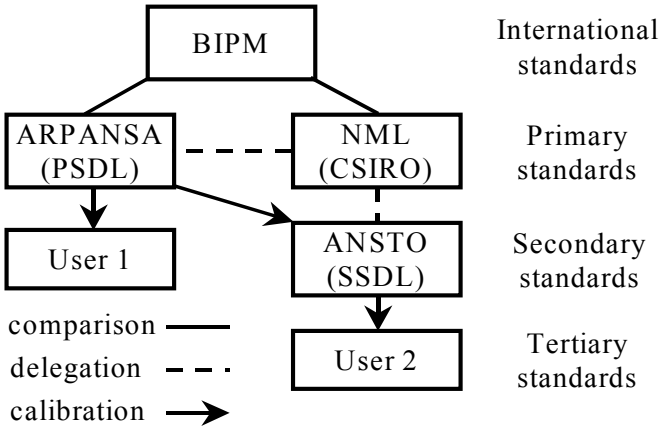

Figure 1: The Australian Absorbed Dose Standards. NML is the National Measurement Laboratory, a division of the CSIRO.

Currently an Australian primary standard of absorbed dose has been established only for ^{60}Co radiation.

Primary absorbed dose standards for other radiations are under consideration, particularly for high energy (MV) X-rays as used in radiotherapy.

II. The ARPANSA Graphite Calorimeters

There are currently three graphite absorbed dose calorimeters at ARPANSA, one of which is the Australian primary standard of absorbed dose.

A small experimental calorimeter was constructed at ARPANSA in 1986 [3].

The previous Australian primary standard calorimeter was constructed at ANSTO in 1978 [4]. This calorimeter is currently being refurbished at ARPANSA after a period of disuse.

A. The Australian Standard of Absorbed Dose

The current Australian primary standard calorimeter was constructed for ARPANSA by the Austrian Research Centre at Seibersdorf (the ÖFZS) in 1991 [5], [6]. The design is based on that of Domen [7]. The calorimeter is shown in Figure 2, with its vacuum connection to a turbo-molecular pump.

This calorimeter is the Australian standard of absorbed dose for ^{60}Co and high energy X-rays. It is shown schematically in Figure 3.

The Core, Jacket and Shield are nested within the Medium, which is enclosed in a lucite vacuum vessel with a mylar front window. There are small vacuum gaps (shown by the thick black lines in Figure 3) between the Core, Jacket, Shield and Medium.

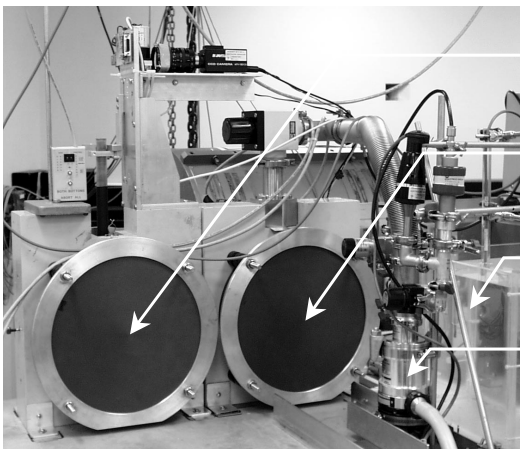

Figure 2: The ARPANSA Graphite Calorimeter and Phantoms.

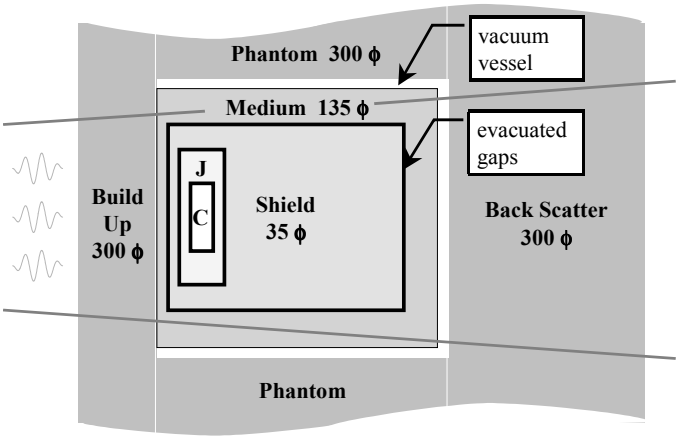

Figure 3: The ARPANSA Graphite Calorimeter Schematic.

The vacuum vessel is surrounded by a doughnut shaped graphite phantom, to which build-up and backscatter disks may be added.

The graphite phantom shown in Figure 2 has interchangeable sleeves for the calibration of various types of ionization chamber in absorbed dose to graphite.

Also shown is a motion control system, which provides for vertical scanning of the radiation beam in the graphite phantom, under computer control. The table can also be scanned horizontally across the beam for two-dimensional beam scans.

A handset facilitates alignment of the equipment with a reference laser beam.

The water phantom is shown at the right hand side of Figure 2. This will be described later.

B. The Heat Flow Mode of Operation

The Medium is kept at a constant temperature by electrical heating.

The Core, Jacket and Shield are heated electrically with the radiation off. The electrical heating is turned off when the radiation beam is on.

All of the energy absorbed in the Core from the radiation beam appears as heat, which passes to the Jacket. The total then passes to the Shield, and the grand total passes to the Medium.

Thus the Core is slightly hotter than the Jacket, which is hotter than the Shield, which is hotter than the Medium.

This is shown by the darkening shades of grey in Figure 3.

This mode of operation is called "Quasi-Isothermal" by Witzani et al. [5].

C. The Calorimeter Electronics

The electronics module (the temperature controller and the measuring bridge) was designed and constructed by the Hungarian Office of Measures (OMH) [8] as part of the ARPANSA calorimeter contract with the ÖFZS.

The Temperature Controller (Figure 4) contains -

- The PID constant-temperature controller for the Medium.
- Three adjustable constant-power heaters for the Core, Jacket and Shield.
- The timer for the electrical heating.
- A digital voltmeter for Core heater power measurements. (An external digital voltmeter is actually used for this because it is more accurate and is more easily calibrated).

The Measuring Bridge contains -

- The Core heater current-sensing resistor (which is mounted in a removable plug at the rear, for calibration purposes).
- Five thermistor bridges for monitoring the temperature drifts of the Core, Jacket, Shield and Medium.

The Core bridge has three configurations using two separate thermistors (C_1 and C_2) and a complementary connection using both thermistors (C_1+C_2).

One bridge at a time is connected to the Phase Sensitive Detector, but all the bridges are permanently energized at 0.5 V_{rms}.

The frequency is set to 11.3 Hz to avoid power line

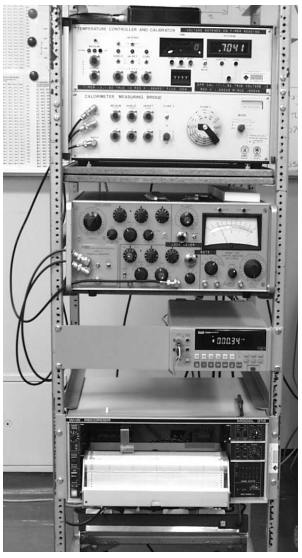

Figure 4: The ARPANSA Calorimeter Electronics.

harmonics.

The Chart Recorder is permanently connected to the output of the Phase Sensitive Detector.

D. Thermistor Bridge Sensitivity

The sensitivity of a single thermistor bridge is given by -

$$\Delta V = -\frac{\Delta R}{R} \cdot \frac{E}{4} \qquad (1)$$

where

ΔV is the voltage change shown by the bridge detector,

$\Delta R/R$ is the fractional change in the thermistor resistance,

and E is the bridge voltage.

The self-heating of the two 10 kΩ thermistors at the bridge voltage of 0.5 V_{rms} is about 16 μW. This is more than the radiation heating power of about 11 μW (the absorbed dose rate is currently about 7.5 mGy/s), but it is a constant heat source that is present whether electrical or radiation heating is taking place.

For E = 0.5 V_{rms} and ΔV = 1 μV_{rms},
$\Delta R / R$ = 8 ppm.

For $\Delta R / R\ \Delta T$ = -3 %/K, this corresponds to about
ΔT = 0.27 mK for a single thermistor bridge,

or ΔT = 0.13 mK for a complementary bridge.

III. Calorimeter Measurements

A. Electrical Heating

The Core electrical heating current I_c is found from the voltage drop across a calibrated series resistor R_i.

$$I_c = (V_{ci} - V_c) / R_i \qquad (2)$$

Two measurements are made with the digital voltmeter -

V_c is the voltage drop across the Core heating thermistor,

V_{ci} is the total voltage drop across the Core heating thermistor and the series resistor R_i.

The electrical heating energy E_e is corrected for the voltage drop in the thermistor leads, up to the point where the Core voltage V_c is measured.

Thus the electrical heating energy E_e (the energy that is denied to the Core during radiation heating) is given by -

$$E_e = (V_c - I_c R_L) I_c T_e \qquad (3)$$

where -

$I_c R_L$ is the voltage drop in the thermistor leads.

T_e is the electrical heating "off" time.

B. No Energy Correction

If the electrical heating energy denied (E_e) exactly matches the radiation energy supplied (E_r) during the radiation heating time T_r, the absorbed dose rate to graphite is given by this simple formula -

$$\dot{D}_c = (E_e / T_r) / m_c \qquad (4)$$

This formula applies only in the ideal case where the electrical and radiation heating rates match exactly.

C. Energy Correction

However, a small correction ΔE is usually needed to E_e. This correction is obtained from the extrapolated chart recorder drift ΔN, which is expressed in chart divisions (in cm).

A small mismatch between the electrical and radiation heating will be seen as a small change in the drift rates as illustrated in Figure 5.

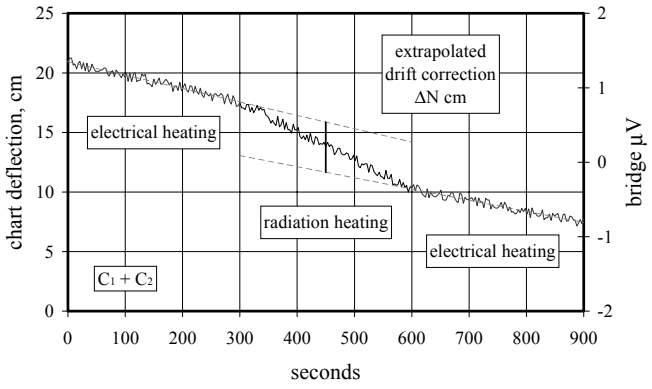

Figure 5: Typical Chart Recorder Trace.

Provided that the three inner bodies (the Core, Jacket and Shield) all have small, linear and parallel drift rates for both the electrical and radiation heating periods, a simple proportionality exists between the chart recorder drift rates, the corresponding temperatures and the heat flows between the bodies.

The complementary bridge C_1+C_2 is used to monitor the Core temperature drift. This doubles the sensitivity.

If the electrical heating in each body exactly matches the radiation heating, all the heat flows Core-Jacket, Jacket-Shield and Shield-Medium will remain the same.

This is difficult to achieve because of the long thermal time constants and multi-body interactions, but with careful adjustment, the electrical heating can be closely matched to the radiation heating in each of the Core, Jacket and Shield.

The Core (with one thermistor), Jacket and Shield bridges are monitored, to ensure that the temperature of each of the three inner bodies drifts at the same small rate in each heating period. These traces have been omitted from Figure 5 for clarity.

When the drifts are the same in each body, constant temperature differences exist between the Core-Jacket,

Jacket-Shield and Shield-Medium, and the heat flows are constant.

Under these conditions, a minor correction to the measured electrical heating energy gives the absorbed dose.

Differences or non-linearities in the temperature drift rates imply incorrect matching of the electrical and radiation heating rates in the three inner bodies.

D. Chart Deflection Components

The extrapolated chart recorder deflection may include components due to the following -

- The Core bridge balance point may be changed during the radiation heating period, to prevent the recorder trace from going off scale. The resulting step change in the chart recorder trace is excluded from the calculation of the energy correction ΔE.
- If the electrical and radiation heating rates are unequal, the temperature drift rates in these periods will differ. This component of ΔN produces the main contribution to the energy correction ΔE.
- If the electrical heating is not turned off for exactly the same time period as the radiation is on, there will be a large drift rate for the (usually short) times during which the radiation and the electrical heating are on together, or are off together. The resulting deflection ΔN is included in the calculation of ΔE.

E. The Fractional Resistance Change $\Delta\mathcal{R}_f$

Changes in the bridge balance conditions are expressed in terms of the fractional thermistor resistance change.

This is related to temperature by an exponential relationship that is approximately linear for small temperature changes. A typical thermistor (10 kΩ at room temperature) has a sensitivity of -3 % / K.

The fractional change in the bridge balance point ($\Delta\mathcal{R}_f$) is the quotient of the difference and the mean of the final and initial values R_2 and R_1.

$$\Delta\mathcal{R}_f = 2(R_2 - R_1)/(R_2 + R_1) \tag{5}$$

F. Energy Correction Calibration

The Energy Correction calibration is a two step process which allows for the Core bridge balance point to be changed during the radiation heating if necessary, to prevent the chart recorder trace from reaching the edge of the chart.

1) Chart Recorder Calibration Factor, C_r

The chart recorder calibration factor, C_r, is found by changing the Core bridge balance point, expressed as a fractional change.

$$C_r = \Delta\mathcal{R}_f / \Delta N \tag{6}$$

Note that this is done using the complementary Core bridge C_1+C_2, as used for the actual absorbed dose measurement, and contemporaneously with that measurement.

Thus the calibration is done for the actual conditions applying during the calorimeter measurement.

2) The Electrical Calibration Factor, C_e

The electrical calibration factor, C_e, is found by turning off the electrical heating without turning on the radiation -

$$C_e = \Delta E / \Delta\mathcal{R}_f \tag{7}$$

This relates the heating energy ΔE to the fractional Core bridge resistance change $\Delta\mathcal{R}_f$.

This is also done using the complementary bridge C_1+C_2, contemporaneously with the absorbed dose measurement.

G. Radiation Heating Energy

The observed deflection (ΔN), evaluated from the extrapolated electrical heating drifts, is first converted to an equivalent fractional Core resistance change using the recorder calibration factor C_r.

The two calibration factors C_r and C_e then give the radiation heating energy E_r -

$$E_r = E_e + [\Delta N\, C_r - \Delta\mathcal{R}_f]\, C_e \tag{8}$$

This shows the subtraction of the effect of an arbitrary change to the bridge balance point ($\Delta\mathcal{R}_f$) from the observed chart recorder deflection.

IV. Absorbed Dose Rate to Graphite

Correcting for the extrapolated chart recorder drift, the absorbed dose rate to graphite is given by -

$$\dot{D}_c = [E_r / T_r / m_c] \prod k_i \tag{9}$$

in which

$E_r = E_e + \Delta E$ is the radiation energy supplied in time T_r,

and where

E_e is the electrical heating energy denied in time T_e, and

$\Delta E = [\Delta N\, C_r - \Delta\mathcal{R}_f]\, C_e$ is the energy correction.

m_c is the Core mass, corrected for buoyancy and for the effect of non-graphite materials, and

$\prod k_i$ is the product of minor corrections. These will be discussed later.

A. Buoyancy Correction

This has been described by Kolrausch [9].

The standard weights and the specimen both displace air, and therefore both experience a buoyancy force.

When the sample density differs significantly from that of the standard weights, these buoyancy forces differ.

The buoyancy correction is given by -

$$m_p = m_n \frac{1-\rho_L/\rho_n}{1-\rho_L/\rho_p} \quad (10)$$

Where the subscripts are the German initials (L = air, p = sample, n = standard weights).

For a typical air density of 1.2 kg/m^3, a graphite sample density of 1800 kg/m^3, and a standard brass weights density of 8000 kg/m^3, this gives $m_p/m_n = 1.00051$.

B. Non Graphite Materials

The effective core mass is the buoyancy corrected graphite mass, corrected for the presence of non-graphite materials (epoxy, polystyrene, thermistors, lead wires) which absorb energy from the radiation beam at a different rate from graphite, and contribute to the heating of the Core.

This correction can be evaluated using the mass energy absorption coefficient and stopping power ratios [5] to calculate the "effective graphite mass" of the non-graphite materials. Strictly, the electron range in the impurity materials should be considered in selection of these parameters [10]. However, for small total impurity mass, as in the present case, the simple total mass of the Core including impurities is very close (0.02%) to the weighted total mass, so the exact weighting scheme chosen is not particularly important. The Core composition is shown in Table 1.

Table 1.

Core Composition.

material	***mass, mg***
graphite (buoyancy corrected)	1557.69
epoxy	1.43
polystyrene	1.39
thermistors + copper leads	1.24
resistance wire	0.12
total mass	***1561.87***
weighted total	***1562.20***
weighted total / total mass	***1.0002***

C. Calorimeter Corrections

Several minor corrections are needed to the measured absorbed dose rate to graphite as shown in equation (11).

$$\prod k_i = k_t k_m k_d k_z k_{rn} k_{an} k_{gap} \quad (11)$$

The corrections are -

k_t ^{60}Co measurements are corrected to a reference date.

k_m X-ray measurements are normalized to a reference charge collected from a transmission monitor chamber. This is normally mutually exclusive with k_t.

k_d All measurements are corrected to a reference distance using the inverse square law. The effective centres of the ^{60}Co and linac sources have been determined by axial beam intensity measurements, corrected for air attenuation and using a robust statistical analysis [11].

k_z The actual depth in graphite of the centre of the calorimeter core is not exactly that required by the PFST (this is discussed later). A fourth power fit (Figure 6) to empirical graphite attenuation measurements has been used to correct the measured absorbed dose to the dose at the reference point.

k_{rn} The radial profile of the radiation beam was measured by scanning with an ionization chamber in the graphite phantom

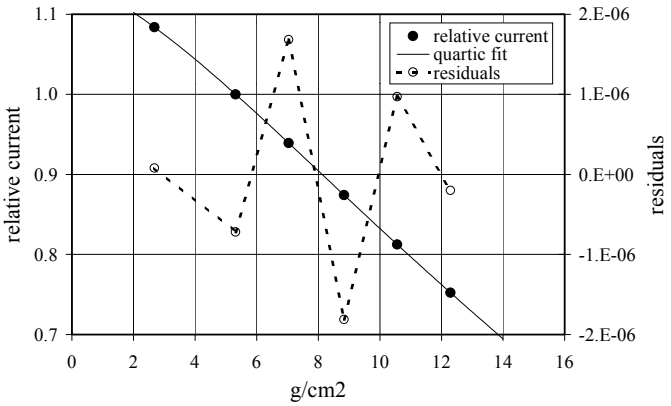

Figure 6: Graphite attenuation, quartic fit and residuals.

as described in section IIA above. The mean absorbed dose rate over the area of the calorimeter Core is corrected to the central axis dose rate.

k_{an} The exponential and inverse square law attenuation of the radiation beam through the thickness of the Core (axial non-linearity) leads to the mean absorbed dose to the Core being slightly different from the dose at the reference point (the geometric centre of the Core). This correction factor is very close to unity for ^{60}Co and MV X-rays.

k_{gap} The vacuum gaps in the calorimeter disturb the radiation fields. The gap correction has been studied by many authors for various calorimeters under different conditions. In this work, Monte Carlo modeling was used [12] to evaluate the gap correction as a function of the radiation beam size, at the reference distance of 650.56 mm. The results (Figure 7) clearly show the dependence of the gap correction on the beam size. These results are in agreement with the findings of other authors for comparable conditions [13], [14], [15].

V. Absorbed Dose to Water

The absorbed dose to graphite may be converted to absorbed dose to water by two independent methods as described below.

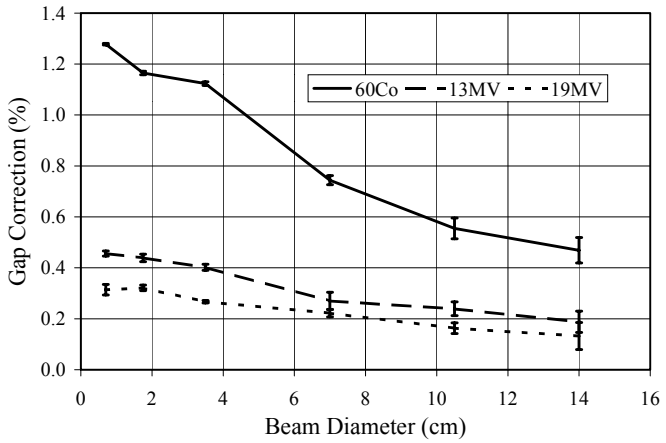

Figure 7: ARPANSA Calorimeter Gap Corrections.

A. The Photon Fluence Scaling Theorem (the dose-ratio or dr method)

The Photon Fluence Scaling Theorem [16] provides an elegant means by which the absorbed dose D_1 measured in material m_1 may be converted to absorbed dose D_2 in another material m_2. The relationship between the absorbed doses is:

$$D_2 = D_1 \Psi_{2,1} \left(\overline{\mu_{en} / \rho}\right)_{2,1} \beta_{2,1} \qquad (12)$$

where the double subscripts denote a ratio of the quantity in materials 2 and 1.

If all the physical dimensions of the two materials m_1 and m_2, including their distances from the radiation source, are scaled by the inverse ratio of the electron densities of m_1 and m_2, and providing that the primary photon interactions are predominantly by Compton scattering, then the total (primary plus secondary) photon energy fluence ratio $\psi_{2,1}$ in equation 12 is given simply by the Inverse Square Law, for point radiation sources.

Note that equation 12 involves only three main factors, all of which have relatively small uncertainties at ^{60}Co.

ψ_{21} is the ratio of the photon energy fluences in m_2 and m_1. For point sources, under these scaled conditions, $\psi_{21} = (R_1/R_2)^2$ (apart from air attenuation which is treated as a correction factor).

$(\mu_{en}/\rho)_{21}$ is the ratio of the mean mass energy-absorption coefficients of m_2 and m_1 for the photon energy spectra at the reference points in m_2 and m_1.

β_{21} is the quotient of the absorbed dose to collision kerma ratios (β = D/K) at the reference points in m_2 and m_1.

The primary photon energy fluence ratio, $\psi_{21} = (R_1/R_2)^2$, can be found precisely by careful measurement, if the effective origin of the radiation beam is known. This has been evaluated with an uncertainty of 0.2 mm for the ARPANSA ^{60}Co source by ionization chamber measurements along the beam axis between 0.6 and 2.7 m.

Starting from the water reference distance of 1050 mm (SSD 1000, depth 50 mm), the scaling factor $(\rho Z/A)_{gw} = 1.6140$ yields the graphite reference distance of 650.56 mm, using a water density at 20 ˚C of 0.9982 g/cc and a measured graphite density of 1.790 g/cc.

Figures 8 and 9 show the water phantom set up at the water reference distance of 1050 mm, and the graphite calorimeter at the graphite reference distance of 650.56 mm.

B. The Cavity Ionization Theory (cit) Method

Alternatively, cavity ionization theory can be used to calculate what the ionization current would be if the graphite phantom surrounding the ionization chamber were replaced by water.

The equations are (a = air, p = perspex, w = water, c = carbon) -

$$\begin{aligned} D_w &= D_c\,(Q_w/Q_c)\,\{(F_c/F_w)(\overline{\mu_{en}}/\rho)_{w,c}\beta_{w,c}p_{w,c}s_{w,c}\} \\ F_c &= \{V\rho/[(W/e)A_{wall}]\}\{\beta_c(\overline{\mu_{en}}/\rho)_c(\overline{L}(\Delta)/\rho)_{a,c}\} \\ F_w &= \{V\rho/[(W/e)A_{wall}]\}\{\alpha_c\beta_c(\overline{\mu_{en}}/\rho)_c(\overline{L}(\Delta)/\rho)_{a,c} \\ &+ \alpha_p\beta_p(\overline{\mu_{en}}/\rho)_p(\overline{L}(\Delta)/\rho)_{a,p} + \alpha_w\beta_w(\overline{\mu_{en}}/\rho)_w(\overline{L}(\Delta)/\rho)_{a,w}\} \end{aligned} \qquad (13)$$

For ^{60}Co at ARPANSA, there are differences between the dr and cit methods of about 0.4%. This is just within the uncertainties of the two methods.

C. Comparison with Nw from TRS-277

Using the new p_{eff} displacement of 0.6 r, the 2nd edition of the TRS-277 protocol gives ^{60}Co calibration factors in absorbed dose to water 0.5 % smaller than those derived from the ARPANSA graphite calorimeter, using the dose ratio method for NE2561 chambers. For NE2571 chambers, this difference is 0.2 %.

D. The Water Phantom

The water phantom is an open-topped perspex tank mounted on wheels, with a computer controlled motion along the beam axis (Figures 8 and 9).

The ionization chamber is mounted in a closely fitting perspex sleeve, at a fixed nominal distance of 1050 mm from the

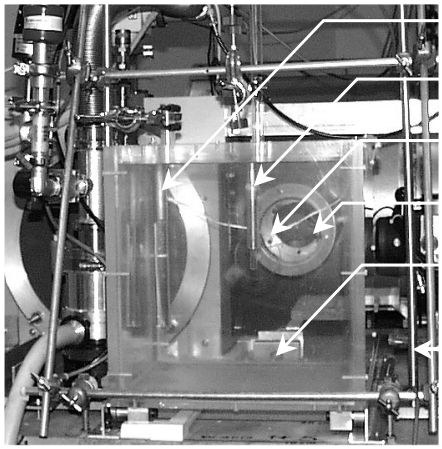

Figure 8: The ARPANSA ^{60}Co Water Phantom (1).

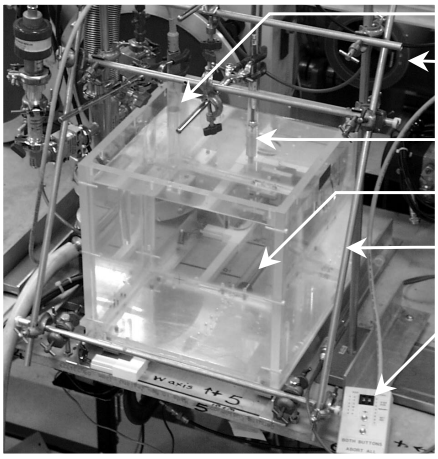

Figure 9: The ARPANSA ^{60}Co Water Phantom (2).

source, by a framework attached to the table.

The air temperature in the ionization chamber is indicated by a calibrated thermistor mounted in a similar sleeve in the tank but outside the primary beam.

There is a 60 mm diameter by 2 mm thick beam entrance window.

The depth of the chamber centre is set to exactly 50 mm from the outside surface of the tank using a perspex depth gauge (Figure 10). The water phantom is moved slightly towards or away from the source (with a minimum step size of 50 μm) using a remote motion control handset (see Figure 9), until the gauge just passes between the chamber sleeve and the inside front wall of the water tank. The gauge is made of perspex rods held together with plastic cable ties.

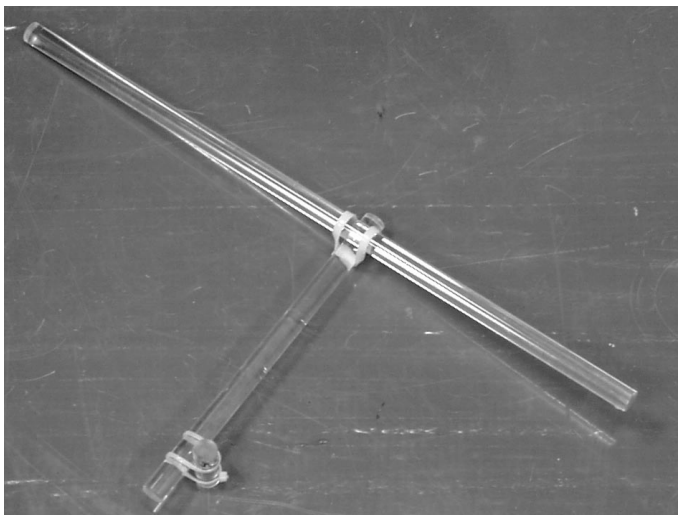

Figure 10: The perspex depth gauge

The gauge is suspended across the tank on the tops of the side walls. The interchangeable spacers have domed ends. The cross-bar is guided by two screws at the sides of the tank, to facilitate the movement of the spacer laterally across the beam.

The distance from the outside of the water tank to a reference plate mounted over the mylar mirror housing is then measured with a micrometer. The ionization chamber current is later corrected to the reference distance of 1050 mm by the Inverse Square Law. As the tank position is always within 1 mm of the water reference distance, this method does not significantly disturb the scaled geometry required by the PFST.

VI. UNCERTAINTIES

The relative standard uncertainty in an ARPANSA absorbed dose to water calibration at ^{60}Co is separated into five components as follows.

Table 2 shows the uncertainties in the physical factors involved in the determination of the absorbed dose to graphite using the calorimeter.

Table 3 shows the uncertainties arising from the measurement of the absorbed dose to graphite using the calorimeter as previously discussed.

Table 4 gives details of the uncertainties involved in the conversion of the measured absorbed dose to graphite into absorbed dose to water using the PFST.

Table 5 lists the uncertainties in the corrections applied to the ionization chamber current measurements.

Table 6 includes the uncertainties due to the repeatability of the primary and secondary standard measurements, and the calibration of the ARPANSA standard current integrator system.

A. Physical Factors

Table 2 shows the percentage relative standard uncertainties in the absorbed dose rate to graphite at ^{60}Co due to physical factors. The dimensions z_c and z_g enter into the calculation of the source to measurement point distance. Their uncertainty affects that in the Inverse Square Law correction to the graphite reference distance. The uncertainty in k_z arises from those in the fit to the empirical graphite attenuation curve, the density of the graphite and the actual thickness of graphite in front of the Core.

Table 2.
Uncertainties in the absorbed dose rate to graphite due to physical factors at ^{60}Co

Percentage relative standard uncertainties of type -	**A : ν**	**B**
k_t – decay correction		0.01
z_c – depth of calorimeter Core in graphite (mm)		0.04
z_g – total width of vacuum gaps in front of Core (mm)		0.02
k_z – correction to the reference graphite depth	0.01 : 4	0.03
k_{rn} – correction to central axis dose	0.02 : 80	0.04
k_{an} – correction for non-linearity of depth dose in Core	0.0003 : 5	
m_c – corrected Core mass		0.01
k_{gap} – vacuum gaps correction		0.02
Combined % relative standard uncertainty in $\dot{D}_c$	***0.07***	

B. Measurement of Absorbed Dose to Graphite

Table 3 shows the percentage relative standard uncertainties in the absorbed dose rate to graphite at ^{60}Co due to factors involved directly in the measurement process. The uncertainties have been weighted to reflect their contributions to the uncertainty in the absorbed dose rate. The uncertainty in the energy correction ΔE is related to the uncertainty of assessing the extrapolated chart deflection ΔN.

Table 3.
Uncertainties in the absorbed dose rate to graphite due to measurement factors at ^{60}Co

Percentage relative standard uncertainties of type -	**A : ν**	**B**
V_c – Core heater voltage		0.02
V_{ci} – Core heater + series R voltage		0.02
R_i – current sense resistance		0.001
R_L – leads resistance		0.03
T_e – electrical heating off time		0.002
T_r – radiation heating on time		0.003
ΔE – energy correction	0.08 : 152	
C_r – chart recorder calibration	0.02 : 25	
C_e – electrical calibration	0.02 : 59	
Combined % relative standard uncertainty in $\dot{D}_c$	***0.09***	

C. Conversion to Absorbed Dose to Water

Table 4 shows the percentage relative standard uncertainties in the conversion from absorbed dose rate to graphite to absorbed dose rate to water at ^{60}Co. The uncertainty in d_{src} arises from the assessment of the position of the effective centre of the source using the inverse square law from axial beam intensity measurements. The uncertainty in k_{pfst} [18] is due to non-compliance with the requirements of the photon fluence scaling theorem.

Table 4.
Uncertainties in the conversion of the measured absorbed dose rate to graphite to absorbed dose rate to water at ^{60}Co.

Percentage relative standard uncertainties of type -	**A : ν**	**B**
d_{src} – source to ref. plate distance	0.05 : 460	
$(\mu_{en}/\rho)_{w,c}$ – mass en. abs. coeff. ratio		0.14
$\beta_{w,c}$ – abs. dose to kerma ratio		0.00
k_{air} – air attenuation		0.01
k_{win} – water phantom window		0.03
k_{pfst} – scaling theorem		0.02
physical factors in $\dot{D}_c$ (Table 2)	0.07	
measurement of $\dot{D}_c$ (Table 3)	0.09	
Combined % relative standard uncertainty in $\dot{D}_w$	***0.19***	

D. Ionization Current Corrections

Table 5 shows the percentage relative standard uncertainties in the corrections applied to current measurements with an NE2561 ionization chamber in water at ^{60}Co.

Table 5.
Uncertainties in NE2561 ionization chamber corrections in water at ^{60}Co.

Percentage relative standard uncertainties of type -	**A : ν**	**B**
k_t - source decay (to reference date)		0.01
k_T – ambient temperature (to 20 C)		0.02
k_P – ambient pressure (to 101.325 kPa)		0.02
k_H - ambient relative humidity (to 50%)		0.01
k_s – saturation (for NE2561 at –200V)		0.03
k_z – depth in water (to 5 g cm^{-2})		0.03
k_{rn} – radial non-uniformity (NE2561)		0.01
k_{sh} – sheath water equivalence		0.01
Combined % relative standard uncertainty in I_{ion}	***0.05***	

E. Absorbed Dose to Water Calibration Factor

Table 6 shows the percentage relative standard uncertainties in an absorbed dose to water calibration factor N_w from ARPANSA, for an NE2561 secondary standard ionization chamber at ^{60}Co.

Table 6.
Uncertainties in N_w from ARPANSA for an NE2561 at ^{60}Co.

Percentage relative standard uncertainties of type -	**A : ν**	**B**
Primary std. abs. dose rate to water	0.05 : 12	0.19
Secondary std. ion chamber current	0.03 : 4	0.05
C_{ref} - reference capacitor value		0.01
V_{ref} – reference voltage measurement		0.006
D_t – time interval measurement		0.002
Combined % relative standard uncertainty in N_w	***0.21***	

The type A uncertainties shown for both the primary and secondary standard measurements are the standard deviations of the means of independent measurements made on different dates.

These values thus include the uncertainty due to positioning of both the radiation source and the detector, and the repeatability of the measurement systems from day to day. These uncertainties were excluded from the previous tables.

The type B uncertainties in C_{ref}, V_{ref} and D_t are associated with the ARPANSA current integrator system.

VII. Comparisons with the BIPM

National primary measurement standards should be compared regularly with the reference standards of the International Bureau of Weights and Measures (BIPM) in Paris.

The Australian absorbed dose to water standard was compared with the BIPM reference standard at ^{60}Co in 1997.

The result was agreement to within 0.2% (N_w ratio 1.0016).

This is well within the combined standard uncertainties of the two primary standards (0.41%).

Further comparisons will shortly be undertaken both with the BIPM, and within the Asia Pacific Metrology Program (APMP).

There will be a multinational "star" comparison in 2000, in which all eight NMIs that have compared their absorbed dose to water standards with the BIPM will participate. This will include ARPANSA.

These comparisons and others will form the basis for a "Mutual Recognition Arrangement", which will facilitate the development of international trade and commerce.

VIII. Future Plans

A recent Opinion Poll conducted amongst ARPANSA's radiotherapy dosimetry clients has indicated overwhelming support for the establishment of a postal TLD quality audit program similar to that operated by the IAEA (primarily for developing countries). This project is very likely to proceed.

The same Opinion Poll showed strong support for the development of absorbed dose standards in high energy photon and electron beams. This will be pursued.

Some work has been done at 16 to 19 MV X-rays in connection with a recent comparison with NPL.

This work has shown that the PFST is of limited use with X-ray beams, in which the position of the virtual source is not well known. Alternatives are cavity ionization theory methods or water calorimetry.

Calorimeter control software will be re-written in LabVIEW and the three graphite calorimeters at ARPANSA will be compared at ^{60}Co.

Because of the difficulty of matching beams and reproducing observations made with research linacs, absorbed dose to water calibration factors of therapy dosemeters will be compared in various clinical X-ray beams.

The software for ARPANSA's current integrator system will be rewritten in LabVIEW. At present, an obsolete Hewlett Packard model 86 computer is used, with software in hp basic.

IX. Conclusions

The Australian standard of absorbed dose has been well established at ^{60}Co.

The Photon Fluence Scaling Theorem provides an absorbed dose to water standard of high accuracy when the position of the effective source is well known. This can be easily achieved at ^{60}Co.

It is a simple matter to re-calculate the scaling factors to provide accurate absorbed dose delivery to arbitrary materials. This has been done recently at ARPANSA to provide precise doses to samples of SiO_2 for geological dating experiments.

Acknowledgements

The authors wish to acknowledge the assistance of Dr David Webb of ARPANSA in the provision of high-energy X-ray beams, and of Mr Keith Pardalis, the ARPANSA Technical Photographer.

References

[1] Commonwealth of Australia, "Australian Radiation Protection And Nuclear Safety Act 1998", Australian Government Publishing Service, 1999.

[2] Commonwealth of Australia, "National Measurement Act 1960", Australian Government Publishing Service, 1993.

[3] R.B. Huntley, "A graphite microcalorimeter as a working standard of ionising radiation absorbed dose", *M.App.Sc. thesis*, Melbourne: RMIT, 1986.

[4] D.F. Urquhart, E.P. Johnson and W.S. Badger, "The Australian commonwealth standard of measurement for absorbed radiation dose", *AAEC/455*, 1978.

[5] J. Witzani, K.E. Duftschmid, Ch. Strachotinsky, and A. Leitner, "A graphite absorbed dose calorimeter in the quasi-isothermal mode of operation", *Metrologia*, vol. 20, pp.73-79, 1984.

[6] The ÖFZS is the Österreichisches Forschungszentrum Seibersdorf Gesellschaft m.b.H. (Austrian Research Centre), A-2444 Seibersdorf, Austria.

[7] S.R. Domen and P.J. Lamperti, "A heat-loss-compensated calorimeter: theory, design and performance", *J. Res. NBS*, vol. 78A(5), pp.595-610, 1974.

[8] The OMH is the Országos Mérésugyi Hivatal (National Office of Measures), Budapest, Hungary.

[9] F. Kohlrausch, Praktische Physik, p.69. Stuttgart: Teubner, 1985.

[10] A. DuSautoy, Private communication, 1999.

[11] K.N. Wise, "Monte-Carlo methods used to develop the Australian absorbed dose standard", Appendix B, "Estimation of virtual source position", *ARPANSA/xxx* (in preparation).

[12] K.N. Wise, "Monte-Carlo methods used to develop the Australian absorbed dose standard", Appendix C, "Determination of the gap corrections", *ARPANSA/xxx* (in preparation).

[13] M. Boutillon, "Gap correction for the calorimetric measurement of absorbed dose in graphite with a ^{60}Co beam". *Phys. Med. Biol*. Vol. 34, pp.1809-1821, 1989.

[14] A.S. Guerra, R.F. Laitano and M. Pimpinella, "Characteristics of the absorbed dose to water standard at ENEA". *Phys Med Biol*, vol. 41, pp.657-674, 1996.

[15] B. Owen and A.R. DuSautoy, "Correction for the effects of the gaps around the core of an absorbed dose calorimeter in high energy photon radiation". *Phys Med Biol*, vol. 36, pp.1699-1704, 1991.

[16] J.S. Priutt and R. Loevinger, "The photon fluence scaling theorem for Compton scattered radiation". *Med Phys*, vol. 9, pp.176-179, 1982.

[17] The NE2561 and NE2571 ionization chambers are manufactured by Nuclear Enterprises Ltd., Bath Road, Benham, Reading, RG7 5PR, England.

[18] A. Leitner and J. Witzani, "The realization of the unit of absorbed dose at the BEV", *in NPL calorimetry workshop, 12-14 October 1994*, NPL, Teddington, U.K., 1994.

[19] LabVIEW is a graphical computer programming language, available from National Instruments Corporation, 6504 Bridge Point Parkway, Austin, Texas.

QUESTIONS AND ANSWERS

Carl Ross: To what extent does your method of operation require that the dose-rate be constant?

Bob Huntley: We don't believe it is a problem because when we do x-ray measurements we normalise them using a monitor chamber which integrates all the dose-rate variations that the calorimeter sees. Perhaps we could improve our standard deviation by using multiple monitors such as have been suggested in the water tank by B and N: that is a good idea because the transmission monitor on the output of the beam does not really tell the whole story. We have confidence in that process.

Simon Duane: The graph you showed was of a run in ^{60}Co - what does a run look like in the LINAC beam?

Bob Huntley: Much the same but just a little bit more ups and downs. If we get really wild things happening we just don't use that run and go and do it again. Wild things do happen sometimes in the LINAC environment.

Jan Seuntjens: Back in the 1980s someone in Gent wrote a paper on the quasi isothermic mode of operation and he provided an algorithm to automate his process of power dissipation. Based on the heat transfer constant between the bodies he calculated what power was necessary to bring it into equilibrium and also, in the isothermic mode, what power was necessary to speed up that process of balancing. I can give you the reference.

Bob Huntley: That would be very useful, thank you.

The Role of the Water Calorimeter in Therapy Dosimetry at the PTB

A. Krauss and M. Roos
Physikalisch-Technische Bundesanstalt (PTB), Fachlabor 6.22
Bundesallee 100, 38116 Braunschweig (Germany)

Abstract

At the PTB, water absorbed dose calorimetry is of increasing importance for the realization and dissemination of the unit of water absorbed dose for radiation therapy using high-energy photon and electron radiation. The calorimetric system at present consists of sealed and unsealed calorimeters for different applications, together with a total absorption calorimeter, for the absolute determination of the heat defect.

To apply the calorimeters for dosimetric measurements some crucial points have to be investigated, such as the handling of the heat defect and of the excess temperature effects caused by material-dependent radiation-induced temperature rises in the detector components embedded in water.

I. Introduction

The Radiology Standards Committee of the Deutsches Institut für Normung (DIN) recommended as early as 1985 that the water absorbed dose be used as the measurand for therapy dosimetry in Germany (DIN 1985, [1]). At present the unit of water absorbed dose is disseminated by calibration of dosemeters under specified conditions at ^{60}Co-γ-radiation in terms of water absorbed dose in a water phantom. The procedures stated in the DIN standard for therapy dosimetry using ionization chambers (DIN 1997, [2]) relate exclusively to these calibrations. The water absorbed dose in high-energy photon and electron beams is obtained by correction factors, k_Q and k_E, which allow for the deviating radiation qualities. The realization of the unit at ^{60}Co-γ-radiation therefore is at present the base and the realization at other radiation qualities essentially enters into the determination of k_Q and k_E factors.

In the following the role of calorimetry in this dosimetric chain will be outlined and the calorimetric equipment and its application as well as some detector properties will be described.

II. The System of Water Absorbed Dose Standards

Up to now, the realization of the unit at ^{60}Co-γ-radiation as well as the realization at the radiation qualities of the linac is performed using the Fricke method [3]. The response of the solution is determined by the total absorption of high-energy electrons of a known radiant energy from a microtron. The calibrated Fricke solution was used to measure the beams of ^{60}Co-γ-radiation sources in terms of water absorbed dose in a water phantom under specified conditions. These sources serve as the working standards of the Physikalisch-Technische Bundesanstalt and are used to calibrate Fricke dosemeters for application at the radiation beams of the accelerators.

When, shortly, the PTB's ^{60}Co-γ-irradiation facility will be replaced by a new one, the calorimeter will act as a primary standard. It allows the water absorbed dose to be measured according to its definition and it allows the uncertainties to be reduced. The water absorbed dose at the high-energy photon and electron beams of the accelerators will then be realized by Fricke dosemeters calibrated by means of the calorimeter at ^{60}Co-γ-radiation. A water calorimeter will also be used to investigate the resultant energy dependence of the chemical yield of the Fricke solution [4] and of the perturbation of the radiation field caused by the vessels into which the solution is filled in, relative to ^{60}Co-γ-radiation.

The next step will be accomplished by the realization of the unit of water absorbed dose at the high-energy photon beams of accelerators, directly by means of a water calorimeter. (Presumably, it cannot be included into the first step, although an additional calorimeter is already available, since the requirements for the PTB linac and its beam line may not yet be fulfilled). Since the uncertainties of the caloric measurements are however essentially increased if the field size is narrowed in comparison with the reference field size for dosemeter calibration (e.g. in the case of stereotactical fields) or if the measurements have to be performed at shallower depths, a combined method (e.g calorimetry and the Fricke method) will be necessary.

The application of the calorimeter in electron beams from accelerators is more difficult because of the steep dose gradients and, in particular, the strong curvature of the depth dose distribution in the vicinity of the depth of maximum dose rate (see, for instance, Roos, [5]). Unfortunately, the reference depths for dosemeter calibration are usually close to this depth rather than to the half-value depth, which would be better suited for caloric measurements.

The procedure being developed at PTB essentially takes advantage of the different values of the specific heat capacity and of the different heat transport properties of materials which, in other respects, are more or less water equivalent [6]. The integration of matched plates of such materials into the water phantom of the calorimeter will the drifts of the calorimeter reading, which result mainly from pronounced curvatures in the depth temperature distributions, to be drastically reduced. (In the case of linear temperature distributions with depth, the heat loss by conduction in the direction of decreasing temperature may be nearly compensated by heat transport from the direction of increasing temperature).

The inclusion of such materials allows the calorimeter to be operated without too large uncertainties. Nevertheless, the radiation quality at the depth of measurement may be kept almost constant. It is thus possible to calibrate energy-dependent dosemeters, such as ionization chamber dosemeters, directly by means of the calorimeter for a few irradiation conditions. A method with low energy dependence (e.g. the Fricke method) will again be used as a link to the remaining irradiation conditions of interest.

III. The Water Calorimetric Equipment

A. Calorimeter

Two water absorbed dose calorimeters to be used at the ^{60}Co-γ-radiation facility and at the 20 MV linear accelerator have been developed at PTB. Some of the design features and operation procedures of the calorimeters are described elsewhere [5], [7-11]. Essentially, the calorimeter consists of a water-filled cubic PMMA (polymethylmethacrylate) tank, each side 30 cm in length, which is mounted inside a thermally insulated container. This calorimeter box is placed inside a second, larger container in which active temperature stabilization is achieved by a forced air stream. The calorimeter can be operated at water temperatures between 4 °C [7] and 20 °C [8], [11]. During irradiation in an extended horizontally directed radiation field, the resulting temperature increase is determined by the output of a bridge circuit, powered either by DC or AC supply.

Different detector types are available for the calorimeter. In the case of non-sealed detectors [6], [7], the amount of non water-material in the vicinity of the thermistors is minimized. This results in both, negligible perturbation of the radiation field and negligible influences due to the material-dependent heating during radiation absorption. This detector is, therefore, suited for the investigation of the respective non-negligible effects of the sealed detectors.

Different types of sealed detectors have been developed. Usually, they consist of a water-filled glass cylinder in which two thin glass pipettes containing a thermistor sensor are mounted opposite to each other (see, for instance, Domen [12]; Krauss [11]). Glass cylinders of different diameter, wall thickness and cylinder length are available for the different measuring tasks. An alternative geometry is a plane-parallel cylinder, the axis being parallel to the beam axis [13]. This design offers the advantage that the flat, thin front and rear walls of the vessel, which are closest to the thermistors, can be built with very precise wall thickness. Finite element heat conduction calculations as well as Monte-Carlo simulations for an investigation of the perturbation of the radiation field can be performed with higher precision.

In the case of the sealed detectors the only material in contact with the water is carefully cleaned glass. The amount of impurities in the water from the vessel walls can, therefore, be minimized, facilitating handling of the heat defect [11], [14], [15].

B. Application of Different Detectors

The different applications of the water calorimeter require different calorimeter properties. In the case of the application as a primary standard at ^{60}Co-γ-radiation the measurements need not be fast. Because of the stability of the radiation field, the measurements may be extended over a prolonged period of time and comparison measurements using different detectors as references must not be performed too often. Handling of the heat defect of the PTB calorimeter with the non-sealed detector type requires a large number of benchmark experiments [10] at the microtron electron accelerator to make absolute measurements possible. However, this accelerator is not available and calorimeters with sealed detectors are, therefore, used. These detector types include a larger amount of non-water material in the vicinity of the thermistors, which causes excess temperature effects [12] and radiation field perturbation effects which have to be corrected.

Primarily, since the excess temperature effect may be kept small and since the wall thickness of plane-parallel detector vessels is constant, the plane-parallel version has been selected in order to reduce the uncertainties.

For measurements at the linac the calorimetric measuring procedure must be fast, since, due to the lower stability of the beams currently available, the measurements have to be referred to measurements using monitor detectors to take account of the changes of the beam properties as a function of time. This is particularly important if the investigations extend over more than one day. Measurements at room temperature are, therefore, to be preferred. As the larger dimensions of the plane-parallel detector in the vertical direction enable convective motion of the water inside the vessel [16], its application should preferably be restricted to 4°C. In contrast to this, the cylindrical detector with appropriate diameter may in many cases also be operated at room temperature, facilitating measurements at the linac. Although convection in the large water phantom outside the detector may occur, the uncertainties of the measurements are usually not too much increased [11], [12].

The calorimeter with the non-sealed detector, operated at 4 °C, is being used to investigate, for instance, the combined energy dependence of the G value of Fricke solution and the vessel-wall perturbation effects. Similarly, the vessel-wall effects of the sealed detectors may be investigated.

In the following the excess temperature effects of the sealed detectors, the construction of the temperature probes and the preparation of the water, crucial for the resulting uncertainties, are discussed in more detail.

IV. Properties of Sealed Detectors

A. Excess Temperature Effects

The excess temperature of the vessel of the sealed detectors depends above all on the wall thickness, the vessel diameter and the irradiation time [17], [18]. The effect can be kept small by a suitable detector geometry, and it can be corrected on the basis of numerical heat conduction calculations.

This has been proved by comparing the results of calculations using the finite element method (Ansys 5.4) with the corresponding measurements for different "benchmark" cylinders of well-defined geometry, made of glass and PMMA [18].

Figure 1 presents the corresponding results for a 120 s irradiation of a PMMA cylinder 30 mm in diameter, with a wall thickness of 3 mm. The numerical results for an identical cylinder of 2 mm wall thickness are given in addition. In that figure the excess temperature has been plotted as a function of time after beginning of irradiation. (The excess temperature is the relative deviation of the radiation-induced temperature rise, with the heat conduction influences allowed for, from the temperature rise, with such influences disregarded). Reasonable agreement is achieved for a period of up to 120 s after the end of the irradiation, which is of significance in practice for the extrapolation of the post-period of the caloric measurement. Towards longer time periods, heat conduction influences due to the irradiation of the more massive cylinder end faces make themselves felt. These have not been taken into account in the computations. Similar results have been obtained for further benchmark experiments with cylinders of different thickness and diameter.

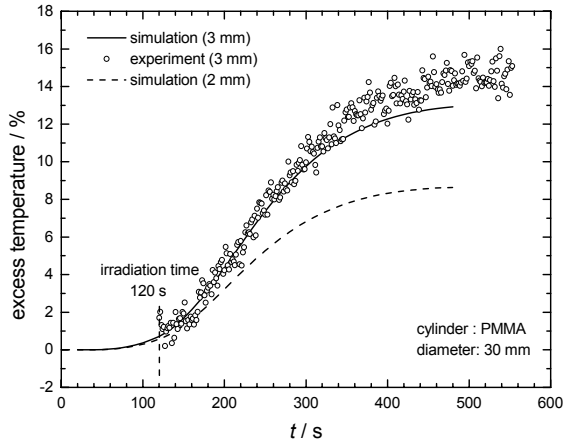

Figure 1: Experimental results and results obtained by numerical computations for PMMA cylinders. The deviation of the radiation-induced temperature rise, with heat conduction influences allowed for, from the temperature rise, with such influences disregarded (excess temperature), is plotted in relation to the latter as a function of the time after beginning of irradiation (dose rate: 0.66 Gy/min; irradiation time: 120 s).

For the geometry and the wall thickness of the plane-parallel and cylindrical detector vessels used in practice in the water absorbed dose calorimeter the excess temperature effects are reduced by about one order of magnitude for the irradiation conditions of figure 1. They can be further reduced for shorter irradiation times [18].

In figure 2 the relative excess temperature as a function of time after beginning of irradiation for a plane-parallel vessel (120 mm diameter, 40 mm length, 0.5 mm front wall thickness) is compared with a cylindrical vessel (40 mm diameter, 120 mm length, 0.3 mm wall thickness). At a time 120 s after the end of the irradiation the excess temperature for the plane-parallel vessel is lower by a factor of about 2, leading to a correction by about 0.15% for linear extrapolation of a 10 - 120 s post-irradiation interval. Even lower corrections are obtained for a lower wall thickness of the front and rear wall or for a greater length of the plane-parallel vessel, resulting in excess temperature corrections below 0.1% for irradiation conditions similar to the reference conditions at ^{60}Co-γ-radiation.

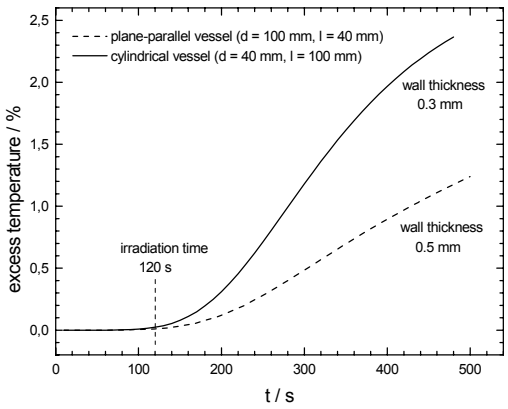

Figure 2: Deviation of the radiation-induced temperature rise, with heat conduction influences allowed for, from the temperature rise, with such influences disregarded (excess temperature), in relation to the latter as a function of the time after beginning of irradiation, computed for glass cylinders of different geometry (dose rate: 0.66 Gy/min; irradiation time: 120 s).

However, the larger volume of this cylinder leads to considerable temperature equilibrium times after a set of irradiations. Assuming a temperature difference of 1.5 mK between the water in the vessel and in the phantom, it can be shown by finite element calculations that the time to reach the equilibrium temperature with a remaining temperature drift at the position of the temperature probes, which is small enough not to affect the caloric measurements, is about 1 hour for the plane-parallel vessel. This is about 60% more than for the corresponding cylindrical vessel and restricts the use of this vessel for applications where measurements need not be too fast.

B. Temperature Probes

The excess temperature developed directly in the thermistors and the glass pipettes of the sealed detector can influence the caloric results by the same order of magnitude as the cylinder wall effect [19], [20]. It can be corrected on the basis of finite element heat conduction calculations, on condition that the geometry and the thermal parameters of the temperature probes are known [18]. In addition to the original temperature probe design by Domen [12], where the 0.25 mm diameter thermistors were embedded in epoxy over a length of about 1.5 mm in the tip of a 0.5 mm diameter glass pipette, we also use probes in which a thermistor of the same size has already been sealed by the manufacturer in a glass rod 8 mm long and 0.5 mm in diameter. The geometry and the materials of these probes can be specified more accurately than for the former ones. Preliminary investigations [11], [18], showed that the excess temperature at the end of a 120 s irradiation (dose rate: 0.6 Gy/min) amounts to

a few μK, and that it strongly drops within about 10 s. However, depending on the irradiation conditions, the exponentially decreasing excess temperature can still affect the caloric measurements towards longer time periods. Detailed experimental work together with numerical calculations is in progress to further investigate the effect.

C. Preparation of the Water

The application of a water absorbed dose calorimeter requires that the heat defect be stable and, preferably, independent of accumulated absorbed dose. Using the sealed detectors, the water inside the vessels can be specially prepared with respect to the heat defect. The so-called H_2-system, which is water saturated with hydrogen, offers the desired properties with a zero value for the heat defect [4], [14].

However, during the preparation process of a nominally pure hydrogen system, an additional contamination, for instance with oxygen, cannot be totally excluded. To prove that the heat defect of such a chemical system is basically predictable on the basis of model calculations, the case of water saturated with a mixture of hydrogen and oxygen in a concentration ratio of about 10 has been studied [11], [21]. The radiation chemistry of this system at room temperature results in a unique dependence of the heat defect as a function of absorbed dose with a sharp peak structure, followed by a stationary state with zero heat defect. Good agreement between calculation and experiment was achieved with respect to the heat defect function, the position of the peak structure and reaching the stationary state. This allows the theoretical heat defect value to be adopted for dose measurements behind the peak region.

Furthermore, this specially prepared water system is also suitable for use in the sense of a quality assurance check for the preparation and filling procedure of the detector glass cylinder. Therefore, measurements are performed in the dose region before the stationary state of the H_2-system is reached. Significant deviations from the theoretical heat defect function indicate the presence of non-allowed impurities in the water.

V. Conclusion

At the PTB, water absorbed dose calorimetry is of increasing importance for the realization and dissemination of the unit of water absorbed dose for radiation therapy using high-energy photon and electron radiation. The calorimetric system at present consists of sealed and unsealed calorimeters for different applications, together with a total absorption calorimeter, for the absolute determination of the heat defect. When, shortly, the PTB's ^{60}Co-γ-irradiation facility will be replaced by a new one, the calorimeter will act as a primary standard. Its application at the linear accelerator, however, is more difficult due to the currently rather poor stability of its radiation fields.

References

[1] DIN 1985. Deutsches Institut für Normung, Begriffe und Benennungen in der radiologischen Technik -Dosisgrößen und Dosiseinheiten- , *DIN 6814-3*, Berlin 1985.

[2] DIN 1997. Deutsches Institut für Normung, Dosismeßverfahren nach der Sondenmethode für Photonen- und Elektronenstrahlung: Ionisations-dosimetrie, *DIN 6800-2*, Berlin 1997.

[3] Feist H 1982. Determination of the absorbed dose to water for high energy photons and electrons by total absorption of electrons in ferrous sulfate solution, *Phys. Med. Biol*. 27 1435-1447.

[4] Klassen N V, Shortt K R, Seuntjens J, Ross C K 1999. Fricke dosimetry: the difference between $G(Fe^{3+})$ for ^{60}Co-γ-rays and high-energy x-rays, *Phys. Med. Biol.* 44 1609-1624.

[5] Roos M 1988 .The current status of water absorbed dose calorimetry in the PTB, *Proc. NRC Workshop on Water Calorimetry* ed. C K Ross, N V Klassen NRC Publication 29637 9-15.

[6] Domen S R 1982. An absorbed dose water calorimeter: theory, design and performance, *J. Res. Nat. Bur. Stand*. 87 (3) 211-235.

[7] Roos M 1987. A water calorimetric determination of absorbed dose to water, *Thermochim. Acta* 119 81-93.

[8] Domen S R, Krauss A, Roos M 1991. The problem of convection in the water absorbed dose calorimeter, *Thermochim. Acta* 187 225-233.

[9] Krauss A, Roos M 1993. The heat defect in the water absorbed dose calorimeter, *Thermochim. Acta* 229 125-132.

[10] Krauss A, Roos M 1994. Water absorbed dose calorimetry at the PTB: handling of the heat defect problem, *Proc. NPL Calorimetry Workshop* Teddington, 1994.

[11] Krauss A, Roos M 1998. Heat conduction, convection and radiolysis of the H_2/O_2 system in the water absorbed dose calorimeter, *Thermochim. Acta* 310 53-60.

[12] Domen S R 1994. A sealed water calorimeter for measuring absorbed dose, *J. Res. Natl. Stand. Technol.* 99, 121.

[13] DuSautoy A R, Williams A J, Rosser K E, Gnaniah S J P 1997. A water calorimeter for high energy photon beams, *Med. Biol. Eng. Comput.* Vol 35 Suppl. Part 2, 1091.

[14] Klassen N V, Ross C K 1991. Absorbed dose calorimetry using various aqueous solutions, *Radiat. Phys. Chem.* 38(1) 95-104.

[15] Klassen N V, Ross C K 1997. Water calorimetry: the heat defect, *J .Res. Natl. Inst. Stand.Technol.* 102, 63-74.

[16] Rogers D W O, Kwarakow I, Klassen N V , Ross C K , Seuntjens J P, Shortt K R, van der Zwan L, Daskalov G 1999. NRC Activities and Publications 1997-1999: Report to CCRI(I) Meeting, BIPM, CCRI(I)/99-24.

[17] Seuntjens J, Ross C K, Klassen N V, Shortt K R 1997. A status report on the NRC sealed water calorimeter, *Technical Report PIRS-584*, NRC Canada, 1997.

[18] Krauss A, Roos M 1999. Heat transport by material-dependent heating during absorption of radiation in the water absorbed dose calorimeter, *Thermochim Acta* 337 45-49.

[19] Palmans H, Seuntjens J 1994. Construction, correction factors and relative heat defect of a high purity, 4 ˚C water calorimeter for absorbed dose determinations in high energy photon beams, *Proc. NPL Calorimetry Workshop*, Teddington, 1994.

[20] Seuntjens J, Palmans H 1999. Correction factors and performance of a 4 ˚C sealed water calorimeter 1999, *Phys. Med. Biol.* 44 627-646.

[21] Krauss A, Roos M 2000. *Radiat. Phys. Chem.*(to be published).

QUESTIONS AND ANSWERS

Ken Gall: Were all those calorimetry runs on one [vessel] filling?

Achim Krauss: That was one filling and during these measurements the sealed detector stayed inside the water phantom of the calorimeter for about 3 months.

Ken Gall: What is the time period for all of this?

Achim Krauss: The time period would be about 8 or 9 weeks - maybe more than 9 weeks.

Jan Seuntjens: How did you perform the measurements in order to make the plot [of figure 1]?

Achim Krauss: The result of the calculations, which included also the result of the irradiation of the cylinder walls, has been normalised to the caloric results at a point 10 seconds after the irradiation has been stopped.

--

Carl Ross: With your water and hydrogen and a small amount of oxygen, you irradiate until the chain reaction happens. Is that done in broad-field situation where you are uniformly irradiating the whole vessel.

Achim Krauss: Yes, almost.

Carl Ross: It's not a ten by ten field?

Achim Krauss: No.

--

Hugo Palmans: You showed a run with the 30 mm PMMA vessel before this slide and you said that there was a reasonable agreement of the post drift curve with the measurements, which I think is excellent, but was the agreement as good for the glass vessels?

Achim Krauss: We also used glass vessels but naturally the glass vessels cannot be manufactured with such precision so we have a variation of diameter along the cylinder axis and therefore we did not have such a reasonable agreement.

--

Andrew Williams: Your plain parallel vessel - that was a glass vessel with a half mm wall thickness?

Achim Krauss: Yes, it was a glass vessel and the diameter was 100 mm with a thickness of 2 mm.for the cylinder wall and a thickness of 0.5 mm for the flat front faces.

Andrew Williams: How did you make the front that thin?

Achim Krauss: We found a company which was able to make that and was it done by grinding it down from the usual wall thickness of about 1mm.

--

Mark Piekmsa: The slide that you showed for the heat defect as a function of dose: why is it such a sharp peak? Is there a physical reason for that?

Achim Krauss: Yes, it can be described in three steps. 1) In the first region up to a dose of about 270 Gy there is a conversion of hydrogen and oxygen essentially to hydrogen peroxide. This is an exothermic effect, increasing slightly with absorbed dose. 2) At that dose [270 Gy] then the small amount of oxygen has been consumed then the chain reaction sets in which hydrogen and hydrogen peroxide is removed to water and this happens over only about a dose range of 10 Gy. 3) When this process has finished a stage of a nominally pure hydrogen system is reached.

Development of A Portable Graphite Calorimeter for Photons and Electrons

M.R. McEwen and S. Duane
Centre for Ionising Radiation Metrology, National Physical Laboratory
Teddington, Middlesex, TW11 0LW United Kingdom

Abstract

The aim of this project is to develop a calorimeter for use in both electron and photon beams. The calorimeter should be more robust than the present NPL primary standard X-ray calorimeter and is designed to be sufficiently portable to enable measurements at clinical accelerators away from NPL. Although intended for therapy-level dosimetry, the new calorimeter can also be used for high-dose measurements at industrial facilities. The system consists of a front end (the calorimeter itself), means for thermal isolation and temperature control, and a measurement system based on thermistors in a DC Wheatstone bridge. The early part of the project focussed on the development of a temperature control system sensitive enough to allow measurements of temperature rises of the order of 1 mK. The control system responds to the calorimeter, phantom and air temperatures and maintains the temperature of the calorimeter to within ± 0.2 mK over several hours. Initial operation at NPL in X-ray and electron beams from the NPL linear accelerator show that the system is capable of measurements of 1 Gy at 2 Gy/min with a random uncertainty of ± 0.5% (1 standard deviation). Operation in Co-60 at a doserate of 1 Gy/min has also been achieved with a similar uncertainty. The result of comparing the calorimeter with the present primary standard calorimeter in Co-60 and 4, 6, 10, and 12 MV photon beams is encouraging, giving agreement at 0.5% level at all energies measured, which is within the measurement uncertainties. Comparison against the electron beam primary standard calorimeter in a 16 MeV electron beam showed a similar agreement. A second calorimeter is currently under development, building on the knowledge gained from the prototype design, to carry out a wider range of measurements in both photon and electron beams. It is intended to carry out measurements "in the field" during 2000.

I. INTRODUCTION

Graphite calorimeters have been under development at NPL for many years. There are separate primary standard graphite calorimeters for high energy photon and electron beams. The photon calorimeter [1] is based on the design by Domen and Lamperti [2] and is a complex device able to measure doserates down to 1 Gy/min. The electron beam calorimeter was first developed for high dose applications in radiation processing and sterilization [3] but has been enhanced to operate at radiotherapy doserates as low as 5 Gy/min [4]. Graphite has obvious advantages as the material to use for a calorimeter in that it is a solid with a high thermal conductivity and zero heat defect (i.e. all the energy deposited by the radiation is expressed as heat). However, its major limitation is that it is not the material of interest. In the majority of dosimetry applications absorbed dose to water is the quantity required and, therefore, corrections are required to convert from absorbed dose to graphite to absorbed dose to water. A water calorimeter would give the desired quantity directly, but water calorimeters tend to be very complex devices and the radiochemical reactions in water lead to a heat defect which makes it difficult to obtain an accurate value of the absorbed dose. Water calorimeters are under development at a number of institutions worldwide - including NPL - and their use is generally restricted to radiotherapy dose levels.

Since the two graphite calorimeters at NPL are of very different designs, it is not possible to define either one as the primary standard for both radiation types. The photon calorimeter can operate in high energy photons from ^{60}Co to 20 MV but is restricted to electron energies above 12 MeV. The electron calorimeter's simplicity of design means that it cannot operate at the limited doserates available for high energy photons. It would be preferable to have a single calorimeter for both electron and photon beams for a range of doserates - from therapy levels up to industrial levels.

NPL offers a number of dosemeter calibration services for high energy photon and electron beams at therapy and industrial doserates. One area of concern for all these services is the validity of the transfer of the calibration from NPL to other radiation facilities. It is assumed that the secondary dosemeters calibrated, whether they are ion chambers or chemical dosimeters, behave in the same way in two radiation beams defined by some beam quality. It is difficult to test this assumption since it has not been generally possible to operate primary standard calorimeters away from NPL. It is a desirable objective to be able to operate a calorimeter in the user's own radiation field. This would enable one to check the transfer of calibrations and investigate beam quality issues. This is primarily a concern at radiotherapy dose levels where the uncertainty associated with a calibration has to be much smaller, but it would also be beneficial to have a calorimeter that could be taken to industrial facilities. Such a calorimeter could also be used as a transfer standard for international comparisons between standards laboratories.

II. DESIGN

A. Design Requirements

The design requirements of this new calorimeter can be stated quite simply:

1. A single calorimeter to operate in high energy photon beams (Co-60 gamma rays and 4 MV to 20 MV X-rays) and electron beams (3 MeV to 25 MeV) at doserates from 1 Gy/min to 10 kGy/min.
2. A simple and robust design, easy to maintain.

3. Portable, to allow measurements at other radiation facilities, primarily in the UK but also in other countries.

There are two main problems with therapy-level calorimetry - measuring the radiation-induced temperature rise, and preventing environmental changes from swamping the measurement. The radiation-induced temperature rise in a material is related to the absorbed dose via the specific heat; a dose of 1 Gy (a typical dose at radiotherapy levels) to graphite leads to a temperature rise of 1.4 mK. To be useful, the calorimeter must be able to measure this dose with an uncertainty better than ± 0.5%, which is equivalent to ± 7 μK. To resolve temperatures to this level at room temperature is a severe problem requiring state-of-the art equipment. The second problem is that of temperature control. To be able to measure the radiation-induced temperature rise in the calorimeter, environmental effects must be kept to a minimum. The radiation-induced temperature rise is obtained by extrapolating the pre- and post-irradiation temperature traces to the mid-point of the irradiation. Changes in these traces due to environmental effects would result in an error in the extrapolation. Ideally, the pre- and post-heat temperatures should be constant, but a linear drift in one direction does not have an effect on the extrapolation. However, any non-linear behaviour in the drift would significantly affect the derivation of absorbed dose. This, therefore, implies that the room where the calorimeter is used must have very stable air conditioning, or the calorimeter must have built-in temperature control. The NPL linear accelerator (LINAC) benefits from a very stable air-conditioning system which keeps the temperature of the irradiation room at ± 0.1 °C, allowing operation of the electron beam calorimeter down to 5 Gy/min with only minimal expanded polystyrene insulation. However, such air conditioning is not generally available in other radiation facilities and therefore the only option is to design a calorimeter with built-in temperature control. Such a control system would have to cope with a wide range of temperatures and rapid temperature changes. For example, a LINAC exposure room in a radiotherapy clinic has a maze entry but no doors, and therefore a calorimeter in such a room could experience a combination of effects due to draughts and heat sources (e.g. the LINAC itself). The situation in industrial facilities is likely to be even more severe, although the requirement for control is not as stringent since the measured temperature rise due to the radiation is much larger.

B. Calorimeter Design

After some consideration it was decided to base the new calorimeter on the present electron beam primary standard calorimeter. Such a device would need further enhancements to allow operation at 1 Gy/min and in more hostile environments than those found at NPL. Graphite was the material of choice since there was already much experience of using graphite calorimeters at NPL. The only other choices are water or water-equivalent plastic. Water is not practicable for a portable calorimeter and little work has been done on plastics, except for polystyrene. Although the conversion from graphite to water adds an additional uncertainty, it was not felt to be a significant problem. The basic elements of the calorimeter are shown schematically in Figure 1. The main calorimeter body is a graphite core and a graphite surround. The core is a disc 20 mm in diameter and 2 mm thick, with holes drilled radially into the disc to accommodate four 22 kΩ bead thermistors of diameter 0.5 mm and length 3 mm. The graphite surround is an octagon 90 × 90 mm in cross section and 6 mm in thickness. The core is thermally isolated from the surround by a nominal 1 mm air gap at all faces and is supported by small expanded polystyrene beads. The octagon is a convenient approximation to the nominal 90 mm diameter circular field of the NPL LINAC at a SSD of 1 m. The thickness of the calorimeter core is chosen so that it can be used in the lowest electron energy available from the NPL LINAC - 3 MeV. The diameter of the core is such that any correction for radial beam uniformity is small.

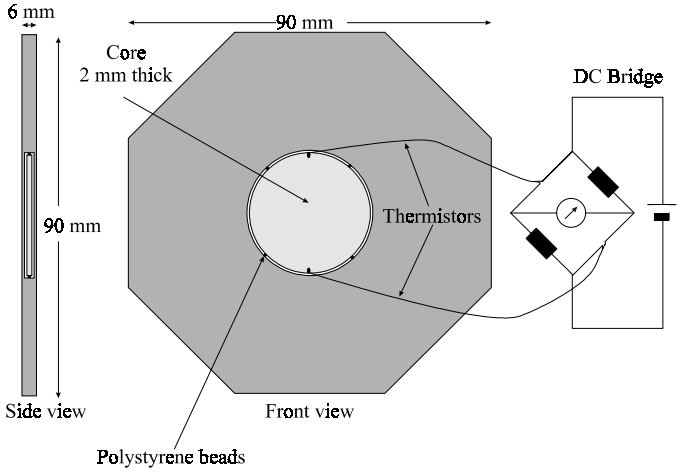

Figure 1: Schematic diagram of calorimeter. For clarity the second bridge and associated thermistors are omitted.

Graphite plates are added in front of the calorimeter body to position the core at the desired measurement depth and also added to the rear to provide backscatter. The optimal thickness of this backing depends on the radiation type, the incident beam energy and on the measurement depth and is chosen so that the temperature rise in the backing is as close as possible to that in the core. One of the major problems with electron dosimetry is the rapid fall-off of the depth-dose curve. If one used a traditional "thick" phantom, such as employed in the photon primary standard calorimeter, there would be significant heat transfer from the core to the graphite surround (especially without the benefit of a vacuum system) making extrapolations more uncertain. The entire calorimeter assembly is enclosed in 35 mm of expanded polystyrene to provide a first level of thermal isolation.

As stated earlier, the absorbed dose to the graphite core D_g is derived directly from the absolute temperature rise ΔT_g and specific heat capacity c_g of the core ($D_g = c_g \times \Delta T_g$). Extensive measurements have been carried out at NPL to measure the specific heat capacity of the graphite core over the temperature range 18-32 °C. Williams [5] looked at several samples of graphite and found no significant difference in the specific heat capacity. He also irradiated a sample up to a dose of 3 MGy and

re-measured the specific heat capacity. Again, there was no significant difference in the result. The result also agreed with previous measurements of the specific heat capacity made at NPL using the method of differential scanning calorimetry [6], but with a much reduced uncertainty.

The most significant drawback of this design is the limited isolation of the core from the surround. By using only a 1 mm air gap, rather than a vacuum gap as in the photon primary standard calorimeter, one increases the heat transfer from the core to the surround. If the time constant associated with this transfer is too small then what is measured is the bulk temperature rise rather than the core temperature rise.

The thermistors that measure the temperature rise in the graphite core are included in opposing arms of two DC Wheatstone bridges constructed from precision resistors with a very low temperature coefficient (<1 ppm/°C). Two commercial 6½-digit voltmeters (DVMs) read the out-of-balance voltages from the bridges simultaneously and are operated under IEEE-488 computer control. The power supply for the bridge is a precision voltage supply (V_{sup} equivalent to 1.4 V) constructed at NPL [7]. The aim of these enhancements to the basic electron calorimeter design was to increase the signal to noise ratio. Two bridges give an immediate improvement. By using thermistors in opposing arms of the bridge one can cancel out some of the induced noise, which theory suggests should be better than single thermistors in individual bridges. Shielded, twisted-pair cable is used throughout to keep noise pickup to a minimum - a linear accelerator is a very electrically noisy environment and therefore every precaution must be taken to minimise the effects of noise. A larger value of the bridge supply can also be used to increase the signal-to-noise ratio, although it also increases the power dissipated in the thermistors and raises the question of non-linear effects due to thermistor self-heating.

The bridge out-of-balance voltage is calibrated directly against the absolute core temperature using a commercial platinum resistance thermometer (PRT). The thermistors used in the calorimeter have been found to be very stable requiring re-calibration only every two years. The effect of accumulated dose on the response of the thermistor type used here has been measured at NPL [8]. No change was measured at the ± 0.1% level for doses in excess of 1 MGy.

It was decided to use a DC bridge rather than an AC bridge for this system for a number of reasons. A DC bridge is simpler to construct; it requires less equipment (the bridge, a stable supply and a DVM); and is simpler to operate (e.g. stray capacitance is not a significant problem). It is also much easier to operate a DC system over a wide range of temperatures, without the need for a complex system of balance resistors as required for an AC system. Although an AC bridge has the potential for an increased signal-to-noise, it is thought that for the temperature rises to be measured (typically 1 mK) a DC bridge will prove sufficient.

C. *Temperature Control System*

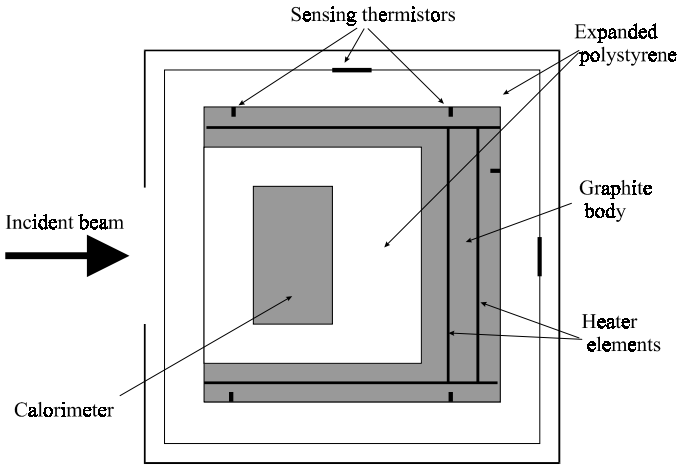

Figure 2: Schematic diagram of the body design - side view.

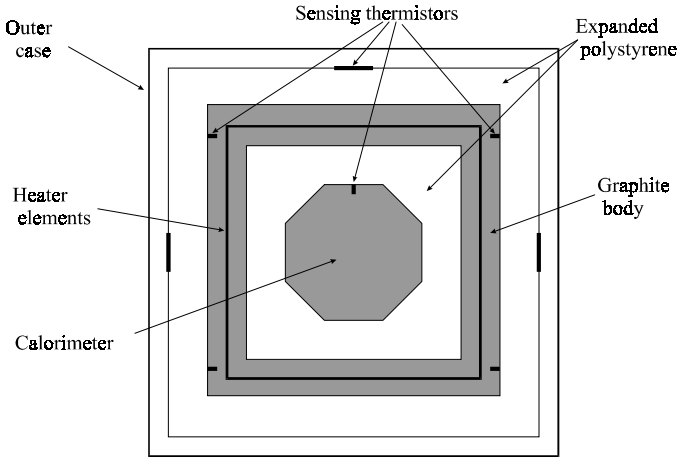

Figure 3: Schematic diagram of the body design - front view.

The temperature control system is shown schematically in Figures 2 and 3. A prototype body was constructed and used in the calorimeter measurements described below. In light of the performance of that system a second prototype was built and this is described here. It consists of a graphite body (total mass ~ 14 kg) which surrounds the calorimeter on five sides. It is not possible to put material in front of the calorimeter since that would affect the measurement depth and prevent operation at the lowest electron energies. Embedded within the graphite body are electrical heater elements which elevate the body temperature to approximately 30 °C. By operating at an elevated temperature one can use the environment as the cooling circuit rather than employing Peltier heat engines. The entire body is surrounded by 25 mm of expanded polystyrene, with an extra 20 mm at the front to reduce the heat transfer from the environment to the calorimeter. This polystyrene is enclosed in 0.4 mm tinned sheet, with 8 μm aluminised mylar at the front, to provide electrically screening. This is shown in Figure 4. An outer aluminium case (again with mylar at the front) is used to protect the calorimeter and acts as a second electrical shield to further reduce noise pickup. This case also provides a stable air volume around the

calorimeter which prevents any drafts affecting the temperature sensors and is easily removed for access.

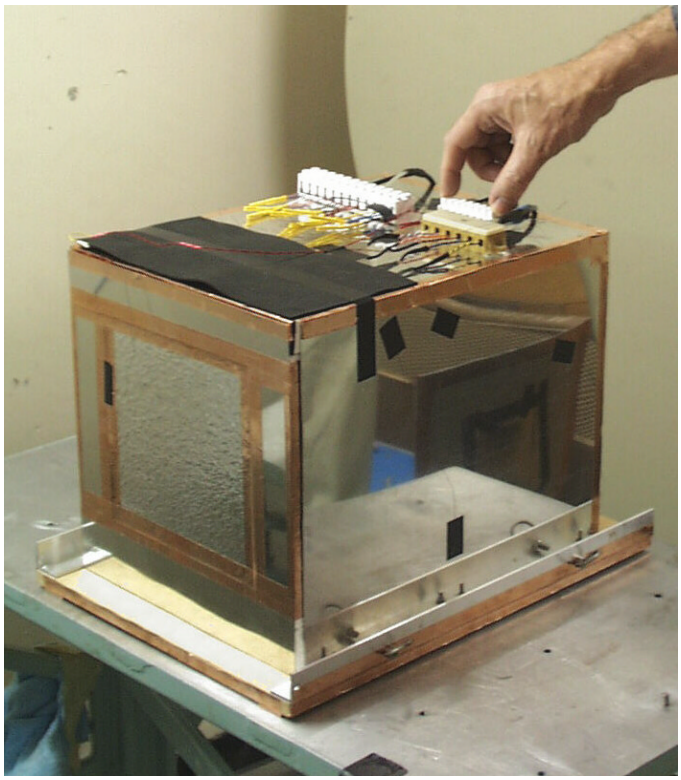

Figure 4: Calorimeter body showing the inner shielding layer.

The current to the heater elements is provided by a computer-controlled power supply. Three temperatures are sensed - the calorimeter surround, graphite body, and outside air. An algorithm running on the controlling PC adjusts the heater current according to the temperatures of the air, body and calorimeter surround in order to keep the calorimeter temperature constant, at 29 °C. An alternative to this system would be to place the calorimeter inside an air-conditioned box. However, to obtain the same stability as the graphite body arrangement one would need such a large volume of air that the system would no longer be portable. The overall dimensions of the body controller are 40 × 30 × 30 cm which makes it relatively easy to transport. It should be noted that there are no fixed heater elements in the calorimeter itself (see below) and that the body is outside the NPL LINAC beam (except behind the calorimeter). This design is therefore best suited to a scattered, rather than swept, beam. The maximum recommended field size is 15 × 15 cm

The temperature sensing thermistors used for the control system are independent of those used to determine the absorbed dose. The sensor for the calorimeter surround is a single thermistor in a DC bridge. The graphite body uses nine thermistors in a series/parallel arrangement in a single arm of a DC bridge. This arrangement behaves like a single thermistor but gives the mean temperature over the whole of the graphite body. Similarly, the air is sensed using four thermistors in a series/parallel arrangement to give the mean air temperature over four sides of the inner case. The three temperature sensors are calibrated in terms of absolute temperature against a PRT in the same way as the thermistors used to measure the absorbed dose.

Separate PCs are used to control the calorimeter temperature and measure the absorbed dose - although this involves more equipment it simplifies the software and allows individual optimisation of the two systems.

Temperature control is achieved as follows. The calorimeter tends towards thermal equilibrium with its environment. Making simple but reasonable assumptions, a model can be set up in which this environment is equivalent to a suitably weighted average of the sensed air and body temperatures. The control algorithm adjusts the power to the body heater so as to maintain this weighted average temperature at a constant value, normally 29 °C. To the extent that the model is valid, it should be that the calorimeter relaxes towards this constant temperature and, provided the air is always cooler than the calorimeter, the effect on the calorimeter of variations in air temperature should be cancelled by variations in the body temperature. (This control algorithm is referred to below as quasi-core constant.)

It turns out that the time constant for ‘settling’ of the calorimeter temperature is about 6 hours, which is rather too long for equilibrium to be achieved overnight, as would be required for measurements in the field. The approach to equilibrium can be accelerated by overheating the body when the calorimeter is cool and warming too slowly, and reducing the power to the body heater when the calorimeter is cool but warming too quickly (or warm but cooling too slowly). The same model as above can be used to make this qualitative idea quantitative, and the result is a control algorithm (referred to below as core constant) for which the time constant is reduced to 1 hour. In this version, variations in the calorimeter temperature have a direct effect on the body electrical heating power, which in turn affect the rate at which the calorimeter temperature drifts. This is to be avoided during radiation measurements, when the pre- and post-heating drifts in the core temperature are extrapolated to determine the absorbed dose. In addition, to further reduce the time for the core to reach equilibrium, a removable heater at the rear of the core can be used to quickly raise the core from room temperature to around the set temperature. This is a simple on/off supply - it is not planned to use it as part of the control algorithm. The heater construction is such that there is little high-Z material to perturb the radiation field.

In the NPL LINAC exposure room, the room temperature control is sufficiently close that, once the system has reached equilibrium, it is enough to maintain the body temperature constant, ignoring the (essentially constant) sensed air temperature. This control algorithm (referred to as body constant) eliminates the possibility that variations in electrical heating power might introduce a systematic error into the radiation measurements.

III. Testing

A. Electrical Noise

As mentioned above, minimising the electrical noise is a priority, and therefore the first stage of testing the calorimeter. A number of the polyimide thermistor probes were constructed,

tested and the ones exhibiting the lowest noise were used in the calorimeter core. Two dual-bridge units with slight constructional differences (different types of enclosure and connectors, different methods of fixing the resistors in position) were used to investigate how construction might affect the inherent noise of the bridge. As for the thermistor tests, the unit with the lowest noise was used for the radiation testing. A comparison was also made between twisted-pair and co-axial cable. The effect of shielding the calorimeter was also investigated and the opportunity was taken to compare the performance of various types of DVM. The required uncertainty of ± 7 μK is close to the resolution of a 6½-digit voltmeter and therefore a 7½-digit instrument could give improved resolution and, possibly, precision. However, DVM resolution has to be considered against acquisition time since both have a direct effect on the extrapolations to determine the absorbed dose. The operation of most high precision DVMs assumes that the measured signal is constant therefore use is made of long acquisition times (> one second) and rolling averages. Such techniques are incompatible with the operation of this calorimeter, where irradiation times are typically 15 s and the relaxation time constant for the core is only 30 s.

B. Temperature Control

Significant effort has been put into developing the control algorithm, outlined above. The control system is somewhat asymmetric in that the body temperature rises much more rapidly at maximum heating power than it falls at zero power. Symmetry could be restored by selecting a higher operating temperature, at the likely cost of greater sensitivity to room temperature variations. The system has been tested in a variety of environments and in various modes of operation, in order to determine the heat transfer coefficients for the three components - air:body, air:calorimeter and body:calorimeter. These depend on the heat capacity of the calorimeter, and so the behaviour of the system varies according to the amount of graphite build-up and backing plates. The likely performance in other, less stable environments than NPL has been evaluated by subjecting the system to periodic variations in room temperature.

C. Thermal Modelling

In order to understand the performance of the calorimeter, extensive modelling of the heat transfer within the calorimeter has been carried out. As a first step, a simple experimental setup was used to acquire data to validate the results of any model. This consisted of an insulated graphite block (90 × 70 × 70 mm) with an electrical heater at one end and thermistors positioned along the major axis. The heater was used to produce a heat pulse that passed along the block. Interfaces and gaps were then introduced into the block to simulate the construction of the calorimeter. A finite-element package (PAFEC) was used to model the setup and reasonable agreement was obtained between experiment and model. The next step was to simulate a calorimeter irradiation - the construction of the calorimeter was described and a calculated 16 MV X-ray dose distribution was used as the "input". The heat transfer from core to surround and within the various graphite plates was then calculated.

D. Calorimeter Performance

The next step was to investigate the performance of the calorimeter, including any systematic effects, and validate it against the present primary standards at NPL. The calorimeter was tested in 4, 6, 10, and 12 MV photons and 6, 10 and 16 MeV electrons using the NPL linear accelerator, as well as in the NPL Co-60 facility. The NPL LINAC is a travelling-wave, two-section research accelerator allowing manual control of all the important operating parameters (pulse current, prf, pulse width, *etc*) at any electron energy in the range 3-20 MeV. A tungsten target (for X-rays) or an aluminium scatter plate (for electrons) is placed at the end of the accelerator flight tube. For the photon measurements a SSD (source-surface distance) of 1 m and field size of 9 cm diameter was used; for the electron measurements a SSD of 2 m and a field size of 15 cm × 15 cm was used. The doserate for photons was varied between 2 and 5 Gy/min while in electrons a higher doserate between 10 and 20 Gy/min was used. By operating at higher doserates one can give the required dose (typically 1 Gy) in a much shorter time and therefore one can investigate more thoroughly the transfer of heat between the calorimeter core and its immediate surround. It is obviously easier to obtain the higher doserates in electrons. A transmission monitor ion chamber is used to correct for current variations in the LINAC output. LINAC pulse repetition frequencies of 200 Hz and 240 Hz were used and the length of the calorimeter irradiations was determined by the number of pulses delivered by the LINAC.

Rather than use the photon primary standard, the calorimeter was compared in X-rays with a calibrated NE2611-type ionisation chamber. NPL maintains a number of these chambers, which are used to calibrate other user chambers and are calibrated themselves against the primary standard on a yearly basis. In the electron beam the calorimeter was compared directly with the electron beam calorimeter. The phantom used in this new calorimeter is much smaller than those previously used and there is a difference in the dose contribution from scattered radiation for which a correction is required before comparing the results from both systems. This effect is likely to be larger for the electron beam where the field size is much larger than the calorimeter phantom. There is also the effect of the body to be taken into account. Although the body is not directly in the beam, there will also be a scatter contribution to the dose measured by the calorimeter core. Measurements were therefore carried out to determine the size of this scatter correction in Co-60, 6, 10 and 16 MV photons and 16 MeV electrons.

IV. Discussion of Results

A. Electrical Noise

Qualitative and quantitative measures were used in assessing noise rejection. Calorimeter runs were viewed graphically and visual comparisons made. The data was then fitted with a linear fit and the RMS deviation used as a measure of the noise in the signal, expressed in terms of temperature. These results are summarised in Table 1.

Table 1.
Results of noise testing.

Component under test	Type-identifier	RMS deviation (μK)	RMS deviation (μK) normalised
Bridge	A	9.1	10.0
Bridge	B	9.5	10.4
Cable	Twisted pair cable	9.4	10.0
Cable	Co-axial cable	10.4	11.1
DVM	7061	8.6	10.0
DVM	2182	10.2	11.9
DVM	1271	13.3	15.5
Calorimeter	Unshielded	11.7	10.0
Calorimeter	Shielded	7.3	6.2
Calorimeter	Electron calorimeter	10.9	9.3

Initial testing of the thermistors indicated that the connectors were critical to minimising the noise. After some investigation it was found that LEMO 00 series (two-pole) gave the best combination of reliability and low noise. Six thermistor assemblies were tested and two were obviously more noisy than the others and were therefore rejected.

There was very little difference in the performance of the two bridge units. The source of electrical noise is often difficult to identify and solder joints/connections are obvious possibilities. The fact that the two bridges showed similar performance indicates that either the joints are good, or they are equally bad in both bridges. There was no difference between the two bridges in each unit. Further refinement of the bridge design is possible by the use of PCB techniques to provide more reliable joints and a larger ground plane.

The difference in the performance of the twisted-pair and co-axial cables was smaller than expected, with the twisted-pair giving approximately 10% less noise (equivalent to 1 μK). Twisted-pair cable gives more noise immunity from magnetic fields, while co-axial cable is better for electric fields. It is generally thought that for a DC bridge in the environment of the linear accelerator, twisted-pair cable gives the lowest noise, but this has not been proved here.

A number of DVMs were tested - Solartron 7061; Wavetek 1271; Keithley 2001 and 2182. The 7061 is the standard DVM used, combining 6½-digit resolution with a reasonably fast acquisition time (0.2 s) and good noise rejection. The other three DVM types were all found to suffer from the same problem - although they have 7½-digit capability, the acquisition time for that resolution was either too long (of the order of 2 s) or the noise rejection wasn't as good as obtained with the 7061. The Wavetek 1271 DVM was the best of rest, offering a faster acquisition time at 6½-digits (0.1 s) but at the price of a noisier signal. The possibility of shielding the DVMs was also investigated but no improvement was observed.

The largest improvement in noise reduction was through the use of electrical shielding around the calorimeter outer case, as shown in Table 1. Without the shielding in place, the calorimeter signal shows large excursions which would make the extrapolations very inaccurate. High frequency noise is not a big problem for calorimetry since the fitting routines used in the extrapolations are very effective. The shielding is very effective in removing the low frequency noise (<0.2 Hz) and reducing the RMS deviation by approximately a factor of 1.6. By way of a comparison, the noise of the electron calorimeter was also measured and found to be as good as the unshielded calorimeter. This is somewhat surprising since the electron calorimeter does not benefit from the cancellation effect of two thermistors in the bridge. However, the electron calorimeter has shorter cabling which will reduce the amount of pickup and may explain the lower noise. The combination of the reduced noise in the new calorimeter and the two bridges gives an improvement in the signal-to-noise over the electron calorimeter of greater than two. This, along with the very stable temperature control, should allow operation of the calorimeter down to doserates of the order of 1 Gy/min.

The results of using different values for the bridge supply for the core thermistors were slightly surprising. Higher values for the bridge supply should improve the signal-to-noise ratio, although the power dissipation in each thermistor is increased. Measurements at bridge supplies of 1.4 V and 2 V showed the expected response but a higher value of 7 V appeared to produce instabilities in the thermistors with large variations in the bridge output. The reason for this is not clear although it is probably related to the complex semi-conductor structure within the thermistor bead. At present there is no plan to use a supply voltage greater than 2 V. The power dissipation of the thermistors raises the core temperature above that of the surround. The value of this temperature difference with a bridge supply of 1.4 V was found to be 1.6 mK. The power dissipation does not vary significantly with temperature (a variation of only 1% over the range 20-30 °C) therefore this difference will act as a constant offset, which will not affect the measurement of absorbed dose. Similarly, there is a temperature difference between thermistor and core - dependent on the power dissipated in the core and the degree of thermal contact between thermistor and core. This "temperature excess" was estimated from the measurements made with different bridge supplies to be ~ 16 mK at a supply voltage of 1.4 V. The effect of the small variation in thermistor power dissipation with temperature on the measurement of absorbed dose has been estimated to be less than 0.01%.

B. Temperature Control

Figure 5 shows the variation in the temperature measured by the various temperature sensors when the control program is started. Initially the calorimeter is at room temperature with all three sensors reading the same temperature. As stated earlier, rapid stabilization of the calorimeter at its operating temperature is a primary requirement of the algorithm, and this is achieved by rapidly heating the body above its operating temperature and

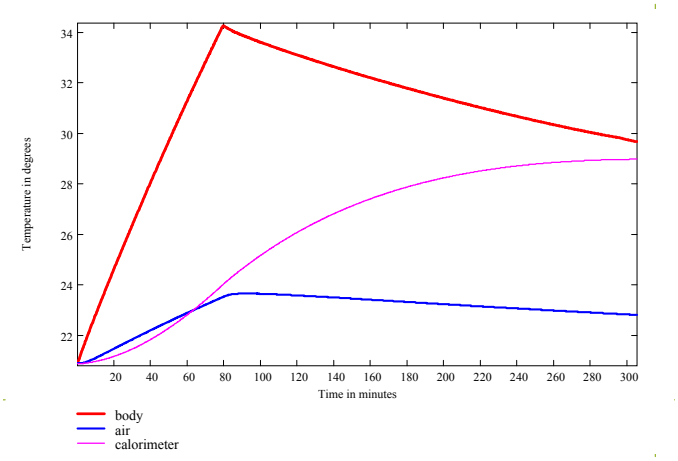

Figure 5: Performance of temperature control system from switch on

then, at the appropriate moment, switching the electrical heating off. This makes the calorimeter temperature drift up to the desired operating temperature and, just before its temperature would start to fall again, the body is turned on again to maintain constant temperatures. The user is able to set the required temperature of the calorimeter and the control program adjusts the body temperature to suit, depending on the air temperature. As can be seen the air sensor also indicates an increase in temperature. This is because the air sensors are placed on the outside of the case of the body and respond to heat conducting through the polystyrene insulation. Although this means that the air sensors do not measure the true air temperature, it does not significantly affect the performance of the control program. Stabilization of the calorimeter is achieved within eight hours.

Figure 6 shows the stability of the calorimeter at a later time when stabilization has been achieved. By varying the body temperature in response to air temperature variations, the calorimeter temperature is maintained to ± 0.2 mK over several hours. As one can see, there is a slight systematic residual in the calorimeter temperature (at the 0.1 mK level) indicating that the control algorithm isn't fully correcting for air temperature variations. Although the long term stability is impressive, one is really interested in the stability of the system over the length of a calorimeter run - typically five minutes. Slow changes in temperature are acceptable since these produce linear drifts in the calorimeter trace and these are typical of the NPL environment. It is not so certain that other radiation facilities are so benign. One of the concerns in developing the algorithm was whether the parameters determined in the model were 'universal' or situation specific. Ideally the control program would perform in the same manner in any radiation facility, but further work is required to see whether this is true. Work is currently underway at NPL to gain a deeper understanding of the physical processes involved in the calorimeter system which should yield a more robust and reliable control algorithm.

As stated above, the program has a number of control modes and the three commonly used are:

1. Body constant - no attempt is made to control the calorimeter temperature.
2. Core constant - the body is varied to keep the calorimeter at a fixed temperature.
3. Quasi-core constant - the body is varied in response to changes in the air temperature but no account is taken of the actual calorimeter temperature.

The normal mode used for calorimetry is Mode (1), although Mode (3) was also used during the radiation tests. Figure 7 shows the response of the control program during a calorimeter run when operated in Mode (2). The program sees the radiation

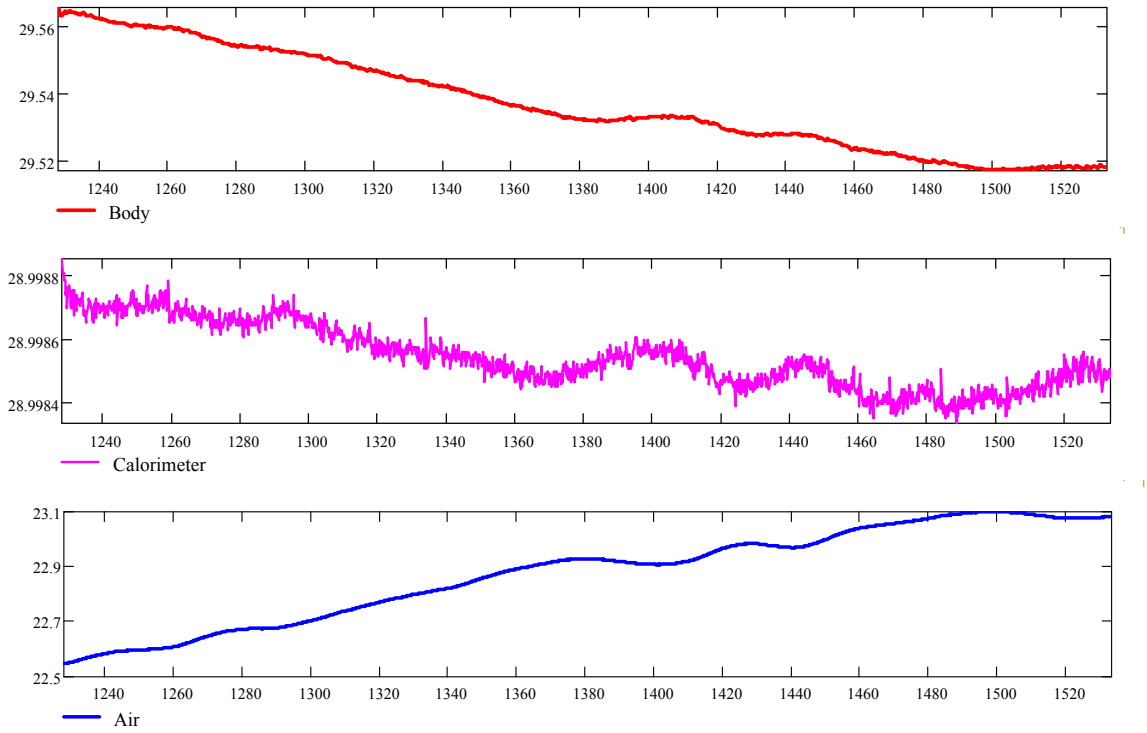

Figure 6: Stability of temperature control system. X axes - time (min), Y axes - temp (°C)

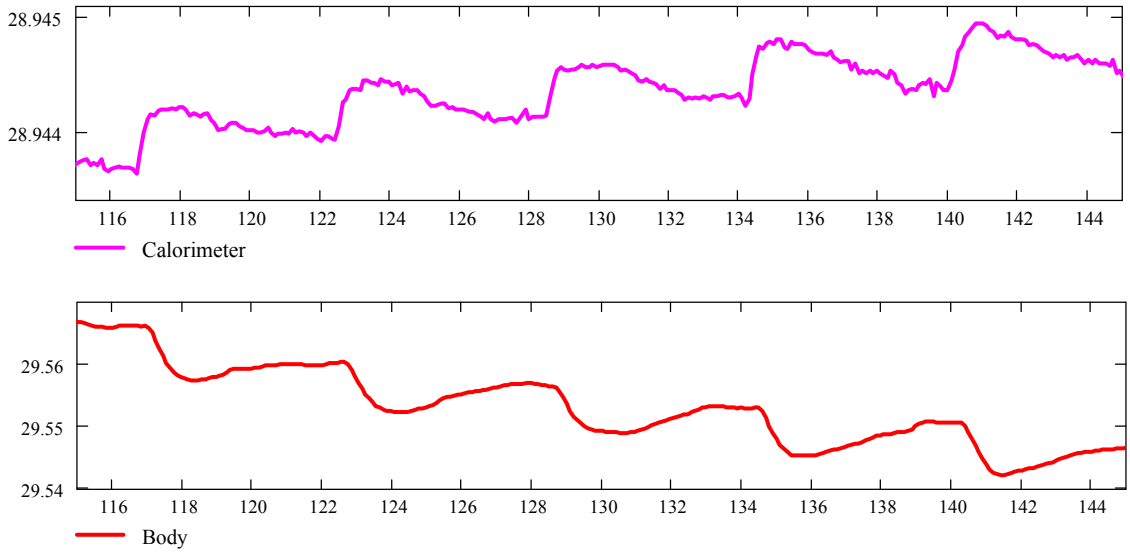

Figure 7: Response of body to changes in calorimeter temperature in core-constant control mode. X axes - time (min), Y axes - temp (°C)

induced temperature rise in the calorimeter and adjusts the body temperature to counteract the effect. This affects the heat transfer from calorimeter to body and changes the shape of the post-irradiation calorimeter trace. The calorimeter signal in Figure 7 also shows a level of noise greater than one would expect for the DC bridge system used. The most likely explanation is a fault in the thermistor connections. In Mode (2), the calorimeter signal directly affects the body temperature set by the control program, and a high level of noise in the sensing thermistor will result in fluctuations in the control temperature.

C. Calorimetry

1) Calorimeter Performance

A primary requirement in carrying out calorimetry is stability of the LINAC output. Beam current variations are taken into account by use of the transmission monitor, but a change in mean energy will change the calorimeter or ion chamber reading per monitor unit. Stability is not crucial if one is just looking at the performance of the calorimeter alone, but is necessary when comparing with the primary standards. The two devices being compared are alternated in the beam on a regular basis to minimise the effects of LINAC drift, but this cannot correct for a step change in energy. Normally, the NPL LINAC is very stable, generating a narrow electron spectrum. However, the ion chamber measurements made during each day showed a larger spread than one would expect, indicating that the LINAC output energy was changing. If one could measure the generated electron spectrum for each measurement then one could correct for these changes but this is not really an option since it would significantly reduce the amount of useful beamtime available during the day. However, the LINAC output was stable enough to produce useful results.

Figure 8 shows a typical calorimeter run in a 16 MV photon beam at a doserate of 5 Gy/min. The irradiation time was kept to a minimum so that any heat transfer between core and surround in the calorimeter would be clearly seen. If one had complete isolation of the core from the surround then the post-heat trace would have exactly the same gradient as the pre-heat trace, but this is obviously not the case here. Curvature in the post-heat trace indicates significant heat transfer from core to surround. The extrapolations will correct for this heat loss but the measurement uncertainty is increased due to the non-linear behaviour. This effect can be minimised by using short irradiation times but one is constrained by the signal-to-noise ratio which, at present, limits the minimum measurable dose to about 0.5 Gy. The typical standard deviation in the calorimeter/monitor ratio for ten calorimeter runs is ± 0.5%. This is the random uncertainty and is due to a combination of effects including noise, extrapolations and drifts in LINAC output, and is slightly larger than one would like. It is hoped to further improve the signal-to-noise, which should reduce this uncertainty.

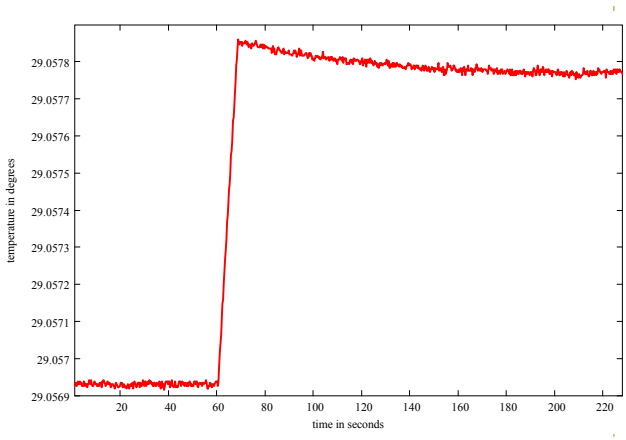

Figure 8: Typical calorimeter run at NPL in a 16 MV photon beam at a doserate of ~ 5 Gy/min

A problem that became apparent during the testing of this calorimeter was the reliability of the transmission monitor. For calorimeter measurements such as these, where the monitor response can significantly affect the result, two monitor chambers (of different designs) are now used.

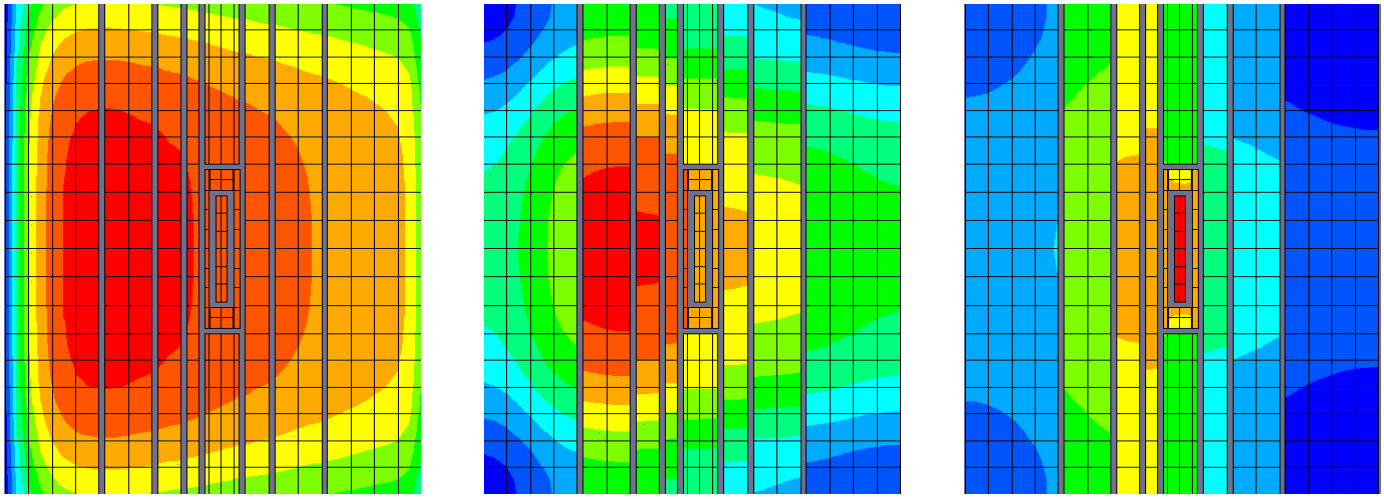

Figure 9: Development over time after irradiation of calorimeter temperature distribution

2) Thermal Modelling

Figure 9 shows how the calculated heat distribution within the calorimeter develops over time after an instantaneous dose from a 16 MV photon beam has been delivered. Analysis of the simulated calorimeter temperature-time traces has showed that heatflow across the core takes typically 0.1-0.2 s. This means that there is no significant heat distribution across the core and the positions of the thermistors is not critical. The interfaces between graphite plates that make up the calorimeter have a significant effect - there is rapid equilibration of temperature within each plate, but a much slower transfer of heat from one plate to another. This, together with the air gap around the core produces an interesting post-heat temperature-time trace as shown in Figure 10. There is a lack of cooling from 2-5 s which is mainly due to radial temperature equilibration in each slice of the surround. From 5 s onwards the core is hotter than the rest of the graphite and cools as you would expect. It would therefore appear that the standard extrapolation techniques will over-estimate the dose by 0.7-1 % because they do not take account of such a change in curvature. However, these conclusions are only valid for this 16 MV depth-dose distribution and measurement depth. It is not possible to carry out an experiment to directly validate the result of the model because you can deliver a measurable dose quickly enough. However, it is possible to deliver an "instantaneous" (i.e. less than 0.2 s) dose using electrons. Further simulations are and measurements are planned to resolve this. It is hoped that this work will enable us to optimise the plate arrangement used to minimise the systematic uncertainty in the extrapolation process.

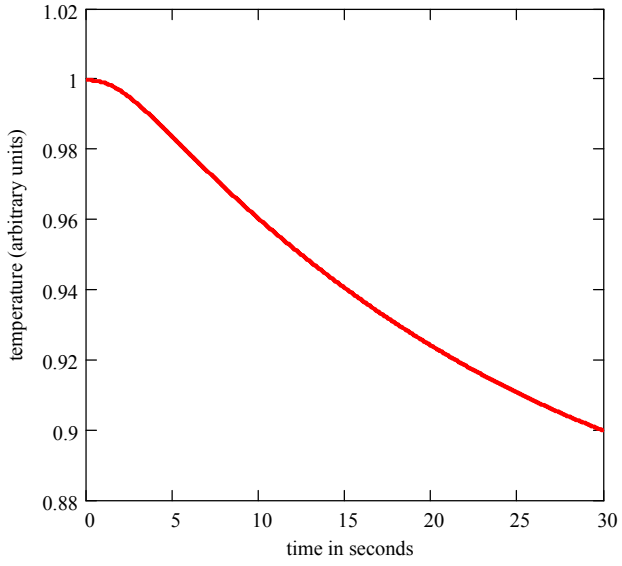

Figure 10: Calculated core temperature-time trace for 16 MV photon beam irradiation.

Typical relaxation time constants were derived from measurements during commissioning of the calorimeter and are given in Table 2. The low value of τ_{cc} is the reason for the curvature seen in the post-heat trace in Figure 8. As noted in the previous section, for accurate dose determination a large value of τ_{cc} is desirable (by comparison the primary standard photon calorimeter has a time constant equivalent to a value of τ_{cc} of ~ 700 s). However, a smaller value of τ_{cc} means that the calorimeter is easier to control and more irradiations can be carried out over a day. This is a desirable feature since there will be limited time available to make measurements with the calorimeter at radiotherapy centres. Unfortunately, there is no simple way to increase the value of τ_{cc} without employing a complex vacuum system (which is not an option for a portable system) or a very large air gap (which would significantly increase the measurement uncertainty).

Table 2.

Time constants for heat transfer between calorimeter components.

Interface	Symbol	Time constant (s)
core:calorimeter surround	τ_{cc}	~30
calorimeter:body	τ_{cb}	~450
body:air	τ_{ba}	~300

3) Corrections

In the comparison of this calorimeter with other standards at NPL a number of corrections are a required. Although the build-up thicknesses for calorimeters and chamber are matched, the finite sizes of graphite plates available mean that corrections are required for slight differences in measurement depth. Corrections were obtained from depth-ionisation measurements. Included in this correction factor is the averaging effect of the 2 mm thick calorimeter absorber, compared to the chamber measuring at a point (taken as the centre of the chamber for the NE2611). A further correction is required to account for a difference in the SSD of the calorimeter or chamber.

As mentioned above, there is a difference in scatter between the devices being compared. Firstly, there is the scatter effect due to the calorimeter body, which is required for both photons and electrons. Secondly, there is correction in electron beams to convert from the small (9 cm × 9 cm) phantom used here to the larger (15 cm × 15 cm) phantom used in the electron calorimeter. The results for photons are interesting because there is no correction required around 10 MV. There are two contributions to the scatter correction - sides and the back of the body - and these are significant at high and low energies but not in the middle of the energy range. The side correction must be due to doubly scattered photons and this appears to only be important at high energies. At low photon energies backscatter is the dominant effect.

A correction is required for beam uniformity - the diameter of the calorimeter core is 20 mm, the diameter of the electron calorimeter core is 50 mm, and the diameter of a NE2611 chamber is approximately 8 mm. The experimental geometry is chosen to minimise the effects of beam non-uniformity, although a correction is still required, which is obtained from beam scans. In photon beams, beam scans were obtained using a PTW LA48 linear ion chamber array. This is an array of 47 liquid-filled ion chambers which gives an instantaneous readout of the beam uniformity. However, this only operates up to 5 Gy/min; therefore beam scans in electron beams were obtained by moving a NACP chamber in a graphite phantom (at the relevant measurement depth) across the beam. Typical beam scans at a number of photon energies are shown in Figure 11. As can be seen, the field size and beam flatness are the same at all energies.

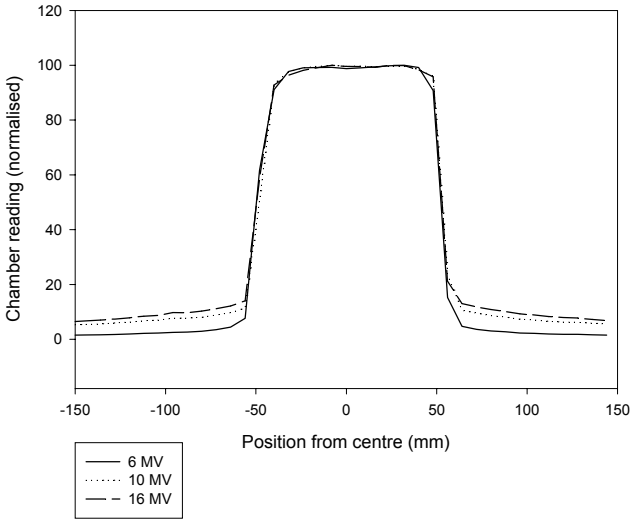

Figure 11: Beam uniformity measurements in photon beams using linear ion chamber array.

The only difference is the in the penumbra, which increases with energy as would be expected.

A correction is also required for the 1 mm air gap around the calorimeter core. Initial results for the X-ray qualities yield a value of approximately 0.7%. Cottens *et al* [9] carried out a series of measurements looking at the effect of the vacuum gaps in a Domen-type calorimeter (similar to the NPL photon primary standard) and saw a maximum effect of 0.7%, which is in good agreement with these calculations. The gap effect for electron beams has not yet been determined but measurements on the electron calorimeter in electron beams with air gaps of 0.5 mm and 1 mm have indicated that the correction is less than 0.3%. It is assumed that this calorimeter has a similar gap effect, although this is smaller than the value in X-rays. There is also a small correction for the impurity effect of the thermistors in the calorimeter core. With four thermistors in a core only 20 mm in diameter this correction could be significant, but calculations based on the thermistor composition indicate that the effect is negligible within the uncertainties. A value of 1.000 was used.

The correction factors (applied to the portable calorimeter) for the various quantities are given in the Table 3.

Table 3.

Summary of correction factors.

E_{nom}	Scatter	Depth	Uniformity	Distance	Gap effect	Overall
Photons			*Comparison with NE2611 chamber*			
Co-60	0.9934	1.0005	1.0000	1.0026	????	????
6 MV	0.9961	1.000	0.9992	1.002	1.0078	1.0090
10 MV	0.9993	1.000	0.9999	1.002	1.0074	1.0086
16 MV	0.9936	1.000	1.0001	1.002	1.0068	1.0025
Electrons			*Comparison with electron calorimeter*			
6 MeV	1.0000	1.0000	0.9948	1.000	1.000	0.9948
10 MeV	1.0000	1.0000	0.9978	1.000	1.000	0.9978
16 MeV	1.0018	0.9992	0.9958	1.000	1.000	0.9978

Table 4.

Uncertainties in photon and electron beams.

Source	"Random" Standard Uncertainty (%)			"Systematic" Standard Uncertainty (%)
	Co-60	4-12 MV	6-16 MeV	All qualities
Calorimeter reading	0.20	0.35	0.22	
Chamber reading	0.08	0.08		
Thermistor calibration				0.05
Specific heat capacity				0.08
Gap effect	0.15	0.07		0.17
Recombination correction				0.10
Beam uniformity	0.05	0.05	0.05	
Depth correction	0.05	0.05	0.05	
Scatter correction	0.08	0.08	0.08	
Thermistor perturbation				0.08
Inverse square correction	0.05	0.05	0.03	0.10
Charge calibration of electrometer				0.03
Combined standard uncertainty	0.29	0.38	0.25	0.26
Overall standard uncertainty	0.39	0.46	0.36	

4) Uncertainties

The uncertainties (quoted as standard uncertainties according to UKAS [10]) in the determination of absorbed dose and calibration of ion chambers in terms of absorbed dose to graphite are given in Table 4.

The uncertainties are split into "random" and "systematic" for the purpose of looking at any energy dependence in the results. The larger uncertainty in the calorimeter reading at 10 MV was due to excessive electrical noise as these measurements were made before the calorimeter was screened properly.

5) Comparison with primary standards

The results of the comparison of this new calorimeter with the photon and electron primary standard calorimeters are shown in Tables 5, 6 and 7.

The results from the Co-60 measurements demonstrate that operation at 1 Gy/min is possible. However, it would appear that LINAC measurements are limited to around 2 Gy/min, presumably due to variations in the output from the accelerator. Since the majority of radiotherapy linacs operate at a doserate of 4 Gy/min the calorimeter would appear to meet the design requirements. Taking the results from all the photon measurements it would appear that the difference between this calorimeter and the photon primary standard is approximately constant across the energy range. There is the slight indication of a trend with energy, although this is probably not statistically significant. The calibration method of the photon calorimeter is currently under investigation and it is believed that the dose measured is less than the correct dose by as much as 0.5%. If this is taken into account, then the two calorimeters agree to within 0.4% at all energies, which is within the combined measurement

Table 5.

Results of calorimeter comparison in high energy photons using chamber NE2561 S/N 295.

E_{nom} (MV)	Measured Doserate (Gy/min)		Ratio
	Primary standard	Portable calorimeter	Portable/primary std
Co-60	1.0740	1.0804	1.0059

Table 6.

Results of calorimeter comparison in high energy photons using chamber NE2611 S/N 122.

E_{nom} (MV)	Chamber calibration factor (Gy/μC)		Ratio
	Primary standard	Portable calorimeter	Portable/primary std
4	89.90	90.34	1.0049
6	89.92	90.62	1.0077
10	88.48	89.10	1.0070
12	87.92	88.67	1.0085

Table 7.

Results of calorimeter comparison in electrons.

E_{nom} (MV)	Calibration of monitor (Gy/V)		Ratio
	Primary standard	Portable calorimeter	Portable/primary std
6	0.2414	0.2412	0.9993
10	0.2221	0.2230	1.0040
16	0.2032	0.2041	1.0042

uncertainties, and is an encouraging result. Operation at Co-60, at a doserate of only 1 Gy/min is particularly satisfying because it provides a method to monitor the stability of the calorimeter.

The results from the electron measurements are also satisfying, showing agreement within 0.4% at all three energies. Further comparisons at other electron energies are planned. A comparison has also been carried out recently to compare directly the primary standard electron and photon calorimeters in a 16 MeV electron beam. Initial results from this comparison indicate agreement at the 0.3% level, which is consistent with the portable calorimeter results. Initial tests have also shown that it may be possible to operate the electron primary standard in a high-doserate photon beam (e.g. 16 MV, 10 Gy/min) so that a comparison of the primary standards in photons could also be carried out. By obtaining a comprehensive and robust set of comparative data with all three calorimeters, there is less chance of a significant systematic error being overlooked.

One concern is that there is a difference between carrying out calorimetry at NPL and making measurements in a radiotherapy centre, where there will be much less time to obtain a result. It is therefore important to demonstrate the repeatability of the calorimeter before it is taken "off-site". It is planned to make regular measurements in the NPL Co-60 facility to look at repeatability, as well as to refine the set-up process.

V. Conclusion

Initial testing of the calorimeter has confirmed the suitability of the design. Radiotherapy doserates can be measured with an uncertainty close to that of the present primary standards. The system is portable, opening up the possibility of making direct measurements in user radiation facilities - particularly radiotherapy clinics. Further work is required to improve the temperature control algorithm by modelling of the heat transfer processes in three dimensions. It is hoped to extend this work to model the heat transfer during irradiation and so derive a correction for the heat transfer from core to surround in the calorimeter.

The result of comparing the calorimeter with the present primary standard calorimeter in high energy photon beams is very encouraging, giving agreement within 0.5% of unity at all energies measured. Further work is required to carry out a wider range of measurements in both photon and electron beams. Once this work is complete, it is hoped to carry out measurements in UK radiotherapy clinics, as well as other radiation facilities. It should be noted that this calorimeter is not intended to replace the present primary standards, but as a transfer instrument between NPL and other radiation users. This will give a direct determination of absorbed dose where it is required, check the validity of dosimeter calibrations provided at NPL, and allow investigation of issues such as beam quality definition.

Acknowledgements

The authors would like to acknowledge the financial support of the National Measurement Policy Unit of the UK Department of Trade and Industry.

References

[1] DuSautoy, A R 1996 The UK primary standard calorimeter for photon beam absorbed dose measurement, *Phys. Med. Biol.* **41** p137.

[2] Domen S R and Lamperti P J 1974 *J. Res. Natl. Bur. Stand.* (US) **78** p595.

[3] Burns D T, McEwen M R and Williams A J 1994 *An NPL absorbed dose calibration service for electron beam radiotherapy, Proc. Int. Symp. on Measurement Assurance in Dosimetry (IAEA-SM-330/34)* ed S P Flitton (Vienna: IAEA) p61.

[4] McEwen M R, DuSautoy A R and Williams A J 1998 The calibration of therapy level electron beam ionisation chambers in terms of absorbed dose to water *Phys. Med. Biol.* **43** p2503-2519.

[5] Williams A J, Burns D T and McEwen M R 1993 *Measurement of the specific heat capacity of the electron beam graphite calorimeter (NPL Report RSA(EXT)40)* (Teddington: National Physical Laboratory).

[6] Richardson M J 1984 *Compendium of thermophysical property measurement methods Vol 1; Survey of measurement techniques, Chapter 17* ed Maglic, Cezairliyan and Peletsky (New York: Plenum Press).

[7] Sanders R P and Thomas C G 1991 *A precision voltage supply for the NPL primary standard electron beam calorimeter (NPL Report RSA(EXT)24)* (Teddington: National Physical Laboratory).

[8] McEwen M R, Burns D T and Williams A J 1993 *The use of thermistors in the NPL electron beam calorimeter (NPL Report RSA(EXT)41)* (Teddington: National Physical Laboratory).

[9] Cottens E, Janssens A, Eggermont G and Jacobs R 1981 *Absorbed dose calorimetry with a graphite calorimeter, and G-value determinations for the Fricke dosemeter in high energy electron beams, Proc. Int. Symp. on Biomedical Dosimetry: Physical Aspects, Instrumentation, Calibration (IAEA-SM-249/32)* (Vienna: IAEA) p189.

[10] UKAS (United Kingdom Accreditation Service) 1995 *The Expression of Uncertainty and Confidence in Measurement and Calibrations (Report NIS 3003 Edition 8)* (Teddington: UKAS).

QUESTIONS AND ANSWERS

Carl Ross: Suppose you go into a clinic and you get a number and you have dose to graphite but the physicist there says "I don't care about dose to graphite, I want dose to water". What do you do next?

Malcolm McEwen: What do we do next Simon?

Simon Duane: The conversion to dose to water, I believe, is not so sensitive to spectral variations as the chamber calibrations to start with, whether in dose to graphite or dose to water, so the check will be that the hospital's chamber calibration in dose to graphite is the same in our beam as it is in their beam.

Ken Gall: How does it compare with what you could do with a transfer chamber. I was hearing remarkable uncertainties on ionisation chambers

Malcolm McEwen: The precision on a chamber is much better but it measures the indirect quantity and there are always questions which keep coming back at the moment about validity of calibrations between one place and another. This is just one way of making a direct measurement of dose in a radiation facility where the dose needs to be measured. So that is the reason for doing it.

--

David Burns: Was the difference that you saw between the new calorimeter and the electron beam calorimeter of about 0.4% reproducible at each of the energies.

Malcolm McEwen: It was fairly constant, yes. These are just some initial results that I have not really had time to go back on. It is not obvious whether it is a systematic difference or whether it is a random effect. It's within the sum of the uncertainties at the moment.

David Burns: So you don't have any leads to follow - you don't know where it is coming from?

Malcolm McEwen: No. There were some early indications that it was possibly an effect due to charged storage - in the graphite the earthing wires can sometimes become disengaged and then you get effects that are not obvious.

David Burns: Did you implement any aluminised graphite surfaces?

Malcolm McEwen: No, we haven't got any non-graphite material apart from the thermistors. Anyhow that would increase the time constant. It's really whether it's worth doing that because you reduce the number of runs you can make. There is probably an ideal place where you want to be but…

David Burns: You have to be careful that you are not replacing A uncertainties with type Bs.

--

Ken Gall: The heat-flow calculations you showed with the discontinuities of the plate gaps - how do you know that the heat was doing this? Is it all calculation or is it partially experimental?

Malcolm McEwen: The way we validated the modelling was we started with a single block and then we cut it in half, then we cut it again and so we were creating exactly the same kind of boundaries.

Ken Gall: So you had experimental results to show that those boundaries did impede the heat conduction.

Malcolm McEwen: Yes. In the end we put a calorimeter core in and simulated the whole set-up. We had electrical heating going through and used this to validate the model so that we were happy with it.

Ken Gall: I was just wondering how the model dealt with that. It's really just a finite element and you say that they are right next to each other. How does it know that there is a conduction gap?

Simon Duane: Perhaps it is best to regard those measurements as calibrating the model. Further down the model just has heat transfer elements. The size of the thermal barrier associated with that transfer element can be set to what we like.

Ken Gall: So you put in those elements, the conductive barriers, and calibrated the rate of heat transfer with the experimental results.

The OFMET Sealed Water Calorimeter

J. Medin[1,2,†], J. Seuntjens[1,§], N. Klassen[1], C. Ross[1] and G. Stucki[2]

[1]Ionizing Radiation Standards, National Research Council, Ottawa, ON, K1A 0R6, Canada

[2]Swiss Federal Office of Metrology, Lindenweg 50, CH-3003 Bern-Wabern, Switzerland

Abstract

As part of a collaborative agreement between the Canadian National Research Council (NRC) and the Swiss Federal Office of Metrology (OFMET), NRC constructed and tested a water calorimeter for use at OFMET. The calorimeter uses two thermistor probes within a sealed glass vessel containing high purity water to measure the absorbed dose to water at a point in a large water phantom. The water phantom is thermally isolated from the environment and operated at 4ºC to avoid convective heat transfer. By calibrating the thermistor probes against temperature, and using the accepted value for the specific heat of water, the absorbed dose can be measured with an uncertainty of about 0.5% (k=1). More than 300 ^{60}Co irradiation runs have been carried out using the OFMET calorimeter at NRC, and in addition 653 irradiations were performed using the ^{60}Co unit at OFMET. The calorimeter response has been measured using three different aqueous systems, and the absorbed dose compared to that obtained using the NRC calorimeter. The two calorimeters were found to agree to better than 0.1% in a direct comparison. Ion chamber calibration factors determined using the OFMET calorimeter at NRC and at OFMET were found to agree within 0.2%. Results from measurements in the ^{60}Co beam and in the accelerator photon beam at OFMET are presented.

I. INTRODUCTION

As part of a collaborative agreement between the Canadian National Research Council (NRC) and the Swiss Federal Office of Metrology (OFMET), a water calorimeter was constructed and tested at NRC for use at OFMET. The calorimeter follows the design of the NRC sealed water calorimeter [1], [2], and uses two thermistor probes within a sealed glass vessel containing high purity water to measure the absorbed dose to water at a point in a large water phantom. Compared to graphite, the thermal diffusivity of water is much smaller, and Domen [3] showed that under appropriate conditions, the temperature increase could be measured directly at a point in a large water phantom.

The relationship between the absorbed dose, D_w, and the temperature rise in the water, ΔT_w, is given by Equation (1) where c_w is the specific heat capacity of water, k_c and k_v are corrections for conductive and convective heat transfer, respectively, k_p is a correction for perturbations of the radiation field by the glass vessels and probes, k_{dd} is a correction for the non-uniformity of the lateral dose profile, k_r accounts for the change of the density of water with temperature, k_t is a correction for transient thermistor response, and k_{HD} is the heat defect (*c.f.* [2] and paper by Ross *et al* in these Proceedings).

$$D_w = \Delta T_w \cdot c_w \cdot k_c \cdot k_v \cdot k_p \cdot k_{dd} \cdot k_\rho \cdot k_t \cdot \frac{1}{(1-k_{HD})} \qquad (1)$$

In the present design, the water phantom is thermally isolated from the environment and operated at 4ºC to reduce the problem associated with convective heat transfer [4], so k_v is assumed to be equal to unity. A summary of the different correction factors together with the selected value of the specific heat capacity of water will be given in the next section.

II. DETERMINATION OF THE ABSORBED DOSE

All measurements in the present project have been performed using two glass vessels with equal dimensions (labelled #4 and #5), and four thermistor probes (labelled #21-#24). The methods for making the glass vessels and thermistor probes are thoroughly described elsewhere together with results from measurements of the wall thickness uniformity [2].

A. Calibration of Platinum Resistance Probes and Thermistor Probes

Since a detailed knowledge of the absolute temperature is not required for calorimetry, the main requirement is that the thermistor probes accurately measure temperature changes. The thermistor probes have to be calibrated before they can be used, and this is done against platinum resistance probes (RTDs). The platinum probes were in turn calibrated against both the NRC temperature standard (two occasions, 13 October 1998 and 26 May 1999) and the OFMET temperature standard (one occasion, 14 July 1999).

Table 1 shows the apparent temperature differences for the same resistance value using the RTD parameters obtained at the three calibration occasions. The resistances where chosen in order to reflect the temperature range used when calibrating the thermistor probes, *i.e.* from –4˚C to 12˚C. The differences are given relative to the results obtained with the RTD parameters from the previous calibration at NRC, *i.e.* using data from 26 May relative to data from 13 October, and data from 14 July relative to data from 26 May.

From Table 1, it can be seen that the stability of the RTD probes and calibration procedure was better than 10 mK over a period of seven months at NRC (8 mK for probe 2 represents the largest change). It also shows a very good consistency between the calibrations performed at NRC and at OFMET, with a maximum difference of 4 mK.

Present addresses:
†Dept. of Radiation Physics, Malmö University Hospital, SE-205 02 MALMÖ, SWEDEN

§McGill University, Medical Physics Unit, Montreal General Hospital, 1650 Cedar Av., Montreal, Quebec, H3G 1A4, Canada

Table 1.
Temperature differences (mK) obtained when using RTD parameters from the three calibrations. The differences are given relative to the previous calibration, *i.e.* data from 26 May 1999 relative to data from 13 October 1998, and data from 14 July 1999 relative to data from 26 May 1999. The fixed resistances were chosen in order to reflect the temperature range used in the thermistor probe calibration (-4°C to 12°C).

	RTD probe 1		RTD probe 2		RTD probe 3		RTD probe 4	
R [Ω]	26 May	14 July	26 May	14 July	26 May	14 July	26 May	14 July
98.4	4	5	7	3	1	4	1	3
100.0	5	3	8	2	2	3	0	4
101.5	6	2	8	2	2	2	0	2
103.1	5	2	8	2	3	1	-1	2
105.4	5	1	7	2	2	1	-1	1

For the calibration of the thermistor probes, an automated system has been developed in which the thermistor probes are mounted in a separate dewar together with two of the RTDs [2]. The dewar contains a solution of 90% water and 10% ethanol (to allow calibration down to –4˚C, *c.f.* below), and the temperature is controlled using a bath running under computer control. Measurements of the thermistor resistance are carried out using the 2-wire ohm mode of a Keithley K2001 multimeter (on the 200 kΩ scale, the bead power dissipation is about 0.5 μW). For use at 4˚C, the thermistors are calibrated at a series of equally spaced temperatures ranging from –4˚C to 12˚C. The temperature is usually increased in steps of 2˚C.

For thermistors, the relationship between the resistance (R) and the temperature (T) is usually approximated by (*c.f.* [5])

$$R = R_{\mathrm{o}} e^{\beta(1/T - 1/T_{\mathrm{o}})} \tag{2}$$

where R_{o} is the thermistor resistance at temperature T_{o} (25˚C), and b is a constant. Empirically, b is found to change by about seven parts per thousand per degree, but since the temperature change during a calorimetric measurement is very small, the approximation is valid.

According to equation (2), ln R changes linearly with $1/T$. However, the measured data are found to be better represented by a second order polynomial of the form [2]

$$\ln R = a_{\mathrm{o}} + \frac{a_1}{T} + \frac{a_2}{T^2} \tag{3}$$

The slope of the curve, d(ln R)/d($1/T$), is given by b, yielding

$$\beta(T) = a_1 + \frac{2a_2}{T} \tag{4}$$

If equation (3) is recast in the form of equation (2), with b defined according to equation (4), then R_{o} becomes a weak function of T

$$R_{\mathrm{o}}(T) = \exp\left(a_{\mathrm{o}} + \frac{\beta(T)}{T_{\mathrm{o}}} - \frac{a_2}{T^2} \right) \tag{5}$$

It may be noted that equation (3) gives the relationship between the temperature T and the resistance R. However, the temperature dependence of b and R_{o} is quite weak and equation (2) remains a useful starting point to estimate the thermistor resistance, and is used in the temperature determination.

Table 2 shows the calibration data for the four thermistor probes used in the present work. These were obtained over a total period of 13 months, and show a maximum variation of 0.030% for b and 0.043% for R_{o}. These variations leads to insignificant deviations in the determined temperature differences, using equation (2).

B. Correction Factors

A more extensive discussion of the different correction factors is given elsewhere (see [2] and Ross *et al* in these Proceedings), and only a short discussion is included below. The values used are summarized in Table 3.

As mentioned in the introduction, using the water calorimeter at 4˚C reduces significantly the problem associated with convective heat transfer, and k_{v} is assumed to be equal to unity. The influence from conductive heat transfer (k_{c}) depends on the radiation quality, the irradiation time, the post-irradiation drift time, and the dimensions of the glass vessel. Calculations have previously been performed using a two-dimensional model based on the following simplifying assumptions: the calorimeter is irradiated uniformly, the glass vessel is an infinitely long cylinder, the thermistor bead is located symmetrically at the end of the glass probe, and each probe is semi-infinite in length [2]. Calculations were performed for two glass vessels of equal dimensions, using both an irradiation time and a post-irradiation drift time of 120 s, yielding the k_{c} value in Table 3 at ^{60}Co. In the measurements performed in high-energy photon beams at OFMET, k_{c} was assumed to be equal to the value calculated for ^{60}Co.

The perturbation of the ^{60}Co radiation field by the glass vessel (k_{p}) has been measured in the NRC beam, using a PTW-M233642 ionization chamber, and amounts to 1.0021 ± 0.0005.

Extensive work has been done in the past to study and determine the heat defect of water, and to find suitable aqueous systems [6], [7]. In the present work, three different water systems have been used in order to determine the absorbed dose at the quality of ^{60}Co: water saturated with N_2 gas (in the

Table 2.
Thermistor calibration data, evaluated at 4.00 °C. All data were obtained at NRC, except the calibrations at 14 July 1999 and 15 November 1999 (OFMET). The percentage difference reflects the change in the parameter compared to the closest previous calibration, *i.e.* 15 October 1998 *vs.* 14 October 1998, 9 March 1999 *vs.* 15 October 1998, and so on.

	Probe 21		Probe 22		Probe 23		Probe 24	
Date	β [K^{-1}] (%−diff .)	R_o [Ω] (%−diff.)	β [K^{-1}] (%−diff.)	R_o [Ω] (%−diff.)	β [K^{-1}] (%−diff.)	R_o [Ω] (%−diff.)	β [K^{-1}] (%−diff .)	R_o [Ω] (%−diff.)
14-Oct-98	3078.15	4276.71	3114.47	4441.35	3090.54	4403.89	3075.81	4541.89
15-Oct-98	3078.09 (-0.002)	4276.70 (0.000)	3114.46 (0.000)	4441.28 (-0.002)	3090.58 (0.001)	4403.79 (-0.002)	3075.69 (-0.004)	4542.06 (0.004)
09-Mar-99	3078.34 (0.008)	4275.40 (-0.030)	3114.30 (-0.005)	4440.23 (-0.024)				
10-Mar-99	3078.78 (0.014)	4275.08 (-0.007)	3114.77 (0.015)	4439.97 (-0.006)				
11-Mar-99					3090.40 (-0.006)	4401.89 (-0.043)	3075.99 (0.010)	4540.43 (-0.036)
12-Mar-99					3090.21 (-0.006)	4402.13 (0.005)	3075.76 (-0.007)	4540.71 (0.006)
12-Jun-99	3078.98 (0.006)	4275.93 (0.020)	3114.96 (0.006)	4440.97 (0.023)	3091.14 (0.030)	4403.06 (0.021)	3076.68 (0.030)	4541.09 (0.008)
13-Jun-99	3078.49 (-0.016)	4276.44 (0.012)	3114.24 (-0.023)	4441.71 (0.017)	3090.54 (-0.019)	4403.62 (0.013)	3076.20 (-0.016)	4541.50 (0.009)
14-Jul-99	3078.19 (-0.010)	4276.74 (0.007)	3114.19 (-0.002)	4441.53 (-0.004)	3090.35 (-0.006)	4403.67 (0.001)	3075.74 (-0.015)	4541.79 (0.006)
15-Nov-99	3078.90 (0.023)	4276.50 (-0.006)	3114.58 (0.013)	4441.75 (0.005)	3090.39 (0.001)	4404.48 (0.018)	3076.30 (0.018)	4541.23 (-0.012)

following called pure water), water saturated with H_2 gas, and water saturated with a 43/57 % mixture of H_2 and O_2 gas. Based on the work by Klassen and Ross [7], the correction factor for the heat defect (k_{HD}) is assumed to be equal to zero for the N_2 and H_2 saturated water systems, and equal to -0.0023 for the H_2/O_2 system.

Table 3.
Correction factors used in the transfer from temperature rise to absorbed dose.

k_v	1.000	
k_c	0.9986 ± 0.15%	
k_p	1.0021 ± 0.05%	
k_{HD}	0.000 (for N_2 and H_2)	-0.023 ± 0.5% (for H_2/O_2)
k_ρ	1.0006 ± 0.02% (only applied at NRC)	
k_{dd}	1.0004 ± 0.02% (applied at NRC)	1.0006 ± 0.02% (applied at OFMET)
k_t	1.000	
c_w	4.2048 J g^{-1} K^{-1} ± <0.005%	

At NRC, the correction for the difference in water density between 4˚C and 22˚C (k_r) amounts to 1.0006, based on a dose gradient for ^{60}Co of 0.5%/mm. At OFMET, no correction is applied since the depth of measurement is determined in the unit of g cm^{-2} both at the calorimetric measurements (4˚C) and at the ionization chamber calibration (room temperature).

The dose profile non-uniformity correction factor (k_{dd}) was previously measured at NRC using a PTW-M233642 ionization chamber with a cavity volume of 0.125 cm^3, and found to be equal to 1.0004. At OFMET, a value of 1.0006 was adopted, determined with a Scanditronix silicon diode detector.

The value for the specific heat capacity of water (c_w) is obtained from measurements by Osborne *et al* [8], and is equal to 4.2048 J g^{-1} K^{-1}.

III. MEASUREMENTS AT ^{60}CO

Results from measurements with the water calorimeter performed at NRC and at OFMET, using two glass vessels of equal dimensions and four thermistor probes, are presented in the

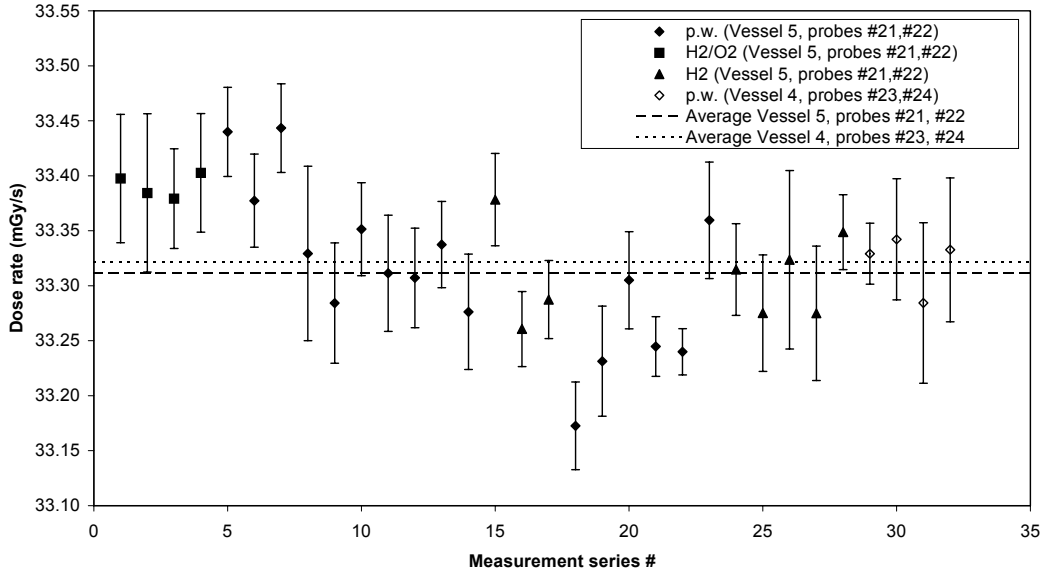

Figure 1a: The dose rate at the NRC ^{60}Co unit determined with three different water systems. The results are corrected for decay to 20 January 1999. The data for H_2/O_2 include a -2.3% heat defect. Each series includes typically 7-14 measurements. The uncertainty bars refer to type A uncertainties (k=1) on the average value, for measurements of ΔT.

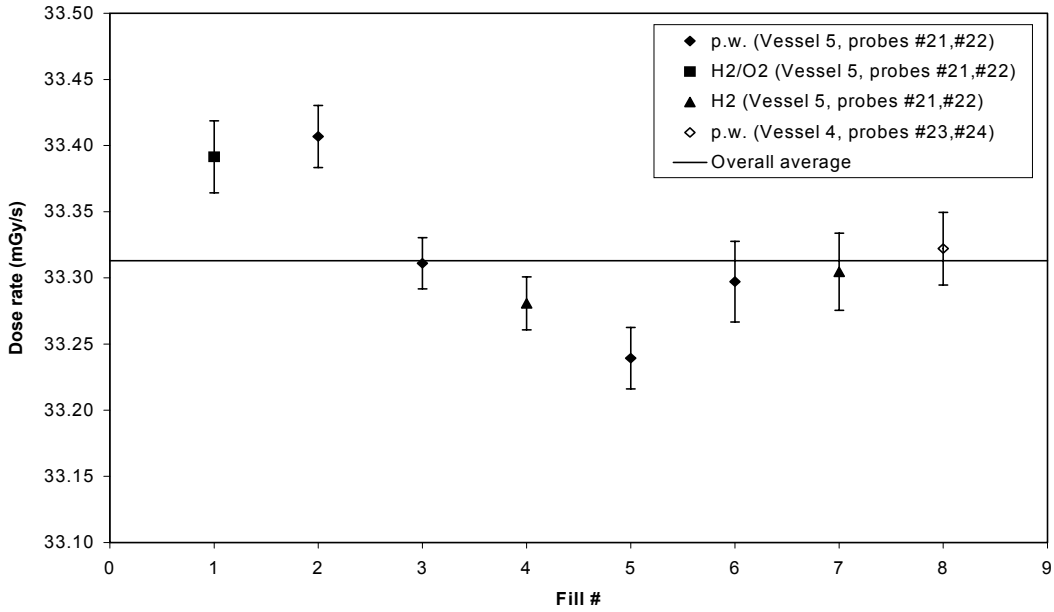

Figure 1b: The results in Figure 1a, summarized in different fills of the two vessels. The uncertainty bars refer to type A uncertainties (k=1) on the average value, for measurements of ΔT.

following two sections. All measurements at both standards laboratories were performed using an irradiation time of 120 s. The pre- and post-irradiation drift times were also 120 s. The dose rates were around 2 Gy/min at both standards laboratories.

A. Results Obtained at NRC

The water used in the sealed glass vessel was purified using a Milli-Q UV Plus water purifier, and had a resistivity of 18.2 MΩ cm. The presence of organic impurities was analyzed with an Anatel A-10 TOC (total organic carbon) monitor [9]. Typically, a reading of 3-4 ppb was obtained, equivalent to a mass concentration of 3-4 mg l^{-1} of organic carbon. The highly purified water was stored in quartz glass vessels and used for rinsing the calorimeter vessels before each new fill. Usually, the storage time in the quartz vessels was very short, less than an hour.

An Eldorado 6 (Atomic Energy of Canada Ltd) ^{60}Co unit was used for the irradiations, with a field size of 10 by 10 cm^2 at the depth of measurement, 5.0 cm. The SSD was 70 cm.

Figure 1a summarizes the results from 352 measurements divided into "series of measurements", where each series includes 7-14 individual calorimetry runs. In Figure 1b, the results are divided into each different fill of the two vessels.

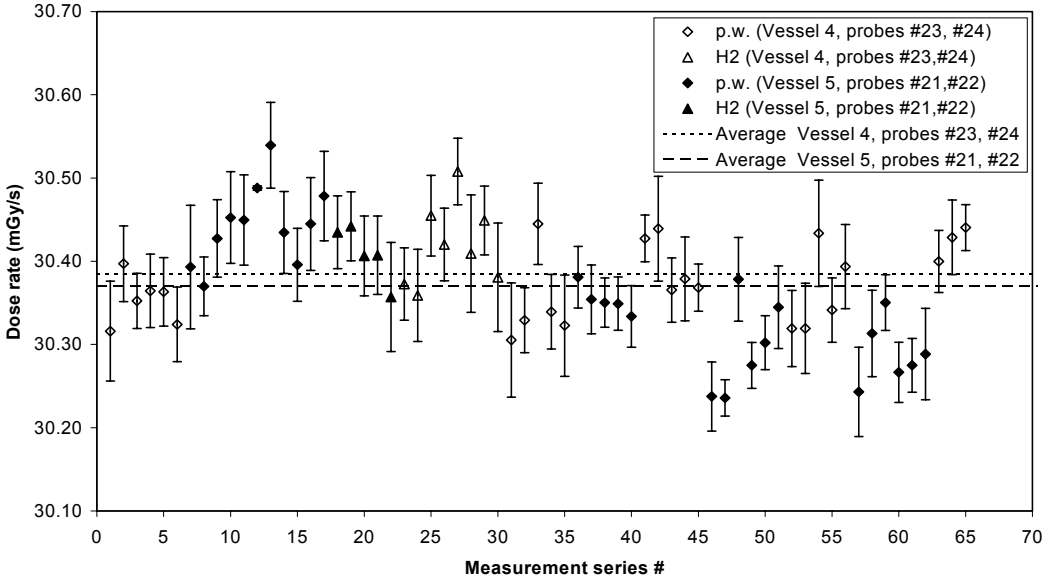

Figure 2a: The dose rate at the OFMET ^{60}Co unit determined with two different water systems. The results are corrected for decay to 1 July 1999. Each series includes typically 8-14 measurements. The uncertainty bars refer to type A uncertainties (k=1) on the average value, for measurements of ΔT.

In summary, the absorbed dose rate determined with the present sealed water calorimeter at the NRC ^{60}Co unit, corrected for decay to 20 January 1999 was (Uncertainties refer to type A (k=2), from the contribution of DT measurements.):

Vessel 5, probes 21 and 22: 33.31 mGy/s ±0.1%

Vessel 4, probes 23 and 24: 33.32 mGy/s ±0.1%

In this evaluation of the absorbed dose rate, the results obtained with the H_2/O_2 system (39 measurements) have been excluded since they are based on a calculation of the heat defect including an additional uncertainty. The results obtained with the H_2/O_2 system was used as a control of the other two aqueous systems since it is much less sensitive to any impurities in the vessels.

The result obtained with vessel 5 is based on 263 measurements, and the result obtained with vessel 4 is based on 50 measurements.

This yields an overall result for the determined dose rate of 33.31 mGy/s ±0.1% (Type A uncertainties (k=2), from the contribution of ΔT measurements and based on 313 measurements). This can be compared with the result obtained using the NRC sealed water calorimeter, 33.34 mGy/s ±0.1%. The total uncertainty is 0.9% (k=2) for both results.

Two cylindrical ionization chambers, one NE 2571 and one NE 2611A, were calibrated in the calorimeter water phantom at the vessels' previous position, using water protective PMMA sleeves. The NE 2571 Farmer chamber has a cavity volume of 0.6 cm^3, graphite wall, and an aluminium central electrode. The NE 2611A Secondary Standard chamber has a smaller cavity volume (0.33 cm^3), a hollow aluminium central electrode and a graphite wall.

Using the overall average dose rate from above, the following absorbed dose to water calibration factors were obtained. These $N_{D,w}$ factors are corrected to 20˚C and 101.325 kPa.

Based on the OFMET water calorimetry primary standard, the results are:

NE 2571, S/N 2807: 45.21 mGy/nC ±0.9%

NE 2611A, S/N 147: 103.5 mGy/nC ±0.9%

Based on the NRC water calorimetry primary standard, the results are:

NE 2571, S/N 2807: 45.15 mGy/nC ±0.9%

NE 2611A, S/N 147: 103.4 mGy/nC ±0.9%

This yields a difference in $N_{D,w}$ of 0.13% (NE 2571) and 0.10% (NE 2611A). The total uncertainties are given with a coverage factor of 2.

B. Results Obtained at OFMET

The water was purified using a Millipore Elix 10 unit connected to a Milli-Q Gradient A-10 water purifier. The water had resistivity of 18.2 MΩ cm, with a presence of organic impurities of 3-4 ppb. The calorimeter vessels were rinsed and filled with highly purified water taken directly from the Millipore unit.

A General Electric, Alcyon II ^{60}Co unit was used for the irradiations, with a field size of 10 by 10 cm^2 at the depth of measurement (5 g cm^{-2}). The SSD was 75 cm.

Figure 2a summarizes the results of 642 measurements divided into "series of measurements", where each series typically includes 8-14 individual calorimetry runs. In Figure 2b, the results are divided into each different fill of the two used vessels, consisting of different number of "series".

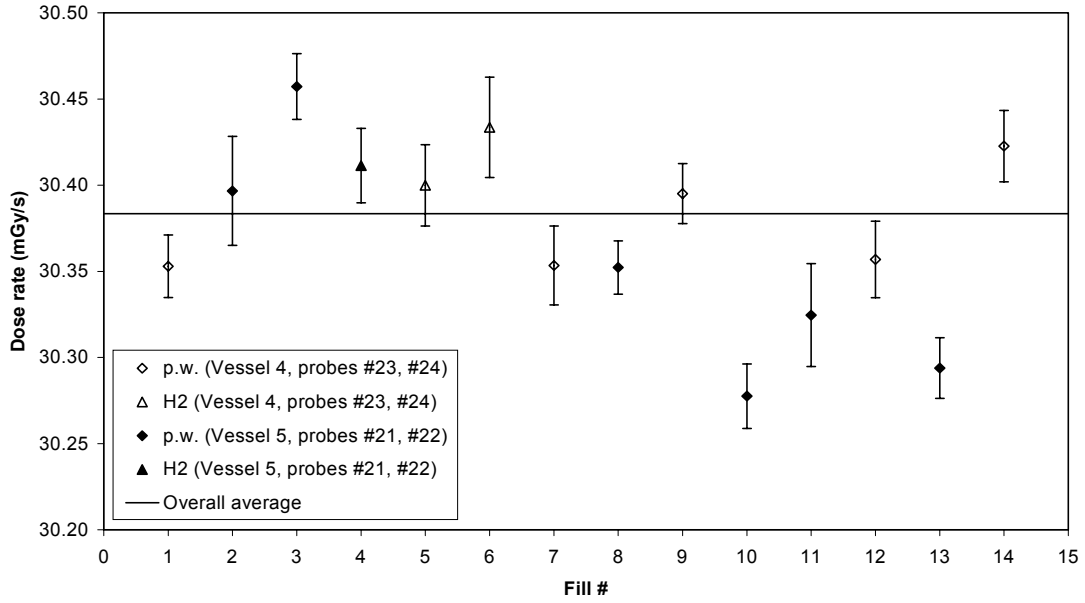

Figure 2b: The results in Figure 2a, summarized in different fills of the two vessels. The uncertainty bars refer to type A uncertainties (k=1) on the average value, for measurements of ΔT.

In summary, the dose rate determined with the present sealed water calorimeter at the OFMET ^{60}Co unit, corrected for decay to 1 July 1999 was: (Uncertainties refer to type A (k=2) from the contribution of DT measurements.)

Vessel 5, probes 21 and 22: 30.37 mGy/s ±0.1%

Vessel 4, probes 23 and 24: 30.38 mGy/s ±0.1%

The result obtained with vessel 5 is based on 307 individual measurements, and with vessel 4, 335 measurements.

This yields an overall result for the determined dose rate of 30.38 mGy/s ±0.1% (Type A uncertainties (k=2) from the contribution of ΔT measurements, based on 642 measurements). The total uncertainty is 0.9% (k=2) for both results.

Based on this determination of the absorbed dose rate in the OFMET ^{60}Co beam, the absorbed dose to water calibration factors for the two chambers previously used at NRC are:

NE 2571, S/N 2807: 45.16 mGy/nC ±0.9%

NE 2611A, S/N 147: 103.3 mGy/nC ±0.9%

This yields a difference, compared to the determination with the OFMET calorimeter at NRC of -0.11% (NE 2571) and -0.19% (NE 2611A), respectively. The total uncertainties are given with a coverage factor of 2.

IV. Measurements in High Energy Photon Beams

Preliminary results have been obtained using the Scanditronix M22 microtron at OFMET at two beam qualities, TPR=0.674 (6 MV) and TPR=0.768 (18 MV). The correction factors are given in Table 4, and explained in the Introduction. Note that since the depth in the water phantom was determined in the units g cm^{-2}, no correction for change in water density should be applied (k_r=1.000). The perturbation correction factors, k_p, for 6 MV and 18 MV were obtained from [2] by interpolation between the values for ^{60}Co and 20 MV. The factor k_{dd} was measured with a Scanditronix silicon diode detector.

The field sizes were at both energies 10 by 10 cm^2 at the depth of measurement (5 g cm^{-2} at 6 MV and 10 g cm^{-2} at 18 MV). The SSD were in both cases 100 cm. The average dose rates were chosen close to the dose rate used in the ^{60}Co measurements, *i.e.* around 2 Gy/min.

Three secondary standard ionization chambers, two of the type NE 2611A and one of the type NE 2561, were calibrated against the OFMET water calorimeter. The calibration factors

Table 4.
Correction factors used in the transfer from temperature rise to absorbed dose in the high-energy photon beam.

k_v	1.000	
k_c	0.9986 ± 0.15%	
k_p	1.0018 ± 0.05% (6 MV)	1.0015 ± 0.05% (18 MV)
k_{HD}	0.000 (for N_2)	
k_ρ	1.000	
k_{dd}	0.9961 ± 0.02% (6 MV)	0.9979 ± 0.02% (18 MV)
k_t	1.000	
c_w	4.2048 J g^{-1} K^{-1} ± < 0.005%	

obtained using the water calorimeter were then compared with chamber calibration factors previously obtained from NPL.

An internal transmission chamber was used as a beam monitor during the individual measurements. The long term stability was achieved by means of an additional external cylindrical reference chamber (NE 2611A).

The calibration factors were obtained in a few steps, according to the following: Firstly, the absorbed dose determined with the water calorimeter was normalized to the accumulated charge from the internal beam monitor during the irradiations. Secondly, the external reference chamber was compared to the internal beam monitor directly after each set of calorimeter measurements (consisting of 7-12 individual runs). From these two steps, the ratio of the absorbed dose to the reading of the external reference chamber is calculated. The chamber to be calibrated was then positioned in the water tank, replacing the vessel. Similar to above, the absorbed dose determined with the NPL calibrated secondary standard chamber was compared to the internal monitor. Secondly, the external chamber was again compared to the internal beam monitor, and the ratio of the absorbed dose to the reading of the external reference chamber calculated. From these ratios, the ratio of the chamber calibration factors determined at NPL and with the OFMET water calorimeter was obtained. The results based on 58 measurements with the water calorimeter at 6 MV and 51 measurements at 18 MV are presented in Table 5.

Table 5.
Ratios of chamber calibration factors determined at NPL and with the OFMET water calorimeter obtained with two high-energy photon beams. The total uncertainties are 2.2% (k=2).

Chamber	TPR=0.674 (6 MV)	TPR=0.768 (18 MV)
NE 2561 (#077)	1.002	0.999
NE 2611A (#127)	0.987	0.992
NE 2611A (#128)	0.990	0.992
Average	0.993	0.994

Based on the average values for all three chambers, these results indicate a 0.6-0.7% difference between the OFMET water calorimeter and the secondary standard calibrated at NPL, at both beam qualities. However, a difference in the results obtained with the two NE 2611A chambers and the NE 2561 chamber can be observed. At 6 MV this difference amounts to 1.4% and at 18 MV it is 0.7%. It should be noted that these differences do not involve the result obtained with the water calorimeter, since it cancels in the comparison. Although the differences are within the stated total uncertainties, further investigations should be performed.

V. SUMMARY

Within a collaborative project between OFMET and NRC, a sealed water calorimeter has been constructed based on the design used at NRC. It was thoroughly tested at NRC and irradiated in the ^{60}Co beam more than 300 times, using two vessels and four thermistor probes. After the transport to OFMET, another 653 irradiations have been performed at ^{60}Co. Three different aqueous system were used at NRC (N_2, H_2, and H_2/O_2), and so far two at OFMET (N_2 and H_2). When comparing the results obtained at the two laboratories, using two cylindrical transfer chambers (NE 2571 and NE 2611A), the results in Table 6 were obtained.

Table 6.
$N_{D,w}$ chamber calibration factors (mGy/nC). The subscripts indicate the standards laboratory where the calorimeter were used in the calibration of the ionization chamber, *i.e.* $OFMET_{NRC}$ indicates the OFMET calorimeter used at NRC. The uncertainties are given with a coverage factor of 2.

Calibration	NE 2571 (#2807)	NE 2611A (#147)
OFMET calorimeter at NRC	45.21 ± 0.9%	103.5 ± 0.9%
NRC calorimeter at NRC	45.15 ± 0.9%	103.4 ± 0.9%
Difference NRC_{NRC} vs. $OFMET_{NRC}$	0.13%	0.10%
OFMET calorimeter at NRC	45.21 ± 0.9%	103.5 ± 0.9%
OFMET calorimeter at OFMET	45.16 ± 0.9%	103.3 ± 0.9%
Difference $OFMET_{NRC}$ vs. $OFMET_{OFMET}$	0.11%	0.19%

These results show that the OFMET water calorimeter used at NRC gave the same response as the NRC calorimeter within the uncertainties. After the transfer to OFMET, it was successfully re-established producing results consistent with previous results obtained at NRC.

In addition to the extended measurements at ^{60}Co, some preliminary measurements were performed at OFMET using the microtron at two different beam qualities, TPR=0.674 (6 MV) and TPR=0.768 (18 MV). Based on the average values for three chambers of the same type (one NE 2561 and two NE 2611A), the obtained results indicate a 0.6-0.7% difference between the OFMET water calorimeter and the secondary standard calibrated at NPL, at both beam qualities. However, a difference in the results obtained with the two NE 2611A chambers and the single NE 2561 chamber can be observed. At 6 MV this difference amounts to 1.4% and at 18 MV it is 0.7%. It should be noted that these differences do not involve the result obtained with the water calorimeter, since it cancels in the comparison. Although the differences are within the stated total uncertainties, further investigations should be performed.

ACKNOWLEDGEMENTS

The knowledge, skill and dedication of NRC's and OFMET's technical and support staff were critical for the successful outcome of this project. The glass cylinders which form the central portion of the sealed glass vessels were ground by Gary Boyd (NRC). The rest of the glass work, including the glass envelopes for the thermistor probes, was done by Peter l'Abbé (NRC). David Marchington (NRC) was responsible for the overall assembly of the calorimeter and he also constructed the internal bead and lead assemblies for the thermistor probes. Leo Heistek (NRC) constructed the bridge circuit and the electronics for automated control. Reto Schafer (OFMET) and Olivier Brunschwig (OFMET) contributed skillful support in the experimental work.

Fruitful discussions and detailed comments on the manuscript by Dr Walter Münch (OFMET) and Dr Renate Moning (OFMET) are greatly acknowledged.

REFERENCES

[1] J.P. Seuntjens, "Comparative Study of Ion Chamber Dosimetry and water Calorimetry in Medium Energy X-Ray Beams", Ph.D. Thesis, Gent University, Gent, Belgium, 1991.

[2] J.P. Seuntjens, C.K. Ross, N.V. Klassen and K.R. Shortt, "A Status Report on the NRC Sealed Water Calorimeter", NRC Report PIRS-0584, National Research Council, Ottawa, Canada, 1999.

[3] S.R. Domen, "Absorbed dose water calorimeter", *Med. Phys.* **7,** pp. 157-159, 1980.

[4] R.J. Schulz and M.S. Weinhous, "Convection currents in a water calorimeter", *Phys. Med. Biol.* **30**, pp. 1093-1099, 1985.

[5] J.S. Laughlin and S. Genna, "Calorimetry", In Radiation Dosimetry, Vol. II, F.H. Attix and W.C. Roesch (Eds.), pp. 389-441, Academic Press: New York, 1966.

[6] N.V. Klassen and C.K. Ross, "Absorbed dose calorimetry using various aqueous solutions", *Radiat. Phys. Chem.* **38**, pp. 95-104, 1991.

[7] N.V. Klassen and C.K. Ross "Water calorimetry: The heat defect", *J. Res. Natl. Inst. Stand. Technol.* **102**, pp. 63-74, 1997.

[8] N.S. Osborne, H.F. Stimson and D.C. Ginnings "Measurements of heat capacity and heat of vaporization of water in the range 0 to 100˚C", *J. Res NBS* **23**, pp. 197-259, 1939.

[9] J. Moulin, P. Melanson and M. Retzik "The measurement and significance of total organic carbon in laboratory water systems", American Laboratory (News Edition), February, pp. 38-40, 1996.

QUESTIONS AND ANSWERS

Tony Aalbers: Over what temperature range are your thermistors calibrated?

Joakim Medin: They are calibrated between -4 to +12 ˚C and the beta values are evaluated at 4 ˚C.

Tony Aalbers: So there was only one fixed point involved?

Joakim Medin: Yes, one fixed point.

--

Tony Aalbers: When you described your 'active' box to subtract A-B instead of using the lock in amplifiers A-B mode, what do you really mean? Are there only capacitor elements in it or also amplifier elements?

Joakim Medin: It's an operational amplifier. I don't know the exact details but Jan does.

Jan Seuntjens: Normally the A minus B mode means that we use the two inputs of the lock in amplifier and do the subtraction within the lock in amplifier. We were worried that maybe the differential effects were temperature dependent or other effects were not handled well with the Stanford Research System so we did the differential part outside the lock in amplifier.

Tony Aalbers: So you got a better handle on the temperature?

Jan Seuntjens: Yes, we could isolate that problem.

Ken Gall: What was the size of the long-term drifts that you saw?

Joakim Medin: It was about 0.2 to 0.3 μV, even a little higher. It was temperature related. We could see that very clearly when we put everything in the wooden box.

Alan DuSautoy: The lock in amplifier has two stages, an a.c. stage and a d.c. stage. Is it possible to change the ratio between those two stages in the LIA because the temperature dependence probably is related to the d.c. stage in your lock in after the demodulation?

Jan Seuntjens: It is possible.

Ken Gall: You use the excitation of the lock in itself?

Jan Seuntjens: Yes - but that does not make a difference because you apply that excitation voltage on both arms so that is not a problem. It was inside the lock in amplifier components which we have not identified which made it temperature dependent.

Alan DuSautoy: What I am asking is what's the amplification after the demodulation? Because if that is too high that will cause the drift.

Jan Seuntjens: I am not sure whether we can isolate the d.c. component.

Tony Aalbers: What I can suggest to everybody, if you have problems or specific questions about operating lock in amplifiers and you are in a laboratory which has a good electrical department, you talk with those guys because sometimes you can prevent problems there and they can help you out. That is my opinion.

Jan Seuntjens: I believe that our electronics person has spoken with electrical people and they basically acknowledged that this amplifier has this problem. From memory he told me that they said that this is the limit of this particular device.

Ken Gall: The specifications of it are actually pretty bad. It performs a heck of a lot better than the specifications.

--

Dave Burns: You got a 0.2% change [in the calibration factor] for the 2611 [calibrated with the OFMET calorimeter at NRC, then with the OFMET calorimeter at OFMET]?

Joakim Medin: Yes there is a slight difference.

Dave Burns: Does that concern you or is it within the stats? Is it a statistical effect?

Joakim Medin: Yes I think it is a statistical effect.

Ken Gall [to Dave Burns]: 0.2% worries you? It is an ionisation chamber that has just travelled across the ocean!

Dave Burns: We can move them around the world and get them to repeat to 0.05%.

Joakim Medin: We have the different set ups of the calorimeter at the two places: we have the uncertainty in the vessel positioning and the probes contribute about 0.15%.

Alan DuSautoy: Is it the same sort of Co source?

Joakim Medin: It has a similar strength but it is not the same type.

Alan DuSautoy: So the scatter would be slightly different?

Carl Ross: Yes, but it would be really surprising if there are spectral differences that are enough to make that large an effect.

Ken Gall: If you consider that a 0.1% of it might just be plain old statistics then a 0.1% effect, that opens up thousands of possibilities because they are all going to be pretty esoteric.

Alan DuSautoy: I'd say that was good agreement.

Jan Seuntjens: The concern is that with an ion chamber you could cross the ocean and should probably get something within 0.05%. That is the basis of using an ion chamber for inter comparisons so I don't know: maybe there is something, maybe not.

Joakim Medin: I would say that I am not too worried about it, that is a summary of my view.

Antonio Guerra: In such measurements, do you put the chamber in the calorimeter tank?

Joakim Medin: In the calorimeter tank, yes.

Hugo Palmans: Why have you mixed up the results for the two chamber types [in Table 5]? They should be the same type but there is definitely a significant difference in the ratio at the two beam qualities between the two chamber types.

Gerhard Stucki: I wouldn't say it is a different chamber type. It is only the old version

Tony Aalbers: The 2611 is the successor of the 2561. Are there differences between the two chambers in construction? I thought not.

Russel Thomas: There is the aluminium rod and Delrin for holding on the graphite cap.

Tony Aalbers: OK, so there is a small difference.

Simon Duane: It is true that in the work that we have done on the two chambers at the NPL we haven't seen a difference between the energy dependence but not everyone fails to see a difference.

Gerhard Stucki: We don't have enough data for excluding any problems with these deviations: we have to do a lot more runs to make clear what the reason is for the difference between the two chambers.

Joakim Medin: That is a very good point.

Jan Seuntjens: But these are differences between chambers and so calorimeters are not involved, not in comparing different types of chamber at the same energy.

Jan Seuntjens [to Hugo Palmans]: I think you have also seen a difference between two chamber types?

Hugo Palmans: I don't remember if it is in the same direction. I should check.

Jan Seuntjens : I think it is in reverse.

Experimental Verification of Simulated Excess Heat Effects in the Sealed Water Calorimeter

H. Palmans

Ghent University, Department of Biomedical Physics, Proeftuinstraat 86, B-9000 Gent, Belgium

Abstract

Beside the chemical heat defect, excess heat is a major potential source of uncertainty on the determination of absorbed dose to water with a sealed water calorimeter (SWC). Excess heat is produced due to the presence of non-water equivalent materials in the measurement set-up and due to the non-homogeneity of dose distributions. Non-water equivalent materials are present in the measuring thermistor probes, the sealing vessel and the phantom walls.

In the past we have been studying the excess heat effect by numerically solving the heat transport equation for a simplified geometry and in simplified irradiation conditions. In the present work, more detailed simulations are performed and contributions from different influence parameters are evaluated separately, especially those from the vessel wall and from finite dimensions of the radiation field. The influence of performing a succession of calorimetry runs on the excess heat is evaluated as well. In order to find evidence for these simulated results, they are compared with experimental data obtained from a large number of calorimetry runs and with systematic measurements as a function of vessel wall dimensions and field size.

I. Introduction

An increasing number of standard dosimetry laboratories are developing SWC's with a design similar to the one proposed by Domen [1] as primary instruments for absorbed dose to water determination [2-10]. The dose measurement with this instrument is based on the measurement of the temperature rise at a point with a small thermistor assuming that the heat profiles after irradiation persist long enough to be accurately measured. Several perturbation effects could alter the temperature rise at the measurement point; the chemical heat defect, perturbation of the scatter field, convective water motion and conductive heat transport. The present work deals only with perturbations due to conductive heat transport.

Several investigators have performed numerical simulations of conductive heat effects and find corrections that are generally not larger than 0.5% [2,3,9,11-14]. The temperature effect at the measuring point is called excess heat or heat loss, depending on the sign of the effect. Very few experimental efforts to study these effects have been reported in the literature. Ross et al. [15] studied the effect as a function of the mass of glass in contact with water in a stirred water calorimeter. However, in that calorimeter type the major transport mechanism of heat from the vessel to the thermistor is forced convection. Krauss and Roos [14] compared post-irradiation drift curves for some thick-walled vessels of glass and PMMA with the results from simulations for a stagnant SWC.

The present work contributes to the study of effects due to heat conduction. Attention is paid to different sources of conductive heat transfers; excess heat formed in non-water materials such as the sealing glass vessel and thermistor probes, and effects from the non-homogeneity of lateral dose profiles. The different effects are evaluated separately. Experimental results for extreme situations are compared with simulated results. The idea is that the corrections calculated for realistic situations are reliable if the simulated corrections for extreme geometries and irradiation times are with a reasonable agreement reproduced in measurements.

II. Materials and Methods

A. Sealed Water Calorimeter

1) Construction

The construction of the SWC at the university of Ghent is based on the design of Domen [1] and has been described in detail in [3]. A short description is given here. The calorimeter tank consists of a 30 cm × 30 cm × 30 cm water phantom thermally isolated by polystyrene foam as shown in figure 1a.

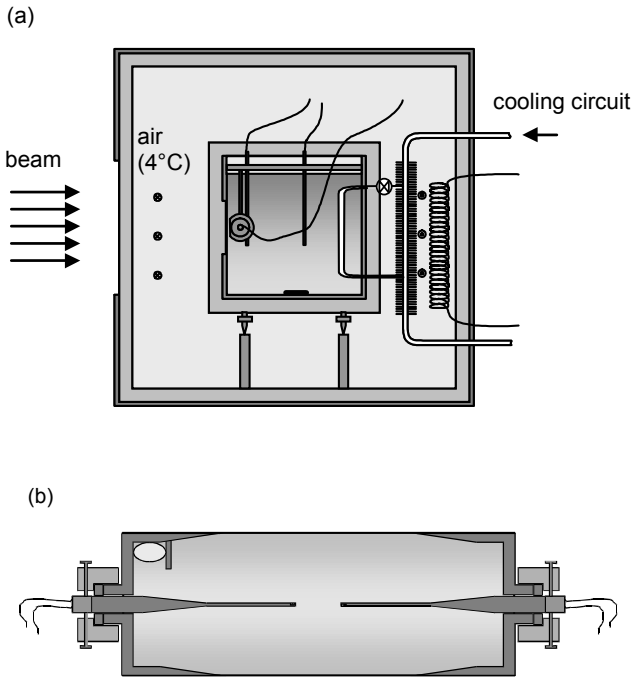

Figure 1: (a) SWC phantom and wooden enclosure. (b) cylindrical glass vessel with thermistor probes positioned.

Isolation of the enclosure allows temperature stabilization of the air surrounding the calorimeter phantom. The operating temperature is 4 ˚C in order to remove any concern related to convection. The water temperature is continuously measured

with calibrated Pt-resistor probes inserted at different positions in the water phantom. The temperature increase due to irradiation is measured at the center of a cylindrical vessel using small thermistors that are embedded in the tip of small glass probes as shown in figure 1b. The probe type used in this work consists of thermistors embedded in glass rods with a diameter of 0.5 mm. The vessel contains de-ionized and 3 times distilled water and has a diameter of 4 cm, a length of 14 cm and a wall thickness varying from 0.3 mm in the central part corresponding with the central axis of the beam to 1.6 mm at the lateral edges. The chemical water system inserted in the vessel for the present study is Ar-saturated pure water. The electronics and the methods to determine the measured temperature increasing are described in [3].

It will be shown below that the thickness of the glass vessel is an important parameter in the magnitude of the excess heat effects. As the glass vessels have a thickness which varies along the length of the cylinder, the thickness was determined by submersing segments of the cylinder in water and measuring the change in weight due to the buoyancy force [3]. Figure 2 shows the thickness as a function of axial position for one of the vessels.

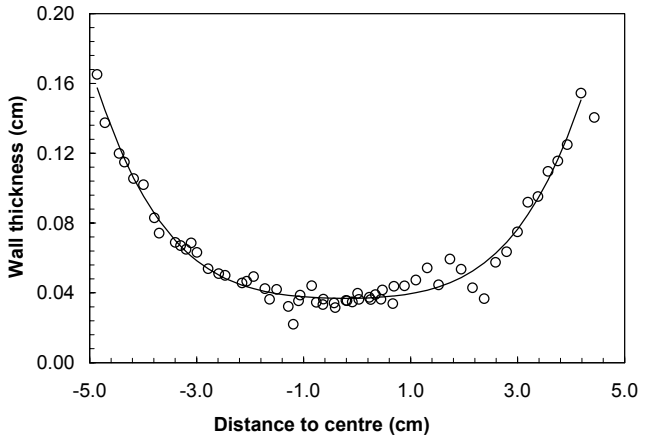

Figure 2: Longitudinal variation of the wall thickness of one of the glass vessels.

2) Correction Factors

Absorbed dose to water D_w is derived from the temperature increase ΔT due to irradiation at the location of the thermistors as:

$$D_w = c_w \cdot \Delta T \cdot k_c \cdot k_{sc} \cdot k_{dd} \cdot \frac{1}{1-h} \qquad (1)$$

where c_w is the specific heat capacity of water at the measuring temperature, k_c a correction factor for conductive heat effects, k_{sc} a correction factor for scattering and attenuation induced by probes and vessel, k_{dd} a correction factor for the non-uniformity of the lateral dose distributions and h the chemical heat defect which corrects for the heat that is released or absorbed in chemical reactions by radiation induced species with each other or with impurities present in the water. The remainder of this text only deals with the factor k_c.

B. Excess Heat

1) Sources of Excess Heat in the SWC

In the present paper, any heat difference compared to the heating of homogeneously irradiated water is called excess heat, no matter what sign the effect has got. Sources of temperature gradients and of excess heat could be the presence of non-water materials (thermistor probes, the sealing glass vessel and the entrance window of the water phantom), non-uniformity of dose distributions and temperature gradients present before irradiation. For two reasons, the use of a sealing vessel has been introduced in the design of water calorimeters. The first is to minimize convection currents when the calorimeter is operated at temperatures deviating from 4 ºC. The second reason is to achieve a higher quality of the water purity which is important to control the chemical heat defect.

2) Simulations of Conductive Excess Heat Effects

The general equation for heat conduction (without convection) is:

$$\frac{\partial T}{\partial t} = \alpha \cdot \nabla^2 T + \frac{1}{c} \cdot \dot{D} \qquad (2)$$

where T is the temperature as a function of time and position, α, c and $\dot{D}$ are respectively the heat diffusivity, the heat capacity and the dose rate as a function of position.

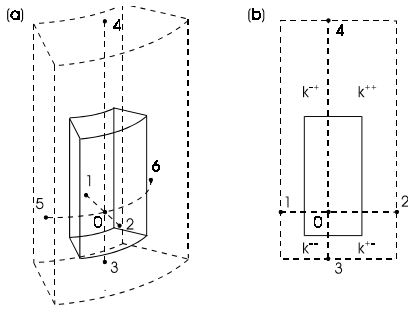

Figure 3: (a) Volume-element in cylindrical co-ordinates in which the heat balance is expressed to obtain a discrete representation of the heat conduction equation (2) and (b) intersection of the volume-element in the (r,z)-space.

Equation (2) can be expressed in discrete steps by evaluating the heat balance for an elementary volume in cylindrical co-ordinates, as shown in figure 3a. The principles of this method have been described in [16] and is extended here for a grid in the *(r,z,θ)*-space with irregular step size. In order to obey the law of energy conservation, the increase of total heat $\Delta Q = m.c.\Delta T_0$ in the volume element surrounding the node with index 0 over a time interval Δt must be equal to the net heat that is conducted from the neighbouring cells surrounding the nodes with indices i = 1 to 6 (figure 3b), plus the energy that is deposited in de volume element due to ionising radiation, $\Delta Q_{ion} = \dot{D}.m.\Delta t$,

where m is the mass in the volume element with volume V ($m = \rho.V$).

The heat that is transferred from one of the six neighbouring nodes with indices i during the time interval Δt is:

$$\Delta Q_{i\to 0} = \frac{\sum_{j=1}^{4} k_{i,j} \cdot A_{i,j}}{l_i} \cdot (T_i - T_0) \cdot \Delta t \qquad (3)$$

where $k_{i,j}$ is the heat conduction coefficient of the medium in a quadrant adjacent to the path from node i to node 0 with j representing the quadrant, $A_{i,j}$ is the area of the conductive canal in that quadrant and l_i the length of the path from node i to node 0. Because of the rotational symmetry around the z-axis, the contributions ΔQ_{5j0} and ΔQ_{6j0} are zero and in the summation in expression (3) only two terms remain.

For example, with the indices denoted in figure 3, the length of the path from node 1 to node 0 is $l_1 = \Delta r^{-}$ and the area of the tube from node 1 to node 0 at the lower side becomes:

$$A^{--} = \frac{\Delta\theta}{2} \cdot \left(r_0^{\,2} - \left(r_0 - \frac{\Delta r^-}{2} \right)^2 \right) = \frac{\Delta\theta}{2} \cdot \Delta r^- \cdot \left(r_0 - \frac{\Delta r^-}{4} \right) \qquad (4)$$

The energy balance becomes:

$$\Delta Q_0 = \sum_{i=1}^{4} \Delta Q_{i\to 0} + \Delta Q_{ion} \qquad (5)$$

yielding:

$$T_0(t+\Delta t) = T_0(t) + \frac{\sum_{i=1}^{4} \Delta Q_{i\to 0} + \left(\sum_{j=1}^{4} V^j \cdot \rho^j \cdot \bar{s}_{m^j,w} \right) \cdot \dot{D}_w \cdot \Delta t}{\left(\sum_{j=1}^{4} V^j \cdot \rho^j \cdot c^j \right)} \qquad (6)$$

where j represents the quadrants - -, + -, - + and ++, m^j the material in quadrant j, $\bar{s}_{m^j,w}$ the m^j to water mass stopping power ratio (averaged over the local electron spectrum), ρ^j the mass density of material m^j and c^j the heat capacity of material m^j. The volume V^{--} of the quadrant - - is:

$$V^{--} = \frac{\Delta\theta}{2} \cdot \left(r_0 - \frac{\Delta r^-}{4} \right) \cdot \Delta r^- \cdot \Delta z^- \qquad (7)$$

and similar expressions can be formulated for the other quadrants.

The previous expressions are only valid for a point P_0 that is not located on the z-axis (for which $r_0 \neq 0$). For the points with $r_0 = 0$ the expressions for ΔQ_{ij0} and the volumes have to be adapted.

Expressions (3-7) allow the choice of an irregular grid such that in those regions where sharp temperature gradients can be expected, the calculations can be performed with a finer resolution than in more homogeneously heated regions. Sharp temperature gradients occur for example in the neighbourhood of the probe tip. The method was implemented in a C-program. The geometry that is simulated is shown in figure 4.

For z = 0 and at the outer edges of the grid, boundary conditions have to be defined. Due to the symmetry of the geometry (figure 4) the temperature gradient at z = 0 is zero and symmetrical. For the outer edges there are two possibilities; a gradient equal to zero or a temperature equal to that for homogeneous water. Both approaches give rise to artefacts. The former introduces an underestimation of the temperature flow out of the region, whereas the latter introduces an overestimation. The artefacts can be limited by choosing the region for the calculations sufficiently large. In the present work a region of 10 cm × 10 cm was chosen except when mentioned else. For the longest irradiation times and a maximum number of successive runs the difference between the two options for the boundary conditions was evaluated to be no larger than 0,001%. Furthermore, the explicit finite differences scheme described in the previous paragraphs is only stable and convergent under certain conditions as discussed in [3].

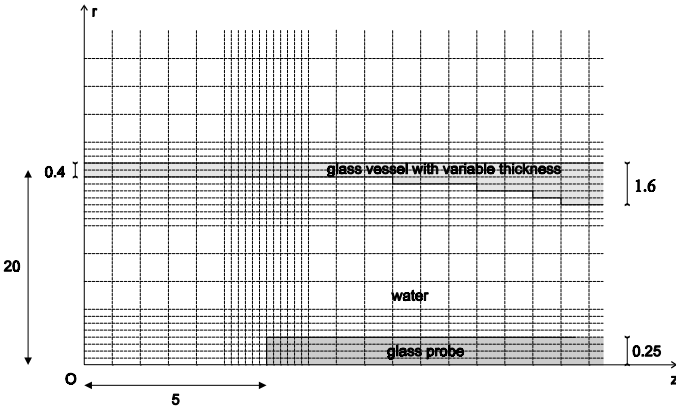

Figure 4: Schematic drawing of the geometry used for the heat conduction simulations, showing the glass vessel with variable thickness and the choice of the irregular grid.

For modelling the non-uniformity of dose distributions, expressions similar to (3-7) were formulated in rectangular co-ordinates.

3) Material Properties

Table 1 shows the thermal properties required for the heat conduction simulations and the vessel material to water stopping power for ^{60}Co irradiation. k_c depends on the photon energy by $s_{g,w}$ the glass to water restricted collision mass stopping power ratio for the local electron spectrum. In the present work it was derived from the calculated electron spectra with an energy cut-off Δ of 300 keV corresponding to a vessel wall thickness of 0.5 mm. For thicker vessel walls and for high-energy photon beams the restricted stopping power ratios differ slightly. However, it was found that the influence on the results is insignificant.

Table 1
Material data used in the heat conduction simulations for ^{60}Co irradiation.

Material	k ($J \cdot s^{-1} \cdot m^{-1} \cdot K^{-1}$)	ρ ($kg \cdot m^{-3}$)	c ($J \cdot kg^{-1} \cdot K^{-1}$)	α ($m^2 \cdot s^{-1}$)	$s_{m,w}$
Water	0.602	1000	4180	$0.144 \cdot 10^{-6}$	1.000
Glass	1.164	2400	836	$0.580 \cdot 10^{-6}$	0.822
PMMA	0.188	1190	1463	$0.108 \cdot 10^{-6}$	0.972

4) Derivation of Correction Factors

Figure 5 shows a typical temperature evolution for a sequence of three calorimeter runs and the evaluation procedure of the correction factor k_c as the ratio of ΔT determined at mid-run for homogeneous water to ΔT for the real situation.

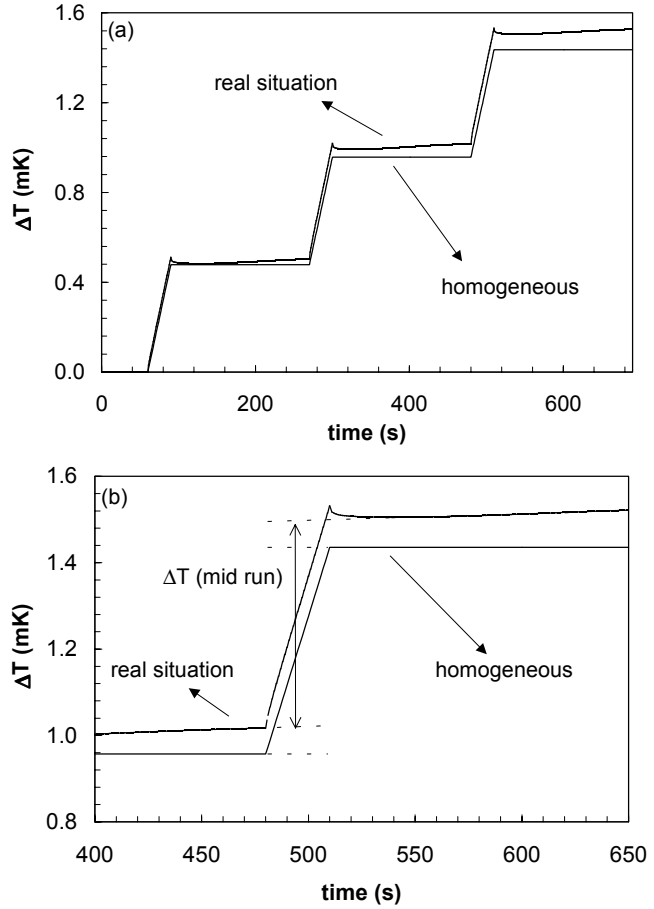

Figure 5: (a) Simulated temperature evolution due to three successive irradiations in homogeneously irradiated homogeneous water (full curve) and the presence of thermistor probes, glass vessel and dose gradients (dashed curve). (b) Detail for the 3rd run with indication of the extrapolation of drift curves to mid-run.

The results for the correction factors depend on the intervals of the linear fittings of the pre- and post-irradiation drift curves. In table 2 the intervals used in the present study are shown. These correspond to the intervals that are used in the routine analysis of the calorimeter runs. The starting point of 20s after irradiation was chosen because the effect of the thermistor probes is reduced to less than 0.1% of the signal in all situations by then.

Table 2
Fit intervals used on the pre- and post-irradiation drift curves to determine the excess heat correction factors.

Irradiation time (s)	Time before start irradiation	Time after stop irradiation
30	-60 to 0	20 to 120
60	-100 to 0	20 to 120
120	-100 to 0	20 to 150
180	-100 to 0	20 to 200

C. Experiments

A large number of calorimetry runs in high-energy photon beams obtained from previous work described in references [3,11,17] was analyzed in order to evaluate if in a series of successive runs, small changes from run to run could be observed and to compare these observations with simulated effects. The same data set was used to examine the post-irradiation drift curves and again, compare these with simulated post-irradiation drifts.

For a new experiment, a number of cylindrical glass vessels with different diameters and wall thicknesses were constructed in order to investigate the SWC response as a function of vessel dimensions. Furthermore, the SWC response as a function of field size was studied. Figure 6 gives a two-dimensional representation of the diameter/wall thickness combinations that were used. The full symbols are those vessels for which SWC measurements have been performed up to now.

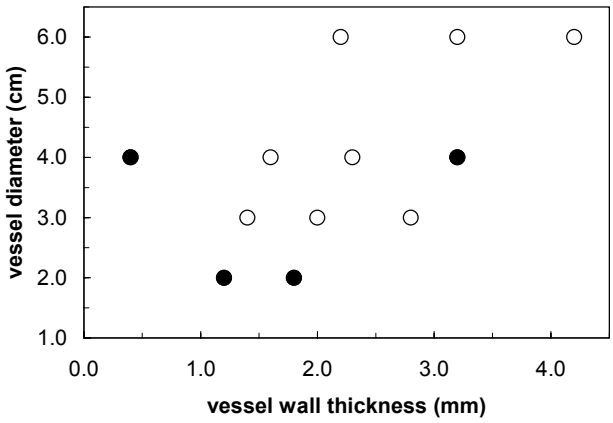

Figure 6: Diameter versus vessel wall thickness of the glass cylinders used for a systematic study of SWC response as a function of vessel geometry.

III. Results and Discussion

A. Numerical Simulations

A specific situation could be simulated in one calculation, but it was found that the effects of probes, vessel and field size, when simulated separately, add up to the results obtained in the complete simulation. The next sections show only the separate

results, which allows a systematic discussion of different influence parameters.

1) Thermistor Probes

Figure 7 shows the simulated corrections as a function of probe diameter for different irradiation times in a ^{60}Co beam. A separation of 1 cm between both probe tips was assumed. The probes were modelled as solid glass rods.

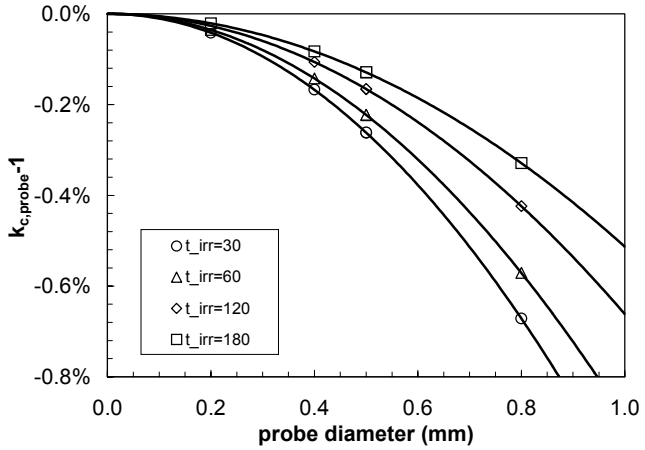

Figure 7: Simulated excess heat correction for the glass probes as a function of probe diameter for different irradiation times. The full curves are quadratic fits through the data points.

The full curves represent quadratic fits through the data points showing that the correction factors for the probes could be reproduced accurately by the following equation:

$$k_{\mathrm{c,probe}} = 1 + a_{\mathrm{probe}} \cdot d^2 \qquad (8)$$

where d is the diameter of the probe in mm. Table 3 gives the values of a_{probe} as a function of irradiation time e.g. for a probe with a diameter of 0.5 mm and an irradiation time of 180 s this results in a correction of –0.13 %.

Table 3
Coefficients a_{probe} in equation (9) for ^{60}Co irradiation and a probe separation of 1 cm.

Irradiation time (s)	a_{probe} (%/mm^2)
30	-1.05
60	-0.89
120	-0.66
180	-0.51

The variation of the probe corrections from run to run were found to be very small and not significant.

2) Glass Vessel

Figure 8a shows the simulated correction for a glass vessel with an outer diameter of 4 cm for 180 s irradiations in ^{60}Co and for different thicknesses of the vessel wall. The results are plotted as a function of the calorimeter run number in a set of subsequent runs, showing a slight evolution of the values.

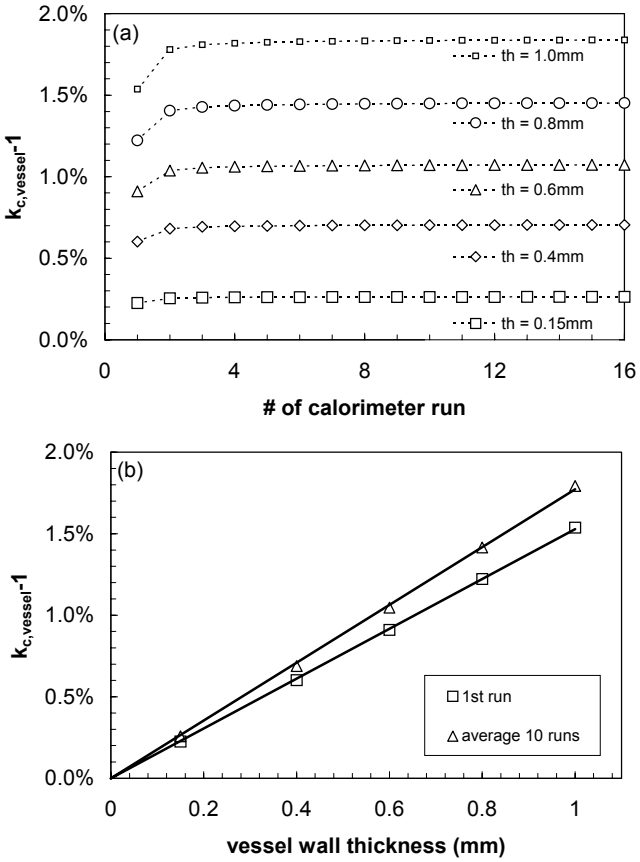

Figure 8: (a) Simulated excess heat correction for the glass vessel with a diameter of 4 cm and an irradiation time of 180 s, plotted as a function of subsequent calorimeter run number. (b) For the same data-set plotted as a function of vessel wall thickness for the 1st run and the average taken over 10 runs. The full curves are linear fits.

Figure 8b shows the simulated corrections as a function of vessel wall thickness for the same situation as for figure 8a, for the first run and averaged over a sequence of 10 runs. The full curves represent linear fits through the data points showing that the correction factors for the vessel could be reproduced accurately by the following equation:

$$k_{\mathrm{c,vessel}} = 1 + a_{\mathrm{vessel}} \cdot th \qquad (9)$$

where th is the vessel wall thickness in mm.

Table 4 gives the values of a_{vessel} as a function of irradiation time and vessel diameter. The numbers in italic are situations where the fits were rather poor. In those situations a simulation of every individual situation is more reliable. Table 5 gives examples for a number of realistic vessel dimensions used by other investigators.

3) Field Size

Figure 9 shows the simulated correction for effects due to the lateral non-homogeneity of the irradiation field for two field sizes and for different irradiation times. The results are again plotted as a function of the calorimeter run number in a set of subsequent runs, showing that there is an evolution of the values.

Table 4
Coefficients a_{vessel} in equation (9) for ^{60}Co irradiation.

Irradiation time (s)	Ø=3.0cm	Ø=4.0cm	Ø=5.0cm	Ø=6.0cm
	a_{vessel} for 1st run (%/mm)			
30	2.14	0.33	0.02	0.00
60	2.33	0.59	0.07	0.01
120	*1.25(*)*	1.30	0.36	0.07
180	*-0.86(*)*	1.53	0.81	0.29
	a_{vessel} average for 10 runs (%/mm)			
30	2.00	0.01	-0.06	0.01
60	2.74	0.43	-0.13	-0.05
120	*1.80(*)*	1.35	0.10	-0.11
180	*-0.40(*)*	1.77	0.65	-0.03

(*) Poor fit

Table 5
Some examples of the vessel excess heat correction for realistic vessel dimensions.

Ref	Ø (cm)	*th* (mm)	t_{irr} (s)	$k_{c,vessel}$-1 (1st run)	$k_{c,vessel}$-1 (10 runs)
[3]	4.0	0.40	180	0.61 %	0.71 %
[1]	3.3	0.25	60	0.45 %	0.51 %
[12]	*6.0*	0.90	120	0.07 %	-0.10 %
[13]	*4.0*	0.30	120	0.39 %	0.41 %

Table 6
$k_{c,field}$-1 for different square field sizes and irradiation times.

Irradiation time (s)	4x4 cm^2	6x6 cm^2	8x8 cm^2	10x10 cm^2	12x12 cm^2
	$k_{c,field}$-1 for 1st run (%)				
30	-0.97	0.00	0.00	0.00	0.00
60	-1.55	-0.02	0.00	0.00	0.00
120	-3.42	-0.14	0.00	0.00	0.00
180	-5.37	-0.58	-0.02	0.00	0.00
	$k_{c,field}$-1 average for 10 runs (%)				
30	-0.53	-0.23	-0.13	-0.06	-0.02
60	-0.86	-0.07	-0.09	-0.05	-0.02
120	-2.41	-0.01	-0.15	-0.09	-0.05
180	-4.21	-0.07	-0.19	-0.16	-0.10

Table 6 shows the correction as a function of field size and irradiation time.

4) Discussion Simulations

The effects for realistic geometries used in routine calorimetry measurements are small. As can be expected the effects increase in magnitude with probe diameter and vessel thickness, whereas they decrease with vessel diameter and field size. In general the magnitude of the effects also increase with irradiation time. In the systematic study as a function of vessel dimensions and field size that was initiated, up to now measurements were performed only for situations where the effects are large, i.e. thick glass vessels, small vessel diameters and small field sizes. These measurements are reported in the next sections.

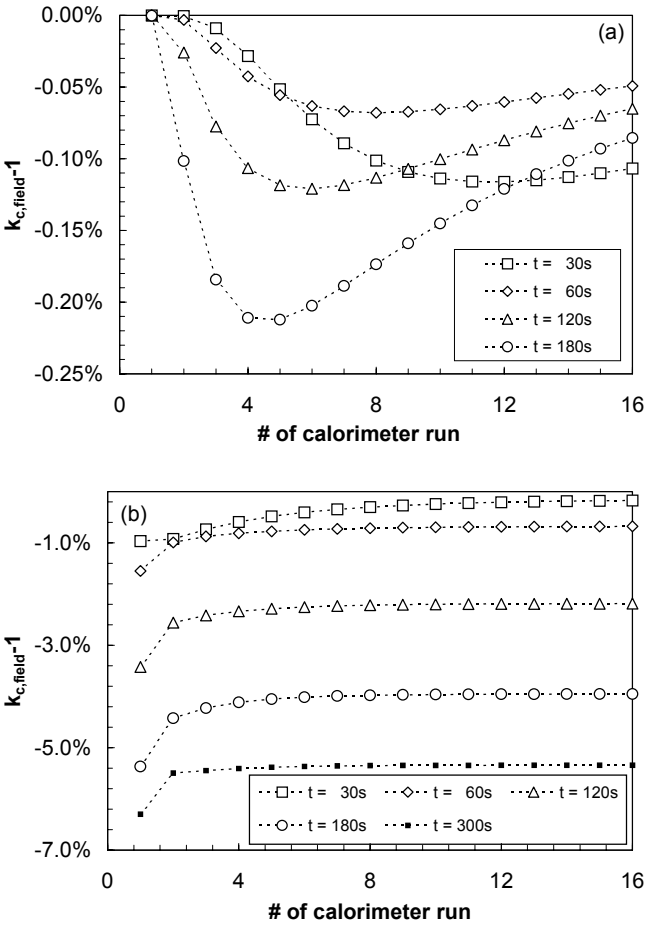

Figure 9: Simulated excess heat (heat loss) correction due to the finite size of the field, plotted as a function of subsequent calorimeter run number for different irradiation times (a) for a field size of 10 cm × 10 cm and (b) for a field size of 4 cm × 4 cm.

B. Experiments

1) Examination of SWC Response a.f.o. Run Number

The calorimetry measurements recorded in Ghent [3,11,17,18] were always performed in sequences of 6-15 calorimetry runs, such that the post-irradiation temperature drift of one run is the pre-irradiation drift of a subsequent run. In the present section the evolution of the SWC response with run number is investigated for some realistic situations used in routine calorimetry measurements. Figures 10a-c show the response of the SWC as a function of the run number in a sequence of irradiations, for three different situations. The values in each sequence were normalized on the first run and the average value for each run number was plotted with a standard error on the mean value. As in the dose determination average values over a sequence of runs are taken, a moving average is represented in figures 10a-c as well (e.g. the 6th data point is the average over the 6 first runs).

In general, no clear evolution of the SWC response with run number is observed. After 8-10 runs the variations become larger, but this is mainly because the values contain fewer data (the average number of subsequent runs is 7-9). The jump from run 1 to run 2 in figure 10b could be an accidental high value of

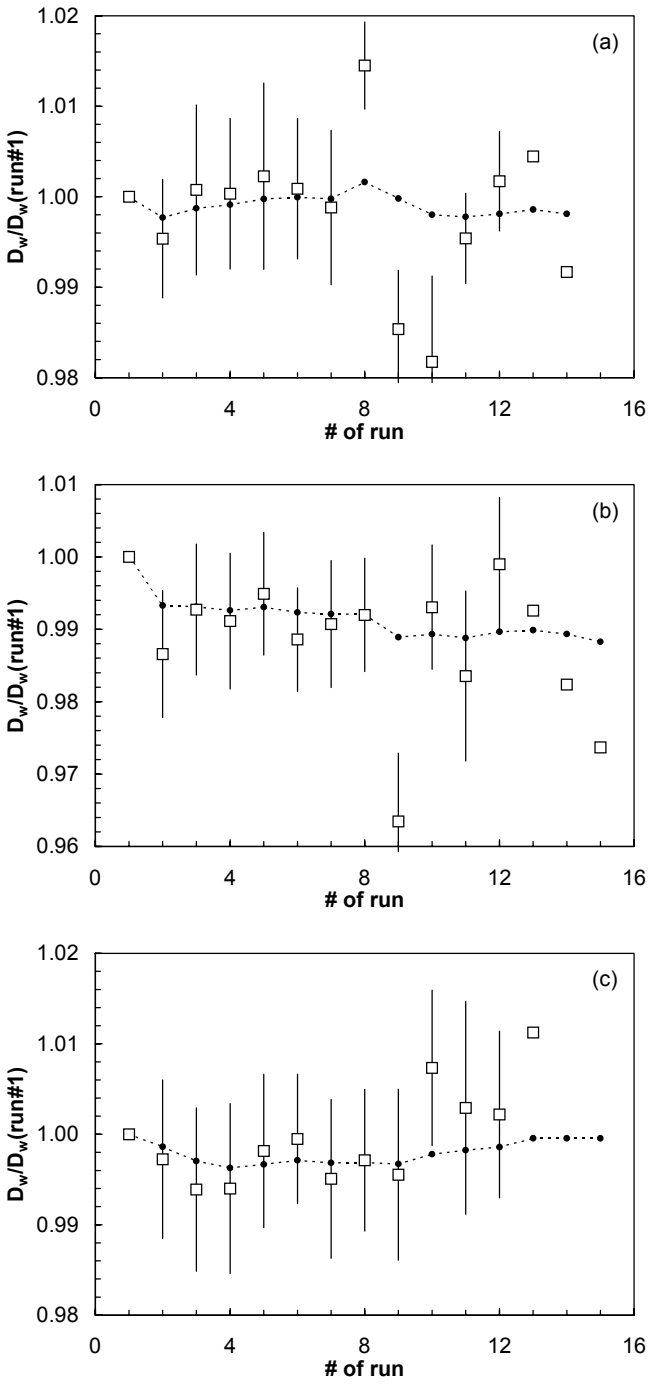

Figure 10: Average response of the SWC, normalized on the first run, in high-energy photon beams plotted as a function of the run number (open symbols) and moving average (dots connected by dotted lines) of these values. (a) For a PMMA vessel, probes with diameter 0.8 mm and 180 s ^{60}Co-irradiations, (b) for a glass vessel with variable thickness, probes with diameter 0.8 mm and 180 s ^{60}Co-irradiations and (c) for a glass vessel with variable thickness, probes with diameter 0.5 mm and 120 s irradiations in 5 MV and 10 MV high-energy photon beams.

the first run. It is clear that a lot more experimental data would be required to resolve small variations, such as those in figures 8 and 9, with statistical significance.

2) Examination of Post-irradiation Drift Curves

Figure 11 shows details of the post-irradiation drift curves for the three situations presented in figure 10. Both simulated and experimental curves averaged over a large number of runs are shown. To this end, the pre-irradiation drift in the experimental runs was subtracted from the whole measurement and the experimental post-irradiation drift curves were normalized in the interval from 20 to 40 s after the end of the irradiation so as to coincide with the simulated values in the same time interval. This method is comparable to the one used in two other contributions to these proceedings [5,19]. The initial discrepancy, especially in

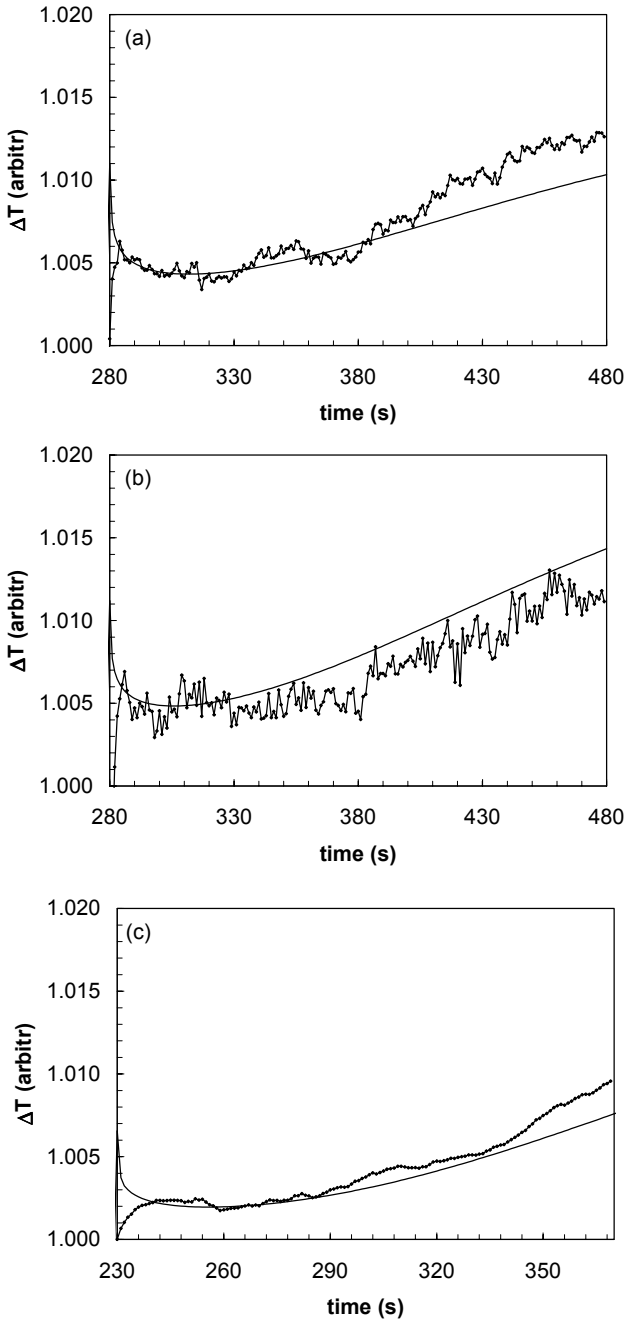

Figure 11: Post-irradiation drift curves for situations of figure 10. Simulations are presented by full lines, experimental curves by connected symbols.

figure 11c, could be explained by blurring due to a non-constant time point at which the irradiation ends.

The experimental data in figure 11a are the average of 170 runs (a total dose of 330 Gy), in figure 11b they are the average of 97 runs (a total dose of 140 Gy) and in figure 11c they are the average of 147 runs (a total dose of 590 Gy). The total doses explain the differences in noise levels between the three situations. Less than 5% of the runs were rejected because of abnormal fluctuations, spikes or abnormally high changes of the drifts before and after irradiation.

It can be observed that for the three situations shown here the agreement is good. For various other realistic situations of that are currently still being analyzed a comparable agreement, although not always that good, is observed. In general a small increase with a comparable magnitude as for the simulated effect of the vessel is observed. It should be noted that these comparisons are not a verification of the absolute values of the excess heat effects, as a normalization in a certain time interval has been applied. They give rather an indication of how correct the effects are simulated by yielding agreement of relative values.

In figures 12, 13 and 14 similar data are shown for a number of situations in which one or more parameters influencing the excess heat are given more extreme values. This provides more sensitive tests of the simulations. These measurements were all performed in ^{60}Co and the irradiation time was always 300 s. For the measurements shown in figure 12 and 13 glass vessels with smaller diameters and thicker walls were used. The number of runs was 47, 48 and 52 for figures 12, 13a and 13b respectively. For the vessel with a 'normal' diameter of 4 cm and a thick wall, the agreement is still fine. For the vessels with a diameter of 2 cm, the curvature of the post-irradiation curve is smaller in the measurements than in the simulations. A possible reason could be that one of the data for the heat properties of glass is not consistent with the glass used in the experiments.

In figure 14 the effects are shown for different field sizes. The number of runs was 25, 21 and 28 for figures 14a, 14b and 14c respectively. Figure 14c shows that the difference between performing one single calorimetry measurement and performing a sequence of calorimetry measurements can result in significant

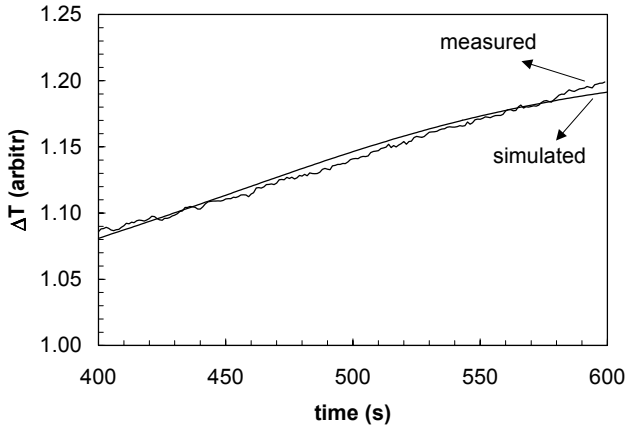

Figure 12: Simulated and measured post-irradiation drift curves for 300 s irradiations and glass vessels with diameter of 4.0 cm and wall thickness 3.2 mm.

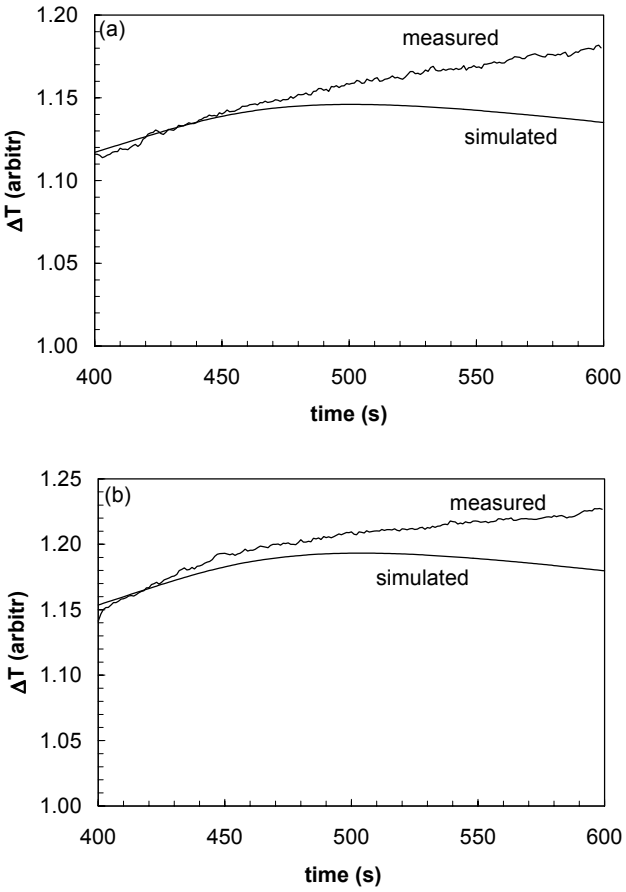

Figure 13: Simulated and measured post-irradiation drift curves for 300 s irradiations, glass vessels with a diameter of 2.0 cm and wall thicknesses of (a) 1.2 mm and (b) 1.8 mm.

differences of the post-irradiation curves. The agreement of the post-irradiation curves for the different field sizes is reasonable. More measurements will be recorded for these situations in the future in order to lower the amplitude of the statistical fluctuations on the drift curves.

3) SWC Response as a Function of Vessel Dimensions

In figure 15, the measured relative dose response of the SWC is shown as a function of the vessel wall thickness for two diameters of the vessel. For the two vessels with a diameter of 2 cm, the SWC response obtained with a large, thin-walled vessel has been used as reference value (plotted near zero wall thickness), as the effect of the latter vessel is negligible compared to the former. The results of simulations are shown as well, i.e. the reciprocals of the excess heat correction factors. Note that for the two diameters the effects point in the opposite direction. This is due to the differences in curvature of the drift curves. In both situations the simulations underpredict the measured effects. For the 2 cm diameter vessel this corresponds with the observations in figures 13a and 13b. For the 4 cm diameter vessel, where the post-irradiation drift curve shows a reasonable agreement, the extrapolation to mid-run yields a value close to unity and could thus be very sensitive to small effects on the drift curves. A small part of the effects is caused by the scatter perturbation of the glass vessel, but preliminary

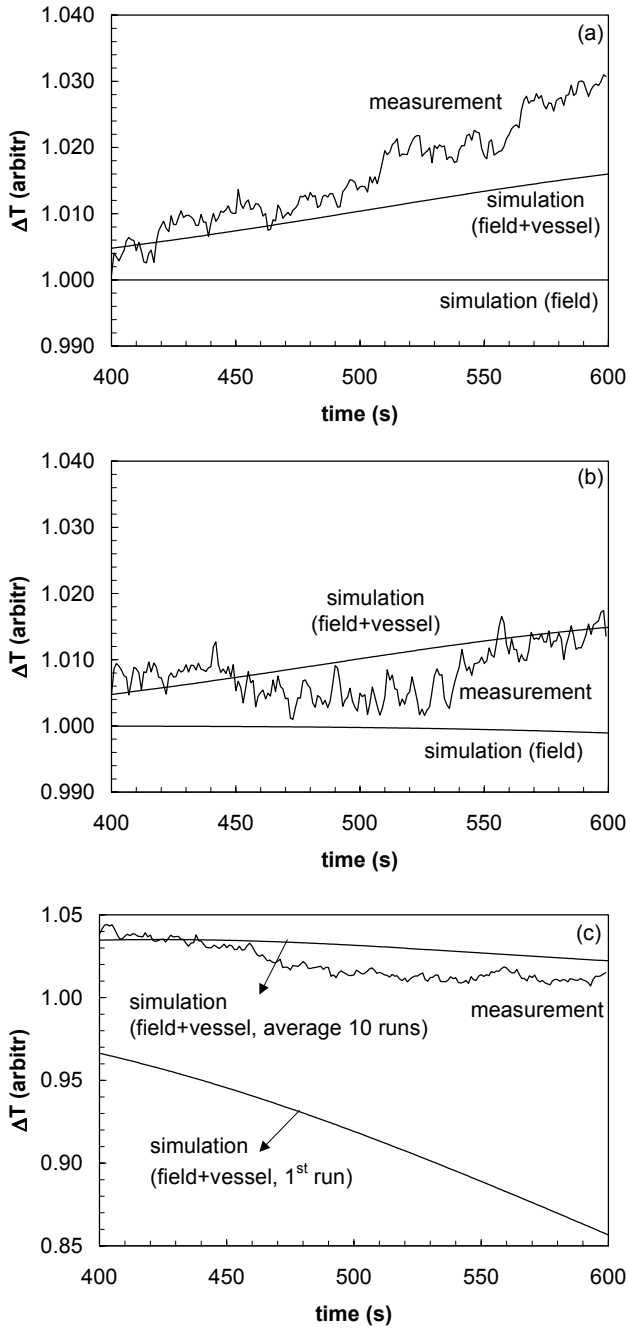

Figure 14: Simulated and measured post-irradiation drift curves for 300 s irradiations and field sizes of (a) 12 cm × 12 cm, (b) 8 cm × 8 cm and (c) 4 cm × 4 cm.

experimental results indicate effects that are not larger than 0.5%. It should also be noticed that, when the deviations between simulations and measurements are expressed as a percentage of the effect, they are not much larger than for the 'normal' situations in figure 11.

4) SWC Response as a Function of Field Size

In figure 16 similar data as in the previous section are shown for the SWC response as a function of field size, obtained with the glass vessel with variable wall thickness. Three field sizes were used; 12 cm × 12 cm, 8 cm × 8 cm and 4 cm × 4 cm. The

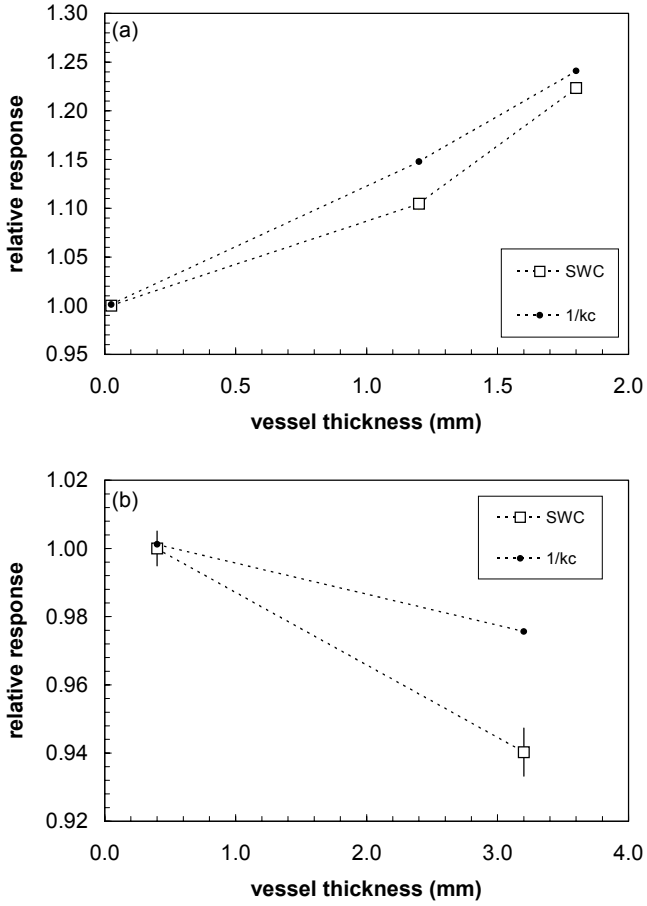

Figure 15: Measured and simulated relative SWC response as a function of vessel wall thickness for vessels with diameters of (a) 2.0 cm and (b) 4.0 cm.

large variation in figure 15a is mainly due to the variation of the output factor. The output factor is defined here as the ratio of the dose for a certain field to the dose for a 12 cm × 12 cm field, both measured on the central axis at a water equivalent depth of 5 cm. The output factors were measured with a Markus chamber. After correction of the SWC results for these output factors, the remaining effects again underpredict the calculated effects, which might be partially caused by the simplifying assumption for the lateral profile; in the simulations a step-function was assumed for the field edges.

IV. Conclusions

The excess heat effect in the SWC has been investigated by numerical simulations and by measurements.

In the simulations, the contributions of probes, vessel and field size were evaluated separately. The effects were studied systematically as a function of probe diameter, vessel diameter, vessel wall thickness, field size and irradiation time. For the effects due to probes and vessels, expressions as a function of probe diameter and vessel wall thickness have been proposed. For realistic dimensions (situations used for routine measurements and situations reported in the literature) and irradiation times the combined effects do in general not exceed 0.5% in absolute value. Slight variations as a function of run

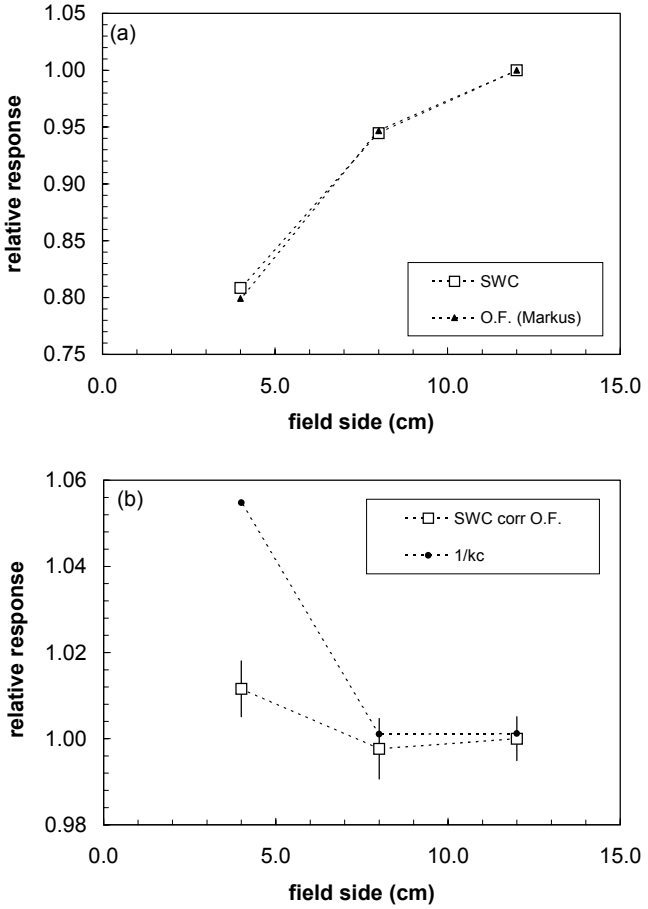

Figure 16: (a) Measured relative response of the SWC and a Markus chamber as a function of field size and (b) relative SWC response corrected for output factor and simulated relative response.

number in a sequence of calorimetry measurements show up from the simulations.

Experimental observations were shown in three ways. Plotting the response of the SWC as a function of run number can not resolve the small variations from the simulations and do not provide indications of a significant evolution of the response as a function of run number. Post-irradiation drift curves were examined for some 'normal' situations used in routine calorimetry measurements and for some 'extreme' situations. For a large number of previously recorded measurements, the simulated and measured post-irradiation drift curves show a good agreement, after normalization of the data in a time interval short after the end of the irradiation. For glass vessels with a small diameter and/or a thick wall, the post-irradiation drift curves do qualitatively show the same features as the simulated curves, but the quantitative agreement is worse. The simulations overpredict the effects observed in the experiments. Regarding the effect of the vessel, a possible reason could be that one of the data for the heat properties of glass is not consistent with the glass used in the experiments. The post-irradiation drift curves for different field sizes agree reasonably with the simulated curves. Also for the SWC response as a function of the vessel wall thickness and the field size, an overprediction of the results by the simulations shows up. For the effect of the field size, this might be partially caused by the simplifying assumption for the lateral profile.

REFERENCES

[1] S.R. Domen, "A Sealed Water Calorimeter for Measuring Absorbed Dose," *J. Res. Natl. Inst. Stand. Technol.*, **99**, 121-141, 1994.

[2] A. J. Williams and K.E. Rosser, "A status report on the NPL water calorimeter," *NPL report* CIRM(EXT)22, NPL, Teddington, UK, 1998.

[3] J. Seuntjens and H. Palmans, "Correction factors and performance of a 4º C sealed water calorimeter," *Phys. Med. Biol.*, **44**, 627-646, 1999.

[4] C.K Ross, J.P. Seuntjens, N.V. Klassen and K. Shortt, "The NRC sealed water calorimeter: correction factors and performance," *These proceedings*, 2000.

[5] A. Krauss and M. Roos, "The role of water calorimetry in therapy dosimetry at the PTB," *These proceedings*, 2000.

[6] J. Medin, J.P. Seuntjens, N.V. Klassen, C.K Ross and G. Stucki, "The OFMET sealed water calorimeter," *These proceedings*, 2000.

[7] K.P. Gall, "A status report on the NIST water calorimeter," *These proceedings*, 2000.

[8] M. Pieksma, E. Van Dijk, A.H.L. Aalbers, "The NMi absorbed dose to water calorimeter (A status report)," *These proceedings*, 2000.

[9] A.S. Guerra, R.F. Laitano, P. Fattibene, E. Gargioni and S. Onori, "The ENEA water calorimeter: characteristics and preliminary results," *These proceedings*, 2000.

[10] J. Daures, A. Ostrowsky, P. Gross and J.P. Jeannot, "Calorimetry for absorbed-dose measurements at BNM-LPRI," *These proceedings*, 2000.

[11] H. Palmans and J. Seuntjens, "Construction, Correction Factors and Relative Heat Defect of a High Purity, 4 ˚C Water Calorimeter for Absorbed Dose Determinations in High Energy Photon Beams," *Proceedings of the NPL Calorimetry Workshop*, 12-14 October 1994, NPL, Teddington, UK, 1995.

[12] J.P. Seuntjens, C.K. Ross, N.V. Klassen and K.R. Shortt, "A status report on the NRC sealed water calorimeter," *National Research Council of Canada Report* PIRS-*584* (Ottawa: NRC), 1997.

[13] A. Krauss and M. Roos, "Heat conduction, convection and radiolysis of the H_2/O_2 system in the water absorbed dose calorimeter," *Thermochim. Acta*, **310**, 53-60, 1998.

[14] A. Krauss and M. Roos, "Heat transport by material-dependent heating during absorption of radiation in the water absorbed dose calorimeter," *Thermochim. Acta*, **337**, 45-49, 1999.

[15] C.K. Ross, N.V. Klassen, K.R. Shortt and G.D. Smith, "A direct comparison of water calorimetry and Fricke dosimetry," *Phys. Med. Biol.*, **34**, 23-42, 1989.

[16] D.R. Croft and D.G. Lilley, Heat transfer calculations using finite difference equations, London: Applied Science Publishers Ltd., 1977

[17] H. Palmans, W. Mondelaers and H. Thierens, "Absorbed dose beam quality correction factors k_Q for the NE2571 chamber in a 5 MV and a 10 MV photon beam," *Phys. Med. Biol.*, **44**, 647-663, 1999.

[18] H. Palmans, J. Seuntjens, F. Verhaegen, J.-M. Denis, S. Vynckier and H. Thierens, "Water calorimetry and ionization chamber dosimetry in an 85-MeV clinical proton beam," *Med. Phys.*, **23** , 643-650, 1996.

[19] J.P. Seuntjens, I. Kawrakow and C.K Ross, "Revisiting convective motion in stagnant water calorimeters operated at room temperature," *These proceedings*, 2000.

QUESTIONS AND ANSWERS

Achim krauss: have you also calculated the factor which was the irradiation of the phantom walls?

Hugo Palmans: No.

Achim Krauss: If you calculate irradiations of 300 seconds and the post-irradiation period of time is also 300 seconds, I guess that could also have an influence?

Hugo Palmans: Yes, I am aware of the fact that this could have an influence. Something that could also have an influence, but which is also very difficult to investigate, is that we always try to start a measurement when there is a slightly increasing temperature drift. With a slightly increasing drift we have found that we can do more successive runs. But a slightly increasing drift means that there must be heat coming from somewhere so that there must be slight gradients present before we start the measurements and of course that could also influence the results.

--

Carl Ross: At Cobalt you are struggling a little bit with signal to noise. What are the options for going to quite high dose rates?

Hugo Palmans: Well, the first option is to replace our source, because it is only 0.3 Gy/min at the measuring point. Another option is to measure in a linear accelerator. That is possible but the stability worse than in Cobalt so I would need to do a lot more measurements.

Carl Ross: But you might get away with only one run.

Hugo Palmans: Well, I don't think that we would get that high a dose rate. We can reach dose rates of 5 Gy a minute. That is possible. I have done a lot of measurements in the linear accelerator but I couldn't until now evaluate all the post irradiation drift curves for those measurements but certainly intend to do that.

--

Andrew Williams: Did you use uniform energy deposition for your simulations?

Hugo Palmans: Yes. We performed separate one dimensional simulations to deal with the effects due to depth dose distributions and assumed that all the corrections are additive. But these corrections are for most measurements and for most situations very small.

The NMi Absorbed-Dose-to-Water Calorimeter (A Status Report)

M. Pieksma*, E. van Dijk and A.H.L. Aalbers

NMi Van Swinden Laboratorium, Department of Temperature and Radiation

PO Box 80000, 3508 TA Utrecht, The Netherlands

Abstract

The NMi Van Swinden Laboratorium strives to realise a primary standard for absorbed dose to water. To this aim, a prototype water calorimeter has been constructed, its main characteristics resembling those of the well-known sealed-water type, but also featuring several differences, most notably with respect to compactness and transportability. The NMi absorbed-dose-to-water standard, which is presently derived from the absorbed dose to graphite, will eventually be replaced by this water calorimeter. A brief overview will be given of the NMi's calorimetric facilities. Improvements on the water calorimeter that are presently being implemented will be indicated. In particular, the approach to control such critical effects as convection and the heat defect is addressed. Future applications of the NMi water calorimeter are briefly mentioned.

I. INTRODUCTION

The Department of Temperature and Radiation, Section Ionizing Radiation of the NMi (Nederlands Meetinstituut) develops and maintains primary dosimetric standards in the Netherlands, including those that are based on calorimetric techniques. The history of calorimetry at the NMi goes back to 1977, when a heat-loss-compensated graphite calorimeter, similar to Domen's original design [1] was brought into operation at the National Institute for Public Health (RIV, later RIVM). The core and core thermistors were replaced in 1985, and up to this date this second version of the graphite calorimeter is still in use. Eventually, in 1991 all measurement standards and calibration facilities were transferred from the RIVM to the NMi.

The facility for absorbed-dose standards at the NMi is centered around a ^{60}Co source (Siemens Gammatron 3), with a strength of about 50 TBq (on January 1st 2000). It is used for both customer calibration services and comparisons with foreign institutes to ensure international traceability. The NMi graphite calorimeter is transportable, allowing direct comparisons as well as absorbed-dose measurements in clinical beams [2].

One of the most important applications of calorimetry lies within the field of radiotherapy, where high precision is demanded regarding the energy delivered to irradiated tumors during curative and palliative treatments. In this case, the quantity of prime interest is absorbed dose to water. To fulfill the demand for absorbed-dose-to-water calibrations, an absorbed-dose-to-water standard was developed at the NMi. This was accomplished by deriving the absorbed dose to water from the absorbed dose to graphite, using a conversion procedure that relies on the so-called photon-fluence scaling theorem of O'Connor [3]. A calibration service based on this standard became fully operational in 1994 [4]. The effort of the NMi to move towards a primary standard for absorbed dose to water, based on water calorimetry, is presented here.

This paper is organized as follows. Several aspects of the present NMi absorbed-dose-to-water standard, including the aforementioned conversion procedure, will be discussed in Section 2. The status and performance of the NMi prototype water calorimeter is presented in Section 3, while in Section 4 improvements are highlighted that are presently being implemented. Finally, we summarize our findings and point out important future applications of the NMi water calorimeter.

II. NMI ABSORBED-DOSE-TO-WATER STANDARD

Absorbed-dose rates at the NMi for both graphite and water are determined under reference conditions, namely in a (vertical) ^{60}Co beam with a radiation field size of 10x10 cm^2 at the point of measurement and with its decay being corrected with respect to January 1st 1995, a SDD (source detector distance) of 1 m (in vacuum, i.e. the dose rates are corrected for the air column), and a measurement depth of 5 g.cm^{-2}. The absorbed dose to graphite is measured with the NMi graphite calorimeter [5]. The conversion of this quantity to the absorbed dose in water is based upon the photon-fluence scaling theorem (see [3], [6], [7] and [8]), which states that if the Compton process dominates, then the ratio of scattered to primary photons in two different phantoms is equal if all distances are scaled in inverse proportion to the electron densities. If the conditions hold for which the theorem is valid, the ratio of absorbed doses at corresponding points in the water and graphite phantoms is given by

$$\frac{D_{\mathrm{w}}}{D_{\mathrm{c}}} = \left(\frac{n_{\mathrm{e,w}}}{n_{\mathrm{e,c}}} \right)^2 \frac{(\overline{\mu}_{\mathrm{en}} / \rho)_{\mathrm{w}}}{(\overline{\mu}_{\mathrm{en}} / \rho)_{\mathrm{c}}} \frac{\beta_{\mathrm{w}}}{\beta_{\mathrm{c}}} \qquad (1)$$

where the subscripts w and c refer to water and graphite, respectively, n_{e} is the electron density, $\overline{\mu}_{\mathrm{en}} / \rho$ is the mean mass energy-absorption coefficient (averaged over the photon energy-fluence spectrum of the ^{60}Co source), and β is the quotient of absorbed dose and collision kerma. In practice, the requirements for scaling are not completely fulfilled at the NMi. First, a reference depth of 5 g.cm^{-2} is used for graphite. However, a measurement depth of 5 g.cm^{-2} in water corresponds to a properly scaled measurement depth in graphite of 5.556 g.cm^{-2}. Consequently, a correction of 1.606 % is applied, based on the measured dose-depth profile of graphite. Second, D_{w} is determined at the reference distance of 1 m instead of the scaled distance, which is 1.67 m. Therefore, the squared term in

* Corresponding author, e-mail address: mpieksma@nmi.nl

Equation (1) is replaced by unity, and a correction is made for the difference in phantom scatter, due to the different field sizes at these different distances. Measurements of the effect of beam size on the phantom scatter factor in water yield a correction of 4.18 %. The estimated numerical value of β_w/β_c is 1.0022.

In table 1 an historical overview is given of the NMi absorbed-dose rates to graphite and water. The average absorbed dose to water rate is 7.476 mGy.s^{-1} ± 0.34 % (2σ standard uncertainty). This latter uncertainty is small compared to the 0.80 % NMi total uncertainty budget, indicating a good reproducibility, which in turn means that statistical uncertainties are well controlled and that systematic errors dominate the accuracy of the results.

Table 1.
History of the NMi absorbed-dose-to-graphite and absorbed-dose-to-water rates. Quoted uncertainties are at the 2σ level. The dose rates are with respect to January 1st 1995.

Date	$\dot{D}_{c,ref}$ (mGy.s^{-1})	$\dot{D}_{w,ref}$ (mGy.s^{-1})
August 1995	7.114 ± 0.034	7.495 ± 0.062
October 1996	7.094 ± 0.034	7.474 ± 0.062
September 1997	7.087 ± 0.034	7.466 ± 0.062
October 1998	7.091 ± 0.034	7.471 ± 0.062

An official key comparison of the absorbed-dose-to-water rates at the NMi and the BIPM was carried out very recently [9]. Three NE2611A cavity ionization chambers were used as transfer standards for this indirect comparison. Measured calibration factors were corrected to standard environmental conditions of a temperature of 22 °C, a pressure of 101.325 kPa, and a humidity of 50 %. A difference of 0.36 % in the calibration factors was observed ($N_{w,NMi}/N_{w,BIPM}$ = 0.9964), which was well within the combined 2σ uncertainty of the comparison of 0.92 %.

III. Water Calorimetry at the NMi

The main reason to build a water calorimeter is to have a direct means to determine the absorbed dose to water. Also, since a conversion step is no longer needed, one may expect that an improved accuracy should in principle be possible.[1] Another reason is that in the near future the NCS (Netherlands Committee for Radiation Dosimetry) will adjust its protocols for dosimetry of high-energy photon beams [12] by replacing the quantity air kerma by the quantity absorbed dose. The new calorimeter ensures that the NMi is in accordance with these new Dutch protocols, as well as with the new protocols of the AAPM [13] and the upcoming protocols of the IAEA [14]. Furthermore, the water calorimeter opens up applications to a broader range of radiation sources and beam qualities than before. These include all varieties of high-energy photon beams, but also high-energy electron and proton beams.

[1] This has yet to be demonstrated. Typical 2σ total uncertainties for recently built water calorimeters range between 1.2 % for the NRC calorimeter [10] and about 2 % for the NPL calorimeter [11],while these uncertainties for graphite calorimeters are generally below 1 %.

The feasibility of a water calorimeter was first demonstrated by Domen [15], [16]. The NMi design is similar to that of the Domen [17] sealed-water type calorimeter (see also Seuntjens and Palmans [18]), however, with several modifications. The NMi water calorimeter is schematically depicted in Figure 1, demonstrating the main modification, which is the compact housing. No air is circulated between the inner and outer polystyrene boxes, rather the amount of space between these two boxes is minimized, enclosing only a compact copper heat exchange system. This thermostat is computer controlled. The core of the system consists of a High Purity Water (HPW) cell, filled with ultra pure, gas-saturated water (see below), and equipped with two thermal bead resistors. Two sets are available, which have nominal resistances of 20 kΩ at either 4 °C or 20 °C. The signals from these thermistor probes are measured using AC Wheatstone bridges, operating in the range of 10-30 Hz, which are connected with EG&G 5209 Lock-in amplifiers. The water phantom has dimensions 30x30x30 cm^3 and windows that can give access to both vertical and horizontal beams. Not shown in Figure 1 is a magnetic stirrer located at the bottom of the water phantom, which can be used for reducing temperature drifts. Finally, the whole system is transportable, which allows, for example, measurements in clinical beams. In the near future, a transportable beam-monitoring system will be added to the setup.

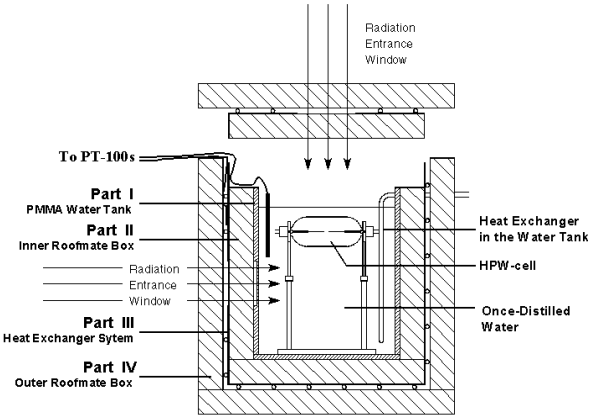

Figure 1: The NMi water calorimeter. In the prototype version, the inner PMMA water tank and the horizontal window were absent, and the HPW cell was equipped with one thermistor only.

Compared to graphite, water has an advantage in the sense that the heat flow by conduction is low, i.e. the thermal diffusivity is small [19], so thermal insulation is not critical. Disadvantages, however, are the large heat capacity, the sensitivity to radiation-induced chemical reactions (called the heat defect), and convection [20]. The heat capacity of water is 4.2 J.kg^{-1}.K^{-1}, which is six times larger than that of graphite. This unavoidably implies that stronger radiation sources are needed to obtain signal rates comparable to those of a graphite calorimeter. The heat flow by convective motion can be minimized by operating the water calorimeter at 4 °C, where water has a maximum density, so, since dρ/dT = 0, the sensitivity to temperature gradients is minimal. In addition,

temperature drifts should be kept as low as possible by proper thermal insulation, and, even more importantly, these drifts should be linear. This can be achieved, as Figure 2 demonstrates.

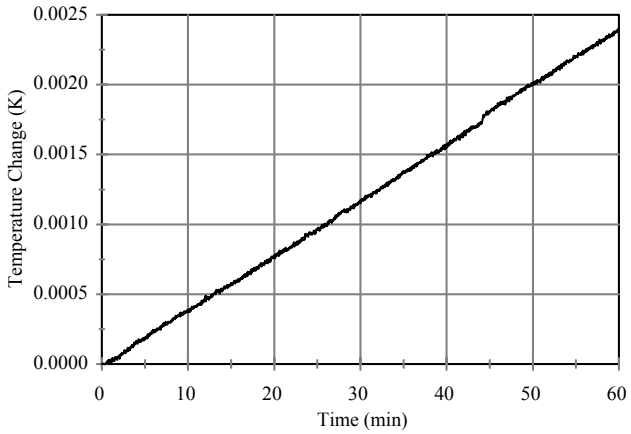

Figure 2: Temperature drift inside the HPW cell during one hour at a working temperature of 4 ˚C.

The heat defect is connected with the water chemistry. Endothermic and/or exothermic chemical reactions induced by irradiation may affect the change in water temperature. The NMi has opted for the following measures to tackle this issue. First, the heat defect depends strongly on impurities present in the water. These are almost completely removed by using water from a commercial water purification system, the Millipore Milli-Q Gradient equipped with a A10 TOC (Total Organic Components) monitor and a Elix 3 prefiltering module. The water quality is expressed in resistivity, which is measured to be 18.2 MΩ.cm at 25 ºC, and in the TOC value, for which the A10 monitor gives a typical reading of 3 ppb. Second, even for theoretically pure water, there is a non-zero heat defect [20]. The solution to this problem is to saturate the water with gases or gas mixtures and to pre-irradiate the water system to achieve chemical equilibrium. In practice, bubbling the water with H_2 and Ar gases has demonstrated the feasibility of a net zero heat defect [10]. Such aqueous systems may be sensitive to unavoidable impurities like O_2. A H_2/O_2 amount of substance gas mixture of 43/57 is probably more robust [21], and it has a known exothermic heat defect of (2.3 ± 0.5) % [10], [20]. These different aqueous systems will be investigated too at the NMi for achieving optimal control of the heat defect.

A prototype water calorimeter was constructed and tested in the NMi ^{60}Co source in 1997-1998, with initial testing focusing on optimization of the electronic circuitry and the behaviour and stability of the phantom temperature. This prototype calorimeter was identical to the calorimeter shown in figure 1, except that only one thermistor probe was used and the inner water tank was absent.

The initial tests [22] showed that temperature drifts inside the water phantom can be controlled to a level of about 0.5 $\mu K.s^{-1}$. Temperature drifts at the point of measurement inside the HPW cell were measured at 4 ºC and 20 ºC. The results are shown in Figures 2 and 3, respectively. Although the absolute drift is smaller at 20 ºC, the condition of linearity is clearly much better fulfilled at 4 ºC. The test measurements also pointed out that in order to have sufficient signal for a period of 5 years the NMi ^{60}Co source needs to be upgraded to a strength of 350 TBq. Scatter of radiation from the window in the copper plate of the heat exchanger was found to increase the absorbed-dose rate at the point of measurement by 0.2 %.

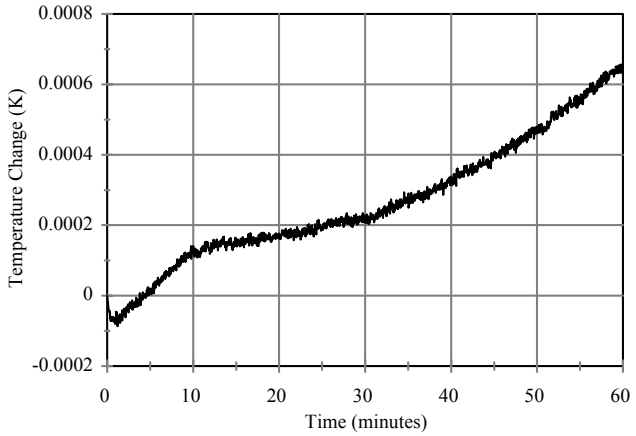

Figure 3: Temperature drift inside the HPW cell during one hour at a working temperature of 20 ˚C. Before the measurement the water was stirred for 20 seconds.

IV. NMi Improved Water Calorimeter

The definite design of the NMi water calorimeter involves improving the prototype in several aspects. First, the insulation of the thermostat will be optimized, thereby further suppressing temperature gradients. Second, a stirrer in the phantom water will help to reduce temperature drifts. Third, the lid construction will be revised to reduce the beam attenuation, which for the prototype calorimeter amounts to 2 %. Fourth and fifth, as was mentioned in the previous section, ultra pure, gas-saturated water will be used to control the heat defect, and operating the calorimeter at 4 ˚C will virtually eliminate convective motion. To this aim, a filling station has been designed and will be constructed. Last, the HPW cell will be equipped with two thermistor probes for increased sensitivity and accuracy, and a calibration facility for these probes will be realized.

Testing of the improved NMi water calorimeter includes characterizing and optimizing the performance of the thermostat and the thermistor probes, and quantifying the effects of convection and saturation of the water with different gases. Next, the water calorimeter will be compared with the NMi graphite calorimeter. After that, a comparison in the clinical accelerator beam available at the BNM-LPRI will be conducted. This will serve to optimize the calorimeter in high-energy photon beams with different beam qualities. Finally, a key comparison between the NMi and the BIPM is planned to establish the NMi absorbed-dose-to-water standard in the international dosimetric community.

V. Summary

The NMi possesses a state-of-the-art graphite calorimeter that can be used in conjunction with the photon-fluence scaling theorem to yield an absorbed-dose-to-water standard. In order to

remain in accordance with national and international protocols for high-energy photon dosimetry, the NMi is striving to replace this standard by a sealed-water calorimeter. To achieve this goal, a prototype water calorimeter has been constructed and tested with positive results.

An improved, transportable water calorimeter is presently under construction. The NMi ^{60}Co source will be upgraded to improve the signal to noise ratio of this apparatus. The new water calorimeter will be used in clinical high-energy photon and electron beams. The clinical absorbed-dose program of the NMi includes the determination of absorbed-dose-to-water beam-quality correction factors, k_Q, of the different types of ionization chambers used in the Netherlands.

A key comparison with the BIPM is required to ensure international traceability. This will establish a new NMi calibration facility for absorbed dose to water.

REFERENCES

[1] Domen S R and Lamperti P J 1974 A heat-loss-compensated calorimeter: theory, design and performance *J. Res. Natl. Inst. Stand. Technol. - A. Phys. Chem.* **78A** 595-610

[2] Hofmeester G H 1981 Calorimetric determination of absorbed dose in water for 1-25 MeV x-rays *Int. Symposium on Biomedical dosimetry: Physical Aspects, Instrumentation, Calibration (Proc. Int. Conf. Paris, 1980)* IAEA-SM-249/56 (Vienna: IAEA) pp 235-58

[3] O'Connor J E 1957 The variation of scattered x-rays with density in an irradiated body *Phys. Med. Biol.* **1** 352-69

[4] Grimbergen T W M and van Dijk E 1994 Absorbed dose measurements at the Netherlands Measurement Institute *Int. Symposium on Measurement Assurance in Dosimetry (Proc. Int. Conf. Vienna, 1993)* IAEA-SM-330/66 (Vienna: IAEA) pp 35-44

[5] van Dijk E and Aalbers A H L 1986 The graphite calorimeter: standard for determining absorbed dose - Measuring temperature variations in a calorimeter (in Dutch) *RIVM Internal Report* 842038003

[6] O'Conner J E 1984 The density scaling theorem applied to lateral electronic equilibrium *Med. Phys.* **11** 678-80

[7] Pruitt J S and Loevinger R 1982 The photon-fluence scaling theorem for Compton-scattered radiation *Med. Phys.* **9** 176-9

[8] Burns J E 1994 Absorbed-dose calibrations in high-energy photon beams at the National Physical Laboratory: conversion procedure *Phys. Med. Biol.* **39** 1555-75

[9] Pieksma M, van Dijk E, Burns D T and Allisy-Roberts P J 2000 Comparison of the standards for absorbed dose to water standards of the NMi and the BIPM for ^{60}Co gamma rays, *to be published*

[10] Seuntjens J P, Ross C K, Klassen N V and Shortt K R 1997 A status report on the NRC sealed water calorimeter *NRC Internal Report* PIRS-0584

[11] Williams A J and Rosser K E 1998 A status report on the NPL water calorimeter *NPL Report* CIRM 22

[12] Mijnheer B J, Aalbers A H L, van Gasteren J J M, Visser A G and Wittkämper F W 1986 Code of practice for the dosimetry of high-energy photon beams *NCS Report* 2

[13] Almond P R, Biggs P J, Coursey B M, Hanson W F, Huq M S, Nath R and Rogers D W O 1999 AAPM's TG-51 protocol for clinical reference dosimetry of high-energy photon and electron beams *Med. Phys.* **26** 1847-70

[14] Andreo P, Burns D T, Hohlfeld K, Huq M S, Kanai T, Laitano F, Smyth V G and Vynckier S 1999 Absorbed dose determination in external beam radiotherapy: An international code of practice for dosimetry based on standards of absorbed dose to water, *to be published by the IAEA* Draft V.6

[15] Domen S R 1980 Absorbed dose water calorimeter *Med. Phys.* **7** 157-9

[16] Domen S R 1982 An absorbed dose water calorimeter: theory, design, and performance *J. Res. Natl. Bur. Stand.* **87** 211-35

[17] DOMEN S R 1994 A sealed water calorimeter for measuring absorbed dose *J. Res. Natl. Inst. Stand. Technol.* **99** 121-41

[18] Seuntjens J and Palmans H 1999 Correction factors and performance of a 4 ^{o}C sealed water calorimeter *Phys. Med. Biol.* **44** 627-46

[19] Ross C K and Klassen N V 1996 Water calorimetry for radiation dosimetry *Phys. Med. Biol.* **41** 1-29

[20] Klassen N V and Ross C K 1997 Water calorimetry: the heat defect *J. Res. Natl. Inst. Stand. Technol.* **102**, 63-74

[21] Ross C K 1999 *private communication*

[22] de Prez L A 1998 Design and construction of a prototype water calorimeter *NMi Internal Report*

QUESTIONS AND ANSWERS

Malcolm McEwen: How big is the calorimeter - you said that it is compact?

Marc Pieksma: It is rather compact: the phantom is 30x30x30 and you have to add maybe 15 to 20 cm on all sides. You can almost carry it. At first I thought you could call it a portable machine but I think that "transportable" is a better word. It is almost portable, maybe with two men.

Jan Seuntjens: How long does it take to bring it down to 4 ˚C? Is there actually tubing going into the water?

Marc Pieksma: There is tubing going into the water to speed up this process.

Jan Seuntjens: You can switch it into the loop then?

Marc Pieksma: Yes, I don't know exactly how long it takes but I think if you don't do it, it could be in the order of days almost but now it is the order of one or two hours, something like that.

Jan Seuntjens: And you stabilise the water that goes through the tubes?

Marc Pieksma: Yes. And there are additional PT100 sensors at different places.

Jan Seuntjens: In the water?

Marc Pieksma: In the water and also close to the tubing.

Jan Seuntjens: And did you check the gradients in the water?

Marc Pieksma: One of Tom Grimbergen's students has worked quite a bit on that, especially temperature stabilisation. He performed all kinds of heat flow calculations and measurements: a lot of work has been done on that. One of the things that can still be optimised is, for example, if you look at all the different sides of the calorimeter, all the tubes have to be connected to the next side, but that means of course tubes going outside and so we want to make it even more compact and make sure that nothing is sticking out and being affected by room temperature. That will also bring down the gradients a bit more I believe.

--

Jan Seuntjens: In one of your slides you mentioned a whole bunch of beams like photon beams and electrons and I saw as low as 3 MeV electron beams. How do you intend to handle heat losses?

Marc Pieksma: Actually I took those numbers from the IAEA protocols where they define high and low energy beams and so that is just a typical range and we will have to see if we go to different clinical situations what the machines will actually provide so we are not really stuck to those numbers yet.

Tony Aalbers: To be frank, I doubt a little bit if we are going to use this calorimeter for all the applications so maybe we have to look at other versions.

Marc Pieksma: Obviously it will take some work to establish, but sometime in the future we should apply it to high energy photon and electron beams in clinical situations. Water calorimetry you know is of course perfectly suited for that.

Jan Seuntjens: Yes, except for low energy electrons it gets tricky.

Marc Pieksma: How low would that be?

Jan Seuntjens: 12 MeV is already very low in terms of heat loss. If you go lower then the extrapolations become [difficult]

Marc Pieksma: Right, I have not performed any measurements yet in a clinical beam so I have to find out.

The NRC Sealed Water Calorimeter: Correction Factors and Performance

C.K. Ross, J.P. Seuntjens*, N.V. Klassen and K.R. Shortt
Ionizing Radiation Standards, Institute for National Measurement Standards, National Research Council
Ottawa, Ontario K1A 0R6 Canada

Abstract

The NRC sealed water calorimeter is based on a design first proposed by Domen at the National Institute of Standards and Technology. Thermistor probes are used to measure the temperature increase at a point in a large water phantom due to energy absorbed from the radiation field. A sealed glass vessel is used to control the water quality near the measuring point. To eliminate convective heat transfer, the calorimeter is operated at 4°C. Apart from correction factors, the absorbed dose to water is obtained from the measured temperature change multiplied by the known specific heat of water. However, there are a number of corrections and perturbations which must be considered. Most of these factors are small and can be estimated accurately. The largest uncertainty (0.3%) is contributed by the heat defect, partly because it depends on knowledge of the radiation chemistry of water, and partly because of the difficulty of preparing high purity aqueous systems. The NRC calorimeter has been used to establish the absorbed dose in a ^{60}Co beam and several high energy x-ray beams with an estimated standard uncertainty of about 0.5%. The performance of the calorimeter, as well as some of the implications of the results obtained, will be reviewed.

I. INTRODUCTION

The absorbed dose to water under reference conditions is the starting point for calculating the absorbed dose to the patient during radiation therapy. Usually, the absorbed dose to water is established using an ion chamber for which an absorbed dose calibration factor has been established. One way of establishing the chamber calibration factor is via cavity theory combined with a ^{60}Co air kerma calibration factor [1], [2]. A more direct approach is to calibrate the chamber against an absolute standard for the absorbed dose to water [3].

The most common way of establishing a standard for absorbed dose is via calorimetry, and several graphite calorimeters have been built for this purpose [4], [5], [6]. Although the graphite calorimeter is itself an excellent device, it gives the absorbed dose to graphite, not to water. Thus, a conversion procedure is necessary in order to obtain the dose to water. In an effort to circumvent this problem, Domen [7] showed that it was possible to directly measure the radiation-induced temperature rise in a large vessel of stagnant water. Unfortunately, the absorbed dose measured in this way was 3 to 4% higher than expected, and later work showed that the most likely reason for the discrepancy was an unexpected heat defect due to impurities in the water (for a review of the literature, see [8]). More recent work indicates that about 1% of the discrepancy may have been due to convective heat transfer (see the paper by Seuntjens *et al* in these Proceedings).

Domen [9] then modified the design of his calorimeter by introducing a small sealed glass vessel which contained high purity water. Extensive measurements with this arrangement using ^{60}Co γ-rays gave results which were in good agreement with the absorbed dose obtained using graphite calorimetry. Seuntjens *et al* [10], [11] further modified the design to permit the calorimeter to be operated at 4°C, thus suppressing the effects of convection. Apart from modest refinements, the NRC sealed water calorimeter follows the design developed by Seuntjens *et al*.

Early work on water calorimetry at NRC was based on a stirred water calorimeter [12]. This design was well suited for measuring the relative heat defect of various aqueous solutions and, with further refinements, the calorimeter was used to measure εG for the Fricke dosimeter [13]. However, an accurate determination of the effect of the heat transferred from material close to, and in contact with, the water proved difficult and contributed significantly to the overall uncertainty. We concluded that a sealed water calorimeter would lead to a smaller uncertainty on the absorbed dose to water, would be more convenient for establishing the dose at different beam qualities and would be better suited for measurements in electron beams.

This report describes the main characteristics of the NRC sealed water calorimeter and provides details of the various correction factors required for its use. The calorimeter has been used to establish the dose for ^{60}Co γ-rays and high energy x-ray beams, and some of the implications of these measurements will be discussed.

II. THE NRC SEALED WATER CALORIMETER

A. Overview

The main elements of the calorimeter are shown schematically in Figure 1. Note that it is intended for use in radiation beams that are directed horizontally. The water is

*Present address:
Medical Physics Unit, McGill University, Montreal General Hospital, Montreal, Quebec, Canada, H3G 1A4.
E-mail: jseuntjens@medphys.mcgill.ca.

held in a Lucite tank, 30 cm on each side. The exterior walls of the tank are insulated with 5 cm thick Styrofoam. A magnetic stirrer for agitating the water is built into the bottom of the tank. The lid on the tank contains several holes through which calibrated platinum resistor probes are inserted to measure the water temperature. The lid also ensures a motion-free air space above the water surface. The window of the tank through which the radiation field enters is machined down to 3 mm over an area of 12 cm by 12 cm. The window is thermally isolated with a removable, 5 cm thick Styrofoam plate. The calorimeter phantom is enclosed in an insulated wooden box, 85 cm on each side, in which the temperature is stabilized using fans and a heat exchanger. The cooling fluid can also be made to pass through a heat exchanger in the water tank so as to accelerate the process of changing the operating temperature of the water in the calorimeter. The calorimeter is designed for operation at any temperature from 0ºC to 25ºC. It typically takes 3 to 4 hours to bring the temperature to 4ºC when starting from room temperature. The bath controlling the temperature of the liquid in the heat exchangers is stable to ± 0.1ºC. An additional calibrated platinum resistor probe monitors the temperature of the air circulating around the calorimeter. There are temperature variations of up to 1ºC in the air space around the calorimeter, but the temperature at a given location is stable to a few millidegrees.

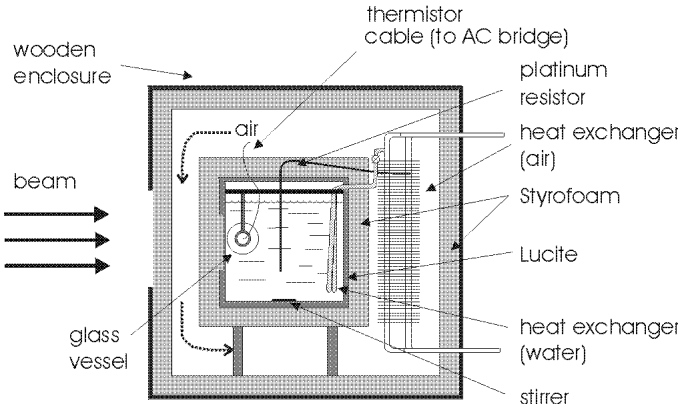

Figure 1: Side view of the sealed water calorimeter. The drawing is not to scale, but the sides of the outer box are approximately 85 cm long. The principal elements of the calorimeter are labelled on the drawing. Note that fluid is only allowed to flow through the heat exchanger in the water when a significant change in operating temperature is required.

B. Glass Detection Vessel

The temperature increase due to irradiation is measured in the centre of a cylindrical glass vessel which is designed to isolate a small volume of high purity water from the water in the rest of the phantom. A typical detection vessel is shown in Figure 2. It consists of a central cylindrical portion, about 75 mm long, which is attached to conical end pieces. The overall length of the assembly is about 14 cm. Threaded fittings on the end pieces hold the thermistor probes in place. The vessel is mounted in the water tank on an adjustable slide so that its position along the beam axis can be varied.

The cylindrical portion of the first vessel we used was formed using glass blowing techniques. This approach led to considerable variation in the wall thickness (see figure 3), and the vessel was not perfectly round. Variation in the wall thickness leads to uncertainties in the wall correction factors, and lack of roundness makes it difficult to establish the probe position within the vessel. This vessel is referred to as #1, and it has an outside diameter of approximately 67 mm.

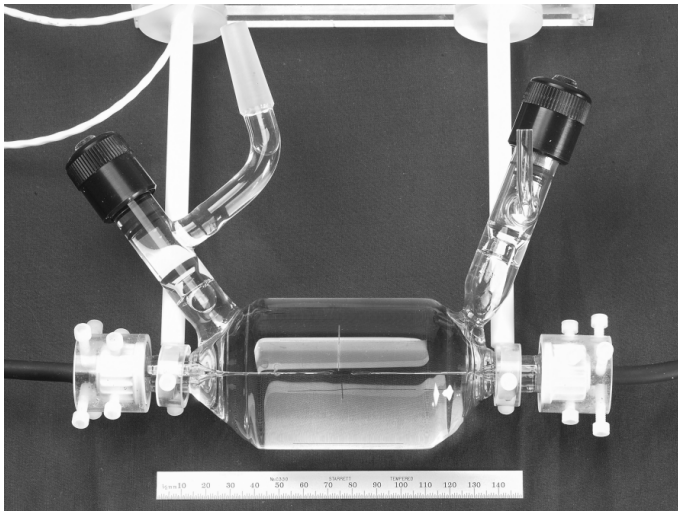

Figure 2 : Glass detection vessel No. 3, with the thermistor probes aligned in the centre. The thick white line in the upper left of the photograph is part of the thermistor signal cable after it has emerged from the waterproof tubing.

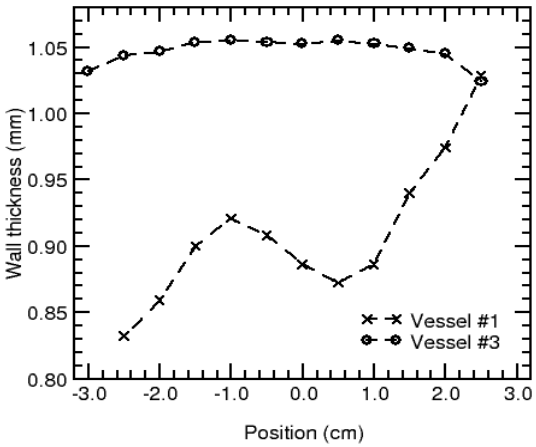

Figure 3: Variation of the vessel wall thickness along the length of the cylindrical portion. The measurements were done using a liquid displacement technique, and thus represent the average wall thickness at that position. Vessel #1 was formed using glass blowing techniques, while the cylindrical portion of vessel #3 was formed by grinding glass tubing to the required dimensions.

Later vessels have been formed by first grinding glass tubing to a wall thickness of 1 mm. Because precision grinding

techniques are used, similar to those used for making lenses, the wall thickness is uniform and the vessels closely circular. The conical end pieces are attached to the central cylindrical section using glass blowing techniques. The first vessel constructed in this way was labelled #3, and it has an outside diameter of 61.53 mm. Its wall thickness as a function of position is shown in Figure 3.

Before the ends were attached to the cylindrical section, an indexing machine was used to mark the circumference at 90º intervals. Ceramic decal lines were placed on each mark and fixed in place by annealing the cylinders at 560ºC. These lines have a width of 0.4 mm and are used for aligning the probes within the vessel, and the vessel within the phantom. Originally, the appropriate positioning of the probe ends with respect to lines on the outside of the vessel was done using a telescope. However, we have found that probe alignment with respect to the decals can be done adequately by eye, certainly within ± 0.2 mm.

A glass valve is attached to either end of the vessel to allow it to be filled, drained and bubbled with various gases. Upon sealing off the vessel, care is taken to be sure a small gas bubble is left behind. This bubble allows the water to expand and contract between 4ºC and 22ºC without breaking the vessel.

When preparing for measurements, the vessel is first filled with high purity water, and then bubbled for one to two hours with H_2, H_2 and O_2, N_2 or Ar gases, depending on the aqueous system to be used. Then the probe position is adjusted and the vessel is suspended in the water phantom. Calorimetric measurements can be started typically three hours later if the water in the tank is at operating temperature and the bubbling is done at room temperature.

C. Thermistor Probes

The glass envelope for each thermistor temperature probe is constructed from Pyrex tubing having a diameter of 8 mm and a wall thickness of 1 mm. The tubing is heated and pulled down to an outside diameter of 0.5 to 0.6 mm over a length of 4 cm. The inside diameter is checked using 0.3 mm diameter wire. Probes of acceptable dimensions are then flame-sealed on the small end and tested for leaks using a helium leak detector. We estimate the thickness of the glass wall at the thermistor bead to be 0.06 mm to 0.11 mm. The 0.03 mm diameter wires of the Thermometrics thermistors (0.25 mm in diameter) are soldered to 0.1 mm diameter copper extension wires, and one wire of the pair is inserted into 0.2 mm diameter microtubing to avoid electrical shorts. The bead and lead assembly is then slid into the glass envelope. Using a piece of microtubing, UV-curable adhesive is injected into the end of the probe to glue the thermistor bead to the glass. A Delrin rod is fitted into the large end of the glass probe to act as a strain relief for the screened cable to which the 0.1 mm copper extension wires are soldered. Waterproofing is achieved by passing the signal cable through a latex rubber tube which is stretched over the end of the glass tubing to form a water-tight seal. The latex tube is sufficiently long that the open end is outside the water phantom. The details of the probe construction are shown in Figure 4.

Before use, the thermistor probes must be calibrated. Our probes are calibrated against platinum resistance probes (RTDs) which in turn are calibrated against NRC temperature standards. Details of the calibration procedure, along with typical calibration data, are described in a separate paper by Medin *et al* in these Proceedings.

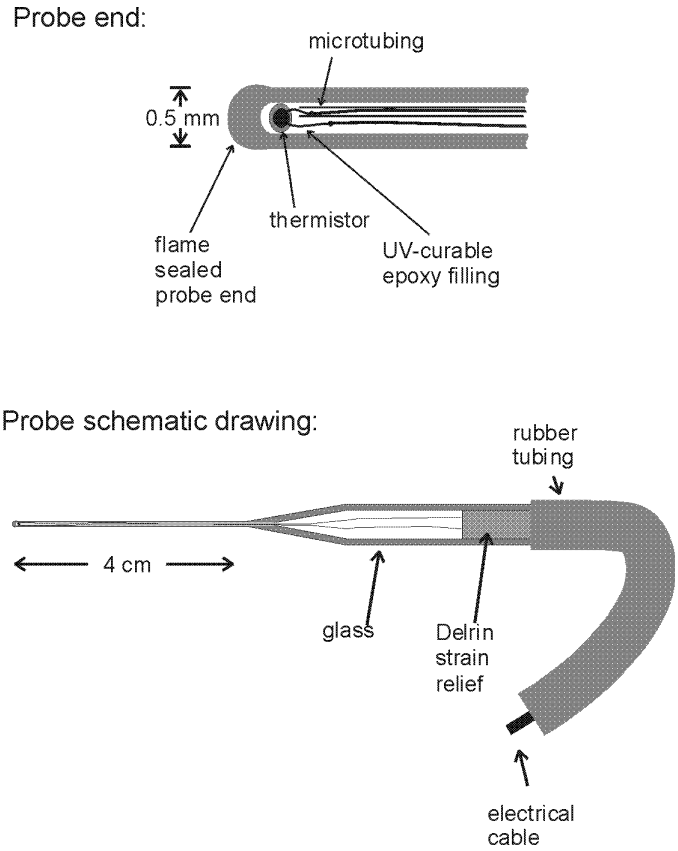

Figure 4: Drawing showing the details of the thermistor probes.

D. Electronics

The circuit to measure the change in thermistor resistance is based on a four-arm AC bridge, operating at a frequency of about 5 Hz. The output voltage from the bridge is measured using a commercial lock-in amplifier. The bridge circuit, as well as the rest of the electronics used with the calorimeter, are shown in Figure 5.

The platinum resistor probes, which are used for temperature monitoring, are connected to a remotely controlled scanning system (based on a Keithley 2001 multimeter equipped with a scanner card). The bridge balancing resistor, the lock-in amplifier and the multimeter are all connected to a PC using a GPIB interface card, thus allowing each to be controlled and read out remotely. The software allows the bridge to be balanced, the characteristics of the lock-in amplifier to be changed, the acquisition of data

according to a preselected scheme and the calculation of the extrapolation curves and the dose. In addition, the stirrer, valve system and bath can be remotely controlled.

The drawing in Figure 5 accurately reflects the configuration of the bridge at 22°C, when each thermistor has a resistance of approximately 5 kΩ. At 4°C, the thermistor resistance increases to approximately 10 kΩ, so the 10 kΩ decade box does not have enough range to permit the bridge to be balanced. To compensate, an extra 10 kΩ resistor is added in series with the decade box.

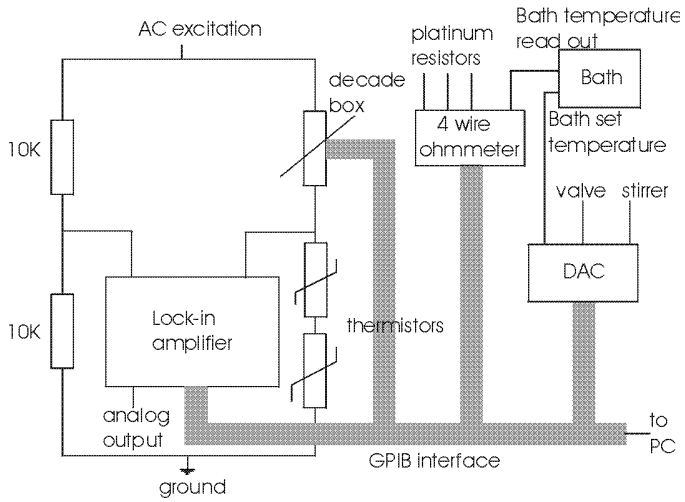

Figure 5: Schematic drawing of the electronics used with the water calorimeter. The lock-in amplifier, the decade box and the 4-wire ohmmeter can all be controlled and read out remotely. The stirrer, valve system and bath are also remotely controlled.

The response of the bridge per unit change in thermistor resistance is obtained by changing the resistance of the decade box by a known amount. A detailed electrical model of the bridge, including the impedances imposed by the lock-in amplifier, is used to relate the measured response to a change in the decade box to the response expected due to a change in the thermistor resistance. The 10 MΩ input impedance of the lock-in represents a significant loading of the bridge circuit, and its effect is largest when the bridge is asymmetric (4°C operation). If ignored, it can lead to errors of up to 0.3% in the estimated voltage change per unit change of thermistor resistance.

III. Determination of Absorbed Dose

The raw data obtained from a calorimeter run consists of the measured bridge voltage as a function of time. Changes in bridge voltage can be converted to changes in thermistor resistance, and these in turn can be converted to changes in temperature using the measured thermistor sensitivity. Ignoring correction factors, the absorbed dose to water, D_w is given by

$$D_w = c_w \cdot \Delta T_w, \qquad (1)$$

where ΔT_w is the measured temperature increase and c_w is the specific heat capacity of water. If the various correction factors are included, the equation for D_w becomes

$$D_w = \Delta T_w \cdot c_w \cdot k_t \cdot k_c \cdot k_v \cdot k_p \cdot k_{dd} \cdot k_\rho \cdot \frac{1}{1-k_{HD}}, \qquad (2)$$

where k_t accounts for any transient effects of the radiation on the thermistor response, k_c and k_v are corrections for conductive and convective heat transfer, respectively, k_p is a correction for perturbations of the radiation field by the glass vessel or probes, k_{dd} is a correction for the non-uniformity of the lateral dose profile, k_ρ accounts for the change of the density of water with temperature and k_{HD} is the heat defect. The following sections summarize our knowledge of the various correction factors.

A. Transient Thermistor Response to Radiation

Domen [9] has reported on results obtained at NIST which show that thermistors can tolerate doses of several MGy with no adverse effects. Calorimetric measurements of the absorbed dose for radiation therapy purposes are unlikely to require doses of more than a few kGy. Thus, we can safely assume that radiation will have no effect on the quiescent behaviour of our thermistor probes.

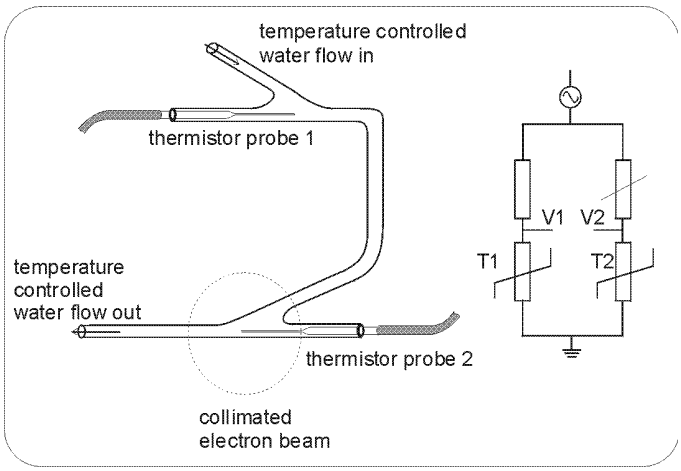

Figure 6: Schematic of the setup used to measure the transient response of thermistors to radiation. The same temperature-regulated water flowed over both thermistor probes. The whole assembly was insulated from the environment using Styrofoam sheets. One thermistor was irradiated with a high dose rate (150 Gy/min) electron beam and the difference in response of the two thermistors was measured. The bridge circuit on the right shows how the difference signal was obtained by placing the thermistors in opposite arms of a Wheatstone bridge.

However, there remains the possibility that radiation might induce transient effects which persist for tens of seconds and thus distort the post-irradiation drift curve. To test this possibility, we constructed the apparatus shown in Figure 6. Two closely matched thermistors were placed in a flow of temperature-regulated water. The thermistors were mounted in opposite arms of a Wheatstone bridge so that the output

voltage was close to zero when water was flowing over the probes. A collimated electron beam was used to irradiate one of the thermistors while the second remained in a field-free region. Because of the flowing water, both probes continued to see approximately the same temperature, and any transient effects after the beam was turned off would be due to radiation-induced changes in the thermistor response. Measurements were carried out at 4ºC and 22 ºC.

The results are summarized in Figure 7. The dose rate from the electron beam was approximately 150 Gy/min, which would give a temperature rise of about 60 mK in 100 s in stagnant water. This would correspond to a signal of approximately 460 μV in Figure 7. The radiation-induced signal when the beam is on amounts to 1 or 2 μV and is due to local heating of the water and probe. However, any transient effects are over in less than 20 s after the beam is turned off. Any other offsets or slope changes are less than 0.2 μV when extrapolated to mid-run, and this is less than 0.05% of the signal due to the absorbed dose in stagnant water.

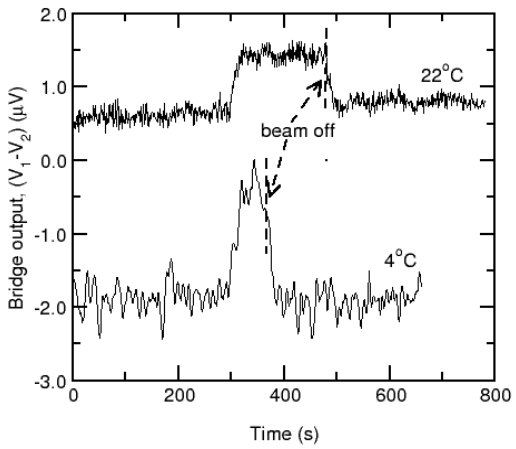

Figure 7: Measured transient response of a thermistor to radiation. The electron beam dose rate was approximately 150 Gy/min, and measurements were carried out at both 4ºC and 22 ºC. A 1 μV change in bridge output corresponds to a temperature change of approximately 130 μK, and in 100 s the signal would have been about 460 μV if the water had been stagnant.

Assuming that thermistor response per unit dose is not altered by dose or dose rate, these conclusions should apply to irradiations at our standard dose rate of about 1.5 Gy/min. Thus, we do not use the first 20 s after the irradiation is stopped in extrapolating to mid-run. Under these conditions, any correction for transient thermistor response should be less than 0.05% and we take k_t to be unity in equation (2).

B. Conductive Heat Transfer

Conductive heat losses in a large water calorimeter may result from two sources. Firstly, because the heat capacity of glass is about one-sixth that of water, the radiation-induced temperature rise in the glass would be about six times that in water, if it were not that most of the heat generated in the glass is transferred to the water. Secondly, temperature gradients within the water because of non-uniformities in the absorbed dose distribution will lead to conductive heat transfer. We now examine each of these effects in more detail.

To calculate the effect of heat transfer from the glass we use the following simplifying assumptions: the calorimeter is irradiated uniformly; the glass vessel is an infinitely long cylinder; the thermistor bead is located symmetrically at the end of the glass probe; each probe is semi-infinite in length. Under these assumptions, rotational symmetry reduces the problem to two dimensions. This two-dimensional space is divided by an irregular rectangular grid with a high resolution in the neighbourhood of the probe, probe tip and vessel, and a low resolution elsewhere. Heat transfer calculations begin at the start of the irradiation. For every rectangular cell of the grid the transport of heat energy is calculated in discrete time steps. The calculated effect on the temperature at the point of measurement can either be subtracted from the measured signal before the run is analysed, or the run can first be analysed to get an approximate temperature change which is then corrected for the effects of heat conduction. Additional details have been reported by Seuntjens and Palmans [14].

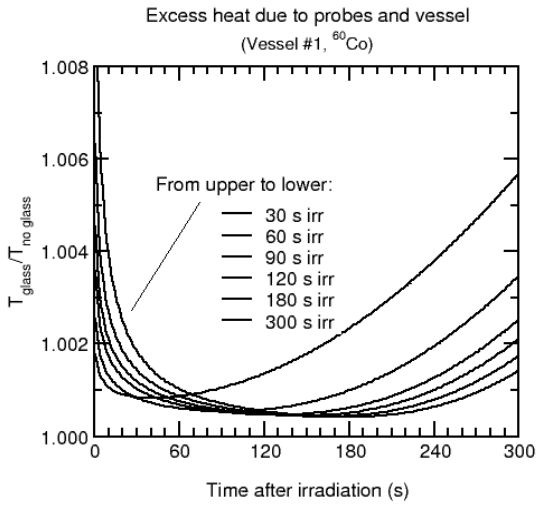

Figure 8: Calculated excess temperature at the end of each thermistor probe, caused by heat conduction from the probes and from the vessel wall. The results apply for vessels with dimensions similar to those of vessel #1. The decrease in temperature immediately after irradiation is due to heat flowing away from the probes. The increase in excess temperature several minutes after the irradiation is due to heat produced in the vessel wall and transported to the point of measurement.

The calculated excess temperature rise in a ^{60}Co beam, for the NRC geometry and for different irradiation times, is plotted in Figure 8 for vessel dimensions similar to those of vessel #1. The decrease in temperature immediately after the irradiation is caused by excess heat from the probe that is conducted away from the probe axis into the water, while the increase in temperature at later times is due to excess heat from the vessel reaching the probes. Table 1 gives a summary

of calculated values of k_c appropriate for ^{60}Co γ-rays for vessels #1 and #3. For 180 s irradiations with probes of 0.5 mm diameter, corrections of less than 0.2% are calculated for fits of the post-irradiation drift in the range of 30 to 180 s.

For beams of ^{60}Co γ-rays or high energy x-rays, the largest dose gradients occur in the buildup region or at the edges of the field. If calorimeter measurements are restricted to depths beyond the dose maximum, and if the field size is reasonably large (10 cm by 10 cm or larger), then the effect of conductive heat transfer due to dose nonuniformities is very small [15], [16]. Table 2 summarizes the various contributions to the conductive heat loss correction for photon beams from ^{60}Co γ-rays to 30 MV x-rays. It is clear that the correction is dominated by heat transfer from the glass vessel.

Table 1.
Calculated correction factor, k_c expressed as %, on the linear extrapolation to mid-run due to excess heat produced in the end of thermistor probes and in the vessel wall for vessels with dimensions similar to those of vessels #1 and #3. A positive value for the correction means the temperature rise obtained by linear extrapolation should be increased accordingly. Calculations were performed for different irradiation times and for different intervals used to specify the post-irradiation drift curve. The first and second row for each irradiation time is for vessels #1 and #3, respectively. The post-irradiation drift interval starts 20 s after the end of the irradiation.

Irradiation time (s)	Post-irradiation drift interval (s)				
	30	60	120	180	240
30	-0.36	-0.29	-0.21	-0.17	-0.14
30	-0.36	-0.29	-0.21	-0.16	-0.08
60	-0.30	-0.24	-0.18	-0.14	-0.10
60	-0.30	-0.24	-0.18	-0.14	-0.07
90	-0.27	-0.21	-0.16	-0.12	-0.07
90	-0.27	-0.21	-0.14	-0.07	+0.04
120	-0.24	-0.20	-0.14	-0.09	-0.04
120	-0.24	-0.19	-0.14	-0.01	+0.11
180	-0.21	-0.16	-0.10	-0.03	+0.04
180	-0.18	-0.12	-0.01	+0.12	+0.27

Table 2.
Calculated contributions to the excess heat correction. They apply to the case of an irradiation run of 120 s, with 120 s pre- and post-irradiation drifts used to extrapolate to mid-run. A negative value means that the measured temperature rise should be decreased by the indicated percentage.

Energy	Glass	Depth dose	Lateral profile	Combined
^{60}Co	-0.133%	-0.023%	-0.022%	-0.178%
10 MV	-0.115%	-0.007%	-0.017%	-0.139%
20 MV	-0.118%	-0.001%	+0.035%	-0.084%
30 MV	-0.121%	-0.020%	+0.050%	-0.091%

The dose gradient along the beam axis is much more severe for electron beams than for photon beams, and conductive heat transfer may be a problem. Some initial calculations of the effect of conductive heat transfer in a 15 MeV electron beam are presented in Figure 9. The calculations only account for the effect of the dose gradient along the beam axis. These preliminary results suggest that water calorimetry should also be feasible for high-energy electron beams.

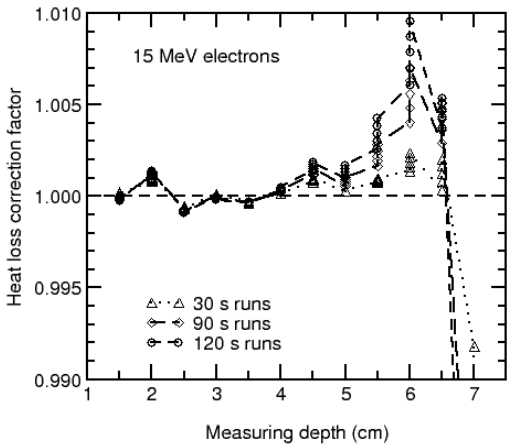

Figure 9: Calculated conductive heat-loss correction due to dose gradients in a 15 MeV electron beam as a function of the depth of the measuring point. The peak of the depth dose curve is at about 2.5 cm. The correction was calculated for several irradiation times, as indicated by the different symbols. The series of identical symbols at each depth shows the effect of using different time intervals (30 to 120 s) to characterize the post-irradiation drift.

C. Convective Heat Transfer

In addition to heat transfer by conduction, heat transfer by convection can occur in a liquid calorimeter. If the water in the calorimeter is heated nonuniformly, buoyant forces will arise due to local density changes in the gravitational field. These forces may lead to flow within the liquid, and this flow will contribute to heat transport. The flow rate may depend on the absorbed dose and on time, and thus the effective heat transfer coefficient at the point of measurement will not be constant. Under these conditions, the standard approach of extrapolating initial and final drifts to mid-run [17] may not accurately account for convective heat transfer.

Schulz and Weinhous [18] pointed out that one way of avoiding altogether the onset of convection is to operate the calorimeter at 4°C, because at this temperature the volume expansion coefficient of water is zero. We assume that k_v in equation (2) is unity when our calorimeter is operated at 4°C. The evidence for convective flow at room temperature and its effect on calorimeter response is described in a paper by Seuntjens *et al* in these Proceedings.

D. Radiation Field Perturbation

The presence of the calorimeter detection vessel and the glass thermistor probes perturbs to some extent the radiation

field when compared to the situation where these objects are absent. We measured the effect of the vessel on the absorbed dose at the measuring point using a PTW-233642 ion chamber. This chamber is small enough to fit inside the glass vessel, and the chamber response was measured with and without the vessel present. The perturbation correction, k_p, is taken as the ratio of the chamber response without the vessel to that with it in place.

For ^{60}Co γ-rays, k_p was measured to be 1.0021 ± 0.0005. Because 0.9 mm of glass would attenuate the ^{60}Co beam by about 0.6%, these measurements show that photon attenuation in the glass is partially compensated by the slightly increased dose contribution from scattered photons when the vessel is present. This observation was confirmed by performing a correlated sampling Monte Carlo simulation of the photon transport through the water phantom. By scoring the fluence in a spherical region on the beam axis at the position of the centre of the vessel with the vessel and probes absent and with both materials present, the correction factor was found to be 1.0028 ± 0.0008, in good agreement with the measurements. The measured value of k_p at all beam qualities is given in column 3 of Table 3.

Table 3.
Values for the energy-dependent correction factors required in equation 2.

Energy	k_c	k_p	k_{dd}	k_ρ	Combined
^{60}Co	0.9982	1.0021	1.0004	1.0006	1.0013
10 MV	0.9986	1.0026	1.0007	1.0012	1.0031
20 MV	0.9992	1.0009	1.0012	1.0010	1.0023
30 MV	0.9991	0.9994	1.0004	1.0008	0.9997

E. Dose Profile Non-Uniformity

The lateral profile of the dose in the *x-y* plane perpendicular to the beam axis at the measuring point is slightly non-uniform depending on the field size and the source to detector distance. We measured the *x-y* dose profile using a PTW-M233642 ionization chamber with a cavity volume of 0.125 cm^3, and used these data to calculate the correction factor, k_{dd}, required to obtain the dose at a point on the beam axis. The correction depends slightly on the spacing between the probe ends. The results are summarized in column 4 of Table 3 for the standard probe spacing of 1 cm.

F. Density of Water

For practical reasons, ion chamber measurements need to be done at room temperature. If the calorimetry measurements are done at 4°C, a small correction, k_ρ, is necessary to determine the dose at 22°C. Because the density of water increases by 0.22% as the temperature decreases from 22°C to 4°C, there will be more water overlying the measuring point at 4°C than at 22°C. Taking the dose gradient for ^{60}Co to be 5%/cm, the extra attenuation at the calibration depth of 5 cm will be approximately 0.055%, leading to a value for k_ρ of 1.00055.

In order to estimate k_ρ for high energy x-rays, we have taken the depth-dose distribution measured at 22°C and scaled the depth axis so that $x' = x/1.0022$. The scaled distribution gives the dose that applies when the water is at 4°C. The ratio of the 22°C distribution to the 4°C distribution, evaluated at the reference depth of 10 cm, gives k_ρ. Values of k_ρ for all beam qualities are given in Table 3.

G. Heat Defect

The use of calorimetry to measure absorbed dose is complicated by the fact that the measured heat energy may not correspond to the energy absorbed from the radiation field. The heat defect is used to quantify the difference between the energy absorbed, E_a, and the energy appearing as heat, E_h, and it is defined by

$$k_{HD} = \frac{E_a - E_h}{E_a}. \tag{3}$$

The heat defect is positive for endothermic processes, while it is negative if the radiation induces exothermic processes in the calorimeter. For water irradiated by low LET radiation, the heat defect is almost entirely due to radiation-induced chemical reactions [13].

The heat defect can be calculated using the established model for the radiolysis of water. In this model, the ionizing radiation first produces localized clusters of reactive species, called spurs. After about 0.1 μs, the spur products act as if they are homogeneously distributed, and are assigned yields, G_i, where the subscript, i, identifies the species. The concentrations of the spur products and other reactive species within the aqueous solution are followed using homogeneous reaction kinetics, where the reactions involved, the rate constants and the values of G_i are obtained from the published literature on the radiolysis of water. In general, there will be n species which participate in m reactions. The rate constant for reaction i is denoted by k_i, and for the aqueous systems we have studied to date, only first and second order reactions are involved. Mathematically, the problem is equivalent to solving a set of coupled first order differential equations of the form

$$\frac{dC_i}{dt} = \rho G_i \dot{D} - \sum_{1^{st},C_i\downarrow} k_j C_i - \sum_{2^{nd},C_i\downarrow} k_j C_i C_k + \sum_{1^{st},C_i\uparrow} k_j C_k + \sum_{2^{nd},C_i\uparrow} k_j C_k C_l. \tag{4}$$

The concentration of species i is given by C_i, and there are n equations similar to equation (4). The first term in the equation gives the production rate of species i at 0.1 μs, where ρ is the density of water and $\dot{D}$ is the dose rate. The labelling

"1st" and "2nd" on the sums indicate that they are to be taken over all relevant first and second order reactions, respectively, while "$C_{i\downarrow}$" and "$C_{i\uparrow}$" indicate that they are to be taken over all reactions in which species *i* is being consumed or produced, respectively. Specific values for the initial yields and rate constants can be found in [19].

At a specified time after the irradiation, the yield of species *i* can be expressed as G_i', where the prime is used to distinguish it from the yield at 0.1 μs. Then the heat defect is calculated using

$$k_{\mathrm{HD}} = \sum_{i=1}^{n} G_i' \cdot \Delta H_i, \tag{5}$$

where ΔH_i is the heat of formation for species *i*. Note that can be negative or positive.

Various computer codes have been developed for solving equation (5). We have made extensive use of the code developed at Atomic Energy of Canada Limited, and referred to as MAKSIMA-CHEMIST [20]. More recently, we have been using the code developed at Harwell in the UK and referred to as FACSIMILE. Both codes give the same results in test cases, but FACSIMILE is more flexible when it comes to calculating secondary output, such as the heat defect.

The computer simulations require values of k_i and G_i. Our most recent set of values is referred to as Model III and was described in [21]. This model is based largely on the data published by Elliot [22]. Elliot has also studied the variation of k_i and G_i with temperature.

The model calculations can be tested experimentally by comparing the relative response of different aqueous systems. Klassen and Ross [19] have identified several aqueous systems which are suitable for water calorimetry. These include pure water, water saturated with H_2 gas and water saturated with a 50/50 mixture of H_2 and O_2 gases.

Because the calorimeter is operated at both 4ºC and 21ºC, the temperature dependence of the heat defect must be estimated. For those systems which attain a steady state after some modest accumulated dose, the situation is quite straightforward. The only concern is whether or not the accumulated dose required to reach steady state (and thus zero heat defect) depends on the temperature. Using data from [22] on the change of G_i and k_i with temperature, the heat defect for H_2-saturated and pure water was calculated for a dose rate of 1.5 Gy/min at 4ºC and 21ºC. At both temperatures, the heat defect after an accumulated dose of 3 Gy was less than 0.1%. Furthermore, the reactions go to completion almost immediately after the irradiation stops.

The situation is more complicated for water saturated with H_2 and O_2 gases. This system is exothermic over a wide range of accumulated dose, and requires that the heat defect be calculated as a function of dose rate and accumulated dose. Although this might be seen as a significant disadvantage, it is largely outweighed by the fact that earlier work [21] had shown that H_2/O_2 water is insensitive to impurities. Using Model III gave the results shown at the top of Figure 10.

These data show that the reactions are taking a long time to go to completion and that the exothermicity is significantly smaller at 4ºC than at 21ºC. We found that our calorimetry data at 4ºC were not consistent with these predictions and this prompted a re-examination of Model III. It was discovered that Elliot had made an error in determining the rate constant for the forward reaction in

$$O_2^- + H_2O \rightarrow HO_2 + HO^-. \tag{6}$$

We corrected the error in Model III, renamed it IIIR and used it to calculate the results shown at the bottom of Figure 10. Now, the reactions go to completion much more quickly, and the calculated heat defect at 4ºC is in reasonable agreement with calorimetry measurements. The calculations indicate a difference of about 0.3% in the heat defect between 4ºC and 21ºC. Additional calorimetry measurements should be able to test this model prediction.

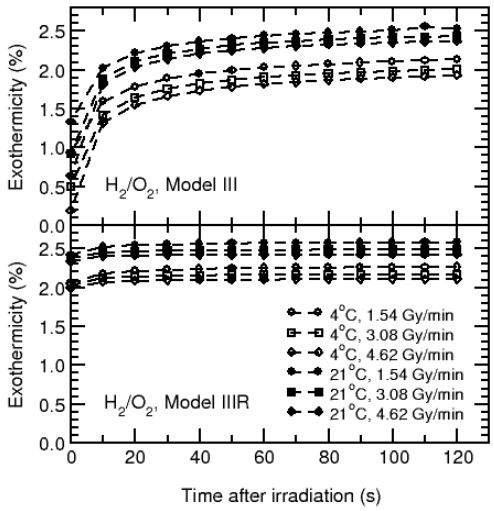

Figure 10: Effect of the irradiation temperature on the calculated heat defect (expressed as percent exothermicity) of water saturated with a 43/57 mixture of H_2 and O_2 gases. Results are shown for three different dose rates, but the irradiation time was adjusted so that the same dose was delivered in each case. The calculations for the upper frame were done using Model III [21]. The results shown in the lower frame were obtained using Model IIIR.

IV. Calorimeter Performance

Figure 11 shows the response of the NRC calorimeter to 20 MV x-rays at a dose rate of about 1.5 Gy/min. The calorimeter was operated at 4ºC, and the power dissipated in each thermistor bead was 6.2 μW. The irradiation time was 120 s, and 120 s of pre- and post-irradiation drift is shown. The resistance change of the thermistors during this irradiation was 0.68 Ω out of a total resistance of about 20,000 Ω. The corresponding temperature change was about 770 μK and the amplitude of the noise signal converted to equivalent temperature amounted to about 10 μK.

Tests for reproducibility of the calorimeter response showed that, for 120 s runs, the sample standard deviation (obtained from a set of 7 to 11 runs) was 0.7 to 0.8%. If the

irradiation times were shorter, i.e., 90 s or 60 s, the sample standard deviation was 0.9% and 1.7%, respectively.

The calorimeter has been used to establish the absorbed dose to water in four different photon beams and the results are summarized in Figure 12. In order to help eliminate systematic effects due to the heat defect, at least two different aqueous systems were used at each beam quality. In addition, the vessel was emptied and refilled several times during the course of the measurements. Furthermore, the ^{60}Co data was obtained using two different vessels [23].

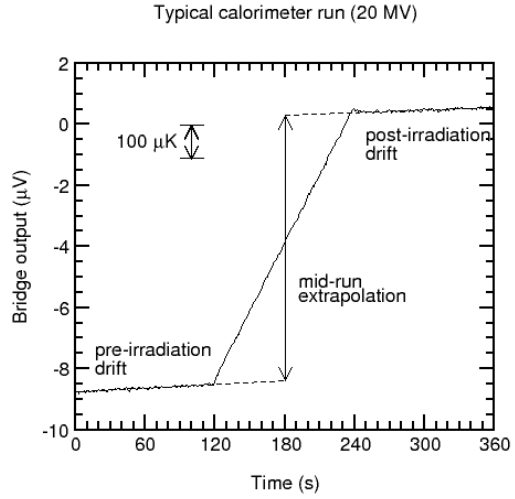

Figure 11: Typical water calorimeter run (120 s) obtained using 20 MV x-rays. The total thermistor resistance is about 20,000 Ω and this run represents a change in the resistance of about 0.68 Ω.

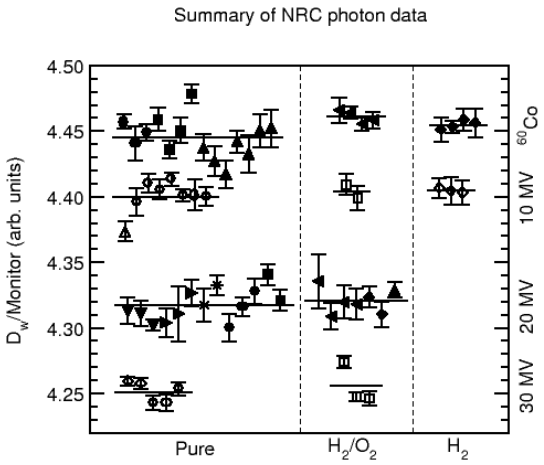

Figure 12: Summary of the results obtained using the NRC sealed water calorimeter to measure the absorbed to water for photon beams. Each datum represents the average value obtained from 10 to 15 individual irradiation runs. The solid horizontal lines represent the average value of the data in each set. The different symbols indicate different fills of the vessel, although the same symbol for different beam qualities does not mean the same fill was involved. The monitor to which the calorimeter response is referenced is a NE2571 ion chamber.

The contributions to the uncertainty on the measured absorbed dose for ^{60}Co γ-rays is shown in Table 4.

V. Derived Results

Section IV summarized how the sealed water calorimeter was used to establish the absorbed dose per monitor unit for several high energy photon beams. These calibrated beams can be used to study problems of interest to radiation dosimetry. Three applications of our calibrated beams are described in the following subsections.

Table 4.
Estimates of the contributions to the standard uncertainty on the absorbed dose to water for ^{60}Co γ-rays when measured using the NRC sealed water calorimeter. The only change for high energy x-rays is the addition of a component for beam monitoring which increases the overall uncertainty by about 0.1%.

Quantity	Uncertainty (%)	
	s_i	u_i
Reproducibility (n=190)	0.06	
Specific heat		0.00
Heat loss (k_c)		0.15
Field perturbation (k_p)		0.05
Dose profile (k_{dd})		0.04
Density (k_ρ)		0.00
Heat defect (k_{HD})		0.30
Probe calibration (β)		0.20
Positioning		0.10
Combined uncertainties	0.06	0.41
Overall uncertainty	0.41	

A. Ion Chamber Calibration Factors

Consider a photon beam for which the absorbed dose to water per monitor unit has been established at a reference point in a water phantom using calorimetry. If an ion chamber (or other dosimeter) is placed at the reference point, a calibration factor, $N_{D,w}$, can be obtained such that the reading of the instrument, Q_a, is related to the absorbed dose to water, D_w, by

$$D_w = N_{D,w} \cdot Q_a . \quad (7)$$

In general, it may not be possible, either because of expense or because calibrated beams are not available, to directly calibrate an ion chamber at every beam quality of clinical interest. In an attempt to circumvent this problem, two recent dosimetry protocols [24], [25] have proposed the introduction of a beam quality conversion factor, k_Q, such that equation (7) is rewritten as

$$D_w = k_Q \cdot N_{D,w}^{Co} \cdot Q_a , \quad (8)$$

where $N_{D,w}^{Co}$ is the absorbed dose calibration factor for ^{60}Co γ-rays and k_Q is given by

$$k_Q = N_{D,w}^{Q} / N_{D,w}^{Co}, \quad (9)$$

where $N_{D,w}^{Q}$ is the calibration factor at beam quality Q. Both the AAPM and IAEA protocols rely on values of k_Q that have been calculated using ion chamber theory. In order to test these calculations we have measured k_Q for several different types of ion chambers, and the detailed results are given in a paper which has been submitted for publication [26]. Figure 13 shows our measured values of k_Q for the NE2571 chamber along with results obtained by others and the curve predicted by the AAPM protocol. The agreement among the data sets measured by different groups, and between the measured data and the calculated values of k_Q is quite satisfactory.

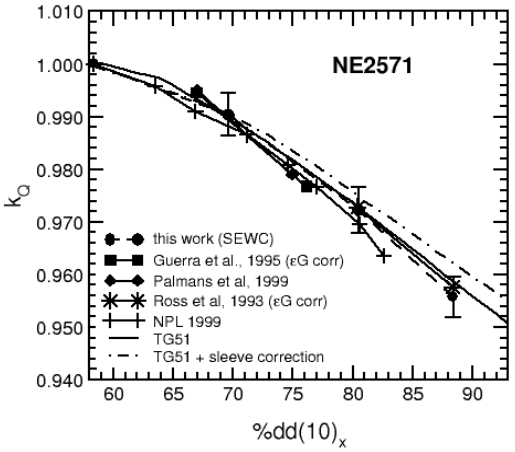

Figure 13: Summary of measured and calculated k_Q data for the NE2571 ion chamber. The data of Guerra *et al* are from [27]; Palmans *et al* from [28]; Ross *et al* from [29]; and NPL from [30]. The solid curve labelled TG-51 is the result obtained using the AAPM protocol [24] while the dashed line shows the calculated effect of including a 1 mm Lucite sleeve on the chamber. Data for other chamber types are presented in [26].

B. Fricke Dosimetry

The Fricke dosimeter is a chemical dosimeter that is capable of high precision and has been widely used in radiation dosimetry. When irradiated, the amount of ferric ion produced is proportional to the absorbed dose, and the ferric ion concentration can be measured using optical absorption techniques. If the Fricke dosimeter is to be used absolutely, the ferric ion yield, $G(Fe^{3+})$, must be determined by calibrating the dosimeter against some dose standard. It is well known that $G(Fe^{3+})$ depends on the energy spectrum of the electrons set in motion in the dosimeter, decreasing as the mean electron energy is decreased [31]. However, existing data are not adequate to determine how $G(Fe^{3+})$ changes with energy between ^{60}Co γ-rays and high energy x-rays.

At the previous NPL Workshop, we presented data obtained using a stirred water calorimeter which indicated that $G(Fe^{3+})$ increases by 1% as the energy increases from ^{60}Co to 20 MV x-rays [32]. Since then, we have used the photon beams calibrated using the sealed water calorimeter to measure $G(Fe^{3+})$ (or more precisely εG, where ε is the extinction coefficient for the ferric ion). The results are summarized in Figure 14 which also includes the data obtained using the stirred water calorimeter. Taken together, these data suggest that $G(Fe^{3+})$ changes by 0.7 (±0.3)% between ^{60}Co and high energy x-rays. More details on this work can be obtained from [33].

C. Intercomparison of Absorbed Dose Standards

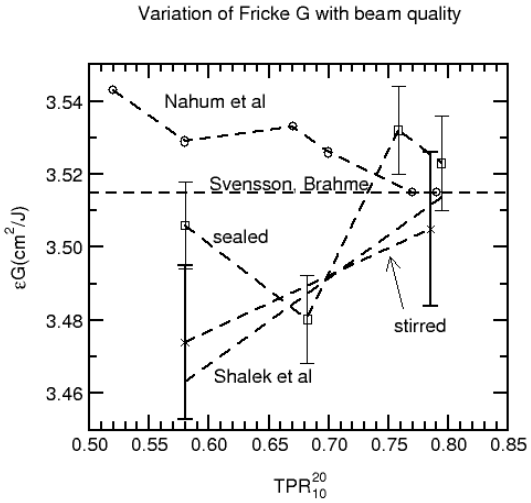

Figure 14: Variation of εG with energy. Our measured data with both the stirred [32] and sealed [33] water calorimeters are shown. The data of Shalek *et al* are from [31]; Nahum *et al* from [34]; and Svensson and Brahme from [35].

Other groups have established absorbed dose standards for both ^{60}Co γ-rays and high energy x-rays. Because the techniques used by different laboratories are not always the same, an intercomparison of dose standards can help to identify systematic errors.

Using ion chambers, the ^{60}Co dose standard of NRC has been compared with the equivalent standard of several other laboratories, and the results are summarized in Figure 15. Only the uncertainties associated with the ion chamber measurements are shown in this figure, and serve to show that the calibrated beams can be compared with an uncertainty considerably smaller than the uncertainty on the absorbed dose. Given that the uncertainty on most absorbed dose standards is about 0.5%, Figure 15 shows that the agreement between the laboratories is quite impressive.

Comparisons have also been carried out between NRC and two laboratories which have the capability of determining the absorbed dose in high energy photon beams. The results are shown in Figure 16, where the average calibration factor for a set of NE2571 ion chambers is given as a function of beam quality for the three laboratories. In this case, the agreement is not as good as for ^{60}Co, with discrepancies as large as 1% between the laboratories.

VI. SUMMARY

The NRC calorimeter is operated at 4ºC to avoid convective heat transfer. Apart from the heat defect, no single correction factor is bigger than 0.3%, and the combined effect of all these corrections is less than 0.3%.

Knowledge and control of the heat defect is the most challenging aspect of water calorimetry. Both pure water and water saturated with H_2 gas are predicted to have a heat defect of zero after a small accumulated dose. This result is insensitive to the details of the model used to describe the radiation chemistry. However, traces of O_2 will affect the response of both systems, and pure water tends to be sensitive to impurities in general. On the other hand, the H_2/O_2 system tends to be rather insensitive to impurities. However, its heat defect is non-zero, and thus the model used to describe the radiolysis of water plays a more important role. Using all three systems, we estimate that the standard uncertainty contributed by the heat defect is 0.3%, and is the largest contribution to the overall uncertainty.

The sealed water calorimeter operated at 4ºC is now the Canadian standard for the absorbed dose to water. Ion chamber calibration factors have been measured for ^{60}Co γ-rays and high energy x-rays, and compared with the calibration factors determined by other laboratories. The agreement for ^{60}Co is excellent, although there are discrepancies as large as 1% for high energy x-rays.

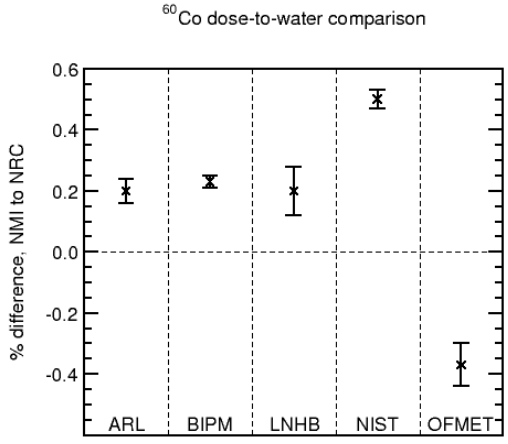

Figure 15: Comparison of the ^{60}Co absorbed dose to water standards of several national laboratories. The comparisons were carried out using ion chambers as transfer instruments. The laboratories are identified as follows: ARL - Australian Radiation laboratory; BIPM - Bureau International des Poids et Mesures; LNHB - Laboratoire National Henri Becquerel; NIST - National Institute of Standards and Technology; OFMET - Swiss Federal Office of Metrology. Only the standard uncertainties arising from the ion chamber measurements are shown.

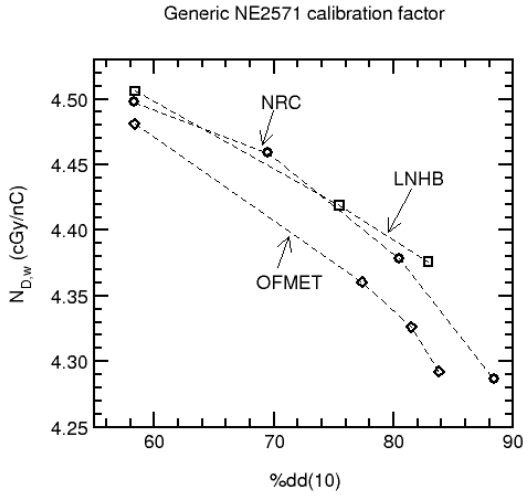

Figure 16: Comparison of the absorbed dose to water for high energy x-ray beams as measured by three national laboratories. The comparisons were carried out using a set of NE2571 ion chambers, which were calibrated by each laboratory in terms of absorbed dose to water. The laboratories are identified as follows: NRC - National Research Council; LNHB - Laboratoire National Henri Becquerel; OFMET - Swiss Federal Office of Metrology.

ACKNOWLEDGEMENTS

The knowledge, skill and dedication of NRC's technical and support staff were critical for the successful outcome of this work. The glass cylinders which form the central portion of the sealed glass vessels were ground by Gary Boyd. The rest of the glass work, including the glass envelopes for the thermistor probes, was done by Peter l'Abbé. David Marchington was responsible for the overall assembly of the calorimeter and he also constructed the internal bead and lead assemblies for the thermistor probes. Leo Heistek constructed the bridge circuit and the electronics for automated control. The original software for reading and analysing the data from the calorimeter was converted into Windows-based applications by a summer student, Dylan Togane.

REFERENCES

[1] AAPM, "A protocol for the determination of absorbed dose from high-energy photon and electron beams", *Med. Phys.*, vol. 10, pp. 741-771, 1983.

[2] IAEA, Absorbed dose determination in photon and electron beams, Technical Report Series 277, International Atomic Energy Agency, Vienna, 1987.

[3] IPSM "Code of Practice for high-energy photon therapy dosimetry based on the NPL absorbed dose calibration service", *Phys. Med. Biol.*, vol. 35, pp. 1355-1360, 1990.

[4] A.R. DuSautoy, "The UK primary standard calorimeter for photon-beam absorbed dose measurement", *Phys. Med. Biol.*, vol. 41, pp. 137-15, 1996.

[5] A.S. Guerra, R.F. Laitano and M. Pimpinella, "Characteristics of the absorbed dose to water standard

at ENEA", *Phys. Med. Biol.*, vol. 41, pp. 657-674, 1996.

[6] B. Chauvenet, D. Baltès and F. Delaunay, "Comparison of graphite-to-water absorbed-dose transfers for ^{60}Co photon beams using ionometry and Fricke dosimetry", *Phys. Med. Biol.*, vol. 42, 2053-2063, 1997.

[7] S.R. Domen, "Absorbed dose water calorimeter", *Med. Phys.*, vol. 7, pp. 157-159, 1980.

[8] C.K. Ross and N.V. Klassen, "Water calorimetry for radiation dosimetry, *Phys. Med. Biol.*, vol. 41, pp. 1-29, 1996.

[9] S.R. Domen, "A sealed water calorimeter for measuring absorbed dose", *J. Res. Natl. Inst. Stand. Tech.*, vol. 99, pp. 121-141, 1994.

[10] J. Seuntjens, H. Thierens and U. Schneider "Correction factors for a cylindrical ionization chamber used in medium energy x-ray beams", *Phys. Med. Biol.*, vol. 38, pp. 805-832, 1993.

[11] J. Seuntjens, A. Van der Plaetsen, K. Van Laere and H. Thierens, "Study of the relative heat defect and correction factors of a water calorimetric determination of absorbed dose to water in high-energy photon beams", *Proc. Symp. on Measurement Assurance in Dosimetry*, IAEA-SM-330/6, (Vienna: IAEA), pp. 45-59, 1993.

[12] C.K. Ross, N.V. Klassen and G.D. Smith, "The effect of various dissolved gases on the heat defect of water', *Med. Phys.*, vol. 11, pp. 653-658, 1984.

[13] C.K. Ross, N.V. Klassen, K.R. Shortt and G.D. Smith, "A direct comparison of water calorimetry and Fricke dosimetry", *Phys. Med. Biol.*, vol. 34, pp. 23-42, 1989.

[14] J. Seuntjens and H. Palmans, "Correction factors and performance of a 4^{o}C sealed water calorimeter", *Phys. Med. Biol.*, vol. 44, pp. 627-646, 1999.

[15] M. Roos, "The current status of water absorbed dose calorimetry in the PTB", In NRC Workshop on Water Calorimetry, C.K. Ross and N.V. Klassen (Eds.), National Research Council, Ottawa, Canada, pp. 9-15, 1988.

[16] J. Seuntjens, "Comparative Study of Ion Chamber Dosimetry and Water Calorimetry in Medium Energy X-Ray Beams", Ph.D. thesis, Gent University, Gent, Belgium, 1991.

[17] J.S. Laughlin and S. Genna, "Calorimetry", In Radiation Dosimetry, Vol. II, F.H. Attix and W.C. Roesch (Eds.), pp. 389-441, Academic Press: New York, 1966.

[18] R.J. Schulz and M.S. Weinhous, "Convection currents in a water calorimeter", *Phys. Med. Biol.*, vol. 30, pp. 1093-1099, 1985.

[19] N.V. Klassen and C.K. Ross, "Absorbed dose calorimetry using various aqueous solutions", *Radiat. Phys. Chem.*, vol. 38, pp. 95-104, 1991.

[20] M.B. Carver, D.V. Hanley and K.R. Chaplin, "MAKSIMA-CHEMIST: A program for mass action kinetics simulation by automatic chemical equation manipulation and integration using stiff techniques", Technical Report AECL-6413, Chalk River Nuclear Laboratories, Chalk River, Canada, 1979.

[21] N.V. Klassen and C.K. Ross, "Water calorimetry: The heat defect", *J. Res. Natl. Inst. Stand. Technol.*, vol. 102, pp. 63-74, 1997.

[22] A.J. Elliot, "Rate constants and G-values for the simulation of the radiolysis of light water over the range 0—300^{o}C, Technical Report AECL-11073, Atomic Energy of Canada Ltd., Chalk River, Canada, 1994.

[23] J.P. Seuntjens, C.K. Ross, N.V. Klassen and K.R. Shortt, "A status report on the NRC sealed water calorimeter", NRC Report PIRS-0584, National Research Council, Ottawa, Canada, 1999.

[24] AAPM, "AAPM's TG-51 protocol for clinical reference dosimetry of high-energy photon and electron beams", *Med. Phys.*, vol. 26, pp. 1847-1870, 1999.

[25] IAEA, "Absorbed dose determination in external beam radiotherapy: An international code of practice for dosimetry based on standards of absorbed dose to water", Technical Report Series Draft V.5, International Atomic Energy Agency, Vienna, 1999.

[26] J.P. Seuntjens, C.K. Ross, K.R. Shortt and D.W.O. Rogers, "Absorbed-dose beam quality conversion factors for cylindrical chambers in high-energy photon beams", *Med. Phys.*, (Submitted, November 1999), 2000.

[27] A.S. Guerra, R.F. Laitano and M. Pimpinella, "Experimental determination of the beam quality dependence factors, , for ionization chambers used in photon and electron dosimetry", *Phys. Med. Biol.*, vol. 40, pp. 1177-1190, 1995.

[28] H. Palmans, W. Mondelaers and H. Thierens, "Absorbed dose beam quality correction factors for the NE2571 chamber in a 5 MV and a 10 MV photon beam", *Phys. Med. Biol.*, vol. 44, pp. 647-663, 1999.

[29] C.K. Ross, K.R. Shortt, D.W.O. Rogers and F. Delaunay, "A test of as a beam quality specifier for high energy photon beams", In Proc. Symp. on Measurement Assurance in Dosimetry, IAEA-SM-330/10, Vienna, pp. 309—321, 1993.

[30] P. Sharpe "Progress report on radiation dosimetry at NPL", BIPM Report CCRI(I)/99-20, BIPM, Paris, 1999.

[31] R.J. Shalek, W.K. Sinclair and J.C. Calkins, "The relative biological effectiveness of 22-mevp x-rays, cobalt-60 gamma rays, and 200-kvcp x-rays II. The use of the ferrous sulfate dosimeter for x-ray and gamma-ray beams", *Radiat. Res.*, vol. 16, pp. 344-351, 1962.

[32] C.K. Ross, N.V. Klassen and K.R. Shortt, "The development of a standard based on water calorimetry for absorbed dose to water", In NPL Calorimetry Workshop, Teddington, UK National Physical Laboratory, 1994.

[33] N.V. Klassen, K.R. Shortt, J. Seuntjens and C.K. Ross, "Fricke dosimetry: The difference between $G(Fe^{3+})$ for ^{60}Co γ-rays and high energy x-rays", *Phys. Med. Biol.*, vol. 44, pp. 1609-1624, 1999.

[34] A.E. Nahum, H. Svensson and A. Brahme, "The ferrous sulphate G-value for electron and photon beams: A semi-empirical analysis and its experimental support", In Seventh Symposium on Microdosimetry, J. Booz, H.G. Ebert, and H.D. Hartfiel (Eds.), Oxford, UK, pp. 841-851, 1980.

[35] H. Svensson and A. Brahme, "Ferrous sulfate dosimetry for electrons. A re-evaluation", *Acta Radiol. Oncol.*, vol. 18, pp. 326-336, 1979.

QUESTIONS AND ANSWERS

Achim Krauss: When you assign the 0.3% uncertainty for the heat defect in your calorimeter, then that means that you actually use the $H_2/0_2$ system where you find the differences between the different models.

Carl Ross: We have to admit to not being completely consistent at this point. The Cobalt data I believe, Jan, does not include the hydrogen/oxygen in our dose number. But the high energy data by and large we have. So, yes.

Achim Krauss: I'm thinking about the fact that: if you use the H_2 system calorimeter, then all the different models you have produce the zero heat effect, and you can show in your experiment that it is really stable independent on accumulated dose or dose rate. I think there is no reason why you couldn't say that the model is right and we can take the zero heat effect without any uncertainty.

Carl Ross: Yes. Well, at least the problem that we encounter is that the business of preparing the fill, purifying the water, bubbling with hydrogen - it is difficult to say that you can always achieve the condition that you have just outlined. You have to be sure that you have purged it of oxygen, for example. So, if you are able to demonstrate conclusively that you can control the quality, then I think you can squeeze the 0.3% smaller, but it is our feeling that we would not feel particularly comfortable for our work in making it much smaller than that.

Ken Gall: Following this point, I think Achim has shown, that with radiation the heat defects change with a hydrogen/oxygen system. Has anyone confirmed that with these radiation chemistry results that you can actually achieve that? Did you ever do radiation chemistry on them? Have you any results?

Achim Krauss: You mentioned a very special H_2/O_2 system - it's not the system used in the NRC calorimeter.

Ken Gall: But doesn't it become the H_2 system in the end? So just how you get to the H_2 is not so important, as long as you get there.

Carl Ross: But you have to be able to address, for example, the question of leaks. No valve is perfect, we have not found a perfect valve, and Norman Klassen has done some detailed measurements of leak rates through the valves and sealing systems we have, and by and large the leak rates are sufficiently small that on the timescale of several days you don't have to worry. But irradiating to see the chain reaction happen and saying 'now I've purged it of oxygen' is potentially dangerous as well, if you have a steady leak of oxygen.

Jan Seuntjens: For a hydrogen system, this leads to dramatic exothermicity. You don't need much oxygen to get a significant heat defect, and therefore the H_2/O_2 mixture is always the final verification.

Revisiting Convective Motion in Stagnant Water Calorimeters Operated at Room Temperature

J.P. Seuntjens[1], I. Kawrakow and C.K. Ross

Ionizing Radiation Standards, Institute for National Measurement Standards, National Research Council

Ottawa, Ontario K1A 0R6 Canada

Abstract

Standards laboratories around the world are increasingly using stagnant water calorimeter systems to establish the dose at a point in water. In order for this technique to work reliably, convective motion in water must be either eliminated, by operating at 4°C or, when operated at room temperature, the calorimeter response has to be proven to be predictable, and if necessary, corrections have to be applied for convective heat transfer. In a sealed water calorimeter such as the Domen system, high purity water is contained in a sealed vessel inside a large tank. In addition to controlling water purity, the vessel is conventionally assumed to act as a convective barrier if the water calorimeter is operated at room temperature. Specifically, the vessel needs to be such that the characteristic Rayleigh number does not exceed a value of 1700. However, experiments at NRC using a 6 cm diameter vessel showed that post irradiation drifts in high-energy photon and electron beams were significantly different at 22°C compared to 4°C and this led to extrapolation, and thus dose, errors of 0.5 - 2% depending on the initial temperature distribution. We performed extensive numerical heat transfer calculations in which convective motion was modeled in detail. The results show that at 22°C, fluid velocities of up to 10 mm/min outside the sealed vessel combined with modest velocities inside the vessel explain the observed post irradiation drift rates as well as the differences in measured dose between 4°C and 22°C. Moreover, our calculations show that, in the case of the NIST calorimeter, which is operated at 22°C and where the vessel diameter is 33 mm, heat transport resulting from movement outside the vessel and excess heat in the vessel wall may lead to dose overpredictions of, on average, 0.5% for 6 consecutive 70 s runs. It is also shown that there is slow but definite movement inside the NIST vessel because of the electrical dissipation in the thermistors and the slight non-uniform dose profile over the vessel when irradiated. The results of our convection calculations are consistent with the recent intercomparisons of absorbed dose standards between NRC and NIST, which show a difference of 0.5%. Our paper also discusses convection in different vessel designs in operation at several standards laboratories.

[1]Present address: Medical Physics Unit

McGill University, Montreal General Hospital

Montreal, Quebec, Canada, H3G 1A4

Email: jseuntjens@medphys.mcgill.ca

I. INTRODUCTION

One technique for establishing the absorbed dose under reference conditions is calorimetry. Because water has absorption properties for ionizing radiation similar to biological tissue, it has been chosen as the standard reference material for radiation therapy. Over the last two decades several standards laboratories have worked on the development of water calorimeters with the intention of direct calibrations of instruments in terms of absorbed dose to water. One major hurdle for water calorimeters to become primary standards was the heat-defect provoked by radiation induced chemical reactions in water. The second major problem for the delay in initiating the work specifically on *stagnant* water calorimeters has been the concern about convection and its effect on the accuracy of measuring the absorbed dose. A definitive way of eliminating convection is to operate the calorimeter at 4°C, where the density of water is maximal. In relation to stagnant water calorimetry this practice has been adopted in the Yale [1] and the PTB (Braunschweig, Germany; [2], [3]) calorimeters and later on also in the Gent (Belgium; [4]) system and the NRC system [5].

Domen [6], who initially introduced the idea of measuring absorbed dose at a point in water at ambient temperature, argued that convection at the point of measurement can be reduced or eliminated by the introduction of barriers. His design concept was based on the so called Rayleigh criterion which states that the characteristic Rayleigh number Ra for water, being the product of the Grasshof (Gr) and the Prandtl (Pr) number should not exceed the value 1700. Ra is proportional to $\Delta T x^3$ where ΔT represents a temperature difference, and x a characteristic distance over which this temperature difference exists. The vessel in the second generation NIST calorimeter [7] therefore serves as a convective barrier in addition to ensuring water purity. Its diameter was chosen as a compromise between reducing the likelihood for initiating convection on the one hand, and concerns about excess heat by the glass wall on the other hand.

There is little information about convection set in motion by the non-uniformity of the dose profiles in a stagnant water tank. In this respect, the criterion for the onset of convection has always been somewhat arbitrary. Therefore, convection in stagnant water calorimeters has been the subject of some discussion. Schulz and Weinhous [8] reported problems with convective heat transfer when their calorimeter was operated horizontally, at high thermistor powers. In a letter to the editor Domen [9] argued that this was due to fluid flow set in motion near their entrance window and that this motion upset the

equilibrium temperature profile around the thermistors. The upset was most pronounced at the higher thermistor powers. In a poster paper, Barnett and Cormack [10] discussed convective effects generated in the beam penumbra in a vertically irradiated open water calorimeter where he used immersible thermistors and no convective barriers.

Another problem exists around the thermistor probe-ends where the gradients are such that the criterion for onset of convection might be easily violated. Domen [11] did a series of measurements of velocity effects around the thermistor bead at several power levels. His investigation was mainly concerned with the effects of *an existing* convective current on the equilibrium situation of a thermistor in water and he provided useful graphs to estimate the cooling rate that a given power and velocity would introduce in a calorimetric experiment. Nonetheless, he also attempted to measure whether power dissipation in a thermistor by itself would lead to natural convective motion. However, he could not observe evidence for convective motion around the thermistor for power dissipations less than 50 μW. In trying to reproduce some of these results at PTB, Domen *et al*. [12] pointed out that the measured threshold may be dependent on details of the probe construction. Based on his investigation of velocity effects of a thermistor in water [11], after convincing himself that the response of his sealed water calorimeter did not depend on the thermistor power dissipation and, most importantly, from the visual linearity of his chart tracings, Domen [7] concluded that convection was probably not a concern in his ^{60}Co measurements. Hence, in the NIST absorbed dose to water standard no corrections for convective heat loss are applied. Moreover, although Domen [7] performed some preliminary numerical estimates of the effects of *conductive* heat loss from the probes and from the vessel affecting the temperature at the measuring point, to our knowledge, in the NIST calorimeter standard, no corrections are applied for conductive heat transport.

At the PTB, the same vessel design has been adopted as in the NIST calorimeter. With this system, Krauss and Roos [3] reported no difference in dose results obtained at 4°C (where convection is eliminated) and 22°C, but no explicit numerical data were mentioned. Krauss and Roos [3] therefore also concluded that convection was probably not a concern in their system. In the present paper, we revisit the problem of convection in stagnant water calorimetry. We provide experimental evidence that large convective currents are present in room-temperature operated stagnant sealed and unsealed water calorimeters regardless of the orientation of the beam with respect to the calorimeter. Using numerical techniques we demonstrate that these convection currents may potentially lead to errors in the extrapolation procedure and thus dose determination. The magnitude of the extrapolation errors depends on the vessel size relative to the field size, the thermistor power, the dose-profile-generated temperature profiles and the irradiation/wait times. We show that, in specific cases, the extrapolation to mid-run to account for heat loss may work rather well even when convection is involved in the heat transport.

II. Materials and Methods

A. The NRC Sealed Water Calorimeter

A stagnant water calorimeter was constructed which can be operated both at 4°C and at room temperature and is described elsewhere [13] and in these proceedings by Ross *et al.* [5]. Briefly, the calorimeter consists of a 30 x 30 x 30 cm^3 water tank. The main elements of the calorimeter are shown schematically in Fig. 1.

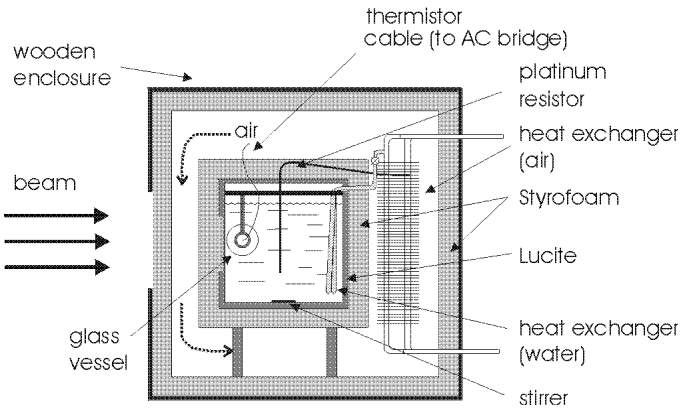

Figure 1: Side view of the sealed water calorimeter. The drawing is not to scale, but the sides of the outer box are approximately 85 cm long. The principal elements of the calorimeter are labeled on the drawing. Note that fluid is only allowed to flow through the heat exchanger in the water when a significant change in operating temperature is required.

Note that it is intended for use in radiation beams that are directed horizontally. The measurements of temperature increase are performed in the center of a cylindrical vessel of 60 - 67 mm diameter, and the thermistor probes are 0.4 - 0.5 mm in diameter at the probe end. The purpose of the vessel is mainly to control the purity of the water, by controlling the radiolysis induced heat defect. In this respect, the performance of the calorimeter was tested using a H_2-O_2 mixture and using H_2 saturated water in comparison with the pure water system. The measuring depth can be set by setting the position of the vessel at the appropriate distance from the front window so as to obtain the required measuring depth, *i.e.*, 5 cm at ^{60}Co, 10 cm at 20 MV, and 3.7 cm at 20 MeV electrons. The electronics consists of a bridge circuit containing the two thermistors in series in one arm of the bridge. The out of balance voltage of the bridge is measured using an AC lock-in amplifier. The voltage is converted into a relative temperature scale by using the measured thermistor sensitivity, and the bridge and amplifier response. In this work we compared shapes of drift curves under different operating conditions (power level, irradiation time, etc). To this end every run was studied relative to its extrapolated pre-drift signal i.e. the pre-drift portion was first linearly fitted and time point by time point subtracted from the uncorrected temperature signal.

Subsequently, the data have been normalized to the integrated linac monitor signal.

Although this paper does not deal with the absolute performance of the NRC sealed water calorimeter, we report comparisons of the calorimeter dose at 4°C and 22°C to introduce our discussion of convection. Therefore we briefly summarize the basic formula and procedure of how absorbed dose is inferred from calorimetric measurements. The absorbed dose to water is determined at a point by measuring the temperature increase, ΔT_w, at that point due to radiation. This is done using thermistors whose material constants were measured against thermometer standards. Once the temperature increase, ΔT_w, is known, the absorbed dose to water, D_w, can be obtained from

$$D_w = \Delta T_w \cdot c_w \cdot k_c \cdot k_p \cdot k_{dd} \cdot k_\rho \cdot \frac{1}{1-k_{HD}}, \qquad (1)$$

where c_w is the specific heat capacity at constant pressure, and the correction factors k_i have following meaning:

k_c a correction for heat loss. This correction is applied *on top of* a linear extrapolation to mid-run, both forward from the pre-drift as well as backward from the post irradiation drift curve. Heat losses can be the result of conduction as well as convection;

k_p a correction for the field perturbation due to scattering properties of calorimeter construction materials differing from water. It is determined by measuring with an ion chamber in the center of the glass vessel, and at the same point without the vessel present;

k_{dd} a correction for the non-uniformity of the lateral dose profile in the measuring plane. This correction is determined by measuring the dose profile in the plane of the thermistors;

k_ρ a correction for the difference in density of water between 22°C and 4°C;

k_{HD} heat defect due to radiation induced chemical reactions. The correction for the heat defect is inferred from measurements with three chemical systems producing known heat defects;

The details of the correction factors in high-energy photon beams and other studied factors are the subject of the paper by Ross *et al* [5] in these proceedings.

B. Radiation Beams and Dose Profiles

Along with construction details of the calorimeter, the shape of the dose profile determines the heat loss problem. We performed experiments using the NRC sealed water calorimeter in three different beams, i.e. ^{60}Co, 20 MV photons, and 20 MeV electrons. In the ^{60}Co beam, the measuring distance was 70 cm, and the field size at the measuring depth of 5 cm was 8.5 cm x 8.5 cm. The dose rate was 1.5 Gy/min, and irradiations were typically 2 min. The NRC 20 MV photon beam is produced by allowing 20 MeV electrons to impinge on a fully-stopping aluminium target. To obtain a flat field, the electron beam is swept along the surface of an imaginary cone, with the apex of the cone being fixed at a point on the surface of a plane x-ray target. We use a cone angle of 4.2°. The dose rate at the reference point of 10 cm amounted to 1.5 Gy/min as in the ^{60}Co case. For the 20 MeV electron measurements, a scattering foil was used for beam flattening. In this case the dose rate was varied from essentially the photon dose rate up to 38 Gy/min. For both linac beams, the field size was set by a jaw system from a clinical accelerator. Fig. 2 shows measured profiles and depth dose curves for the modalities used in these experiments. The shape of the profile and the position of the vessel influence the heat loss pattern in the calorimeter.

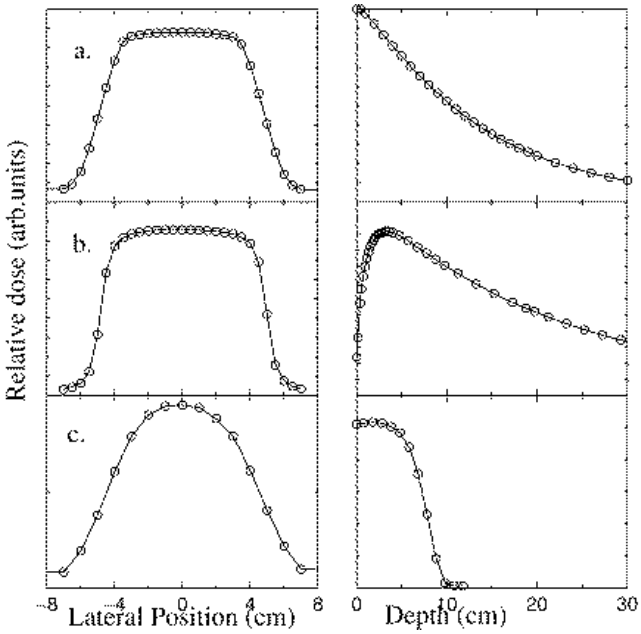

Figure 2: Dose profiles for the ^{60}Co (a), 20 MV photons (b) and the 20 MeV electron (c) beams. The center of the 6 cm diameter vessel is at 5 cm, 10 cm and 3.7 cm in the ^{60}Co, 20 MV photon and the 20 MeV electron beam respectively.

III. Heat Transfer Calculations

A. Numerical Details

We have chosen to develop our own conduction-convection code to simulate the heat and mass transport associated with the small temperature rises induced in a water calorimeter. General purpose codes to solve the heat transport problem including convective flow are available, but are generally mainly used for the purpose of calculating a much wider range of temperatures and flow rates. By limiting ourselves to small temperature rises, a number of simplifications can be built into the governing equations. The problem of heat transport through conduction and convection in the calorimeter was modeled numerically using the control volume method. The basic differential equations are the

continuity equation, the motion equations and an equation expressing the conservation of energy. In the case of natural convection in an incompressible fluid, the pressure gradient is only resulting from volumetric expansion and the presence of the gravitational field. We furthermore ignore the energy contributed by viscous dissipation[1], and assume that the thermal conductivity, viscosity, and specific heat capacity are temperature independent at the operating temperatures we studied (*i.e.*, 4°C and 22°C). This is reasonable in view of the order of magnitude of the temperature changes and fluid velocities studied, *i.e.*, less than 0.5°C and 100 mm/min respectively.

Under these conditions, the problem amounts to integrating the following set of equations using boundary conditions imposed by the calorimeter, vessel and probe geometry:

$$\sum_j \frac{\partial u_j}{\partial x_j} = 0 \tag{2}$$

$$\rho \frac{\partial u_i}{\partial t} + \rho \sum_j u_j \frac{\partial u_i}{\partial x_j} = \nu \sum_j \frac{\partial^2 u_j}{\partial x_j^2} - \frac{\partial p}{\partial x_i} + B_i \tag{3}$$

$$\rho c_p \frac{\partial T}{\partial t} + \rho c_p \sum_j u_j \frac{\partial T}{\partial x_j} = \sum_j \frac{\partial}{\partial x_j} k \frac{\partial T}{\partial x_j} + \rho \frac{dD}{dt} \tag{4}$$

where:

u_i the ith component of the velocity field, i.e., $u_1 = u$, $u_2 = v$, $u_3 = w$;

x_i, the i'th component of the coordinates in a cartesian system, *i.e.*, $x_1 = x$, $x_2 = y$, $x_3 = z$;

t, the time;

ρ, the density of the medium, in this case either water or glass. The water is considered to be incompressible, except for the density change due to volumetric expansion needed to generate boyancy forces (see further);

ν, the dynamic viscosity of the medium, in this case water. Because it is assumed to be temperature independent, it can be taken as constant throughout the geometry;

p, the pressure field (see further);

B_i, the i'th component of the body force, in this case only generated in the vertical direction by the gravitational field, *i.e.*, $B_1 = B_3 = 0$, $B_2 = -\rho g$;

c_p, the specific heat capacity at constant pressure in this case for water and glass;

T, the temperature field;

k, the thermal conductivity of the medium, in this case water or glass;

dD/dt, the dose rate at the point of interest. For this we assumed the radiation absorption characteristics for glass to be the same as for water, *i.e.*, the dose in glass was assumed to be the same as the dose in water.

The volumetric expansion enters into the motion equations (Eq. 2) through the body force and the pressure gradient. The temperature dependence of the density is approximated by:

$$\rho(T) = \rho_0 + \frac{\partial \rho}{\partial t}(T - \bar{T}) = \rho_0(1 - \beta(T - \bar{T})) \tag{5}$$

where T - $\bar{T}$ is the temperature rise (compared to the average ambient temperature) producing the local density decrease. For the calculation of the pressure gradient in equations (3) we split up the pressure into two components:

$$p = p_0 + p' \tag{6}$$

where $p_0 = -\rho_0 g y$ so that the terms involving the pressure gradient and the body force in the vertical direction (y) become:

$$-\frac{\partial p}{\partial y} + B_2 = \frac{\partial p'}{\partial y} + \rho_0 g - \rho_0 g(1 - \beta(T - \bar{T})) = -\frac{\partial p'}{\partial y} + \rho_0 g \beta (T - \bar{T}) \tag{7}$$

In all this ρ_0 represents the nominal density of water. Ignoring density variations in the continuity equation is justified considering the maximal temperature increases and the corresponding velocity gradients near temperature inhomogeneities. The cartesian coordinate system was chosen as represented in Fig. 3 with the gravitational field pointing downward according to the negative y-axis, and for horizontal irradiations, the depth dose profile developing in the x-direction, and the lateral profiles in the y and z direction. Measured profiles (section II.B) were used as input to the calculations.

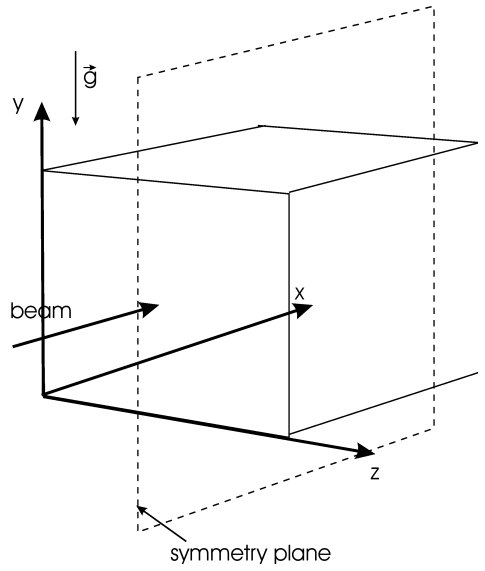

Figure 3: Choice of the coordinate system for the integration of the heat transport equations.

[1]For water flow of the order of 100 mm/min, the viscous dissipation can be compared with the conduction term by comparing $\mathrm{Pr}\, v^2/(c_p T)$, 1.3 10^{-11}, with unity [14].

In order to discretize the equations, a grid is constructed covering essential elements of the complete calorimeter geometry. The voxels of the geometry were of variable size depending on the thickness of the non-water components present in the geometry. For example, near the probe ends the minimal size of a single dimension of a voxel could amount to 0.1 mm, whereas away from any glass structure the voxel dimension was typically 2 cm.

The temperature was calculated at each grid point by discretization of the equation for conservation of energy, using the control volume method as described in Patankar [15]. For the energy equation, this method amounts to evaluating the energy balance over the finite volume around the point of interest (point *P* in Fig. 4).

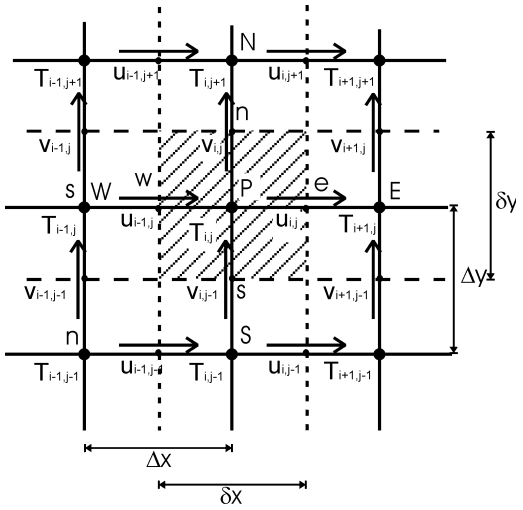

Figure 4: Two dimensional representation of the grid arrangement (extension to the third dimension is straight-forward). Shown are a calculation point *P* around which a control volume is constructed. The velocity components u, v, w are calculated on grids staggered in x, y, and z direction respectively.

Although the grid is not necessarily regular, the faces of a control volume around a point *P* have been chosen to cross midway between two neighbouring grid points. Thermal properties of the materials, such as thermal conductivity *k*, in the geometry in-between two grid points, *e.g.,* at the "east" interface "e" of the control volume, were interpolated as:

$$k_e = \frac{2k_P k_E}{k_P + k_E} \tag{8}$$

where k_E represents the thermal conductivity at the grid point lying just East of the current calculation point *P*.

In order to express the energy balance over a control volume in a problem incorporating fluid flow, the velocity at each grid point is required. The calculation of the velocity field requires the evaluation of the pressure gradient over the faces of the control volume around the point at which the velocity needs to be established. The pressure field is calculated on the same grid as the temperature field. To simplify the calculation of the pressure gradient, velocities in each dimension were calculated on a grid staggered in that direction, *i.e.*, the grid for the calculation of u, the velocity component in the x-direction, is staggered in the x-direction over half the distance between two neighbouring temperature grid points. In this way the faces of a control volume on the staggered grid coincide with the grid points on the pressure (and temperature) grid, so that the pressure gradient calculation becomes more straightforward.

The discretization of the equation for the temperature field was carried out using the techniques described in Ref [15] where the discretization coefficients are calculated according the so-called Power-Law scheme. To ensure physically realistic temperatures regardless of the duration of the chosen time step, the discretization equation of the temperature field has been carried out using a fully implicit method, by which the temperature field at the new time point is calculated based on the field at the point of interest at the previous time step, T^* plus a summation of contributions from the neighbouring cells of the field *at the new time*, and a source term as:

$$a_P T_P = a_{P_0} T_P^* + a_E T_E + a_W T_W + a_N T_N + a_S T_S + a_L T_L + a_R T_R + S \tag{9}$$

In an iterative loop at a given time point, the maximum temperature increments are calculated until a prescribed accuracy is achieved. The temperature field is initially calculated by making use of the flow field at the previous time step (initially zero). The home made solving algorithm then proceeds with a double iteration loop as follows:

1. An estimated flow field u^*_j (j=1,2,3) is calculated using a discretization of the motion equations (3) in an explicit scheme. For this purpose use is made of an initial estimate of the pressure field p and the velocity fields u_j (j=1,2,3) based on the evolution over the last three time steps. The time step for the pressure and velocity field is different from the time step for the calculation of the temperature field, so that the velocity iteration loop can, but does not necessarily needs to be executed at every time step. We chose a time step of 0.5 s, for both temperature and flow field calculation.
2. In order to correct the guessed flow field u^*_j to get u_j a pressure correction is calculated by iteration. The equation for the calculation of the pressure correction is essentially a discretization of the continuity equation (2) where the velocity components are composed of the guessed velocities of step 1 plus a term containing the pressure correction. By enforcing continuity in an iterative process, a pressure correction is calculated.
3. This pressure correction is used to improve the estimated velocity field upon which the maximal change in velocity anywhere in the geometry is calculated and, if found too large, returned to step 1 with a more accurate estimate of the velocity field.

The iteration loop proceeds until a prescribed accuracy of the velocity, being the maximum change in velocity throughout the field in the previous iteration step, has been achieved. A verification of the final velocity field is performed, by evaluating and logging the left term of continuity equation (2). With this new flow field the program performs the calculation of the temperature field at the new time step.

Every second the temperature in the center of the thermistor is recorded as well as its ratio to the true temperature assuming no heat transport. At larger selected time increments, the three velocity components on a line along the beam axis, through the center of the thermistor are recorded. At chosen time points we saved the velocity field of the entire geometry to the disk and complementary programs were written to plot streamlines based on these velocity fields as well as maximum and minimum velocity vector lengths.

B. Simulation Geometries and Analysis of Calculated Drift Curves

The sealed water calorimeter is assumed to consist of two materials, i.e., water and glass. In the case of the open water calorimeter, the foils were of polyethylene, or the thermistors were of glass when used freely without foils. For all calculations, the dimensions of the calorimeter tank were 30 x 30 x 30 cm^3. The electrical power dissipation in the thermistors was also simulated since it gives rise to initial movement of the water near the thermistors inside the vessel or around the foils. For this purpose, flow patterns were allowed to develop for a time span of at least 1000 s after the onset of electrical power before radiation was turned on. During this pre drift period, to save cpu time, the heat transport outside the vessel was assumed to be entirely through conduction. Generally a sequence of at least 5 runs was simulated with times of about 2 - 3 mins between each run. Pre-drift and post-drift were extrapolated linearly to mid-run and compared with (i) the true temperature rise, and (ii) a calculation which only includes conduction.

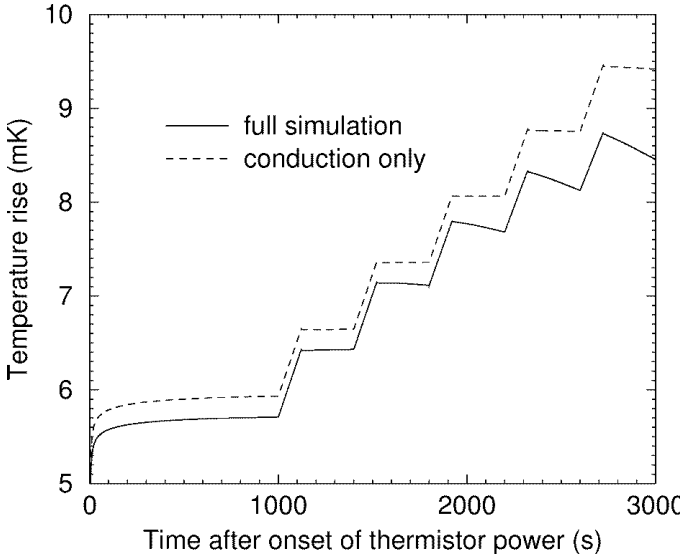

Figure 5: Example of raw temperature drift curves for ^{60}Co in a full simulation compared to simulating conductive heat loss only. After 1000s of pre-drift, during which power dissipation in the thermistors is the only heat source, a sequence of irradiations commences.

Fig. 5 shows an example of the simulated ^{60}Co drift curves in a full simulation of the NRC calorimeter and in conductive mode only.

The above described analysis has been used further to calculate the ratio of the real temperature and the true temperature rise over a single run (see section IV). For the sealed water calorimeter, the vessel, probe dimensions and power dissipation and the beam dimensions are summarized in Table 1.

Table 1.
Vessel position and dimensions, probe dimensions, power dissipation, radiation types, and duration used in the heat flow calculations of the sealed water calorimeter.

Vessel type	Vessel dimensions.	Probe	Beam			
	l,h,w (mm^3)	l.h.w [Power(μW)]	Orientation	Field size (cm^2)	Radiation type & Dose Rate	Measuring Depth & Irradiation time
NRC	65,65,100	0.40,0.40,46 [6.4]	H	10 x 10	^{60}Co, 1.5Gy/min	5 cm, 120 s
		0.40,0.40,46 [6.4]	H	10 x 10	20 MV X, 1.6Gy/min	10 cm, 120 s
		0.40,0.40,46 [0.6-324]	H	10 x 10	20 MeV e^-, 2 to 40Gy/min	3.9 cm, 120 s - 30 s
NIST	30,30,100	0.40,0.40,46 [9,30,100]	V	15 x 15	^{60}Co, 1.8Gy/min	5 cm, 70 s
LNHB	100,120,120	0.30,0.30,58 [1,8,50]	H	10 x 10	^{60}Co, 1.8Gy/min	5 cm, 120 s

We also performed simulations for the first generation [6] open water calorimeter. The foils were simulated as a square of 12 cm by 12 cm each of 18 μm thick polyethylene. To simulate the NIST conditions, a large uniform field and a collimated, vertical ^{60}Co beam of 1.1 Gy/min (180 s irradiation time, 160 s after drift and a sequence of 5 runs) were used. Simulations were also carried out in exactly the same geometry but simulating only the thermistor beads (immersible detector) without the foils.

IV. Results and Discussion

A. Measured Calorimeter Dose Differences Between 22°C and 4°C

To our knowledge, numerical data showing a direct comparison of dose measurements with a stagnant water calorimeter operated at 22°C and 4°C have not yet been reported in the literature. At NRC we compared dose measurements at 4°C with those at 22°C. Table 2 shows the results of the calorimeter response at 4°C and at 22°C for ^{60}Co and 20 MV photons.

Table 2.
Comparison of the response of the NRC sealed water calorimeter at 4°C and 22°C for ^{60}Co and 20 MV radiation. Irradiation times amount to 120 s, and the dose rate is 1.5 Gy/min and 1.6 Gy/min for ^{60}Co and 20 MV respectively. At 20 MV the response is expressed in terms of an apparent calibration factor of the NE2571 chamber (SN 667).

Radiation Quality	System	Apparent Calorimeter Response		Ratio 22°C/4°C
		22°C	4°C	
^{60}Co	Pure water	1.617 (±0.12%) Gy/min	1.606 (±0.10%) Gy/min	1.0068
20 MV	Pure water	4.346 (±0.13%) Gy/nC	4.323 (±0.10%) Gy/nC	1.0053
	H_2/O_2	4.449 (±0.14%) Gy/nC	4.421 (±0.16%) Gy/nC	1.0063

For the pure water systems, 200 to 300 runs are involved in the dose ratio numbers, while for the H_2/O_2 there are about 120 runs involved. All runs had 120s pre-drift time, irradiation and post irradiation drift time and the fit on the post irradiation drift curve for the extrapolation procedure commenced 20s after irradiation stop. All discussed calorimeter correction factors at 22°C and 4°C were included in the analysis. From a separate investigation of the up-to-date values of the specific heat capacity of water we concluded that the Osborne *et al.* [16] data were probably accurate to better than 0.05%. Other mechanisms for response differences between 22°C and 4°C were examined and found to be insignificant. Since the thermal diffusivity of water at 22°C is only higher than that at 4°C by about 6%, the only remaining possibility for a significant response difference between 22°C and 4°C could be convective motion.

Another indirect comparison of sealed water calorimeters operated at 22°C and 4°C is the comparison of the absorbed dose standards between NRC and NIST [17]. The results of this comparison show that Domen's 22°C operated calorimeter gives a dose number that is 0.5% higher that the 4°C operated NRC calorimeter, although some caution should be exercised when comparing the two calorimeters, since some of the correction factors such as the conductive effect of the 3.3 cm diameter vessel is not explicitly accounted for in the NIST case.

Contrary to the two above observations is the work of Krauss and Roos [3] who report no differences between operating their calorimeter at 4°C and 22°C.

B. Temperature Drift Curves at 22°C and 4°C

1) High Dose-rate Irradiations in 20 Mev Electrons and Thermistor Power Dissipation Effects

In order to study the calorimeter response at 4°C and 22°C more easily, we performed irradiations in a high dose-rate electron beam and also varied the thermistor power dissipation. Fig. 6 shows calorimeter temperature drift curves generated by irradiating the calorimeter with 20 MeV electrons (dose rate 38 Gy/min, 30 s).

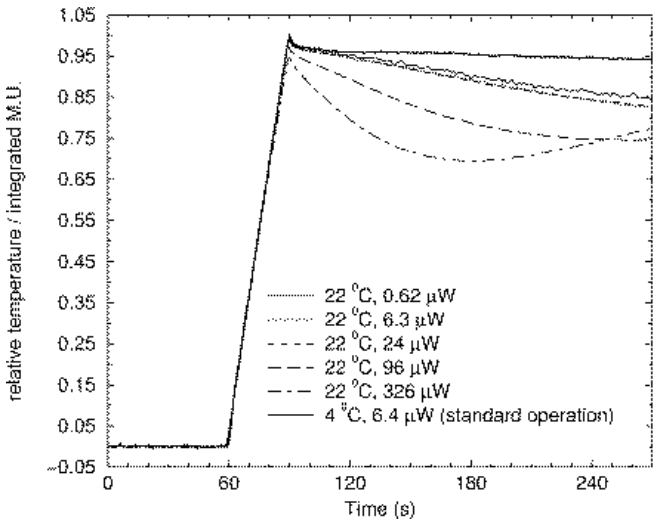

Figure 6: Examples of typical 30 s runs with the calorimeter operated at different power levels (0.62 μW, 6.3 μW, 24 μW, 96 μW, and 324 μW) at 22°C and at 4°C (6.3 μW). The dose rate amounts to 35 Gy/min and the temperature rise at the measuring point is about 4.6 mK.

At 22°C drift curves at several power levels are shown, and the post irradiation drift rates above 24 μW, are significantly different in shape compared to each other and compared to the 4°C drift. An important observation is that, at least at the low thermistor powers, although there is no visible non-linearity on

the increasing part of the temperature curve, the post irradiation slopes are significantly different from the 4°C operation: At 22°C and low thermistor powers there is a 26% decrease in 5 min compared to a 3.7% decrease over the same time span at 4°C. There exists a significant dose gradient over the water in the vessel, as obvious from Fig. 2. The fact that the post irradiation drifts are so different demonstrates that the heat-loss to the cold water areas outside the field or downstream at 22°C is more efficient than at 4°C, by a magnitude that cannot be explained by the 6% difference in thermal diffusivity. The fact that this is even true at the lowest thermistor powers means that 22°C movement is most significant outside the vessel, although at this point movement inside the vessel can also not be ruled out. When the thermistor power is increased above 24 μW, the situation at 22°C gets gradually worse proving that movement around the thermistor probes begins to play a significant role in the heat-loss from the thermistor probes at higher power levels. We also performed experiments at 4°C for thermistor powers of 6.4 μW, 98 μW and 150 μW (not shown) and no significant dependence of the post irradiation drift rate - and therefore calorimeter response - on power level was observed. The calorimeter response resulting from extrapolation to mid-run at 22°C (for 0.6 μW) was approximately 1% high compared to the 4°C result (at all powers).

Simulations of these experiments were performed at 22°C and at 4°C. It turned out that, as expected, at 4°C, the velocities were of the order of 10^{-6} - 10^{-5} mm/s and that convergence to the preset velocity accuracy (10^{-8}) was very slow. The result of a complete 4°C calculation however was in agreement with the result of a calculation at 4°C with only conductive heat loss. Therefore, in the remainder of the paper, we have used simulations with conduction only as being equivalent to the 4°C result. Fig. 7 shows a comparison of measured and calculated post irradiation drift curves for 3 consecutive 30 s runs at 38 Gy/min and 6.4 μW, with approximately 300 s in between the start of each run.

Except for the first run, the agreement between the experimental and the numerical result is excellent. The deviation for run 1 can be attributed to the following fact. The post irradiation drift curves are generated by linearly fitting a 60 s pre-drift, and subtracting the whole run from this extrapolated pre-drift, and are therefore strongly dependent on the linearity of the pre-drift. Since the post irradiation drift shows a typical concave shape, this assumption gives rise to some uncertainty in the extrapolation at least from run 2 on. Further calculations (not shown) show that the 4th, 5th, etc runs produce post irradiation drift curves which are close to run 2 and 3 shown in Fig. 7. This means that the dose obtained by extrapolation to mid run yields a reproducible dose value which is wrong by up to 3% to 4%, yet with reasonable statistical uncertainty. Fig. 8 shows the simulation of the experiments summarized in Fig. 6.

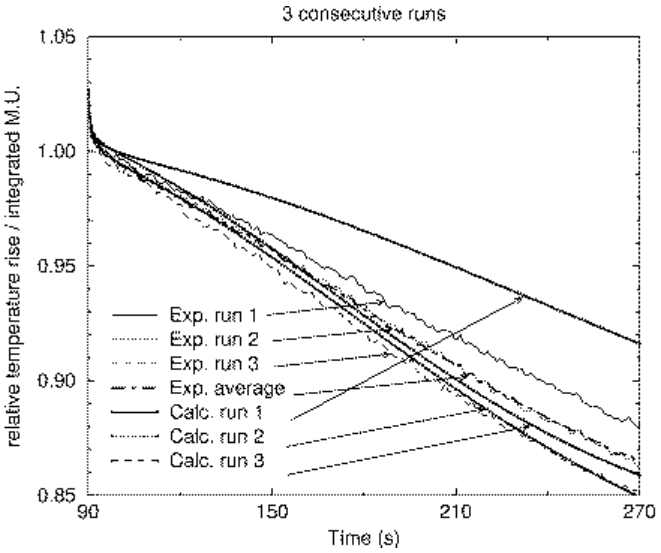

Figure 7: Three consecutive calorimeter 30 s runs in 20 MeV electrons with approx. 5 min between the start of each irradiation. The operating temperature amounts to 22°C and the thermistor power level is 6.4 μW. The dose rate amounts to 35 Gy/min and the temperature rise at the measuring point is about 4.6 mK.

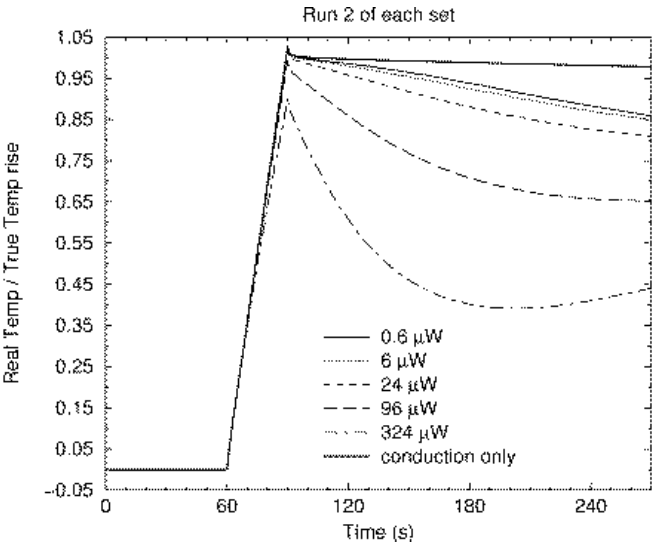

Figure 8: Simulation of calorimeter drift curves in 20 MeV electrons for different power levels under the same conditions as the experiment (Fig. 6). The second run at each power level was extracted from the calculations and the run was subtracted from the extrapolated pre-drift.

We extracted run 2 out of a simulated sequence of 8 runs. As in the experiments there is not much difference between 0.6 μW and 6.3 μW and the shape of the post irradiation drift curves is qualitatively reproduced at all powers although the calculated effect at high powers is slightly more dramatic than measured.

Fig. 9 summarizes the flow patterns inside the vessel, solely as a result of thermistor power, for several thermistor powers. The calculations show that for our vessel size, around the thermistor probes, the upward velocities near the

thermistor tip are of the order of 0.5 mm/min at 6.4 μW, 2 mm/min at 24 μW, 4.5 mm/min at 96 μW, and 9 mm/min at 324 μW. Thus, there exists a definite flow pattern inside the vessel before any run starts, and the shape of the flow pattern is qualitatively approximately the same, except for the very high powers where the region of maximum velocity has significantly moved upwards. The presence of the velocities reported here are not inconsistent with those in the paper of Domen [11] where he studied the drift effects of those velocities in a forced convection setup. As radiation is turned on, the existing flow is supplemented with more dramatic flow generated by the non-uniform dose profile over the vessel (Fig. 10).

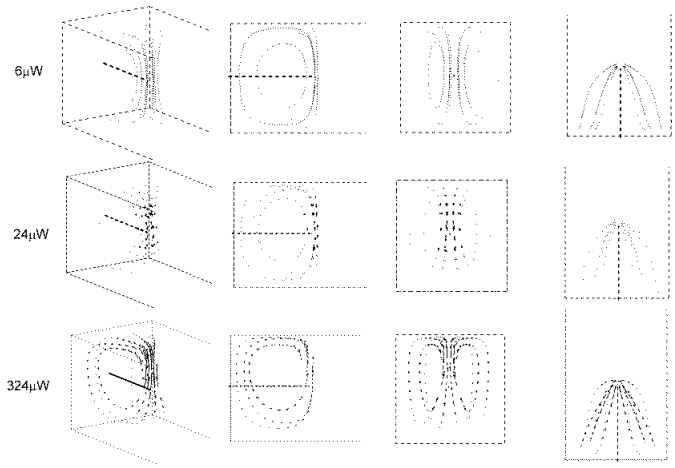

Figure 9: Flow pattern in the vessel as a result of electrical power dissipation for thermistor powers 6.4 μW, 24 μW, and 324 μW. From left to right, 3D-view, front view, side view, top view.

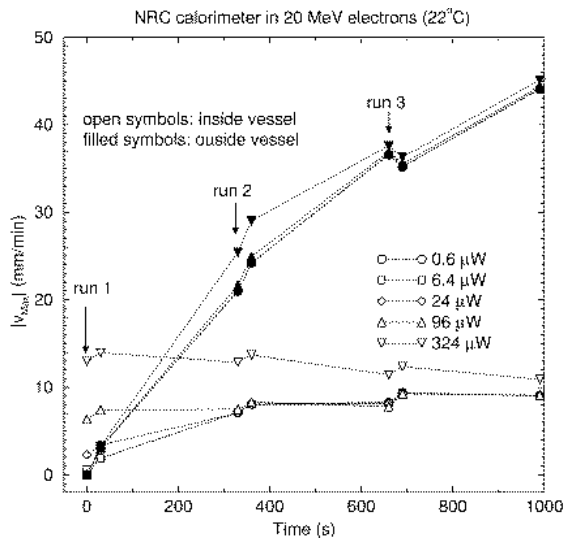

Figure 10: Calculated maximum velocity vector anywhere inside (open symbols) or outside (filled symbols) the vessel during the high-dose rate electron irradiations. The start of each 30 s run is indicated. Note that the first irradiation commences after 1000 s of pre-drift of power dissipation in the thermistor region have expired.

Inside the vessel, for the lower thermistor powers (0.6 μW, 6.4 μW, and 24 μW) the change in fluid velocity upon onset is significant during the first two runs, and the influence of the initial thermistor power dissipation quite limited. Therefore, the post irradiation drift slopes are not very dependent on the thermistor power at these powers and mainly determined by the heat-loss resulting from the irradiation induced flow pattern in and outside the vessel. At the high power levels (96 μW, 324 μW) the maximum velocity is nearly only determined by the initial power dissipation and the shape of the post irradiation drift curve is significantly determined by the initial electrical power level (Fig. 6). As irradiations are carried out, the maximum velocities inside the vessel converge to a uniform terminal velocity regardless of the thermistor power dissipation. Outside the vessel, all thermistor power dissipations are nearly equivalent in how they affect the velocity outside the vessel. Note that maximum velocities after three 30 s runs are of the order of 40 mm/min. Note that at 324 μW, the maximum velocity inside the vessel *decreases* as irradiations are carried out, and the flow pattern set up outside the vessel removes heat from the vessel.

2) Low dose-rate irradiations in 20 MeV electrons

One would expect the post irradiation drift slopes to be less and even similar to the 4°C case when the calorimeter were to be operated at a much lower dose rate because the temperature gradients in the vessel are smaller and convection would gradually disappear. Fig. 11 shows measured drift curves when the calorimeter was irradiated with 20 MeV electrons at dose rates of 2.4 Gy/min and run times of 120 s.

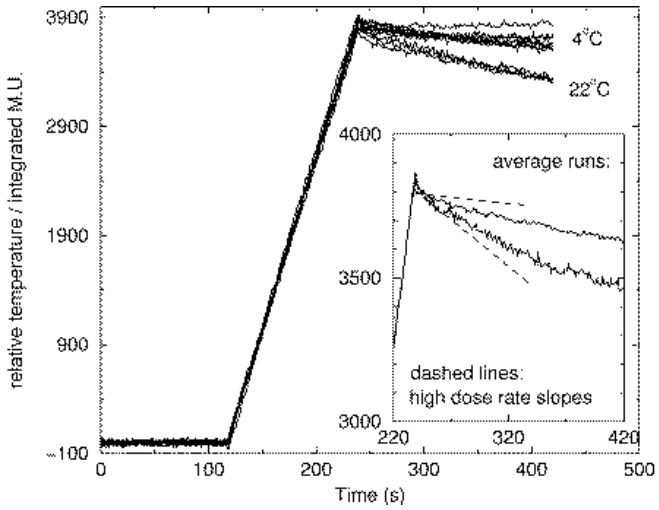

Figure 11: Examples of typical 120 s runs with the calorimeter operated at 22°C and 4°C at dose rates of 2.4 Gy/min. The temperature rise at the measuring point is about 1.1 mK and the thermistor power is 6.4 μW.

The thermistor power dissipation was 6.4 μW in all irradiations. In the inset, the average post irradiation drift slopes are indicated together with the slopes from the high dose rate experiments. Again, although during the runs no

obvious "onset point" can be recognized, the post irradiation drift slopes are still significantly larger at 22°C (-18% / 5 min) compared to 4°C (-7% / 5 min) and the difference is smaller than for the high dose rate experiments as indicated by the dashed lines in the inset. This indicates that convection is still part of the heat transfer process, although to a lesser extent.

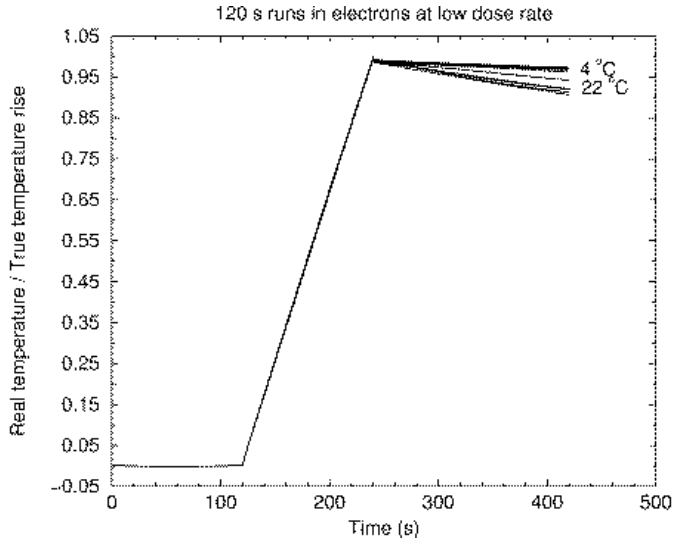

Figure 12: Calculated 120 s runs for the same conditions as the experiments shown in Fig. 11.

Fig. 12 shows the simulations carried out under the same conditions normalized on the true temperature rise. The calculated slopes are -15% / 5 min at 22°C and -5% / 5 min at 4°C which compare reasonably well with the experiments. Also clear from Fig. 12 is the larger, yet acceptable spread on the post irradiation drift curves. A larger spread on room temperature calorimeter operation compared to 4°C has been mentioned before in the context of convection investigations [3].

In the experiments, the calorimeter response at 22°C resulting from extrapolation to mid-run is about 1% higher than at 4°C compared to about 1.5% in the calculations, and the 4°C extrapolated result is 0.2% to 0.3% low compared to the true answer. The fact that convection is part of the heat transport in the low dose-rate electron experiments means that for the photon experiments (section IV A), convective motion is likely to be present and responsible for the observed difference in extrapolated temperature rise.

3) Irradiations in ^{60}Co and 20 MV Photon Beams

Calculations were carried out to simulate the irradiations at ^{60}Co and in 20 MV X-rays. The situation at both radiation qualities is similar because the dose rate, irradiation time and lateral as well as depth gradients are similar. The differences between drift curves at 4°C and 22°C are also much less than in the case of the 20 MeV electron irradiations. Fig. 13 shows measured average calorimeter runs at 4°C and 22°C.

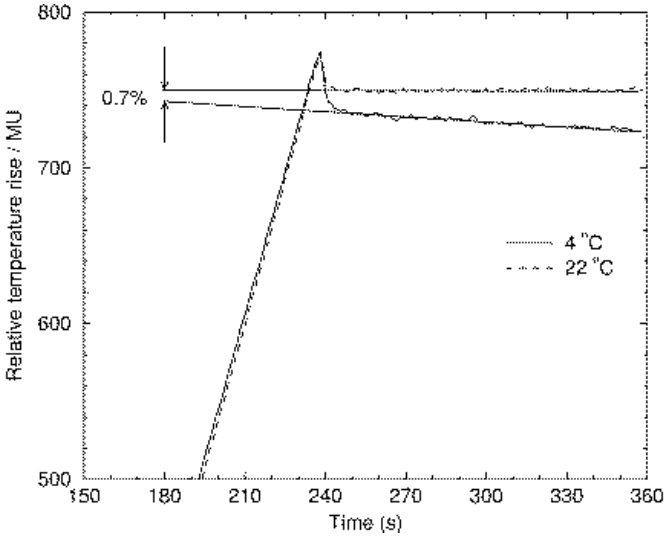

Figure 13: Measured calorimeter response at 4°C and at 22°C calculated by subtracting all runs from their respective extrapolated pre-drift and then averaging typically 10 to 15 runs. The response is normalized on the integrated linac monitor reading.

The extrapolation to mid run yields a difference of approximately 0.7% and it turns out that, contrary to the electron work, the post irradiation drift slope at 22°C is slightly *lower* than at 4°C but both for ^{60}Co and for 20 MV X-rays the post irradiation drift slope amounts to no more than 2% / 5 min. Because of noise, no significant difference in spread on the measured runs at both temperatures could be detected.

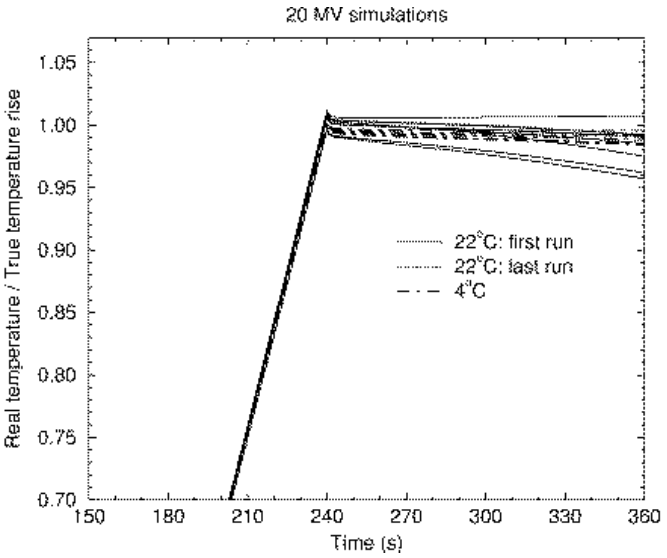

Figure 14: Calculated calorimeter response at 4°C and at 22°C calculated as the ratio of the real temperature to the true temperature increase during an entire run. The same conditions were used as the experiments shown in Fig. 13.

Fig. 14 shows the simulation of the same experiment. Typically 8 runs were simulated after having achieved a steady state drift, resulting from powering on the thermistors. Note

that at the end of the irradiation (240 s) some but not all of the runs, at 22°C show a response larger than expected from conduction. The spread on the calculated response is larger at 22°C than at 4°C, but of just comparable magnitude as the electronic noise. The difference in average post irradiation drift slope between both temperatures is small and the slopes are comparable with the experiments. At ^{60}Co the differences between post irradiation drift curves at 4°C and 22°C are slightly smaller than for the 20 MV case. The post irradiation drift slopes at ^{60}Co are between -1% / 5 min and 12% / 5 min averaging to 6% / 5 min. The effect of extrapolating to mid-run at 22°C and at 4°C is summarized in Table 3. The differences between 4°C and 22°C can be compared with the experimentally measured differences of 0.7% at ^{60}Co and 0.6% at 20 MV respectively. Note that, due to the fact that the geometry is cartesian, the corrections obtained are not the same as reported in Ross *et al* [5].

Table 3.
Calculated ratio of the extrapolated response to the true temperature rise at 4°C and 22°C for the NRC ^{60}Co and 20 MV irradiations and their average values for a sequence of 8 irradiations.

Run No.	^{60}Co		20MV	
	4°C	22°C	4°C	22°C
1	1.0021	0.9993	1.0018	1.0054
2	1.0027	1.0027	1.0023	1.0057
3	1.0030	1.0067	1.0026	1.0219
4	1.0030	1.0121	1.0027	1.0097
5	1.0030	1.0100	1.0026	1.0104
6	1.0029	1.0083	1.0026	1.0107
7	1.0029	1.0088	1.0025	1.0109
8	1.0028	1.0062	1.0024	1.0093
Average	1.0028	1.0068	1.0024	1.0105

C. Calculated Streamlines in the Sealed Water Calorimeter

In Fig. 9 we showed the flow pattern inside the NRC vessel and the maximal magnitude of the velocity for normal operating powers is less than 1 mm/min. Inside the vessel this flow is accelerated by non-uniformities of the dose generated temperature profile but remains of the order of a couple of mm/min and did not exceed 10 mm/min for the highest dose rates studied. If the dose profile over the vessel is perfectly uniform, the velocities inside the vessel remain extremely small. Outside the vessel the flow is much more dramatic.

Fig. 15 illustrates this point and shows the maximal velocity inside and outside the vessel of the NRC calorimeter irradiated at 20 MV. Although the dose profile is not perfectly uniform over the vessel, the velocities inside the vessel remain smaller than 3 mm / min after three irradiations. Before the first irradiation, for 6.4 μW, the maximal velocity inside the vessel was about 0.5 mm / min.

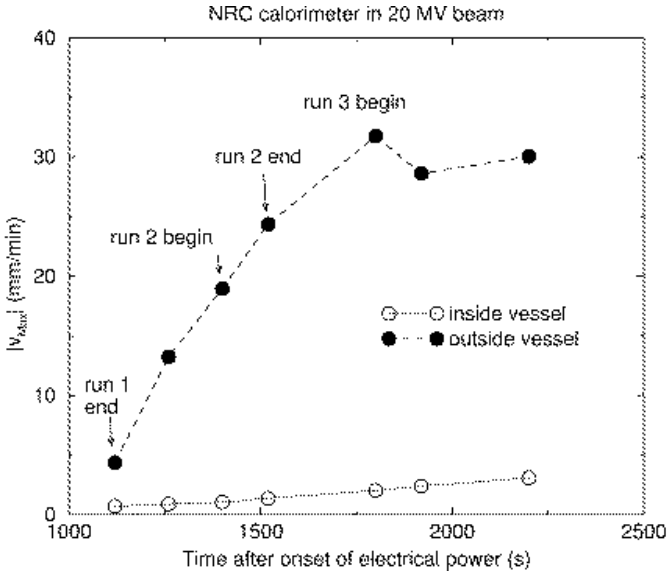

Figure 15: Maximal velocity inside and outside the vessel of the NRC calorimeter irradiated at 20 MV under the same conditions as before.

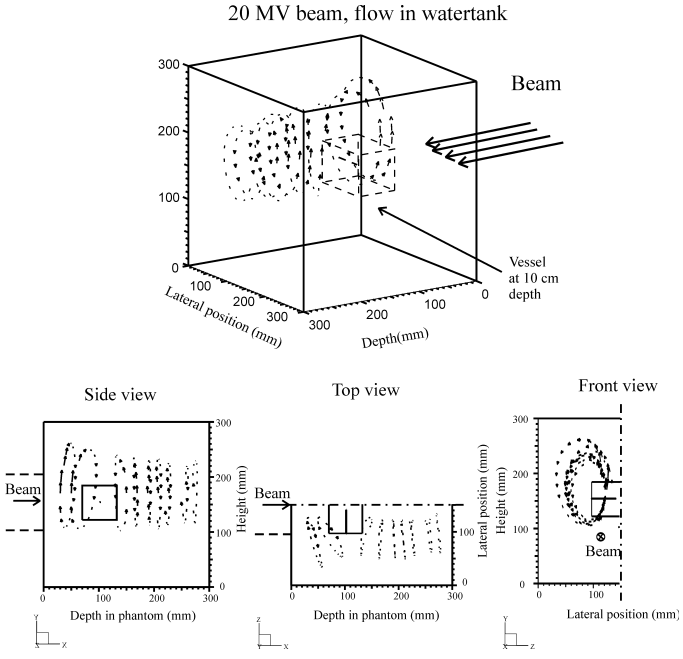

Figure 16: Flow pattern in the calorimeter tank after the first 120s 20 MV run. The upper panel shows a qualitative 3D view. The lower panel depicts cross sections representing side view, top view and front view respectively. The length of the arrows indicates the distance traveled in one minute. Note that the calculations are performed for a phantom symmetrical across a plane perpendicular to the z-axis.

The flow pattern in the calorimeter tank, *i.e.*, outside the vessel after the first irradiation run at 20 MV is shown in Fig. 16. Because of symmetry, the flow consists of two rotating regions in the form of a cylinder with axes parallel to the beam

axis. Close to the central axis the water moves upward, towards the phantom side walls the flow is downward. Near the vessel, the flow is distorted by the presence of the vessel. At shallow depths the individual streamlines are more or less in one plane. At larger depths, where doses are lower, the streamlines get more distorted and are no longer planar. This is clear from the top view of the calorimeter with the streamlines generated after a ^{60}Co irradiation in comparison with a 20 MeV electron irradiation as depicted in Fig. 17.

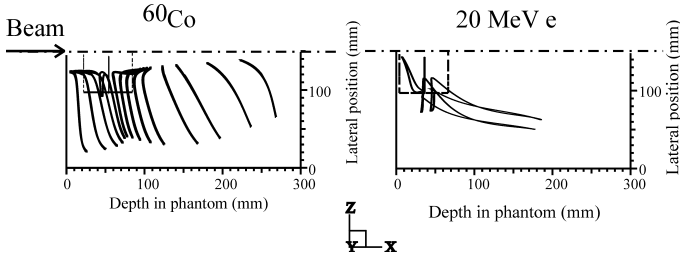

Figure 17: Top view of the calorimeter phantom in the ^{60}Co and high dose rate 20 MeV electron irradiations. Stream lines have been constructed indicating the circular flow between regions of lower temperature and higher temperature.

Water flows from the lower regions in the calorimeter to the higher regions in heated areas and returns to the lower regions in the colder areas of the calorimeter. For ^{60}Co and 20 MV (not shown), the flow is much more to the sides of the calorimeter tank; for the 20 MeV electron irradiations, colder regions are surrounding the back of the vessel and the stream lines are bent towards the back of the calorimeter which provides a more efficient cooling path. This is the main reason why the post irradiation drift curves in electron beams are steeper than for high-energy photon beams even at comparable dose rates.

D. Convection in Other Sealed Water Calorimeters

1) The NIST Calorimeter

Domen [7] reported extensive measurements with his room temperature operated sealed water calorimeter. Because this calorimeter is irradiated vertically and the vessel diameter is smaller than for our system we have studied the simulated response under a number of circumstances. Domen reported work at 9 μW, 30 μW and 100 μW. Fig. 18 shows the maximal velocities inside and outside the vessel, before irradiation and, subsequently, after 70s runs are performed.

Velocities inside the vessel are less than 0.6 mm/min, less than 1.6 mm/min, and less than 4 mm/min at 9 μW, 30 μW and 100 μW respectively. The velocity increase during the runs is much more limited than in the case of the NRC calorimeter at ^{60}Co (between 0.6 mm/min and 3.6 mm/min at 6 μW after a comparable accumulated dose). The velocities calculated at 9 μW and 30 μW are not experimentally detectable using the method used by Domen [11] where he reports to detect convective motion only above thermistor

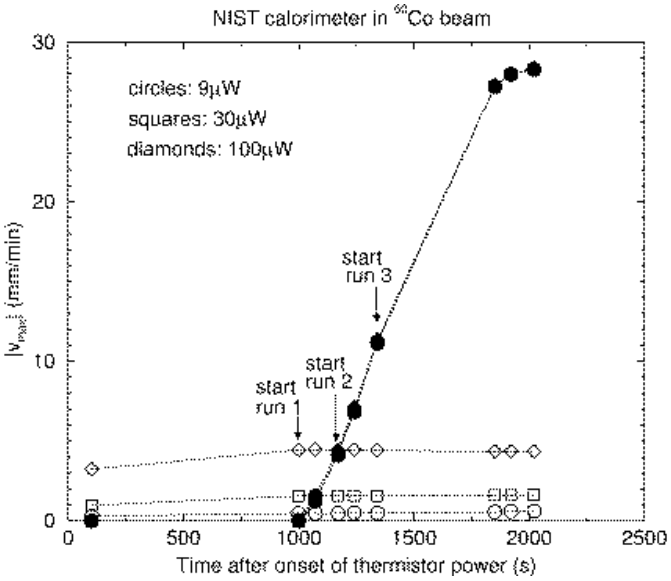

Figure 18: Maximal velocities in the NIST calorimeter inside and outside the vessel before and after ^{60}Co irradiations of 1.8 Gy/min.

powers of 50 μW. Because the off-axis dose rate inside the vessel only drops by at most 5% and the beam is vertical, *i.e.*, the 16% drop in depth dose does not provide a boyancy force to drive convection, the velocities remain small during the irradiations. In this sense, one can view the vessel structure combined with the field size and the vertical beam as being sufficient to slow down convective motion inside the vessel.

Outside the vessel, the situation is much more dramatic and the velocities are comparable to those reported for the NRC calorimeter. The fact that the beam is vertical does not help to slow down the convection because of the free flow between the warm regions inside the field and the cold regions outside the field. Fig. 19 shows the stream lines after a single 70 s calorimeter run (30 μW).

The upper panel shows streamlines coming up under the vessel, which flow over the vessel and then move outside the field. The top view (lower panel) shows that the streamlines form a ring around the vessel, removing heat from the central axis portion of the field.

Fig. 20 shows post irradiation drift curves for 9 μW, 30 μW and 100 μW in both conductive heat loss mode only, and in full (conductive and convective) heat loss mode. At 9 μW, the first 2 runs of the full simulation cannot be distinguished from pure conductive heat loss whereas further runs clearly show an increasing heat loss after irradiation stop. At 30 μW and at 100 μW however, there is a clear distinction between the conductive simulation and the full simulation, and the post irradiation drift curves including convective heat loss produce a significantly steeper post irradiation drift. However, by extrapolating to mid-run the difference compared with the true temperature rise is remarkably constant as summarized in Table 4.

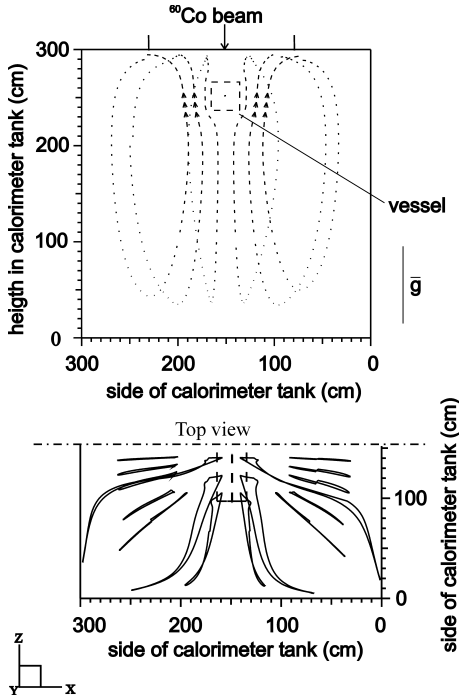

Figure 19: Flow pattern in the NIST calorimeter after one 70 s run. Upper panel: side view. Lower panel: top view. The vessel is indicated by the dashed line.

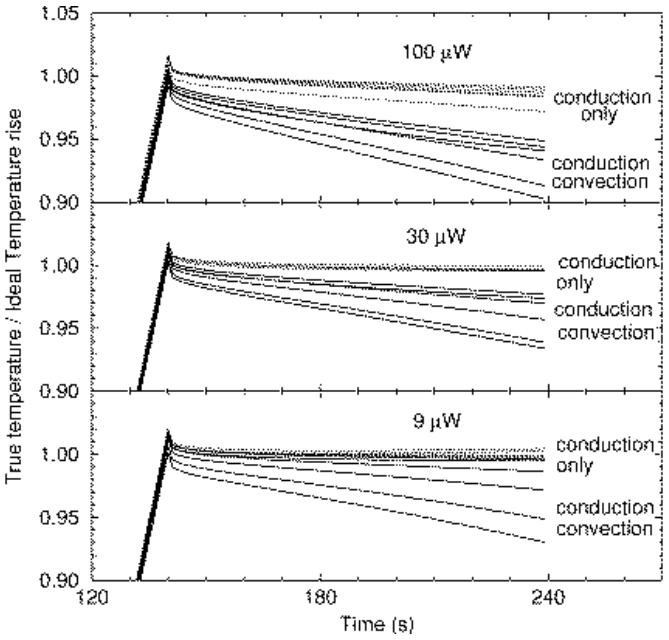

Figure 20: Post irradiation drift curves for 70 s runs performed with the NIST sealed water calorimeter at power levels 9 μW, 30 μW and 100 μW.

The insignificant power dependence of the extrapolated signal was also observed by Domen [7]. Comparing column 4 of Table 4 with the post irradiation drift rates at ^{60}Co with the NRC calorimeter shows that they are comparable *i.e.* an average decrease of -9% / 5 min in the NIST case compared to -6% / 5 min in the NRC case. In his paper [7] Domen also

Table 4.
Calculated ratio of the extrapolated response to the true temperature rise with the NIST calorimeter (22°C) with the full simulation compared to a simulation accounting for conduction only. Also shown are the average post irradiation drift rates expressed in %/5min and in terms of an average "negative" dose rate [11].

Power	Real/true temp. rise		Post irradiation drift rate	
(μW)	Full (cond. +conv)	Cond. Only	%/5min	Average "Negative" dose rate (Gy/min)
9	1.0052	1.0039	-3 to -15	-0.04
30	1.0051	1.0039	-6 to -18	-0.05
100	1.0023	1.0038	-12 to -24	-0.08

showed a sequence of 5 runs with 30 μW thermistor power dissipation. After this sequence of runs which takes approximately 11 min, the drift has significantly changed. The change in drift rate derived from Fig. 21 in his paper after 5 runs have been finished is approximately –16 μK/min. Our calculated change in drift rate amounts to –30 μK/min with convection present and +4 μK/min when conduction is the only mode of heat loss. The positive sign in the last case is because of the excess heat of the vessel reaching the measuring point. This agreement is reasonable considering the fact that the simulation is in a cartesian system and the real geometry is cylindrical, and secondly, other sources that may change the background drift such as temperature inhomogeneities have not been modeled.

Another verification of the velocities calculated in our work results from combining the post irradiation drift rates, expressed in terms of "Average negative dose rate" (column 5 of Table 4) with the measurements of Domen [11]. For the power dissipations used velocities between 1 and 2 mm/min are derived by making use of Fig. 6 in Ref [11]. These velocities are consistent with the calculated velocities, the maximal values of which are plotted in Fig. 18.

Finally, it should be noted that the calculated over-response when conduction is modeled as the sole heat loss mode, is not the most optimal estimate of this correction factor since the real probe geometry is cylindrical and not squared and the excess heat directly after the end of the irradiation may be slightly lower than calculated here.

2) The LNHB Calorimeter

LNHB (Saclay, France) is considering a relatively large vessel to be used in their water calorimeter. Although the intention is to operate at 4°C, we investigate what the difference in response there would be between 22°C and 4°C operation. The vessel is positioned against the front window of the calorimeter tank. The dimensions of the vessel (12 x 12 cm^2 on a side and 10 cm deep) and irradiation conditions were summarized earlier in this paper (Table 1). The calculations

were performed using a single probe extending to the center of the vessel. Five sequential ^{60}Co runs were simulated. Note that the field diameter at the measuring point is smaller than the vessel diameter. This was chosen in order to avoid excess heat from the side wall.

Table 5.
Calculated ratio of the extrapolated response to the true temperature rise with the LNHB calorimeter (22°C) with the full simulation compared to a simulation accounting for conduction only.

Power	Real / true temperature rise	
(μW)	Full (cond.+conv.)	Cond. Only
1	0.9997	1.0014
8	0.9928	1.0014
50	0.9464	1.0012

Table 5 summarizes the results obtained after extrapolation to mid-run. The result based on the full simulation is consistently lower than the result with only conduction, which shows the typical excess heat over-response from the probe and the upstream wall which is about 5 cm away and consists of both the phantom wall and the vessel wall (1 mm glass). Furthermore, a significant dependence of the response of the calorimeter is observed over a power region much smaller than the NIST sealed water calorimeter. This is because the field diameter is smaller than the vessel diameter. A drop in calorimeter response as a function of power was also observed by Domen [6] in an open calorimeter system (see next section).

E. Convection in Open Water Calorimeters

Another type of situation that, retrospectively, deserves attention is the first generation, open water calorimeter [6]. In this calorimeter, the temperature rise was measured by thermistors sandwiched between two polyethylene films and positioned at 5 cm depth in water. The large convective currents calculated outside the vessel in the sealed water calorimeters suggests that dramatic effects must have been involved in the open water calorimeter.

In Domen's work the ^{60}Co beam was directed vertically downward and the irradiations were performed with a large field (covering the whole calorimeter tank) and with a collimated field. Domen observed a significant power dependence of the calorimeter response in the uncollimated beam. When Domen compared his water calorimeter results with the results from graphite calorimetry, converted into absorbed dose to water a discrepancy of 3.5% was found. This discrepancy was confirmed by other authors [18,10,19] and has commonly been attributed to problems with impurities giving rise to an exothermic heat defect in these open calorimeters [20]. In order to determined what contribution, if any, of this over-response must have been due to convective motion, we performed calculations of the open water calorimeter in vertical beams using (i) a collimated beam of 15x15 cm^2 and (ii) a perfectly uniform large field, covering the entire calorimeter. The details of the geometry were given in section III B.

Table 6.
Calculated average ratio of the extrapolated response to the true temperature rise for the NIST vertically downward irradiated (^{60}Co) open water calorimeter for a sequence of five 3 min irradiations. In the lower part of the table, calculated ratios are presented for the same calorimeter without foils, irradiated under the same conditions. One standard deviation on the extrapolated signal is indicated in brackets.

Calorimeter with polyethylene foil detector				
P	Collimated field		Large field	
(μW)	full calc.	Cond. only	full calc.	Cond. only
0	1.012 (0.009)		1.0030 (0.0001)	
9	1.009 (0.006)	1.0003 (0.0003)	1.0017 (0.0003)	1.0018 (0.0003)
30	1.000 (0.004)	0.999 (0.001)	1.000 (0.001)	1.0014 (0.0010)
100	0.958 (0.018)		0.995 (0.018)	
200	0.865 (0.023)		0.974 (0.009)	
Calorimeter with bare thermistor detector				
P	Collimated field		Large field	
(μW)	Full calc.	Cond.only	Full calc.	Cond.only
9	0.94(0.10)		0.996 (0.003)	

Table 6 shows the average ratio of the extrapolated response to the true temperature rise for the NIST open water calorimeter. Column 2 shows that even at the lowest thermistor powers, for the collimated field, convection is influencing the extrapolation. However, the over-response is only around 1% but uncertainties about field size (we used the same data for the lateral profile as in the simulations for the sealed water calorimeter) and other approximations may allow for larger effects. Column 3 of Table 6 shows a 3% dependence of the calorimeter response on power dissipation for a perfectly uniform field which compares reasonably well with the 4% response reduction as a function of power obtained by Domen [6]. For this field geometry, upon going to zero power dissipation the convective effects disappear, as in that situation the boyancy forces become absent throughout the phantom. In the lower part of Table 6 large effects are shown when the foil structure is replaced by thermistors directly immersed at the same position in water, and in fact no reasonable calorimeter runs can be made under these conditions (Fig. 21).

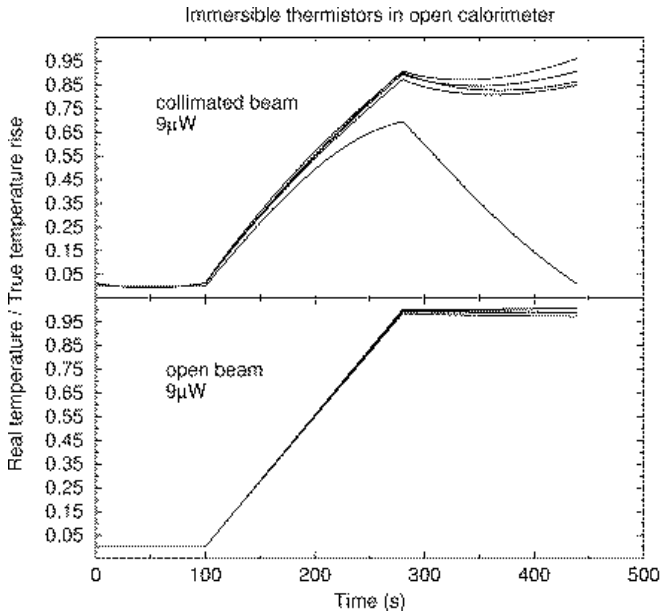

Figure 21: Post irradiation drift curves for 180 s runs performed with an open water calorimeter (power 9 μW) with immersible thermistors in a collimated field (upper panel) and a large uniform field (lower panel).

However, if the field size is made uniform (lower part of Table 6, column 3), there is no visible evidence for convection, and the response is not significantly different from the true temperature rise. This observation was also made experimentally by Barnett and Cormack [10] where convection gradually became less important, but not absent, as the field was opened up. Barnett and Cormack [10] also investigated the power dependence of their calorimeter with foils and found an insignificant dependence of the calorimeter response on thermistor power. That result is not inconsistent with our calculated power dependence given the restricted power range (less than 60 μW) used in Barnett and Cormack's work, and the uncertainties on their measurements.

V. SUMMARY

We have experimentally demonstrated that convection forms an essential part of the heat transfer process in the NRC sealed water calorimeter when operated at room temperature and irradiated with clinical dose rates in electron and photon beams. Using numerical methods, we have reproduced the post irradiation drift slopes observed in our experiments and shown that, although no obvious non-linearities can be observed in the measured drift curves in photon beams, convection is still present and can affect the extrapolation procedure at the 0.5% - 0.7% level. The velocities produced by our program are consistent with those derived from experimental analyses of temperature drift curves produced by thermistors in a forced convection experiment [11].

There are two sources for convective motion in stagnant water calorimeters: (i) thermistor power dissipation and (ii) dose profile non-uniformity. Both sources violate the idealized, one dimensional gradient conditions under which the Rayleigh criterion can be applied. In sealed water calorimeters, convection is present inside as well as outside the vessel. Inside the vessel, the velocities depend strongly on the diameter of the vessel in relation to the field size, and on the thermistor power dissipation. In the NRC vessel velocities are less than 3 mm/min at ^{60}Co (power 6.4 μW; dose rate: 1.5 Gy/min). In the smaller diameter NIST vessel, for a comparable power dissipation and dose rate, the calculated velocities are less than 1 mm/min. These velocities as well as the velocities present solely as a result of power dissipation are, for low powers, not detectable using the method used by Domen [11]. This is consistent with the observation in that paper that no significant heating could be observed upon initiating downward convection at power levels lower than 50 μW. At high dose rates (about 40 Gy/min) in a non-uniform radiation field (20 MeV electrons) the velocities in the NRC vessel are less than 10 mm/min. At low powers, in the NRC vessel, the irradiations provoke a significant change over the velocities initially present. At high thermistor powers, maximum velocities do not change significantly, and the convection as a result of thermistor power is the more important effect. The dose uniformity over the vessel volume is essential in controlling convection inside the vessel. If a portion of the vessel is falling outside of the radiation field convective motion evolves more rapidly than when the entire vessel is irradiated.

Outside the vessel the velocities are of the order of a few cm per minute regardless of whether the calorimeter is irradiated vertically or horizontally, at least when the field is not uniform over the entire calorimeter. The movement in the phantom changes the overall heat loss from the vessel, and affects the drift curves. There is no clear onset point of convection visible on typical drift curves from a sealed calorimeter. In high-energy photon beams, for horizontal irradiations, the streamlines are removing heat from the portion along the central axis of the field. This movement is cylindrical in two regions symmetrical with respect to a vertical plane passing through the beam axis through the middle of the calorimeter. For electron beams streamlines also extend to the back of the calorimeter providing a more efficient cooling pattern, and hence steeper post irradiation drift curves.

In open water calorimeters, when no barriers are used and when the field is collimated. convective effects are more dramatic than in sealed water calorimeters in the same conditions. The power dependence of the calorimeter response observed by Domen [6] was demonstrated to be due to convection.

We can thus conclude that, with the exception of idealized conditions, (*i.e.*, perfectly uniform lateral dose profiles, vertical irradiations without a dose build-up region) there is convective motion present in stagnant water calorimeters operated at room temperature. Given the large velocity effects outside the sealed vessels, the extrapolation procedure deals exceedingly well with convective heat loss, and could, in some fortuitous cases, produce the correct temperature rise. However, in general, errors should be expected up to 1% for

calorimeter operation at low powers (10 μW or less) in high-energy photon beams, but 3% or higher in high dose-rate, high-energy electron beams.

ACKNOWLEDGEMENTS

We wish to thank Steve Domen for many animated discussions about convection in water calorimeters operated at room temperature. J.P.S. is funded by NCI grant No. RO1-CA66852.

REFERENCES

[1] R. J. Schulz, C. S. Wuu and M.S. Weinhous, "The direct determination of dose-to-water using a water calorimeter", *Med. Phys*. Vol. 14, pp. 790-796, 1987.

[2] M. Roos, "The current status of water absorbed dose calorimetry at the PTB", NRC workshop on water calorimetry, NRC Report 29637, pp. 9-16, 1988.

[3] A. Krauss and M. Roos, "Heat conduction, convection and radiolysis of the H_2/O_2 system in the water absorbed dose calorimeter", *Thermochimica Acta* Vol. 310, pp. 53-60, 1998.

[4] J. Seuntjens and H. Palmans, "Correction factors and performance of a 4°C sealed water Calorimeter", *Phys. Med. Biol*. Vol. 44, pp. 627-646, 1999.

[5] C. K. Ross, J. P. Seuntjens, N. V. Klassen and K. R. Shortt, "The NRC sealed water calorimeter: correction factors and performance" (these proceedings), 2000.

[6] S. R. Domen, "An absorbed dose water calorimeter: Theory, design, and performance", *J. Res. Natl. Bur. Stand*. Vol. 87, pp. 211-235, 1982.

[7] S. R. Domen, "A sealed water calorimeter for measuring absorbed dose", *J. Res. Natl. Inst. Stand. Technol.* Vol. 99, pp. 121-141, 1994.

[8] R. J. Schulz and M. S. Weinhous, "Convection currents in a water calorimeter", *Phys. Med. Biol*. Vol. 30, pp. 1093-1099, 1985.

[9] S. R. Domen, "Comments on 'Convection currents in a water calorimeter'", *Phys. Med. Biol*. Vol. 31, pp. 1166-1168, 1986.

[10] R. B. Barnett and D. V. Cormack, "A comparison of temperature detectors for a water calorimeter", Presented at the 1987 AAPM meeting in Detroit, 13 pages, 1987.

[11] S. R. Domen, "Convective velocity effects on a thermistor in water", *J. Res. Natl. Bur. Stand*. Vol. 93, pp. 603-612, 1988.

[12] S. R. Domen, A. Krauss and M. Roos, "The problem of convection in the water absorbed dose calorimeter", *Thermochimica Acta* Vol. 187, pp. 225-233, 1991.

[13] J. P. Seuntjens, C. K. Ross, N. V. Klassen and K. R. Shortt, "A status report on the NRC sealed water calorimeter", Technical Report PIRS-584, NRC Canada, Ottawa, K1A 0R6, 1999.

[14] J. P. Holman, "Heat transfer", 8th edition New York: McGraw-Hill Companies, Inc., 1997.

[15] S. V. Patankar, "Numerical heat transfer and fluid flow", Washington: Hemisphere Publishing Corporation, 1980.

[16] N. S. Osborne, H. F. Stimson and D. C. Ginnings, "Measurements of heat capacity and heat of vaporization of water in the range 0°C to 100°C", *J. Res. Natl. Bur. Stand*. Vol. 23, pp. 197-259, 1939.

[17] K. Shortt, J. Shobe and S. Domen, "Comparison of dosimetry calibration services at the NRCC and the NIST", *Med. Phys*. (in press), 2000.

[18] H. Kubo, "Absorbed dose determination with a water calorimeter in comparison with an ionization chamber", *Phys. Med. Biol* Vol. 28, pp. 1391-1399, 1983.

[19] O. Mattsson, "Water calorimetry at the radiation physics dept. Gϕteborg", NRC Workshop on Water Calorimetry, NRC Report 29637, pp. 17-24, 1988.

[20] C. K. Ross and N. V. Klassen, "Water calorimetry for radiation dosimetry", *Phys. Med. Biol*. Vol. 41, pp. 1-29, 1996.

QUESTIONS AND ANSWERS

Ken Gall: With regard to these recommendations, you say perfectly uniform over the vessel area, that's the entire vessel, not just the sealed core part.

Jan Seuntjens: Preferably the whole calorimeter. Although, if you keep the profile exactly uniform over the vessel area it also helps a lot - and it works only in photon beams. Well, its cobalt.

Ken Gall: It's hard for me to understand how much of the effect is from within the small vessel. You say there is some small convection in the core, but it seems to me that most of the problem is through convection outside. Is that true?

Jan Seuntjens: I have not come up with a good way to analyse the data such that I can make that conclusion. In this [NIST] calorimeter I think it works out that inside the vessel there is movement, but it remains small, 1 or 2 mm per minute. I would agree with you that the largest effect comes from outside for this calorimeter. Yet for the NRC calorimeter we see with the bigger vessel, that between run 1 and run 2 inside the vessel we have a significant increase in velocity, so the terminal velocity inside the vessel at which the system becomes happy and stable is higher in this vessel, because it is larger. So in this case, movement inside the vessel is also important.

Ken Gall: Steve Domen has put forward the concept of putting baffles in the larger tank just below the pure water core. So that would presumably help matters a bit.

Jan Seuntjens: It could help, but I would still be worried because what you do, essentially, if you start adding barriers to the system, is to generate new cells of convection in-between those barriers. You won't stop it. The concept of stopping convection is not realistic at room temperature. That's the whole - you won't stop it. You will always have movement,

because you will never have a uniform field, you will never have a uniform dose , so you will always have pressure gradients and the driving force is always there. And the thing is, with the low thermal diffusivity of water, the low dose profile stays present so the driving force for convection remains. Even in-between runs, if you looked at an increase in velocity between the runs, it kept on increasing so even if you don't irradiate the profile is still there and the convection is still increasing.

The second practical advice that I would give there is that if you have baffles, how are you going to make the phantom uniform in the first place?

Ken Gall: You modelled the greater heat that was generated in the glass wall, and so forth, as contributing to the convection process?

Jan Seuntjens: Yes. The glass is there.

Ken Gall: And did you consider the extra heat that would be generated in the water outside the pure water core? Because of heat defect it must be a few percent different, which has got to be comparable to the water temperature change due to convection. The excess heat being generated in the non-pure water outside the core must be a comparable consideration.

Jan Seuntjens: No. Steve [Domen] has done. In his initial report he has done some estimates of that, and concluded that it's only 2%. The temperature rise in the glass is a factor of 5 higher than the temperature rise in the immediately neighbouring water voxel. So that is a much more significant term. It's possible that in the long run, if you do long runs, that you have to think about this.

Hugo Palmans: I don't think what you just said is an argument, because the effects due to excess heat are additive, so if that is 3.5% of the water outside the vessel, would give change of 0.2% , then that will remain, even in the presence of the larger effect due to the vessel.

Jan Seuntjens: Yes. It's something that has to be done.

Alan DuSautoy: Your results at around 20ºC seem to depend on the time between runs. Is it true that, say, order of magnitude, if you doubled the time between runs you'd halve the effect, or something like that?

Jan Seuntjens: No. I don't think that would reduce the effect. The velocities remain present, so the effect remains there.

Alan DuSautoy: So if you do one irradiation, the velocities will be there, but eventually they are going to decay.

Jan Seuntjens: Yes, but it would be impracticable. You would have to wait a very long time.

Alan DuSautoy: So you are talking about hours rather than minutes?

Jan Seuntjens: Hours, yes.

Antonio Guerra: May I ask you, how many runs are you able to do with sufficient reproducibility at room temperature? Also, using a very low power level.

Jan Seuntjens: In the experiment, the reproducibility at 22 ˚C was not worse than at 4 ˚C, so we could do about 10 runs: that's what we normally do at 4 ˚C, and it was perfectly possible at 22 ˚C. Normally we don't wait very long [between runs]. We don't have such a large amount of data on the post-irradiation drift curve, so we would stop at 2 minutes and start the pre-drift of the next one. But that's the whole wishy-washy business of 22º - you don't see it - it looks OK. It becomes significant when you average enough runs. There is a half percent difference, or one sixth at Cobalt.

Ken Gall: Jan, your experimental results compare 4 ˚C and 22 ˚C results today. Is there anyone else who compared 4 ˚C and 22 ˚C experimentally?

Jan Seuntjens: I've seen only one written statement and that's Krauss I think. I believe he stated in his 1998 paper that they have compared with a NIST type of vessel in their calorimeter 4 ˚C and 22 ˚C, and they didn't see a difference.

Achim Krauss: We made measurements independent on the thermistor power, and we saw no difference for the different thermistor powers, and so we said there cannot be convection, because one sign of convection should be that it is dependent on thermistor power and we showed that it is not true.

Jan Seuntjens: Yes, but I wouldn't rely on this any more.

Ken Gall: I guess one of the questions is, you show that the model agrees well with your experiments, with your geometry, your vessel and so forth, but it would be very interesting to get a comparison between the model and experiments for other vessel geometry.

Jan Seuntjens: Yes, that was our intention, but Steve [Domen] sent me some of his runs and analysis of his experiments and I still have to do detailed calculations for the times he uses in his calorimeter. But there are some indications that it's going to look good because in his paper he produces a drift curve for a typical set of 5 runs and what you see is that after 5 runs the drift change is of an order that cannot be explained in the time-frame of conduction, so the drift changes he sees before the first run and after the fifth run can only be explained if you include convection. But this has to be properly calculated for exactly his conditions.

Carl Ross [to Hugo Palmans]: Have you looked at the issue of 2% [excess heat being generated in the non-pure water outside the core]?

Hugo Palmans: Yes, but for only one or two situations because I have been doing measurements for very small vessel sizes, about 2cm high, and then it was about 0.4% and I assumed 3.5 % excess heat outside the vessel but I did not simulate it systematically.

Development of the NPL Water Calorimeter

A.J Williams and K.E Rosser
Centre for Ionising Radiation Metrology, National Physical Laboratory
Teddington, Middlesex TW11 0LW United Kingdom

Abstract

This paper describes the development of the NPL water calorimeter for high energy photon and electron beams. Work started on the calorimeter in 1995 as part of the UK's National Measurement System Ionizing Radiation Research Program. Each research program runs for three years at a time, so the calorimeter is now in the second research program which started in 1998. This description of the development of the calorimeter is therefore split into two parts covering the two research programs since 1995.

I. The First Water Calorimeter

The design and development of the first water calorimeter along with the results of experimental measurements made has been described in detail previously [1], [2], so only a brief description is given here.

A. Construction and Set-up

1) The Temperature Controlled Phantom

A schematic diagram of the calorimeter is shown in Figure 1. A 25 cm by 25 cm water phantom was fixed inside a temperature controlled enclosure. The temperature of the enclosure could be controlled at any temperature between about 4 ˚C and 22 ˚C, however it was normally operated at 4 ˚C so that convection within the water phantom was suppressed.

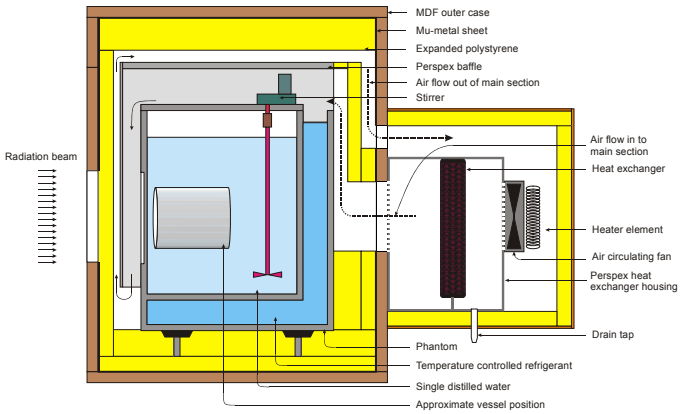

Figure 1: The temperature controlled enclosure. A stable temperature of 4 ˚C was maintained within the water phantom by 1) circulating temperature controlled air around the top and front of the phantom and 2) temperature controlled water around the other four sides.

The temperature control was achieved by:

1) circulating 4 ˚C water around four of the water phantom's six sides (rear, left, right and bottom) and;
2) circulating 4 ˚C air around the other two sides (top and front).

The temperature of both the circulating water and air was controlled by computer.

2) The Calorimeter Vessels

A photograph of the 4 to 10 MV calorimeter vessel is shown in Figure 2. There were three vessels in total, one each for 4 to 10 MV photons, 12 to 19 MV photons and 16 MeV electrons. Unlike most other water calorimeter vessels in use today, the radiation entered through the thin (0.8 mm) flat front wall rather than through the curved side wall. Using a vessel with this orientation in the radiation beam allowed the curved walls of the vessel, which can be difficult to make thin and uniform, to be positioned well away from the measurement point.

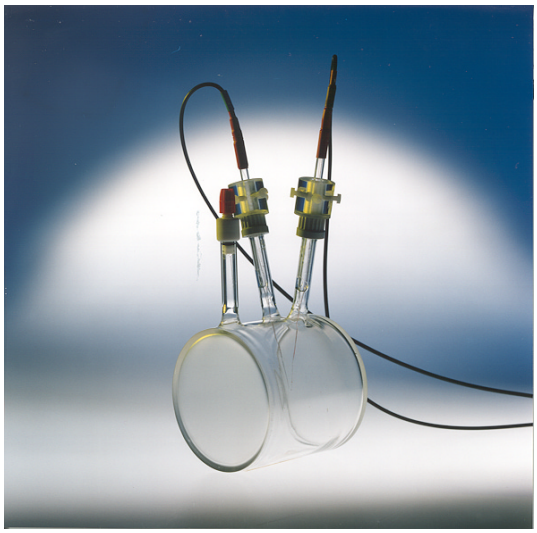

Figure 2: A photograph of the 4 to 10 MV calorimeter vessel. The radiation enters the vessel through the 0.8 mm thick flat front wall rather than through the curved side wall as with other water calorimeters

The dimensions of the vessels were optimized using heat-flow modelling. The modelling revealed that the vessel optimized for use in 4 to 10 MV photons (at a measurement depth of 5 cm) was not suitable for use in 12 to 19 MV photons (at a measurement depth of 7 cm). This can be seen quite clearly in Figure 3. The front wall of the 5 cm vessel was positioned at the peak of the depth dose distribution when positioned for use at a measurement depth of 7 cm. Heat from the front window migrated to the measurement point raising its temperature. In order to avoid this, a separate vessel was built for use at a measurement depth of

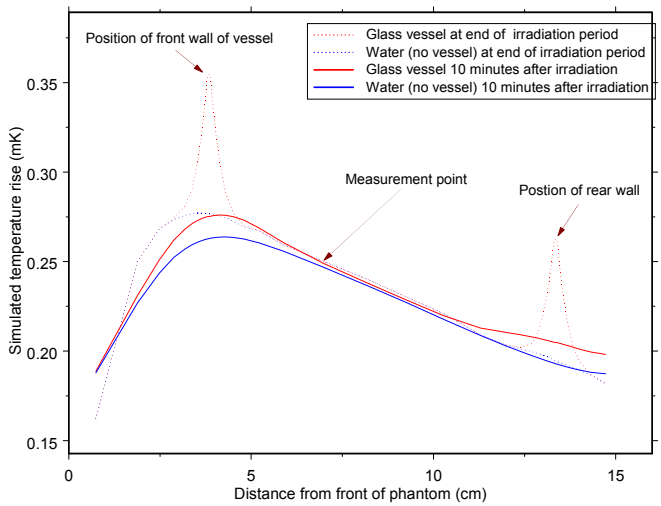

Figure 3: Plot of the temperature distribution within the 4 to 10 MV calorimeter vessel when used in 16 MV photons. The front wall of the vessel is almost at the peak of the depth dose distribution which results in it having a much larger temperature rise than the surrounding water. The excess heat then migrates to the measurement point, raising its temperature.

7 cm which had the front wall moved forward away from the measurement point.

The vessels were suspended in the water phantom using a clamp mechanism as shown in Figure 4. The clamp was attached to a sliding carriage allowing its position and therefore the vessel depth to be easily be adjusted as required.

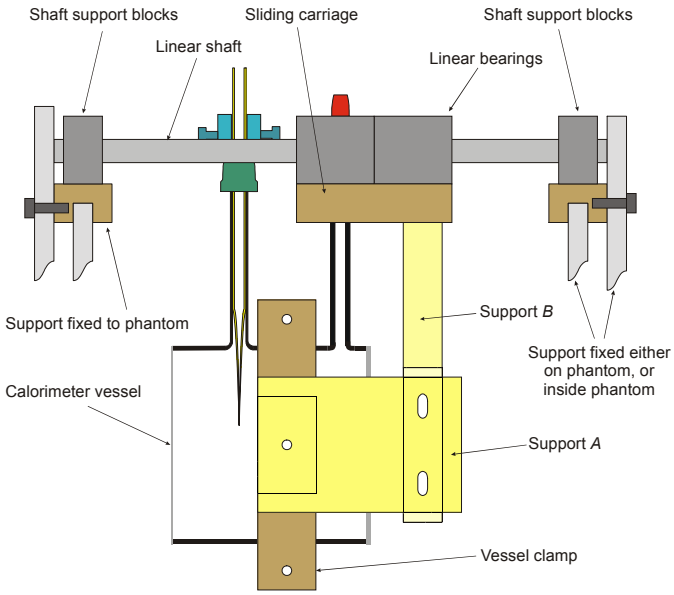

Figure 4: The vessel support. The vessel was held securely by a clamping mechanism that was attached to a sliding carriage allowing it, and therefore the calorimeter vessel, to be positioned at almost any depth within the phantom.

3) The Temperature Sensors

The temperature sensors used were 10 kΩ (at 4 ˚C) thermistors, of the 'thermoprobe' rather than the 'thermobead'

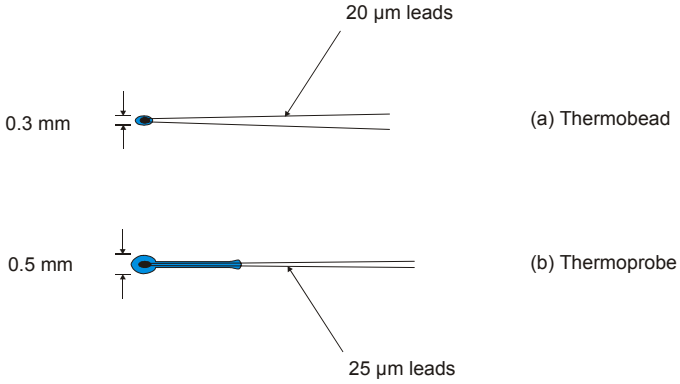

Figure 5: The 'thermobead' and 'thermoprobe' thermistors.

style, supplied by Thermometrics [3] (see Figure 5). The sensing element was a bead thermistor hermetically sealed in the tip of a shock resistant glass rod, of nominal diameter 0.5 mm. The thermoprobe was fixed into the end of a glass pipette using glass solder (a low melting point glass powder) as shown in Figure 6. Thus the thermistor bead was exposed directly to the water, and the only material in contact with the water was glass. The probe construction was carried out by Alan Ainsworth, an expert in precision glass working.

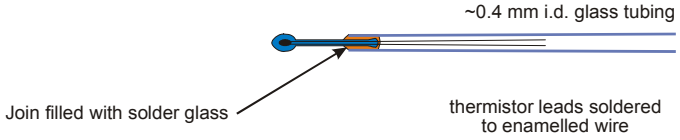

Figure 6: The thermistor probe. The thermoprobe is fixed inside a glass pipette using solder glass - a low melting point glass powder. Therefore the thermistor bead is exposed directly to the water and the only material in contact with the water is glass.

4) The Electronics

The thermistors were connected to two d.c. Wheatstone bridges as shown in Figure 7.

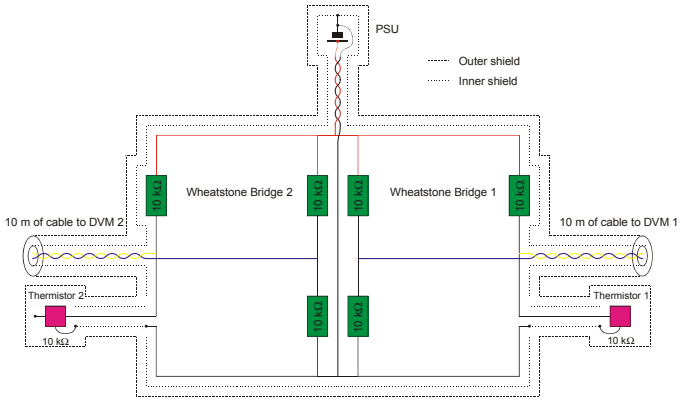

Figure 7: Water calorimeter double d.c. bridge. The system had two electrical shields to reduce noise pick-up from the linear accelerator.

The bridges were double shielded in an attempt to minimise external interference. This was necessary because the NPL linear accelerator environment in which the bridge operated was known to be electrically noisy. The system was powered by a battery powered 2 V precision power supply. The 2 V from the supply

could be stepped down to 1 V and 0.4 V by putting a precision resistor in series with the bridge. The power dissipation in each of the thermistors was therefore 100 μW, 25 μW, or 4 μW, depending on the step-down resistor used. The bridge output voltages were read by two digital multi-meters (DMM), each with a resolution of 10 nV. The out-of-balance bridge voltages were calibrated against a platinum resistance thermometer. The end result was a system with a maximum temperature resolution of 0.5 μK, and a r.m.s. noise of 3 μK.

5) The Gas Saturation System

In order to control the heat defect of the calorimeter, the calorimeter vessel was filled with ultra-pure water that had been saturated with either argon or hydrogen using the apparatus shown in Figure 8. The whole system (reservoir, tubing valves, calorimeter vessel and thermistor was cleaned with chromic acid and the rinsed with ultra-pure water prior to use. Once the calorimeter vessel was filled and installed into the main water phantom, the system was pre-irradiation with a dose of about 20 Gy, after which the system was assumed to have a zero heat defect.

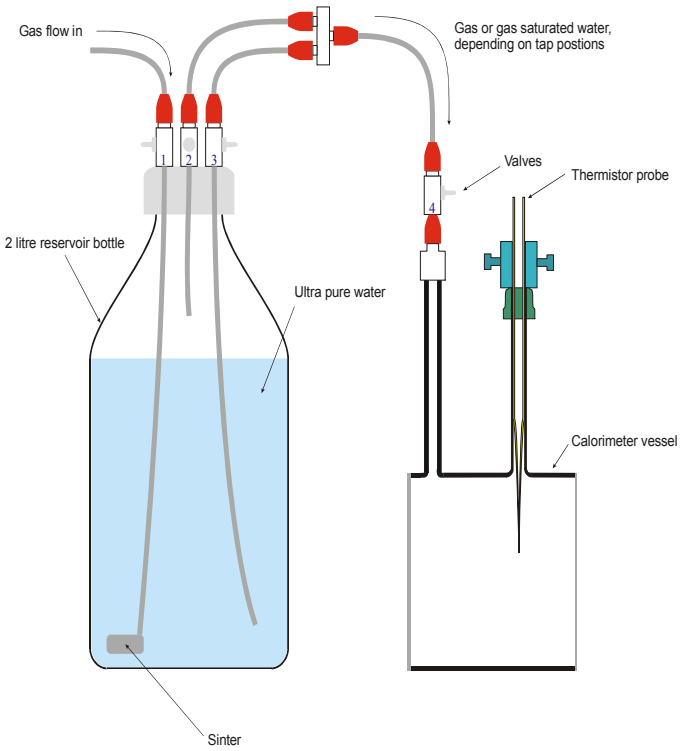

Figure 8: The water preparation system. Argon or hydrogen enters a reservoir bottle full of ultra-pure water via a sinter. When valve 2 is open and 3 is closed, the gas exits the bottle via the calorimeter vessel. When valve 2 is closed and 3 is opened, the gas saturated water exits the reservoir bottle and fills the calorimeter vessel.

B. Results

A plot of typical calorimeter run is shown in Figure 9. The calculated temperature rise was converted to absorbed dose to water D_w using equation (1), where c_p was the specific heat capacity of water at 4 ˚C (4.2045 J.kg^{-1}.K^{-1}), ΔT was the calculated temperature rise and k_{hd} was the heat defect (0.0%).

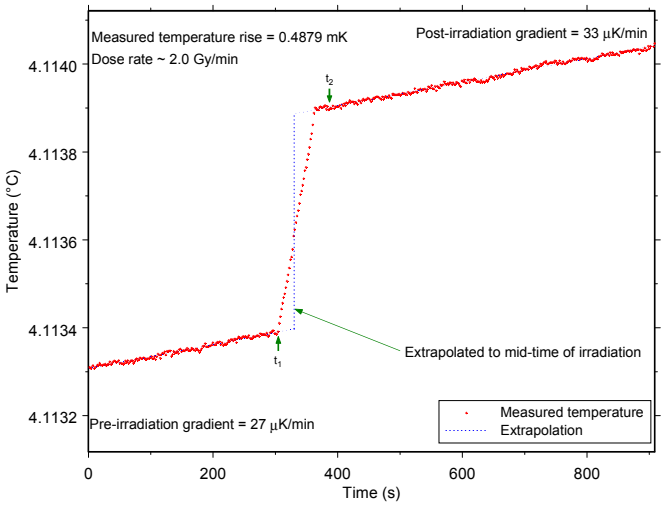

Figure 9: A typical calorimeter run in 16 MV photons. The temperature gradients calculated at times t_1 and t_2 were used to evaluate the temperature rise.

$$D_w = c_p \Delta T \frac{1}{1 - k_{hd}} \quad \textbf{(1)}$$

1) Comparison of Water and Graphite Calorimetry

A number of secondary standard 2571 ionization chambers were calibrated against the water calorimeter in 4, 10 and 16 MV photon beams a dose-rates of between 1 and 3 Gy.min^{-1}. The derived chamber calibration factors were compared with those derived from graphite calorimetry. They agreed to within the measurement uncertainties as shown in Figure 10 [2].

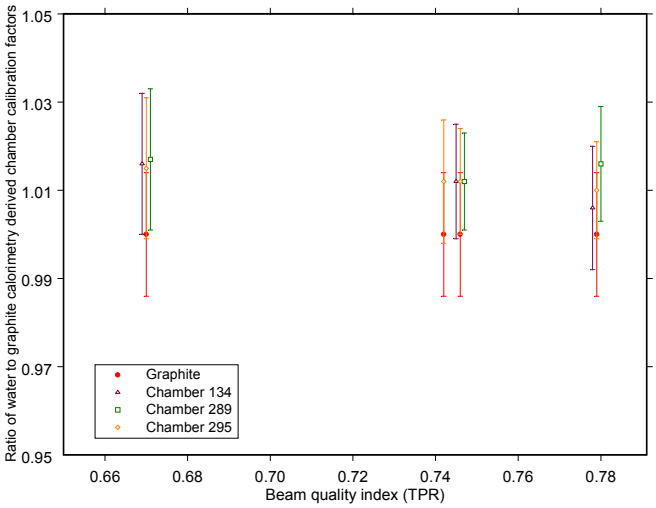

Figure 10: Comparison of graphite and water calorimetry via ion chamber measurements. The measurements agree within the experimental uncertainties.

The expanded uncertainty on the measurement of absorbed dose to water was between 0.9% and 1.6% depending on beam quality. These values are lower than previously reported [1] due to a more rigorous analysis of the uncertainties according to UKAS guidelines [4]. A significant contribution to the decrease

was the reduction in the quoted uncertainty on the specific heat capacity of water from 0.6% to 0.2%.

C. Conclusion

The uncertainties on the calibration factors derived from water calorimetry were comparable to those derived from the primary standard graphite calorimeters, but ideally the uncertainties on the calibration factors would be consistently lower than the 1.4%/1.5% for those derived from the graphite calorimeters.

II. The Second Water Calorimeter

A number of problems were identified with the first water calorimeter that needed to be addressed before it could be considered for use as the new Primary Standard for absorbed dose to water in high energy photon and electron beams.

- the calorimeter repeatability was poor - up to 0.6%.

This was caused by two factors: (1) the background temperature stability was not good enough - the inner phantom had to be stirred almost continuously in order to provide adequate temperature stability and (2) the signal to noise of the d.c. temperature measurement system was too low (just 40 in 6 MV photons).

- the uncertainty on the heat defect of the water was too high (0.5 %) and;
- the uncertainty on the specific heat capacity of water was too high (initially 0.6%).

Therefore, the water phantom and enclosure was redesigned, an a.c. temperature measurement system was built to replace the d.c. system, and investigations into the heat defect and specific heat capacity of water were planned with the aim of reducing their contribution to the overall uncertainty on the measurement of absorbed dose to water by autumn 2001.

A. Construction and Set-up

1) The New Phantom and Enclosure

A schematic diagram of the new calorimeter phantom and temperature controlled enclosure is shown in Figure 11. There were two major improvements over the previous phantom:

i. the refrigerant now circulated around all six sides of the phantom, except for the 15 cm diameter beam entrance window: if the refrigerant circulated in front of the beam entrance window, the minimum measurement depth required of 3.3 cm would not have been obtainable.

ii. the air space above the water in the inner phantom was sealed: all connections to the thermistor probes etc. were made via an access panel in the front face of the phantom.

The combination of the above two changes meant that the only link between external temperature fluctuations and the calorimeter vessel temperature was via the 15 cm diameter front window.

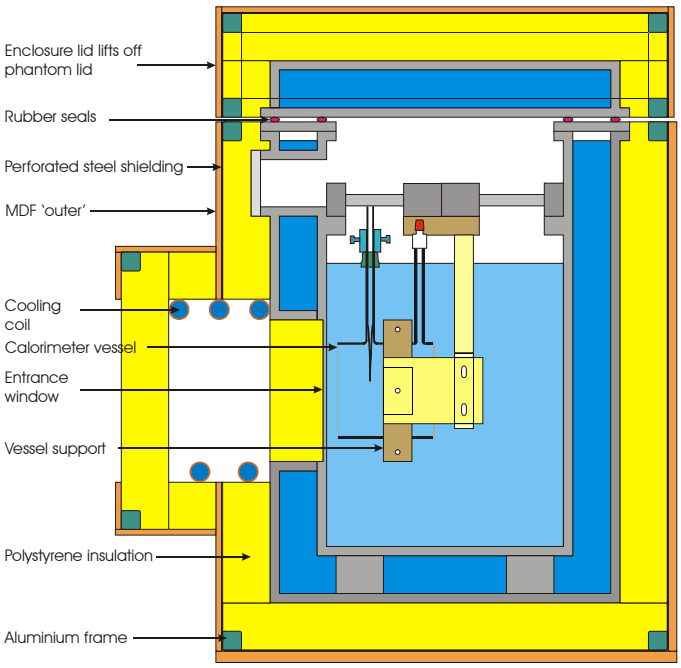

Figure 11: New phantom and enclosure. Except for the beam entrance window, refrigerant at 4 ˚C circulates on all six side of the inner phantom. The air space above the inner phantom is sealed, reducing the likelihood of evaporation. The phantom was surrounded by at least 5 cm of expanded polystyrene insulation, held in place by a rigid aluminium frame. The region in front of the beam entrance window was cooled by circulating the phantom refrigerant through an air-cooling coil.

The enclosure was split into two sections, corresponding to the lid and base of the phantom. Five centimetres of expanded polystyrene insulation surrounded the phantom, held securely in place by a strong light-weight frame made out of 40 mm cross-section aluminium. In order to prevent external temperature fluctuations entering the inner phantom through its front window, the refrigerant was passed through an air cooling coil that was fixed in front of the entrance window. The phantom beam entrance window also had an additional 5 cm of expanded polystyrene insulation making a total of 10 cm of insulation.

An outer casing of medium density fibreboard (MDF) was fixed to the frame, with perforated steel sheet sandwiched between the frame and the MDF to form the electrical shield. There was a 25 cm diameter hole in both the MDF and the perforated steel sheeting corresponding to the phantom's beam entrance window. Four carrying handles, two on the front and two on the sides, were fixed through the MDF into the aluminium frame.

In order for a stable temperature to be maintained inside the phantom, the flow of refrigerant around the outside of the inner phantom needed to be directed so that there were no 'hot spots'. Therefore, a system of baffles was used to ensure a well directed flow of refrigerant around the phantom. The refrigerant entered the phantom base at three points through the rear wall, from where it was directed around the sides of the phantom to the front face, then down around the beam entrance window to the bottom of the phantom. The refrigerant left the phantom by three

equidistant ports at the rear of the phantom. The flow in the phantom lid was less complicated: the refrigerant entered the rear left of the lid and was directed in a zig-zag path to the exit port on the rear right of the lid. The total refrigerant flow rate was approximately 25 $l.min^{-1}$, supplied by a Grant RG1400 recirculating chiller unit [5].

2) *Phantom Temperature Monitoring and Control*

With the development of the new phantom and enclosure, the opportunity was also taken to improve the temperature monitoring and control of the system. On the monitoring side of the system, the original setup had three dedicated temperature inputs: refrigerant temperature entering and leaving the phantom and air temperature in the phantom enclosure. Each input channel required its own DMM (5½ digit, 24-bit multi-function device) which was read at a rate of approximately one reading per second. If this temperature monitoring system was simply expanded, each additional channel would require another DMM. Not only would this be expensive, but it would also take up a lot of space.

Therefore the three DMMs were replaced with a National Instruments NI4351 [6] voltage/temperature logger - a dedicated voltage or temperature (using thermocouples or PRTs) sixteen channel device with 5½ digit, 24-bit resolution and read-rate of approximately ten channels per second. To accompany the voltage logger, a fourteen channel d.c. bridge was built. One of the voltage logger channels was used as a null correction and another to measure the bridge's supply voltage. This left fourteen channels for temperature measurements.

On the control side of the system, the original setup had two voltage outputs in the form of a large 0-30 V, 3 A, dual channel

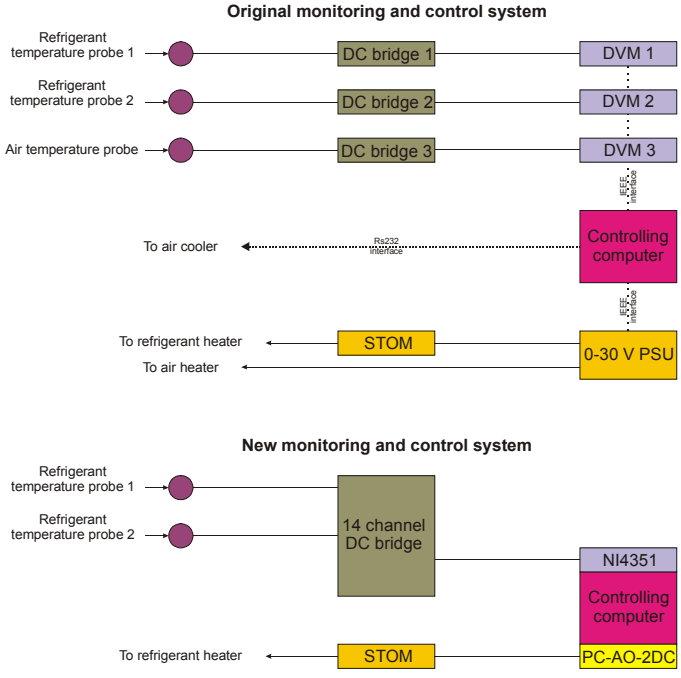

Figure 12: Schematic diagram of old and new monitoring and control systems. The original DVMs were replaced with an National Instruments 16 channel voltage logger PC card, and the original PSU with a National Instruments analogue voltage output PC card.

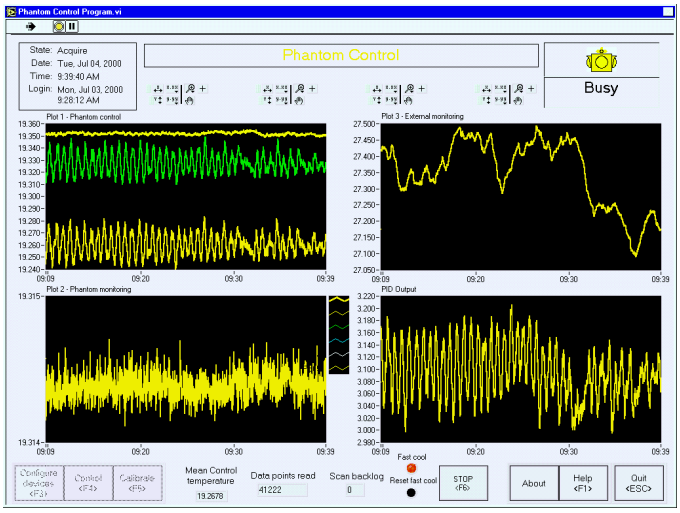

Figure 13: Screen shot from enclosure temperature control program. In this instance, the system was being tested at 19.3 ˚C. Plot 1 shows the temperature of the refrigerant as it leaves the chiller (bottom), as it enters the phantom (middle) and as is leaves the phantom (top), plot 2 shows the temperature of the inner phantom, plot 3 shows the room temperature and plot 4 shows the electrical heating level on a scale of 0 to 5. During the timescale visible, although the room temperature fluctuated by 0.5 ˚C (plot 3), the phantom temperature was stable to better than 0.2 m˚C (plot 2).

power supply, one channel to control the refrigerant heating power and one to control the air heating power. This was replaced with a National Instruments PC-AO-2DC an internal 0-10 V dual channel DAC computer card.

Figure 12 shows a schematic diagram of the new temperature monitoring and control system compared to the original one. Both the NI4351 and PC-AO-2DC could be controlled directly using the software LabVIEW [7], so a new control program was written using LabVIEW. A typical screen-shot from this program is shown in Figure 13.

3) *A New a.c. Temperature Measurement System*

In order to reduce the uncertainty on the measured temperature rise in the calorimeter, the d.c. temperature measurement system was replaced by an a.c. system. The development of the system is described in detail elsewhere in these proceedings [8] (Williams and Rosser), and is therefore only described briefly here.

The main components of the temperature sensing system, as shown in 14, were:

- a bridge made from Vishay [9] precision resistors;
- an EG&G 5209 Lock-in-Amplifier (LIA) which provided the bridge drive voltage, output amplification and phase sensitive detector;
- one or two temperature sensing thermistor probes and;
- two resistance networks (Resnets) to balance the resistive component of the bridge output (one NPL built, one commercial Burster IEC1422).

When designing circuits with low signal levels it is necessary to reduce interfering signals by keeping the circuit compact and

by adding appropriate magnetic and electrostatic screens connected to the circuit earth. In this case, this was achieved by building the circuit shown in Figure 15.

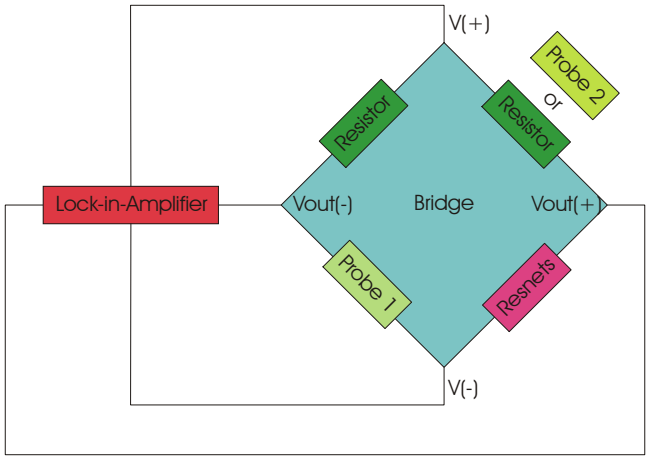

Figure 14: Measuring assembly overview. The main components are: the bridge made from precision resistors, the EG&G 5209 lock-in-amplifier, the thermistor probe(s) and the resistance networks (NPL built and Burster IEC1422).

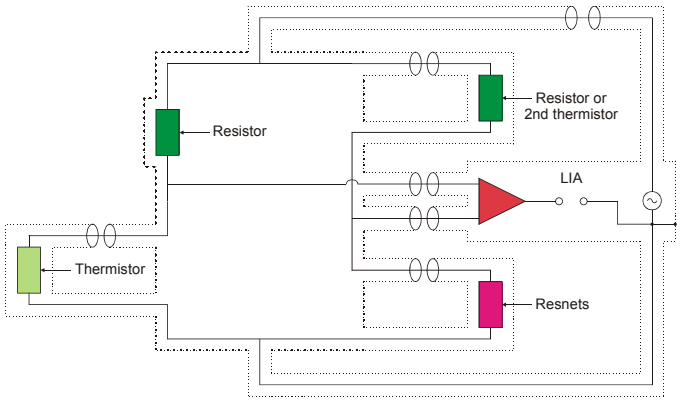

Figure 15: Actual screened bridge circuit. The ideal circuit was modified to take into account the distance of some components from the main part of the bridge.

B. Results

1) Enclosure Performance

Figure 16 shows a plot of the phantom control temperatures, the room temperature and the inner phantom temperature of the new phantom and enclosure over a period of 10 days. The system was set up in NPL's Mobaltron ^{60}Co exposure room which had poor overall temperature control although it was air conditioned. The room temperature fluctuated by about 1 ˚C on a 24 hour cycle in addition to along term drifts of about 2 ˚C. Nevertheless, the temperature on the refrigerant (flow) was independent of room temperature. As might be expected, the refrigerant (return) temperature tracked the room temperature, but with a 1000:1 reduction in amplitude. A change in temperature of 3 mK over a period of 12 hours translated into a mean temperature gradient of about 4 μK.min^{-1}. The inner water phantom temperature had the 24 hour cyclical fluctuations in temperature but also drifted

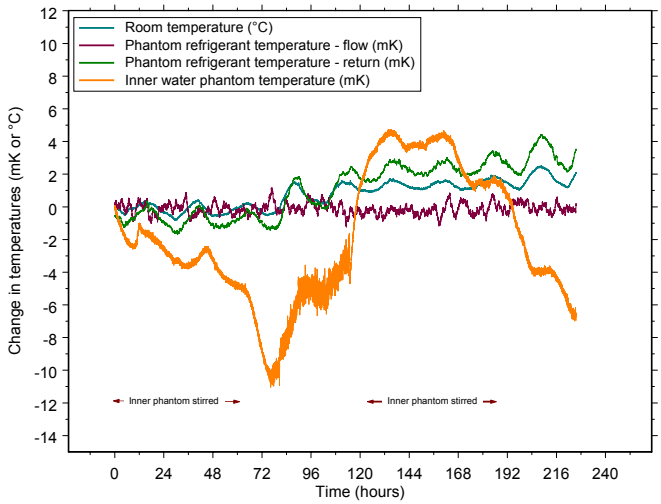

Figure 16: Phantom temperature stability over a 10 day period. The room temperature cycled by 1 ˚C on a 24 hour basis as well as having a long term upward drift of about 2 ˚C. The refrigerant flow temperature was not visibly influenced by the room temperature, but the refrigerant return temperature tracked the room temperature - with a 1000:1 reduction in amplitude. The inner water phantom temperature followed the 24 hour cyclical variations, but also drifted significantly as soon as the stirrer was switched off.

significantly once the stirrer was switched off. The temperature gradient peaked at about 100 μK.min^{-1}, but was on average between ± 10 μK.min^{-1}.

2) Irradiations in ^{60}Co

The new calorimeter phantom and enclosure was tested in the NPL ^{60}Co Mobaltron irradiator with the d.c. and a.c. temperature measurement systems. These results are described in greater detail elsewhere in these proceedings [9] (Williams and Rosser), so only a summary is given here.

The dose-rate from the Mobaltron unit was approximately 1 Gy/min and the irradiation time used was 2 minutes which

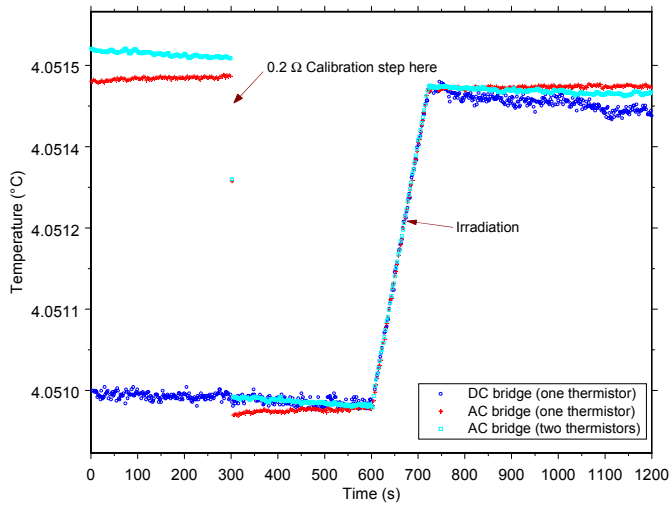

Figure 17: Typical bridge outputs for a 2 minute ^{60}Co irradiation. There is no obvious difference between the a.c. bridge with one or two thermistors, but both are less noisy than the d.c. bridge.

resulted in a temperature rise of about 0.5 mK A plot of a typical irradiation for the a.c. and d.c. bridges is shown in Figure 17. The two a.c. temperature plots have had a small offset added to them so that the temperature at the start of the irradiation period coincides with that of the d.c. system. The temperature drift rates are different because the measurement were not carried out simultaneously. About fifteen irradiations were carried out for each bridge set-up.

For each run, the measured temperature rise was converted into the absorbed dose-rate to water. The results of the comparison are shown in Table 1. The uncertainties listed are one standard deviation (σ_{sd}) and the standard uncertainty (σ_{su}) as calculated according to UKAS (1997) [10]. Both a.c. bridges have an uncertainty on the measurement of dose-rate that is half that of the d.c. system, and a signal-to-noise ratio that is triple that of the d.c. system.

Table 1.

Comparison of a.c. and d.c. bridge results in ^{60}Co radiation. There is very little difference between the two a.c. bridges, but both are significantly better than the d.c. bridge

System	Dose-rate (Gy/min)	σ_{sd}	σ_{su}	Signal-to-noise
d.c. - one thermistor	1.035	± 1.6%	± 0.41%	95
a.c. - one thermistor	1.015	± 0.7%	± 0.18%	270
a.c. - two thermistors	1.028	± 0.8%	± 0.20%	300

C. Future Investigations

1) The Heat Defect of Water

Computer simulations and experimental measurements are planned for autumn 2000. Chemsimul [11] will be used to calculate the heat defect under NPL Linac and ^{60}Co beam conditions for pure (Argon saturated), hydrogen saturated and hydrogen/oxygen saturated water. The results of these simulations will then be compared against experimental measurements made using the water calorimeter.

2) The specific heat capacity of water

The value of the specific heat capacity of water used for the calculation of absorbed dose to water was taken from Kaye and Labey [12] (original data from Osborne *et al* [13]). However, no uncertainty is given, although it is generally *believed* that the accuracy of the measurements is about 0.02% [14]. Initially, early investigations by Rosser [15] led to an uncertainty of 0.6% being adopted. More recently, the uncertainty used when calculating the overall uncertainty of the calorimeter was 0.2%, based on data by Williams *et al* [16]. Further investigation is required before the accuracy of Osborne's measurements of the specific heat capacity of water of 0.02% is accepted.

III. CONCLUSION

The new water phantom and enclosure, combined with the use of the a.c. temperature measurement system has enabled the standard uncertainty on the measurement of temperature rise in the calorimeter to be reduced to 0.2%. Once the investigations into the heat defect and the specific heat capacity of water are completed later in 2000, it should be possible for NPL to measure absorbed dose to water with an uncertainty that is less than the current primary standard graphite calorimeters, namely ± 1.4% and ± 1.5% for photon and electron beams respectively.

IV. ACKNOWLEDGEMENTS

The authors also acknowledge the financial support of the National Measurement Policy Unit of the UK Department of Trade and Industry.

REFERENCES

[1] A.J. Williams and K.E. Rosser, "A Status Report on the NPL Water Calorimeter", *NPL Report*, CIRM 22, December 1998.

[2] A.J. Williams and K.E. Rosser "Comparison of the NPL water calorimeter with other dosimetric techniques for high energy photon beams", *NPL Report* CIRM 23, March 1999.

[3] Thermometrics, Crown Industrial Estate, Priorswood Roas, Taunton, Somerset, UK.

[4] UKAS, The Expression of Uncertainty and Confidence in Measurement, NAMAS M3003, UKAS, Feltham, Middlesex, UK, 1997.

[5] Grant RG1400 recirculating chiller supplied by Grant Instruments Ltd., Barrington, Cambridge, Great Britain.

[6] NI-4150 supplied by National Instruments, 21 Kingfisher Court, Hambridge Road, Newbury, Berkshire, Great Britain.

[7] LabView 5.1 supplied by National Instruments, 21 Kingfisher Court, Hambridge Road, Newbury, Berkshire, Great Britain.

[8] A.J. Williams and K.E. Rosser, "A comparison of a.c. and d.c. bridges for the purposes of high precision temperature measurement", *Proceedings of NPL Workshop on Recent Advances in Calorimetric Absorbed Dose Standards*, NPL Report CIRM XX, pp.xx-xx, September 2000.

[9] VHP202 series resistors manufactured by Vishay-Mann Ltd., Wymondham, Norfolk, Great Britain.

[10] "The expression of uncertainty and confidence in measurement", NAMAS M3003, December 1997. Available from UKAS, Feltham, Middlesex, Great Britain.

[11] Chemsimul, February 2000 edition supplied by Riso National Laboratory, Roskilde, Denmark.

[12] Kaye & Labey, Tables of Physical and Chemical Constants, 16th Edition, published by Longman Group Ltd., ISBN 0-582-22629-5.

[13] N.S. Osborne, H.F. Stimson and D.C. Ginnings, *B. of S. J. Res.* **23**, pp.197-260, 1939.

[14] D.C. Ginnings and G.T. Furukawa, "Heat capacity standards for the range 14 to 1200˚K", *J. Amer. Chem. soc.* **75**, pp.522-527, 1953.

[15] K.E. Rosser, *Private communication*.

[16] I.S Williams, R. Street and S.R. Gopale, "An automated high precision calorimeter", *Pramāna* **11**, no. 5, pp.519-527, 1978.

QUESTIONS AND ANSWERS

Jan Seuntjens: What was the explanation for the calorimeter run where you had two thermistor plots and one was dropping off very dramatically.

Andrew Williams: This was pretty much due to non-uniform temperatures within the phantom. Once we had stirred the system properly and allowed it to settle it just went away. The longer you ran without stirring, the more chance it had of coming back again. That I think was partly due to our early phantom design with the air flow over the top which wasn't really conducive to creating a stable temperature within the inner phantom. Our new phantom hopefully will be a lot better and we won't have so much of a problem.

--

Achim Krauss: What was the thickness of the front window of your calorimeter vessel?

Andrew Williams: It was 0.8 mm.

A Comparison of A.C. and D.C. Wheatstone Bridges for the Purpose of High Precision Temperature Measurement

A.J. Williams and K.E. Rosser

Centre for Ionising Radiation Metrology, National Physical Laboratory,

Teddington, Middlesex TW11 0LW United Kingdom

Abstract

This paper describes the comparison of an a.c. and d.c. bridge. Both types of bridge can be used to measure the small change in resistance associated with a change in temperature of a thermistor. The aim was to identify the system with the highest resolution and sensitivity, and lowest noise for the same thermistor power level of 6.25 μW. It was found that the a.c. bridge system was significantly better then the d.c. system, having at least three times the signal to noise ratio and half the uncertainty in the measured temperature change.

I. Introduction

The motivation for this investigation was the requirement for a high resolution, low noise, low power temperature measurement system for the NPL Water Calorimeter[1],[2]. This demanded a system which could measure a temperature rise of just 0.25 mK (with a rate of temperature change of 4.2 μK.s^{-1}) to an uncertainty of 0.25% or better, with the power dissipation in the temperature sensor of less than about 6 μW. The temperature sensors used in the system are miniature glass bead thermistors housed in a glass probe. Their construction has been described in detail previously[1]. Their nominal resistance at the standard operating temperature of 4 ˚C is approximately 10 kΩ, and they have a sensitivity of approximately 3 mK.Ω^{-1}. So for a change in temperature of 0.25 mK, there is a corresponding change in thermistor resistance of 0.08 Ω.

II. A.C. Bridge

A. Theory

For more detailed information on bridges than that given below, the reader is referred to "Electronics for Experimentation and Research" by Brian Jones[3], from which the following information on a.c. bridges was taken.

A basic bridge arrangement is shown in Figure 1. At balance, the output voltage ΔV is zero, therefore

$$\frac{Z_1}{Z_2} = \frac{Z_3}{Z_4} \qquad (1)$$

For a.c. signals the bridge has to be balanced in amplitude and phase, so that two balance conditions are implied. These two conditions can alternatively be described as balances of the in-phase and out-of-phase components of the signal or the resistive and reactive parts of the bridge.

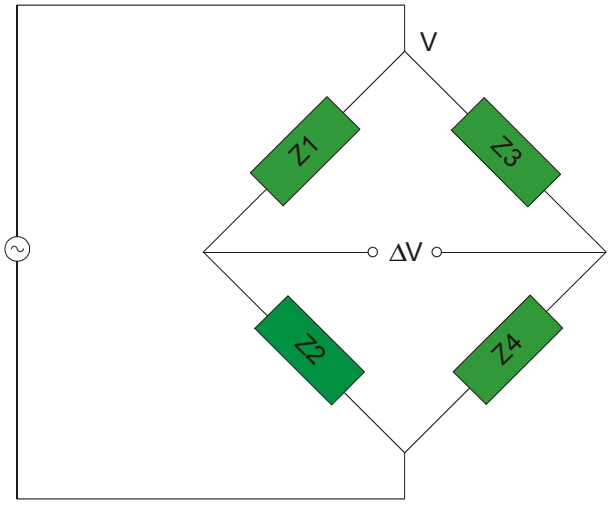

Figure 1: A basic a.c. bridge circuit. Optimum sensitivity is obtained when Z_1=Z_2 and Z_3 = Z_4.

At balance, the relationship between the impedances given in equation (1) is independent of the type of source, voltage or current, or its quality, magnitude or internal impedance. The precision of the balance point is, however, dependent on the amplitude of the source and the detector sensitivity and noise. Optimum sensitivity is obtained for a high-impedance detector when $Z_1 = Z_2$ and $Z_3 = Z_4$. For an a.c. bridge, as there are two balance conditions, both the resistive and reactive parts must be nulled. When a phase sensitive detector is used, the phase of the reference signal should be chosen that it is affected mainly by only one of the variable components of the bridge (the resistive phase in this case).

A bridge circuit may be used in two ways, *at null* and *near null*. In this instance the bridge will be used near null, when it is ideal for the observation of small changes in a component. Near null the offset voltage

$$\Delta V \propto \frac{\Delta Z}{Z} \qquad (2)$$

i.e. the detector only has to measure ΔV to the accuracy needed in ΔZ. For the a.c. system described later in this report, using a drive voltage of 0.5 V a 0.1 Ω change in resistance corresponds to a change in bridge voltage of approximately 1 μV, which can be easily measured with a resolution of 1nV to give a signal-to-resolution ratio of 1000. Compare this to a direct measurement of the thermistor resistance when Z and $Z + \Delta Z$ would have to be measured directly and subtracted. Even a high quality resistance

meter, for example a Solartron 7061, can only measure Z (10 kΩ) and $Z + \Delta Z$ (10.0001 kΩ) with a resolution of 0.01 Ω, giving a signal-to-resolution ratio of just 10.

B. Design and Construction

The main components of the temperature sensing system as shown in Figure 2 are:

- a bridge made from Vishay[4] precision resistors;
- a Lock-in-Amplifier (LIA). This provides the bridge drive voltage, output amplification and phase sensitive detector;
- one or two temperature sensing thermistor probes and;
- two resistance networks (Resnets) to balance the resistive component of the bridge output.

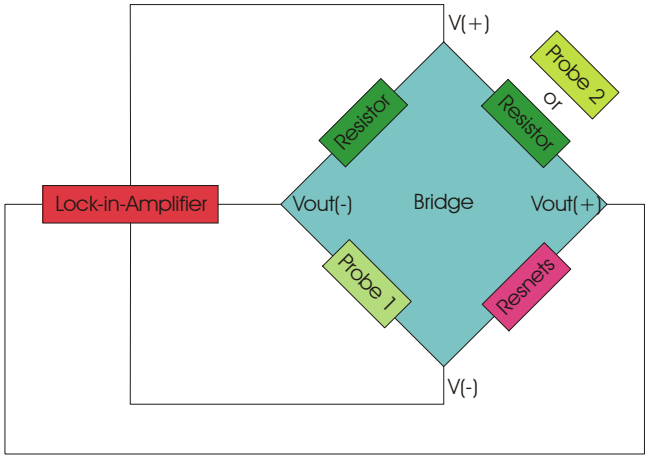

Figure 2: Measuring assembly overview. The main components are: the bridge made from precision resistors, the lock-in-amplifier, the thermistor probe(s) and the resistance networks.

When designing circuits with low signal levels it is necessary to reduce interfering signals by keeping the circuit compact and by adding appropriate magnetic and electrostatic screens connected to the circuit earth. Figure 3, taken from Jones, shows such a circuit for an a.c. bridge system. The breaks in the screens are to eliminate earth loops.

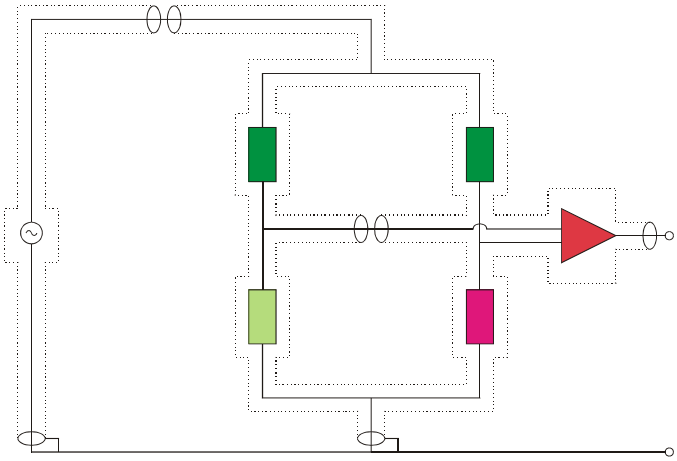

Figure 3: A bridge circuit with screening to reduce capacitive pick-up. The breaks in the screen are to prevent earth loops.

In this instance, it was not possible to build the ideal circuit because some of the bridge components, for example the thermistors, are some distance from the bridge. Therefore the above figure was used as a guide. The resulting circuit is shown in Figure 4.

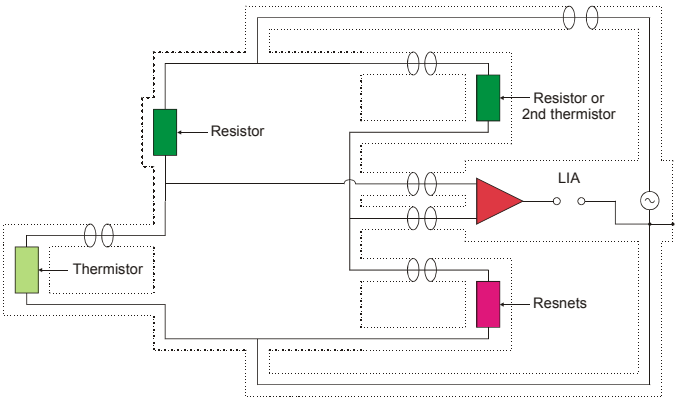

Figure 4: Actual screened bridge circuit. The ideal circuit was modified to take into account the distance of some components from the main part of the bridge.

The Wheatstone bridge is housed in an aluminium die-cast enclosure which is itself inside a 19" rack mounting enclosure (see Figure 5). The purpose of the outer enclosure is to minimise movement in the cabling, thus minimising any change in the cable's capacitance which may change the bridge output. As can

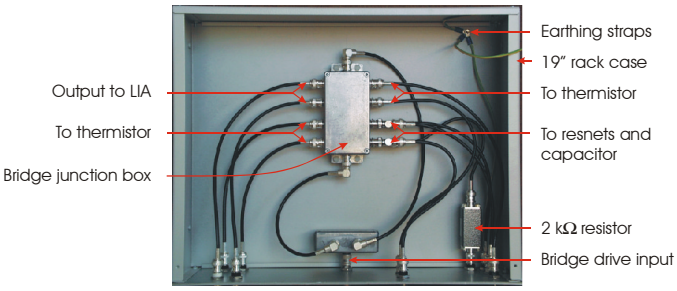

Figure 5: 19" rack mounting bridge enclosure showing the inner enclosure and connector cabling. The main purpose of the enclosure was to prevent unnecessary movement of the cabling which could cause its capacitance to change.

be seen more clearly from Figure 6, the inner enclosure acts as a junction box for the various bridge components. Inside it there is a single 10 kΩ ± 0.001% precision resistor which forms the top left arm of the bridge, and the terminal posts which are used to connect the other components of the bridge together - most of the

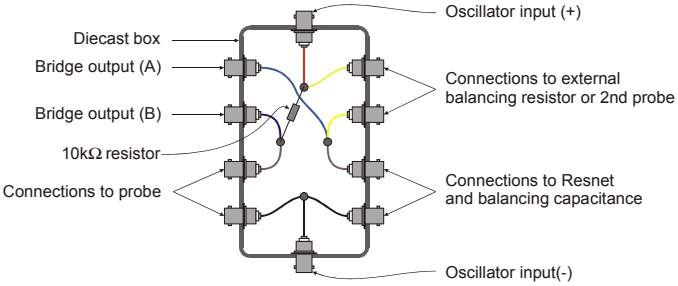

Figure 6: The inner enclosure acts mainly as a junction box - the only active component is a precision resistor.

bridge components are external to the inner enclosure. All connections between the inner enclosure and the external components are made using low noise coaxial cable. The precision resistor, which forms the top right arm of the bridge, is housed in its own small enclosure external to the 19" rack-mounting case. This allows the resistor to be easily replaced with a second temperature sensing probe if required. The bottom right arm of the bridge is connected to the two Resnets which are in series to each other, and in parallel to an external balancing capacitor. The bottom left arm of the bridge is connected to the primary temperature sensing probe via approximately 12.5 m of low noise coaxial cable. The connections between the LIA and the Resnets to the bridge have been kept as short as reasonably possible as shown in Figure 7: this helps to minimise any change in capacitance due to movement in the cables and reduces the likelihood of picking up external interference.

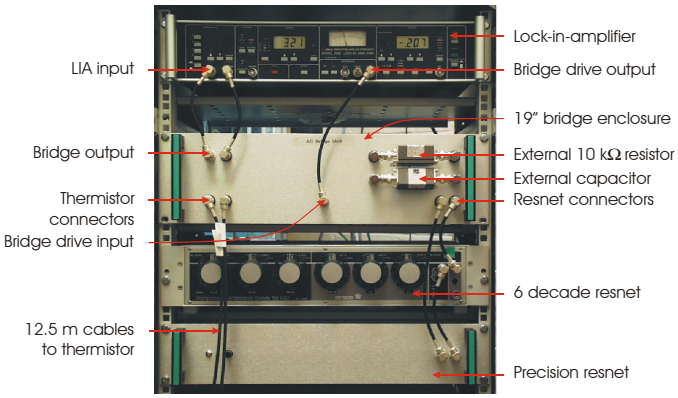

Figure 7: A.C. bridge system. The cable runs between components were kept as short as possible to reduced the likelihood of movement that would change their capacitance. A balancing resistor and capacitor are easily accessible on the front panel for balance adjustment.

1) The LIA

The LIA used is an EG&G 5209[5]. Its principle of operation, as described by the operating manual, is as follows: "In operation, the signal to be measured [in this case the out-of-balance bridge voltage] is made to appear at a reference frequency. The signal is then amplified and applied to a phase-sensitive detector operated at the reference frequency. Because of the frequency translation effects of the phase-sensitive detector, the result is a detector output that includes a value representing the amplitude of the signal of interest as well as a.c. components that may be due to noise and interference. The a.c. resulting from the noise is then reduced to any arbitrary degree by low-pass filters under your control."

The main sections of the LIA are described briefly below:

- Sensitivity section. This section contains the two input connectors which can be operated in current (single-ended, virtual ground) or voltage mode (single-ended or differential, with floating or direct ground), and the sensitivity or amplification options.
- Filters section. This section contains the signal channel filters. The options are Flat (no filter), Bandpass (attenuates above and below f_o), Lowpass (attenuates above f_o) or Notch (attenuates at f_o). There are also two optional notch filters set to 50 Hz and 100 Hz to remove mains-born interference.
- Tuning and reference sections. The tuning section sets the frequency and level of the internal oscillator in the reference section. If the internal oscillator is used to drive the bridge, the reference channel is locked to its frequency. The tuning section also indicates the reference frequency, the filter frequency f_o and indicates and sets the phase shift in the reference channel.
- Output section. This section, amongst other functions, sets the LIA's noise bandwidth via the output time constant (increased time constant = reduced noise bandwidth), the time constant filter's roll-off rate and the dynamic reserve/output stability.

2) The Resnets

Two different Resnets are used. The first is a commercially available Burster 1422[6], which is an IEEE programable, six decade device with a resolution of 0.01 Ω. This is used as the bridge balancing resistor. However, as the accuracy of the 0.01 and 0.1 Ω ranges is relatively poor(± 0.5% and ± 2% respectively), a second Resnet, an NPL built device which is controlled via a computer's parallel or printer port, is used to provide an accurate resistance change. This is achieved by switching a 200, 100, 50, 25, or 12.5 kΩ resistor in parallel with a 100 Ω resistor, as shown in Figure 8. The end result is a change in resistance in the range 0.05 Ω to 0.8 Ω. with an uncertainty of less than 0.05%.

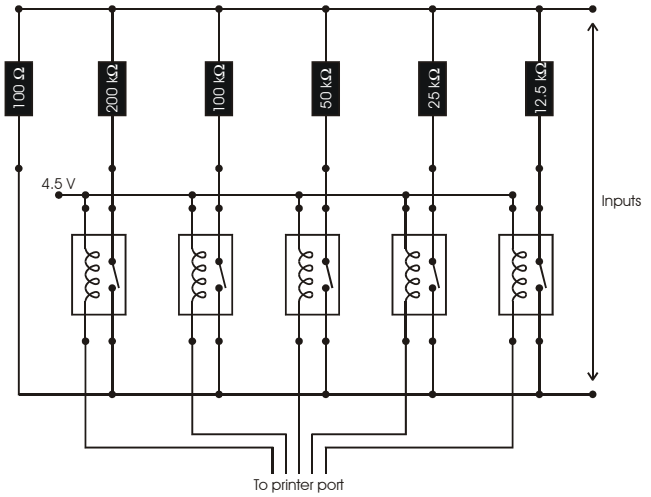

Figure 8: Precision Resnet. Very accurate changes in resistance are made by switching large value resistors (greater than 12.5 kΩ) in parallel with a 100 Ω resistor.

C. Optimization of the A.C. Bridge

To optimize the performance of the a.c. bridge, there are a number of parameters on the LIA that need to be adjusted. The most important are the bridge drive voltage and frequency, and the selection of signal channel filters.

1) Bridge Drive Voltage

The higher the bridge drive voltage, the less susceptible the system to external interference. However, for this application of precision temperature measurement, there is the limiting factor of the power dissipation in the temperature sensor that needs to be less than about 6 μW. For the 10 kΩ thermistors temperature sensors used, this requires that the bridge drive voltage be about 0.5 V_{rms} or less (0.5 V = 6.25 μW).

2) Bridge Drive Frequency

The NPL Primary Standard X-ray Calorimeter uses three a.c. bridges, operating at 162.6, 172.6 and 182.6 Hz[7]. The main criteria in choosing these bridge drive frequencies was that they were not a harmonic of the mains frequency which can vary from 48 to 52 Hz, and that they were not so close together that they would interfere with each other. For this investigation, however, the noise rejection capabilities of the drive frequency were taken into consideration. The output waveform of the LIA was viewed using an oscilloscope. With the signal channel filter set to Band Pass, as the drive frequency was increased from 10 Hz up to 400 Hz the noise pick-up on the output waveform varied, passing through minima at approximately 21, 74 and 321 Hz. Therefore three different bridge drive frequencies were selected for testing, at frequencies of 21.2, 73.6, and 321 Hz.

Fourier transforms of the bridge output (the output waveform can be extracted from the LIA after amplification and prior to the p.s.d) were made with the signal channel filters set to Flat then Band Pass. The bridge drive frequency was set to 21 Hz and the bridge was set to be out-of-balance by inserting a 0.2 Ω offset into the Resnet (equivalent to a temperature signal of 0.5 mK). The results of these measurements can be seen in Figure 9. The following points should be noticed:

- the transform using the Flat filter shows interference over a broad range of frequencies, in particular at multiples of the 50 Hz mains frequency;
- the 50 Hz mains frequency signal level is greater than the 21 Hz bridge drive frequency signal level, and;
- the selected frequencies of 21, 74 and 321 Hz are not too close to any major source of interference;
- the transform using the Band Pass filter shows significant attenuation of all frequencies except the bridge drive frequency of 21 Hz, with the response of the filter being clearly visible, and;
- there is still strong pick-up of the 50 Hz mains frequency, although its signal level has now dropped by about 20 db such that it is below the 21 Hz bridge drive frequency power level.

3) Filters

Tests were performed with and without the F and 2F line rejection filters. However, all tests were performed using a Band Pass output filter set to match the bridge drive frequency, as this attenuated all frequencies except the reference frequency.

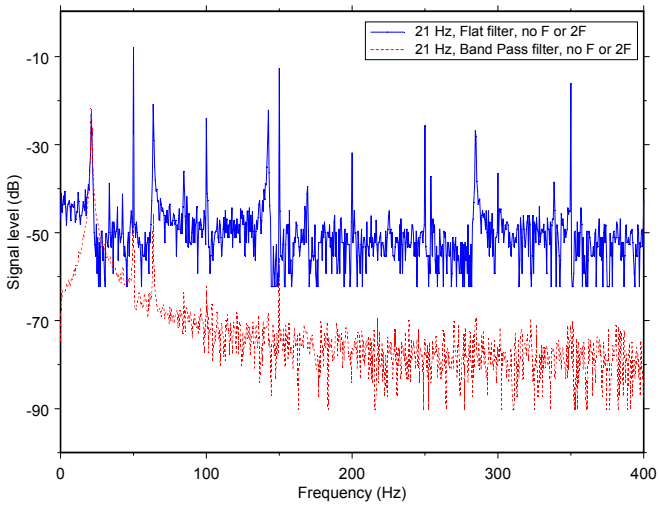

Figure 9: Fourier transforms of a.c. bridge output. Using a flat filter, the system picks up interference over a wide range of frequencies. The use of a band pass filter significantly reduces the level of interference.

D. A.C. Bridge Test Methods

For each combination of bridge drive frequency and input line filters, the following measurements were carried out.

Using a precision resistor in place of the temperature sensor:

- long term stability
- sensitivity (stability)
- signal-to-noise

Using one or two temperature stabilized thermistors:

- sensitivity (stability)
- signal-to-noise

The long term stability of the bridge was measured by recording the bridge output voltage over a period of up to 24 hours with the Resnet resistance remaining constant. The standard deviation of the bridge output was used as an indicator of the stability of the system.

The sensitivity stability was calculated by repeatedly measuring the change in bridge output for a 0.1 Ω (for a single thermistor set-up) or 0.2 Ω (for a double thermistor set-up) change in Resnet resistance - equivalent to a change in temperature of the sensors of 0.3 mK.

The signal-to-noise ratio was calculated by dividing the change in bridge output as measured for the sensitivity calculations by the r.m.s. noise on the pre-calibration step data.

Three sets of measurements were made. The first used a 10 kΩ precision resistor in place of the one temperature sensing thermistor. The resistor was housed in an aluminium box with the connections to the a.c. bridge circuitry being made via 50 Ω BNC connectors so that the resistor and its wiring was fully shielded. The second set of measurements was made with a single 10 kΩ (nominal) thermistor as the sensor (one of the NPL water calorimeter thermistor probes was used. Its temperature was maintained at 4°C by the calorimeter's temperature controlled enclosure). The third and final set of test

measurements used two of the water calorimeter's 10 kΩ (nominal) thermistors as the sensors, again temperature stabilized at 4 ˚C.

E. Test Results

1) Long Term Stability - with Precision Resistor in Place of Thermistor

The results of the long term stability tests are shown in Table 1. Three settings have very similar standard deviations; 21.2 and 73.6 Hz with the F filter, and 321 Hz with no filter. The full

Table 1.

a.c. bridge long term stability results.

	Filter	Frequency (Hz)		
		21.2	73.6	321
σ (mΩ)	none	5.6	12.7	2.6
	F	2.4	2.6	4.3
	F2F	3.7	4.5	6.1

24 hour plots for these three settings are shown in Figure 10. A 0.1 Ω step, equivalent to a temperature change of 0.3 mK, has been inserted into the data to indicate the relative size of the deviations.

2) Bridge Sensitivity and Signal-to-noise Ratio - with Precision Resistor

Figure 11 shows a typical calibration run at 21.2 Hz, with both F and 2F filters. The pre- and post-calibration step data were fitted using linear regressions, and extrapolated for i) approximately four seconds after the time of the calibration step, as the bridge output took approximately four seconds to stabilize after the calibration step, and ii) from thirty seconds either side of t Table 2 he step, as this would be the time taken for the resistance of the sensor to change by 0.1 Ω when irradiated at 1 Gy.min^{-1}.

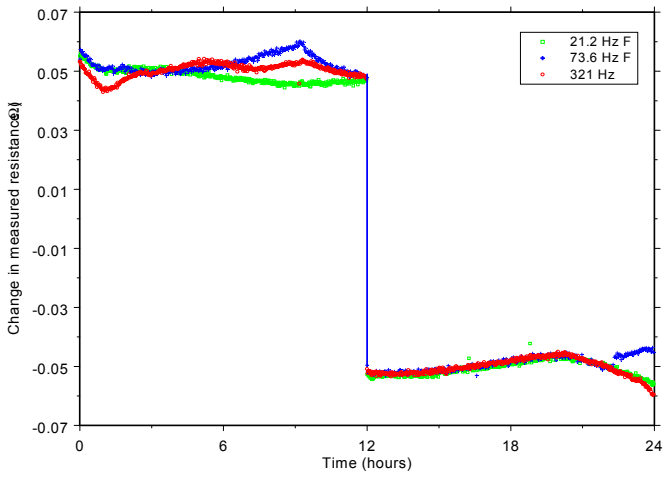

Figure 10: Long term stability of bridge output voltage for various drive frequencies. A 0.1 Ω step has been inserted into the data to indicate the relative size of the deviations.

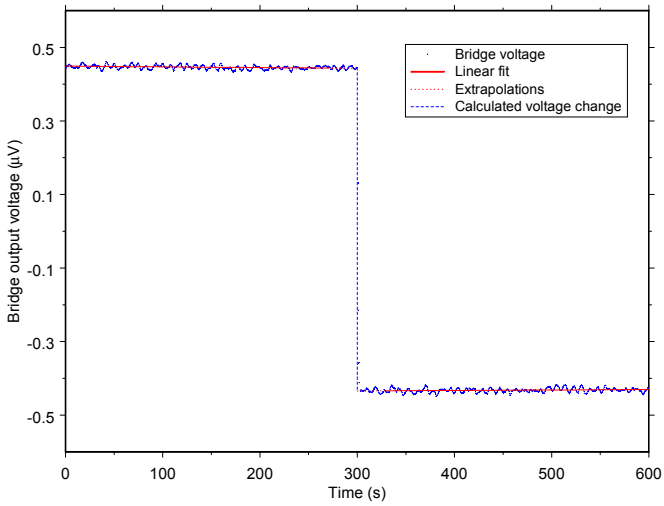

Figure 11: 21 Hz bridge output test. The bridge balance resistance is changed by 0.1 Ω to calculate the bridge sensitivity. This is repeated to calculate the uncertainty on the measurement of bridge sensitivity.

Table 2.

Bridge sensitivity calculated using 10 kΩ precision resistor. The sensitivity decreases as the input filters are enabled and as the drive frequency approaches the filter frequencies.

	Ex	Filter	21.2	73.6	321
Sensitivity (μV/Ω)	2	None	-11.35 ± 0.36%	-11.23 ± 0.25%	-11.31 ± 2.0%
		F	-9.273 ± 0.24%	-5.525 ± 0.6%	-10.02 ± 0.22%
		F2F	-8.803 ± 0.20%	-2.236 ± 0.35%	-10.04 ± 0.24%
	30	None	11.35 ± 0.45%	11.23 ± 0.32%	11.31 ± 2.75%
		F	9.274 ± 0.30%	5.525 ± 0.78%	10.02 ± 0.26%
		F2F	8.806 ± 0.27%	2.233 ± 0.47%	10.04 ± 0.28%
Signal-to-noise	2	None	208 ± 9%	209 ± 8%	172 ± 35%
		F	199 ± 11%	183 ± 10%	230 ± 8%
		F2F	161 ± 6%	156 ± 6%	230 ± 7%
	30	None	210 ± 9%	209 ± 8%	181 ± 31%
		F	200 ± 11%	186 ± 10%	229 ± 8%
		F2F	162 ± 7%	154 ± 7%	231 ± 7%

Table 2 shows the results of the bridge sensitivity and signal-to-noise tests with a precision resistor in place of the thermistor probe. The column *Ex* gives the extrapolation length in seconds. The uncertainties shown in all the following tables in this section are a sample standard deviation (1 σ). For a calibration run of eighteen measurements, and using a coverage factor of $k = 2$ (providing a level of confidence of approximately 95%), an expanded uncertainty of 0.09% for the 21.2 Hz, F2F sensitivity calibration factor is obtained.

3) Bridge Sensitivity and Signal-to-noise Ratio - with One Thermistor Probe

Figure 12 shows a typical calibration run at 21.2 Hz, with the F line rejection filter only. The pre- and post- calibration step data were fitted, as for the precision resistor tests, but this time using linear and quadratic regressions, and extrapolated for i) approximately four seconds after the time of the calibration step, and ii) from thirty seconds either side of the step.

Table 3 shows the results of the bridge sensitivity and signal-to-noise tests using a single calorimeter thermistor probe. The resistance of the thermistor was about 9.33 kΩ.

4) Bridge Sensitivity and Signal-to-noise Ratio - with Two Thermistor Probes

Figure 13 shows typical calibration runs at 321 Hz, with the F and 2F line rejection filters. For these tests, a 0.2 Ω change in resistance was used rather than 0.1 Ω, because this is the combined change in the resistance of the two thermistors for a temperature change of ~0.3 mK. The pre- and post- calibration step data were fitted, as for the precision resistor tests, but this time using linear and quadratic regressions, and extrapolated for

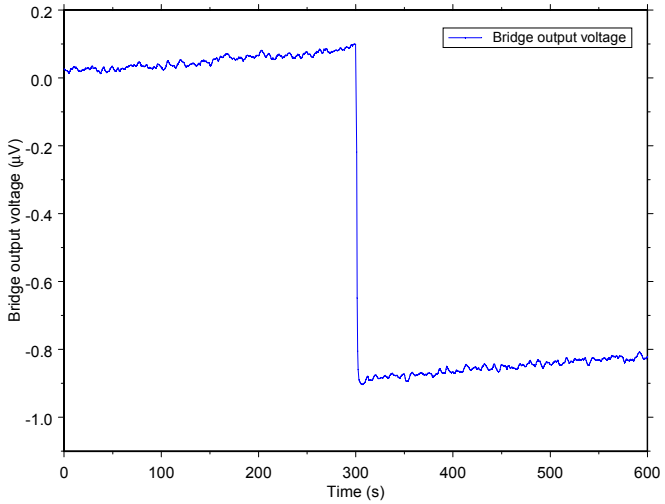

Figure 12: 21 Hz bridge output test using a single thermistor. The bridge balance resistance is changed by 0.1 Ω to calculate the bridge sensitivity

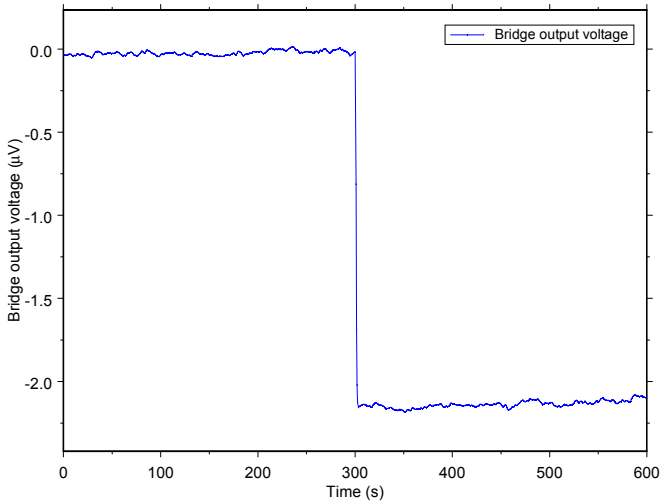

Figure 13: 321 Hz bridge output test using two thermistors. The bridge balance resistance is changed by 0.2 Ω to calculate the bridge sensitivity.

Table 3.

Bridge sensitivity calculated using a single 10 kΩ thermistor probe. As before, the sensitivity varies with input filter. However the signal-to-noise ratio is lower and the uncertainty on the sensitivity measurement is higher than the results shown in Table 2.

	Ex	Filter	21.2 Hz	73.6 Hz	321 Hz
Sensitivity (μV/Ω)	2	None	12.17 ± 0.51%	11.98 ± 1.1%	12.15 ± 0.94%
		F	9.849 ± 0.54%	5.865 ± 0.55%	11.75 ± 0.90%
		F2F	9.422 ± 0.57%	2.414 ± 0.72%	10.68 ± 0.63%
	30	None	12.18 ± 0.70%	11.99 ± 1.2%	12.14 ± 1.5%
		F	9.831 ± 0.76%	5.863 ± 0.70%	11.76 ± 1.3%
		F2F	9.431 ± 0.75%	2.414 ± 1.1%	10.81 ± 0.72%
Signal-to-noise	2	None	153 ± 13%	105 ± 37%	157 ± 10%
		F	153 ± 8%	136 ± 16%	143 ± 14%
		F2F	154 ± 9%	118 ± 14%	146 ± 14%
	30	None	153 ± 14%	110 ± 39%	159 ± 12%
		F	153 ± 7%	139 ± 15%	148 ± 10%
		F2F	155 ± 9%	118 ± 14%	145 ± 16%

Table 4.

Bridge sensitivity calculated using two 10 kΩ thermistor probes. As before, the sensitivity varies with input filter, but the signal-to-noise ratio is significantly higher, and the uncertainty on the sensitivity lower than the single thermistor measurements.

	Ex	Filter	21.2 Hz	73.6 Hz	321 Hz
Sensitivity (μV/Ω)	2	None	12.19 ± 0.47%	12.02 ± 0.73%	12.16 ± 0.64%
		F	9.898 ± 0.77%	5.881 ± 0.49%	11.87 ± 0.98%
		F2F	9.453 ± 0.43%	2.410 ± 0.64%	10.65 ± 0.65%
	30	None	12.18 ± 0.62%	12.01 ± 0.89%	12.16 ± 0.78%
		F	9.891 ± 0.92%	5.88 ± 0.62%	11.87 ± 1.1%
		F2F	9.458 ± 0.59%	2.408 ± 0.97%	10.64 ± 0.82%
Signal-to-noise	2	None	188 ± 12%	203 ± 14%	185 ± 9%
		F	194 ± 12%	197 ± 11%	174 ± 10%
		F2F	183 ± 11%	173 ± 12%	195 ± 14%
	30	None	193 ± 14%	203 ± 14%	193 ± 9%
		F	196 ± 14%	201 ± 13%	185 ± 13%
		F2F	188 ± 12%	175 ± 11%	202 ± 15%

i) approximately four seconds after the time of the calibration step, and ii) from thirty seconds either side of the step.

Table 4 shows the results of the bridge sensitivity and signal-to-noise tests using two calorimeter thermistor probes. The mean resistance of the thermistors was about 9.25 kΩ.

F. Comparison of A.C. Test Results

From the three sets of measurements, the following general observations were made:

- With no input line filters in place, the calculated sensitivity is independent of frequency within the measurement uncertainties.
- With the input line filters in place, as the bridge drive frequency gets closer to the frequency of either the 50 Hz (F) or 100 Hz (2F) filters, part of the output signal is attenuated, resulting in a lower value for the bridge sensitivity. In the case of 73.6 Hz measurements, the output signal is attenuated by approximately a factor of two for each input line filter.
- A decrease in the uncertainty of the bridge sensitivity does not always correspond with an increase in the signal to noise ratio. For example, for the 21.2 Hz measurements using the precision resistor, the opposite is true.

The top three LIA settings for each sensor type (i.e. highest signal-to-noise and lowest uncertainty on the sensitivity) are summarized in Table 5, with both the 2 second and 30 second extrapolation results being taken into account. As expected, the tests with the precision resistor gave the highest signal to noise ratio (~230), and lowest uncertainty on the sensitivity measurement (~0.2%). When a single thermistor was added to the system, the signal-to-noise ratio dropped by almost 35% (to ~150), and the uncertainty on the sensitivity more than doubled to ~0.5%. Adding a second thermistor improved both the signal-to-noise ratio and the sensitivity uncertainty. This was because the bridge output change doubled for the same temperature change compared to that for a single thermistor. However, the increase in the signal-to-noise ratio was not as much as expected. This was because, as it was later discovered, the second calorimeter thermistor probe was much more noisy than the first (the lowest uncertainty on the sensitivity calibration that could be achieved using this thermistor in a single sensor set-up was 0.9%, while the signal-to-noise ratio was only 100). Unfortunately, there was insufficient time to repeat the double thermistor probe measurements with a new probe. Therefore it is not possible to tell whether the second probe was faulty, or the first probe was exceptionally good. Of all the best LIA settings listed in Table 5, the drive frequency of 21.2 Hz appeared frequently, being the second best choice when using a precision resistor, and first choice when using one or more thermistors. However, rather than opting for the first single thermistor set-up where no line filters were used, the single F filter configuration was used. This was because using the F filter significantly reduced the 50 Hz noise component entering the p.s.d, as shown in Figure 14, and therefore the likelihood of mains noise interfering with the system for only a minor increase in uncertainty on the sensitivity measurement.

Table 5.

LIA settings for best results

Sensor	Order	LIA setting	Signal-to-noise	Sensitivity μV/Ω
Precision resistor	1	321, F	230	10.02 ± 0.22%
	2	21.2, F, 2F	161	8.803 ± 0.20%
	3	321, F, 2F	230	10.04 ± 0.24%
Single thermistor probe	1	21.2, none	153	12.17 ± 0.51%
	2	21.2, F	153	9.849 ± 0.54%
	3	73.6, F	136	5.865 ± 0.55%
Two thermistor probes	1	21.2, F, 2F	183	9.453 ± 0.43%
	2	21.2, none	188	12.19 ± 0.47%
	3	73.6, F	197	5.881 ± 0.49%

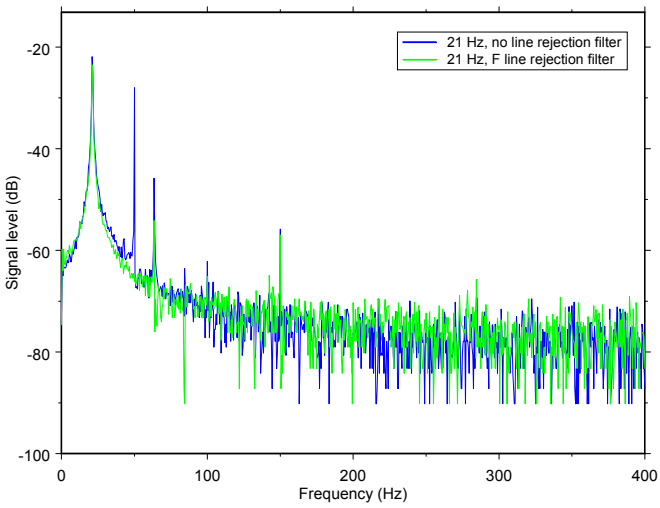

Figure 14: Fourier transforms of bridge output signal at 21.2 Hz. The 50 Hz notch filter significantly reduces the 50 Hz noise component entering the p.s.d.

III. D.C. BRIDGE

A. Design and Construction

The d.c. bridge has been described previously [1]. It was used as the temperature measurement system on the NPL water calorimeter. A brief description of the system follows.

The system is based around two Wheatstone bridges which are double shielded in an attempt to reduced the influence of the electrically noisy environment of the linear accelerator (a combination of RF and mains born interference),. The braid on twisted pair cable makes up the inner shield, while the outer shield is made up of RF screened aluminium boxes and RF screened conduit as shown in Figure 15. The bridges are powered by a 2 V, NPL designed and built, battery powered precision

voltage supply. The 2 V from the supply can be stepped down to any voltage below 2 V by putting an appropriate precision resistor in series with the bridge. The out-of-balance bridge output voltages, read by two digital multi-meters (DMM), can be calibrated against a platinum resistance thermometer to give temperature as a function of bridge output voltage.

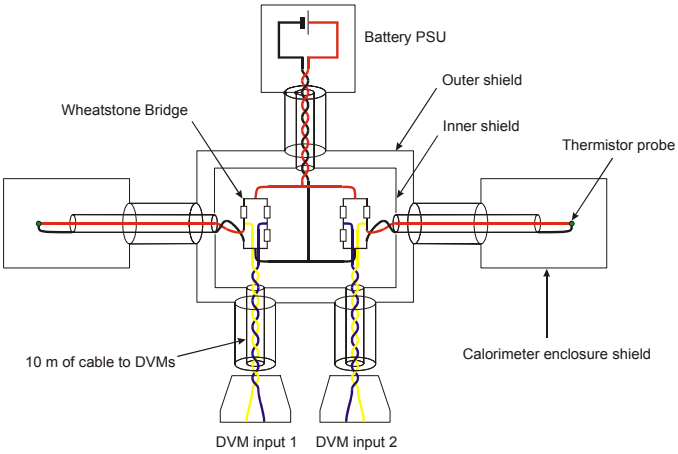

Figure 15: D.C. bridge. Two d.c. Wheatstone bridges have been double shielded to reduce electrical interference. The first shield is made up of a die cast aluminium box and twisted pair cable with braided shield, the second from an RF shielded aluminum box and conduit with braided shield.

B. D.C. Bridge Test Methods

The DMM is an important part of a d.c. bridge system: it needs to be high resolution and low noise. Therefore four different DMMs were tested, a Hewlett Packard 3458A[8], a Keithley 2001[9], a Solartron 7061[10], and a Wavetek 1271. For these tests, the bridge supply voltage was set to 0.5 V, the same as for the a.c. bridge tests.

The following tests were carried out.

Using a 10 kΩ precision resistor in place of the temperature sensor:

- Long term stability

Using a 10 kΩ precision resistor and the NPL Resnet (to allow a 0.1 Ω change in resistance to be made) in place of the temperature sensor:

- Sensitivity
- Signal-to-noise

Using a 10 kΩ thermistor probe and the NPL Resnet:

- Sensitivity
- Signal-to-noise

C. Test Results

1) Long Term Stability

Figure 16 shows the long term stability of the d.c. bridge system using the four different DMMs. The Wavetek 1271 has the best long term stability and the lowset noise level while the Keithley 2001 has the worst long term stability and the highest noise level.

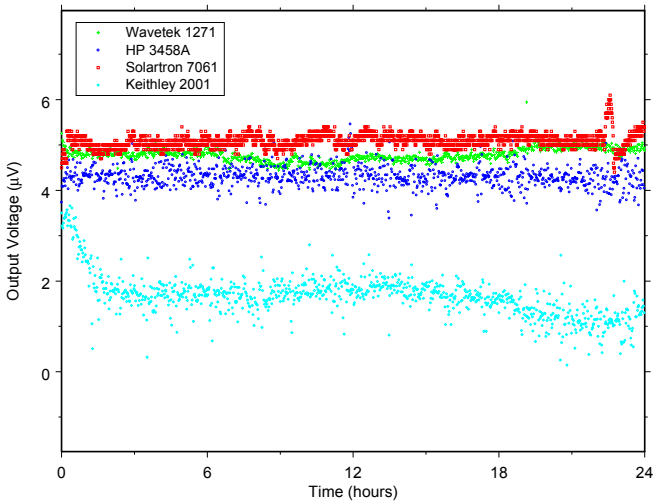

Figure 16: Long term stability of d.c. bridge system with four different DMMs. The Wavetek 1271 has the best stability and lowest noise level.

2) Sensitivity and Signal-to-noise

Figure 17 shows typical bridge output plots for the four DMMs when using a precision resistor in place of the thermistor probe. Table 6 shows the results of the sensitivity and signal-to-noise measurements made using the precision resistor, and with the calorimeter thermistor probe.

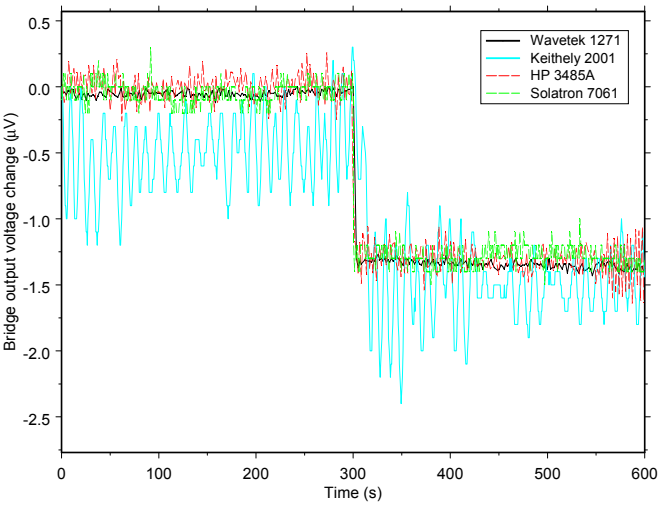

Figure 17: d.c. bridge output test using a precision resistor. The bridge balance resistance was changed by 0.1 Ω to calculate the bridge sensitivity.

The noise level when using the Keithley 2001 almost completely swamps the signal, the HP 3458A also shows bursts of considerable noise pick-up. In contrast, the noise levels when using Solartron 7061 and Wavetek 1271 are much lower, as reflected in the higher signal-to-noise ratios, with the Wavetek having the edge due to the fact that it has a resolution of 10 nV compared to the Solartron's 100 nV. Even so, these results are considerably worse than the equivalent a.c. bridge test results.

Table 6.

D.C. bridge sensitivity calculation results using a precision resistor. Of the four different DMMs tested, the noise level using the Keithley was so high that it swamped the test signal. At the other end of the scale, the Wavetek 1271 had the highest signal-to -noise ratio and lowset uncertainty on the calculated sensitivity although they were considerably worse than the equivalent a.c. bridge results.

Sensor	DMMs	Keithley 2001	HP 3458A	Solartron 7061	Wavetek 1271
Precision resistor	sensitivity	1.59 ± 208%	12.70 ± 2.3%	12.93 ± 6.9%	12.70 ± 1.4%
	signal-to-noise	0	7 ± 40%	15 ± 24%	56 ± 11%
Calorimeter thermistor	sensitivity				11.96 ± 2.7%
	signal-to-noise				45 ± 7%

IV. Measurements Using ^{60}Co Radiation

The optimized version of each bridge, that is single d.c. bridge with Wavetek 1271, single a.c. bridge at 21.1 Hz using F, and double a.c. bridge using 2.12 Hz and F2F, was compared in a ^{60}Co radiation beam from a Mobaltron irradiator. The dose-rate from the Mobaltron unit was approximately 1 Gy/min and the irradiation time used was 2 minutes which resulted in a temperature rise of about 0.5 mK A plot of a typical irradiation for each of the three bridges is shown in Figure 18. The two a.c. temperature plots have had a small offset added to them so that the temperature at the start of the irradiation period coincides with that of the d.c. system. The temperature drift rates are different because the measurement were not carried out simultaneously. About fifteen irradiations were carried out for each bridge set-up.

For each run, the measured temperature rise was converted into the absorbed dose-rate to water. The results of the comparison are shown in Table 7. The uncertainties listed are one standard deviation (σ_{sd}) and the standard uncertainty (σ_{su}) as calculated according to UKAS (1997)[11]. Both a.c. bridges have an uncertainty on the measurement of dose-rate that is half that of the d.c. system, and a signal-to-noise ratio that is triple that of the d.c. system.

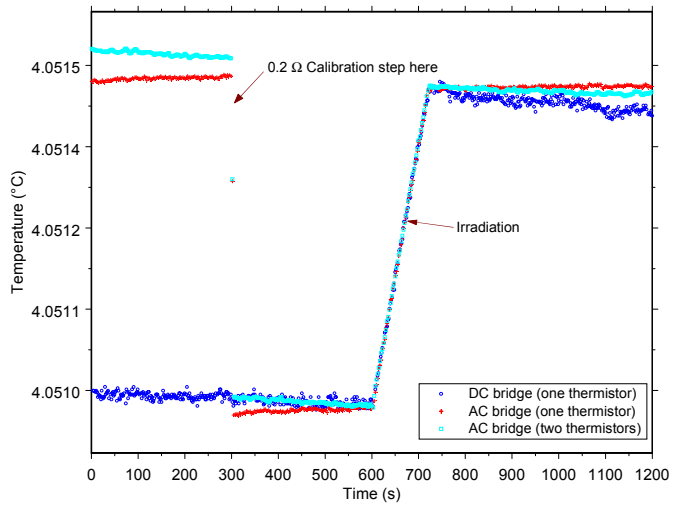

Figure 18: Typical bridge outputs for a 2 minute ^{60}Co irradiation. There is no obvious difference between the a.c. bridge with one or two thermistors, but both are less noisy than the d.c. bridge.

Table 7.

Comparison of a.c. and d.c. bridge results in ^{60}Co radiation. There is very little difference between the two a.c. bridges, but both are significantly better than the d.c. bridge

System	Dose-rate (Gy/min)	σ_{sd}	σ_{su}	Signal-to-noise
d.c. - one thermistor	1.035	± 1.6%	± 0.41%	95
a.c. - one thermistor	1.015	± 0.7%	± 0.18%	270
a.c. - two thermistors	1.028	± 0.8%	± 0.20%	300

Surprisingly, the double thermistor a.c. bridge is no better than the single thermistor a.c. bridge. There are a number of possible reasons for this:

- the double thermistor system has been compromised by the noisy second thermistor, and/or
- the signal-to-noise limit for an a.c. bridge system has been reached, and/or
- the temperature instabilities in the calorimeter are limiting the system's performance.

V. Summary of Results

Table 8 summarizes all the tests carried out on the a.c. and d.c. bridges. In every test, the a.c. system has considerably out-performed the d.c. system in terms of increased signal-to-noise ratio and reduced uncertainty on the sensitivity calculation or dose-rate calculation. Even the least favourable comparison gives the single a.c. system triple the signal-to-noise and half the uncertainty of the single d.c. system. In view of the evidence gained, the preferred temperature measurement system for use on the NPL water calorimeter is the double a.c. bridge system.

Acknowledgements

The authors would like to thank Chris Thomas for his assistance in constructing the d.c. bridge. The authors also

acknowledge the financial support of the National Measurement Policy Unit of the UK Department of Trade and Industry.

Table 8.

Summary of results.

	sensor/system	signal-to-noise	uncertainty (%)
0.1 Ω tests ~0.3 mK	precision resistor a.c.	230	0.2
	double thermistor a.c.	183	0.4
	single thermistor a.c.	153	0.5
	precision resistor d.c.	56	1.4
	single thermistor d.c.	45	2.7
^{60}Co irradiations ~0.6 mK	double thermistor a.c.	300	0.8
	single thermistor a.c.	270	0.7
	single thermistor d.c.	95	1.6

REFERENCES

[1] A.J. Williams and K.E. Rosser, "A Status Report on the NPL Water Calorimeter", *NPL Report*, CIRM 22, December 1998.

[2] A.J. Williams and K.E. Rosser "Comparison of the NPL water calorimeter with other dosimetric techniques for high energy photon beams", *NPL Report* CIRM 23, March 1999.

[3] B.K. Jones,"Electronics for Experimentation and Research", Prentice-Hall International, ISBN 0-13-250754-4.

[4] VHP202 series resistors manufactured by Vishay-Mann Ltd., Wymondham, Norfolk, Great Britain.

[5] EG&G 5209 LIA manufactured by EG&G Instruments, Princeton Applied Research, P.O. Box 2565, Princeton, NJ 08543-2565, USA.

[6] Burster IEC 1422 IEEE programable resistance decade supplied by Cropico, Croydon, Great Britain.

[7] A.R. DuSautoy "The UK primary standard calorimeter for absorbed dose measurement". *Phys. Med. Biol.* Vol 41, pp. 137-151, 1991.

[8] Hewlett Packard HP 3458A manufactured by Hewlett Packard Ltd, Cain Road, Bracknell, Great Britain.

[9] Keithley 2001 manufactured by Keithley Instruments Ltd, The Minster, 58 Portman Road, Reading, Great Britain.

[10] Solartron 7061 (no longer available) manufactured by Solartron, Victoria Road Farnborough, Great Britain.

[11] "The expression of uncertainty and confidence in measurement", NAMAS M3003, December 1997. Available from UKAS, Feltham, Middlesex, Great Britain.

QUESTIONS AND ANSWERS

Carl Ross: What is the peak to peak noise under the best conditions that you observe and how does that compare to what you expect theoretically from Johnson noise?

Andrew Williams: I haven't done any theoretical comparison with Johnson noise. The r.m.s. deviation on the AC bridge is about a microK.

Carl Ross: Do you have it in volts?

Andrew Williams: No, not off the top of my head. [It's about 5 nV r.m.s at 4 ˚C with a 0.5 V drive voltage.]

Jan Seuntjens: The answer to that question would be interesting but there was another graph showing where you operated the bridge for several hours. Did you do any temperature stabilisation of the lock-in amplifier? Joakim Medin has done some experiments that show that the lock-in amplifier, if it is not temperature stabilised, just connected with resistors, we see variation as a function of environment temperature.

Andrew Williams: No I haven't checked that out. We do stabilise the power to most of the devices using a power stabilizer which maintains a stable 230 V because we find that our mains does go up and down by quite a lot which does affect the bridge output.

Ken Gall: What about the stability of the other resistors? You simply state that there are precision resistors but that whole network resistance box and so forth?

Andrew Williams: At the moment the [NPL] resistance box is just made from wire wound resistors which are just 0.1% accuracy [±3 ppm]. I have ordered high precision metal foil ones from Vishay. They are top of the range resistors which are 0.001% accuracy and 0.6 ppm stability so at the end of the day there should not be much noise or fluctuation from the resistor side of things.